UNIVERSITY OF OKLAHOMA

GRADUATE COLLEGE

THE FORMATION OF SMALL-SCALE ATMOSPHERIC VORTICES VIA HORIZONTAL SHEARING INSTABILITY

A DISSERTATION

SUBMITTED TO THE GRADUATE FACULTY

in partial fulfillment of the requirements for the

Degree of

DOCTOR OF PHILOSOPHY

By

MICHAEL SCOTT BUBAN
Norman, Oklahoma
2014

THE FORMATION OF SMALL-SCALE ATMOSPHERIC VORTICES VIA HORIZONTAL SHEARING INSTABILITY

A DISSERTATION APPROVED FOR THE
SCHOOL OF METEOROLOGY

BY

_____
Dr. Michael Biggerstaff

_____
Dr. Conrad Ziegler

_____
Dr. Alan Shapiro

_____
Dr. Evgeni Fedorovich

_____
Dr. Louis Wicker

_____
Dr. S. Lakshmivarahan

Acknowledgments

I would like to thank my advisor, Dr. Conrad Ziegler for his collaboration and patience throughout this project. His thought-provoking ideas and attention to detail have helped me think more critically and objectively. I would like to thank my committee members, Dr. Mike Biggerstaff, Dr. Alan Shapiro, Dr. Evgeni Fedorovich, Dr. Louis Wicker, and Dr. S. Lakshmivarahan for their comments and suggestions.

I would also like to thank Dr. Edward Mansell for help with COMMAS model code. Partial funding for this research was provided by National Science Foundation (NSF) grants AGS-0130316 and AGS-0638572 and by the NOAA/National Severe Storms Laboratory.

Finally, I would like to thank my parents, family, and friends for their support and encouragement throughout this process.

Table of Contents

List of Tables

List of Figures

Abstract

Motivated by recent high-resolution observations of small-scale atmospheric vortices along near-surface boundaries, this study presents a series of simulations that attempt to replicate the dynamics of the dryline and surrounding boundary layer with special emphasis on misocyclones. The first simulation was a real data case, initialized and forced through time-dependent lateral boundary conditions via analyses of temperature, moisture, and momentum from the 22 May 2002 IHOP dataset. The second series of simulations were barotropic runs, initialized with a north-south oriented constant vorticity shear zone and north-south periodic boundary conditions. The third series of simulations were baroclinic, where the shear zone also contained and east-west temperature gradient. The barotropic and baroclinic simulations had varying magnitudes of shear and shear zone widths (corresponding to differing initial vorticity values) across the runs. Additionally, several barotropic simulations were rerun with moisture included to assess preferred could formation regions.

The real data simulation produced several misocyclones with characteristics consistent with those observed along near-surface boundaries in the atmosphere. Several of these misocyclones also had features resembling those observed in many laboratory studies and other numerical studies. Many of these features were also found in the barotropic simulations (i.e. instabilities developed into elliptical cores that precess, contain pressure perturbations in their centers, and evolve with cores connected by vorticity braids). To assess

the instability mechanism, the results were compared to linear theory. Excellent agreement was found between predictions from linear theory in terms of wavenumber of maximum growth as a function of shear zone width and growth rate as a function of shear zone vorticity, suggesting to a very good first approximation, horizontal shearing instability (HSI) is responsible for the growth of initial small perturbations. It was also found that predictions of linear theory tend to extend well into the nonlinear regime. The baroclinic simulations were more complicated and allowed for tilting and stretching of vorticity not seen in the barotropic simulations. As the shear zones contract due to frontogenesis, vorticity increases, thus increasing the growth rates and the wavenumber of maximum growth. An attempt was made to model the contraction and apply a "modified linear theory" to the results, by allowing linear theory to have a time-varying shear zone width. This modified model provided excellent agreement with the simulated results in terms of growth rate and wavenumber of maximum growth.

Finally, an attempt was made to assess preferred regions of cumulus formation by including moisture in the real data case and in several barotropic simulations. It was found that maximum updrafts and simulated cumuli tend to form along the periphery of cores and/or along the braided regions adjacent to the cores. Due to the important modulating effect of misocyclone development via HSI and subsequent moisture transport, cumulus spacing and size/depth was also dependent on the shear zone width and vorticity.

Chapter 1

Introduction

1.1. Motivation

Coherent vortices are commonly observed features of natural fluid flows. In the atmosphere, vortices have been observed across wide-ranging scales. The largest vortices are on the order of 1000 km in horizontal dimension (i.e., extra-tropical cyclones and hurricanes), while the smallest vortices are on the order of 10 m (i.e., tornado suction vortices and dust devils). In addition, even smaller fluid vortices (on the order of a few mm) have been observed during laboratory experiments. There appears to be a relationship between the size of the vortex and the duration if its lifecycle (e.g., Fujita 1981). For example, hurricanes and extra-tropical cyclones may last from several days to more than a week, whereas dust devils may only last a few minutes. Even smaller scale vortices associated with boundary layer (BL) turbulence may last only a few seconds. This is not too surprising, as dissipating effects of viscosity (given essentially the same fluid) should be more efficient as the length scale decreases. Although there have been a plethora of observations of atmospheric vortices across the scales, the mechanisms by which vortices form and are maintained within a fluid initially void of vortices is not well understood on the smaller scales.

The environment in which vortices initiate, grow, and decay will modulate or even dictate the mechanisms by which these processes occur. For example, the environment in which vortices form may be characterized by the presence or absence of horizontal virtual temperature gradients (i.e., either baroclinic or barotropic) and also may have varying degrees of thermal stratification. The basic flow in which vortices eventually develop may contain differing amounts of pre-

existing vorticity that is modulated by shear zones possessing differing widths or magnitudes of shear.

The present study is primarily focused on identifying the hypothesized horizontal shearing instability mechanism (HSI) from which small-scale vortices form and understanding the dynamics that govern their growth and decay, with applications to small-scale atmospheric vortices and their effect on sensible weather. Specifically, the present study is focused on vortices that form along a surface-based interface (i.e., "boundary") that separates fluids with two different velocities. This interface may take the form of a discontinuity (vortex sheet) or a zone of finite width (shear layer). Both barotropic and baroclinic cases will be examined. In contrast with the case of larger atmospheric vortices, the present study will subsequently neglect the Coriolis force since only small-scale (i.e., ~1-4 km horizontal scales) vortices will be examined.

1.2. MISOCYCLONE OBSERVATIONS

High-resolution observations of the planetary BL have revealed the presence of small-scale misovortices (i.e., ~1-4 km in width) along various surface-based boundaries (Crook et al. 1991; Atkins et al. 1995; Pietrycha and Rasmussen 2004; Kawashima and Fujiyoshi 2005; Arnott et al. 2006; Murphey et al. 2006; Marquis et al. 2007; Buban et al. 2007). Vortices having a core circulation diameter between 40 m and 4 km are termed “misocyclones” (Fujita 1981, Wakimoto and Wilson 1989). Recent field observations have demonstrated that misocyclones on this scale are characteristically coherent structures (e.g., Marquis et al 2007, Buban et al 2007) that persist for upwards of 30 minutes or longer and remain attached to the near-surface boundaries within which they form and evolve.

Several studies have hypothesized that these misocyclones may assist convection initiation (CI) by rearranging the moisture and convergence fields

(Pietrycha and Rasmussen 2004; Buban et al. 2007; Lee et al. 2000; Kanak 2008). Other studies have suggested that misocyclones may be associated with non-supercell tornadogenesis by providing a pre-existing source of vertical vorticity that convective updrafts can subsequently intensify via stretching (Carbone 1982, 1983; Wakimoto and Wilson 1989; Wakimoto and Atkins 1996; Lee and Wilhelmson 1997a,b; Wakimoto et al. 1998; Ziegler et al. 2001).

1.3. LABORATORY EXPERIMENTS

Various laboratory experiments have been conducted to study the instability of fluids in the presence of parallel or near-parallel shear. These studies include both stratified and unstratified fluids. Generally, a device is used to generate and bring into juxtaposition two fluid streams with differing velocities. By injecting dyes or by using fluids with differing light-scattering properties, the behavior of the resulting flow can be visualized (e.g., typical experimental apparatus design as described by Winant and Browand, 1974). The initially laminar flow eventually succumbs to instability which subsequently amplifies and moves downstream.

For example, Sato (1959) obtained measurements from wind tunnel experiments approximating a laminar shear layer between two parallel streams. It was found that the wave frequency of the initial (i.e., "natural" or unforced) growth in the shear layer coincided with numerical calculations of Lesson and Fox (1955) for the wave frequency of maximum amplification. Wind tunnel measurements of Browand (1966) were in good agreement with the wave speed and frequency of the maximum amplification and spatial growth rate as calculated by Michalke (1965b) for the case of a hyperbolic tangent velocity profile. Winant and Browand (1974) found that unstable waves grow and the fluid is observed to roll up into discrete vortices after two streams of fluid of different velocities are brought together. Scotti and Corcos (1972) carried out an experiment on a statically stable free shear layer,

where two uniform streams of air were brought together in a wind tunnel. They found unstable modes developing for Richardson number less than 0.25, as predicted theoretically by Miles (1961). Scotti and Corcos (1972) also calculated growth rates for various wavenumbers and Richardson numbers, and their results compared favorably with the numerical results for both the hyperbolic tangent and error function velocity profiles as obtained by Hazel (1972). Wang (1975) expanded upon the study by Scotti and Corcos (1972) to investigate the stability boundaries of a free shear layer using two streams of salt water with larger Richardson numbers, and found results also consistent with Hazel (1972). Thorpe (1971) used a long thin tube to produce a stratified free shear flow via vertical tilting. His experimentally derived growth rates matched those predicted assuming an error function velocity profile.

1.4. NUMERICAL RESULTS

Many studies have been conducted to numerically approximate the stability characteristics of parallel free shear flows. A constant vorticity layer can be approximated by a vortex sheet in the limiting case of small wavenumbers (i.e., large wavelengths). The Kelvin-Helmholtz instability of an infinite vortex sheet has been numerically treated by Rosenhead (1931) with the inclusion of a nonlinear component. His numerical method approximates the vortex sheet with a series of discrete point vortices. Each point vortex then has a velocity potential and the position of each point vortex at a subsequent time is governed by the collective velocity potential of all other vortices. The step-by step integration leads to new positions of the point vortices, and the new "vortex sheet" position is formed by connecting these point vortices by a curve. It is found that the initial instability grows linearly, with subsequent growth due to a second order nonlinear term, eventually leading to a roll-up of the vortex sheet into discrete vortices.

Pozrikidis and Higdon (1985) have considered finite vortex layers consisting of constant vorticity to study the growth of periodic disturbances. They employ a contour dynamics procedure (CD) wherein contours of vortex regions are followed in time. Since there is a velocity potential associated with the rotational fluid, the velocity at any point can be evaluated by integrating over the vortex region. Using a finite number of marker points, the velocities are calculated and the points marched forward in time to give the evolution of the vorticity contours. Their results show that the growth rates are a function of the shear layer width (that in turn is defined as a constant times wavenumber) and compare well with predictions based on linear theory. Guha et al. (2013) applied the CD technique and a direct numerical simulation (DNS) to a piecewise linear shear layer and found that both the CD and DNS procedures agreed with linear theory.

Drazin and Howard (1962) derived general stability criteria for inviscid unbounded parallel flow. Their method, for fixed phase speed (c), was to seek asymptotic solutions to Rayleigh's equation by expansion into a power series in wavenumber (α). The dispersion relations for the piecewise linear shear and rectangular jet profiles were calculated, with results consistent with linear theory. The approximations were then used to calculate growth rates for the cases of *tanh* and $sech^2$ velocity profiles using the first 2 terms and first 3 terms of their expansions.

Hazel (1972) numerically computed stability characteristics for both the *tanh* and error function velocity profiles for various Richardson numbers, using 2 different computer algorithms. Their first method involved fixing α and J (Richardson number) and calculating c by integrating inward from the boundaries, then applying matching conditions at the origin. Their second method fixes $c = 0$, then calculates α and J. In the homogeneous case ($Ri = 0$), their results compare

well with the experimental results of Scotti (1968).

The numerical calculations for various free shear layers (e.g. Lesson 1950; Esch 1957; Betchov and Szweczyk 1963) have shown that the neutral stability curve asymptotically approaches the values determined from inviscid linear theory at large Reynolds numbers. Similar results have been obtained by Tatsumi and Kakutani (1958) who calculate results for a $sech^2$ plane jet. Experiments have also shown that for large Reynolds numbers, the behavior of free shear layers is not appreciably affected by viscosity (e.g. Sato 1960; Schade and Michalke 1962; Michalke and Wille 1965).

The experimental results of Sato (1959, hereafter referred to as "S59") confirm the theoretical result for the wavelength of maximum amplification. S59 also finds differences in the amplitude distribution of the most-unstable wave as well as a phase reversal in a region far removed from the critical layer. In contrast, linear theory predicts a phase reversal at the critical layer. This discrepancy has subsequently been traced to a comparison of spatially growing waves, with linear theory for temporally growing waves. S59 transforms the temporal growth rate into a spatial growth rate using the wave phase velocity. It has later been determined that this transformation is not valid, and new calculations have been performed for the spatial instability case (e.g. Gaster 1965; Michalke 1965b). In the case of temporally growing waves, the wavenumber is real and the phase speed is complex, whereas in the spatially growing case the phase speed is real and the wavenumber is complex. In contrast to the latter investigations, the present study will examine the temporal instability, as the along-stream boundary conditions are periodic and the instabilities grow in time.

Chapter 2

Linear Theory

2.1. GOVERNING EQUATIONS

The present study of horizontal shearing instability in relation to observed misovortex development commends an introductory review of the linear theory for the initial growth of infinitesimal disturbances in parallel shear flows. Early analysis of this problem is attributed to Rayleigh (1880). To complement the present review of linear theory, a rederivation of the classical Rayleigh problem is presented in Appendix A.

To facilitate analysis of the stability of parallel shear flows, it is typically assumed that the flow is inviscid and incompressible (e.g., Drazin and Reid 1981). Assuming the Boussinesq approximation and neglecting viscous terms, the equations of motion take the form

$$\frac{\partial u}{\partial t} + u\frac{\partial u}{\partial x} + v\frac{\partial u}{\partial y} + w\frac{\partial u}{\partial z} = -\frac{1}{\rho_0}\frac{\partial p}{\partial x}, \tag{2.1}$$

$$\frac{\partial v}{\partial t} + u\frac{\partial v}{\partial x} + v\frac{\partial v}{\partial y} + w\frac{\partial v}{\partial z} = -\frac{1}{\rho_0}\frac{\partial p}{\partial y}, \tag{2.2}$$

$$\frac{\partial w}{\partial t} + u\frac{\partial w}{\partial x} + v\frac{\partial w}{\partial y} + w\frac{\partial w}{\partial z} = -\frac{1}{\rho_0}\frac{\partial p}{\partial z} - \frac{\rho}{\rho_0}g, \tag{2.3}$$

where *u, v,* and *w*, are the *x*-, *y*-, and *z*- component velocities, p is the pressure, ρ is the density, g is the gravitational acceleration, and ρ_0 is a constant reference density. The Boussinesq continuity equation is written as

$$\frac{\partial u}{\partial x} + \frac{\partial v}{\partial y} + \frac{\partial w}{\partial z} = 0, \tag{2.4}$$

and the thermal energy equation is expressed as

$$\frac{\partial \rho}{\partial t} + u\frac{\partial \rho}{\partial x} + v\frac{\partial \rho}{\partial y} + w\frac{\partial \rho}{\partial z} = 0. \tag{2.5}$$

As described in Chapter 3.2, the numerical model employed in the present study is based on a governing equation set with the same dominant physical processes (i.e.,

nonhydrostatic momentum and fluid temperature-density conservation) as assumed in equations. (2.1)-(2.5).

2.2. LINEARIZATION OF THE GOVERNING EQUATIONS

With the additional assumptions that the base state zonal flow, pressure, and density are functions of z only, it follows that $U = U(z)$, $P = P(z)$, $\bar{\rho} = \bar{\rho}(z)$ and $V = W = 0$. The governing equations are expanded by assuming that a given variable is the sum of the base state and a small perturbation value. For example, *u* and *p* are expanded as $u(x,y,z,t) = U(z) + u'(x,y,z,t)$ and $p(x,y,z,t) = P(z) + p'(x,y,z,t)$ respectively, where base state values are capitalized and perturbation quantities are primed (for density, the base state is noted with an overbar). . Substituting expanded variables into equations (2.1) – (2.5) and neglecting terms involving products of perturbation quantities, there follows

$$\frac{\partial u'}{\partial t} + U\frac{\partial u'}{\partial x} + w'\frac{\partial U}{\partial z} + \frac{1}{\rho_0}\frac{\partial p'}{\partial x} = 0, \tag{2.6}$$

$$\frac{\partial v'}{\partial t} + U\frac{\partial v'}{\partial x} + \frac{1}{\rho_0}\frac{\partial p'}{\partial y} = 0, \tag{2.7}$$

$$\frac{\partial w'}{\partial t} + U\frac{\partial w'}{\partial x} + \frac{1}{\rho_0}\frac{\partial p'}{\partial z} + \frac{\rho'}{\rho_0}g = 0, \tag{2.8}$$

$$\frac{\partial u'}{\partial x} + \frac{\partial v'}{\partial y} + \frac{\partial w'}{\partial z} = 0, \tag{2.9}$$

$$\frac{\partial \rho'}{\partial t} + U\frac{\partial \rho'}{\partial x} + w'\frac{\partial \bar{\rho}}{\partial z} = 0, \tag{2.10}$$

which express the linearized Boussinesq, inviscid equations of motion, mass continuity, and density conservation.

2.3. NORMAL MODE ANALYSIS OF THE LINEARIZED EQUATIONS

Since the linearized equations all have coefficients that are only functions of *z*, all variables can be separated into a height-dependent part and independent normal modes that are dependent on *x, y,* and *t*. For example we can write:

$$u'(x,y,z,t) = \hat{u}(z)e^{i(kx+\beta y-kct)},\ p'(x,y,z,t) = \hat{p}(z)e^{i(kx+\beta y-kct)}, \text{ etc.} \tag{2.11}$$

Here it is assumed that the physical quantity is represented by the real part of each variable expression, e.g., $u' = \left[\mathrm{Re}(\hat{u})\cos(kx+\beta y-kc_r t) - \mathrm{Im}(\hat{u})\sin(kx+\beta y-kc_r t)\right]e^{kc_i t}$. Since c_r is the real part of the complex velocity while c_i is the imaginary part of the complex velocity, the normal mode solutions thus represent travelling waves with a phase velocity of c_r that grow in proportion to $e^{kc_i t}$. If $kc_i < 0$, the wave decays exponentially and is stable. If $kc_i > 0$, the wave grows exponentially and is unstable.

Taking the form of (2.11) and inserting into (2.6) – (2.10) yields

$$-ikc\hat{u}E + Uik\hat{u}E + \hat{w}\frac{dU}{dz}E + ik\frac{\hat{p}}{\rho_0}E = 0, \tag{2.12}$$

$$-ikc\hat{v}E + Uik\hat{v}E + i\beta\frac{\hat{p}}{\rho_0}E = 0, \tag{2.13}$$

$$-ikc\hat{w}E + Uik\hat{w}E + \frac{1}{\rho_0}\frac{d\hat{p}}{dz}E + \frac{\hat{\rho}}{\rho_0}gE = 0, \tag{2.14}$$

$$ik\hat{u}E + i\beta\hat{v}E + \frac{d\hat{w}}{dz}E = 0, \tag{2.15}$$

$$-ikc\hat{\rho}E + Uik\hat{\rho}E + \hat{w}\frac{d\overline{\rho}}{dz}E = 0, \tag{2.16}$$

where $E = e^{i(kx+\beta y-kct)}$. To simplify the resulting analysis, take $\left(\frac{\partial}{\partial t}+U\frac{\partial}{\partial x}\right)$ of (2.14) and use (2.16) to eliminate $\hat{\rho}$ to yield the expression

$$-k^2c^2\hat{w}E + Uk^2c\hat{w}E + Uk^2c\hat{w}E - U^2k^2\hat{w}E - \frac{1}{\rho_0}\frac{d\hat{p}}{dz}ickE + \frac{1}{\rho_0}\frac{d\hat{p}}{dz}ikUE - \frac{g}{\rho_0}\frac{d\overline{\rho}}{dz}\hat{w}E = 0$$

Simplifying the above, it follows that

$$ik(U-c)\hat{u} + \frac{dU}{dz}\hat{w} + ik\frac{\hat{p}}{\rho_0} = 0, \tag{2.17}$$

$$ik(U-c)\hat{v} + i\beta\frac{\hat{p}}{\rho_0} = 0, \tag{2.18}$$

$$-k^2(U-c)^2\hat{w} + ik(U-c)\frac{1}{\rho_0}\frac{d\hat{p}}{dz} - \frac{g}{\rho_0}\frac{d\overline{\rho}}{dz}\hat{w} = 0, \tag{2.19}$$

$$ik\hat{u} + i\beta\hat{v} + \frac{d\hat{w}}{dz} = 0. \tag{2.20}$$

Defining the new variables

$$\tilde{k} = \left(k^2 + \beta^2\right)^{\frac{1}{2}},\ \tilde{u} = \left(k\hat{u} + \beta\hat{v}\right)/\tilde{k},\ \tilde{p} = \tilde{k}\hat{p}/k,\ \tilde{\bar{\rho}} = \tilde{k}^2\bar{\rho}/k^2,$$

adding k multiplied by (2.17) to β multiplied by (2.18), and dividing the result by k yields the expression

$$i\tilde{k}(U-c)\tilde{u} + \frac{dU}{dz}\hat{w} + i\tilde{k}\frac{\tilde{p}}{\rho_0} = 0\,. \tag{2.21}$$

Eq. (2.21) is the component of the linearized equations in the direction of the wavenumber vector, $\boldsymbol{k} = k\mathbf{i} + \beta\mathbf{j}$. Equations (2.19) and (2.20) can then be transformed as

$$-\tilde{k}^2(U-c)^2\hat{w} + i\tilde{k}(U-c)\frac{1}{\rho_0}\frac{d\tilde{p}}{dz} - \frac{g}{\rho_0}\frac{d\tilde{\bar{\rho}}}{dz}\hat{w}\,, \tag{2.22}$$

$$i\tilde{k}\tilde{u} + \frac{d\hat{w}}{dz} = 0\ . \tag{2.23}$$

This is known as *Squire's transformation* (Drazin and Reid 1981).

2.4. STABILITY ANALYSIS OF TWO-DIMENSIONAL MODES

It is readily evident that equations (2.21) – (2.23) have exactly the same form as equations (2.17) – (2.20) in the special case of two-dimensional wave motion with $\beta = \hat{v} = 0$ and also that the eigenvalues c depend only on the sum of the squares of the wavenumber, so that $k \le \tilde{k}$. Therefore, the relative growth rate kc_i is greatest for some total wavenumber $\tilde{k}$ when $\beta = 0$. In other words, k cannot exceed $\tilde{k}$ and $k = \tilde{k}$ if and only if $\beta = 0$. The physical result is that a three-dimensional wave propagates at some angle to the base flow, and only the component of the wave in the direction of the base flow contributes to wave growth. Since there exists a most-unstable two-dimensional mode for each three-dimensional mode, assessing stability only requires the analysis of two-dimensional modes.

The stability analysis of two-dimensional modes is facilitated by introducing

a streamfunction such that

$$u' = \frac{\partial \psi}{\partial z}, \;\; w' = -\frac{\partial \psi}{\partial x}, \;\; v' = 0 .$$

Inserting the streamfunction in the linearized equations and equating normal modes, it follows that $\psi(x,z,t) = \phi(z)e^{ik(x-ct)}$ and hence $\hat{u} = \phi'$ and $\hat{w} = -ik\phi$. Using the latter definitions and solving (2.16) for $\hat{p}$, there follows

$$\hat{p} = \rho_0 \left[U'\phi - (U-c)\phi' \right].$$

Using this result in (2.18) yields,

$$ik^3 (U-c)^2 \phi + ik(U-c)\left[U''\phi - (U-c)\phi'' \right] + \frac{g}{\rho_0}\frac{d\bar{\rho}}{dz} ik\phi = 0 .$$

Defining $N^2 = -\frac{g}{\rho_0}\frac{d\bar{\rho}}{dz}$ and rearranging, there follows

$$(U-c)\left[\phi'' - k^2\phi \right] - U''\phi + \frac{N^2}{(U-c)}\phi = 0 , \qquad (2.24)$$

which is the *Taylor-Goldstein* (TG) equation (Hazel 1972; Drazin and Reid 1981; Carpenter et al. 2013). The TG equation describes an eigen-problem for the eigenvalue c and the eigenfunction ϕ in terms of the arbitrary profile of U and the static stability N^2. The eigenvalues and eigenfunctions are generally complex. For the complex phase speed, the real part c_r indicates the actual phase speed of the disturbance, while the imaginary part c_i indicates exponential growth (instability) for positive values and exponential decay (stability) for negative values.

2.5. RAYLEIGH STABILITY ANALYSIS

If the static stability is neglected (e.g., assuming constant density profiles), the TG equation reduces to the *Rayleigh stability* equation

$$(U-c)(\phi'' - k^2\phi) - U''\phi = 0 . \qquad (2.25)$$

Equation (2.25) together with the boundary conditions

$$k\phi = 0 \text{ at } \pm\infty \qquad (2.26)$$

define the basic eigenvalue problem for free shear layers.

Rayleigh's stability equation (2.25) with the specified boundary conditions (2.26) is difficult to solve in general when U is a smoothly varying function. However, the approximation of a smoothly varying function with a piecewise-linear function facilitates the solution of eqs. (2.25)-(2.26). The resulting solutions are either exponential or hyperbolic functions within each piecewise-linear sub region, which in turn must satisfy matching conditions at the interfaces between the regions.

If we assume that either U or U' has a discontinuity at some level $z = z_0$ and let $\Delta f = f(z_0 + 0) - f(z_0 - 0)$ represent the jump in f at z_0, then the first matching condition can be determined as follows. First, we rewrite our equation for pressure as

$$\frac{\hat{p}}{\rho_0} = \left[U'\phi - (U-c)\phi'\right]$$

and require that the pressure be continuous across the interface at $z = z_0$. Therefore,

$$\Delta\frac{\hat{p}}{\rho_0} = \Delta\left[U'\phi - (U-c)\phi'\right] = 0\,,$$

so that the first matching condition is that

$$\Delta\left[U'\phi - (U-c)\phi'\right] = 0 \text{ at } z = z_0\,. \tag{2.27}$$

For the second matching condition, we again take the pressure equation and divide by $(U-c)^2$ to get

$$-\frac{\hat{p}}{\rho_0(U-c)^2} = \left[\frac{\phi'}{(U-c)} - \frac{U'\phi}{(U-c)^2}\right] = \left(\frac{\phi}{U-c}\right)'.$$

If we integrate across the discontinuity from $z_0 - \varepsilon$ to $z_0 + \varepsilon$ and take the limit as $\varepsilon \to 0$,

$$\Delta\left(\frac{\phi}{U-c}\right) = -\lim_{\varepsilon\to 0}\int_{z_0-\varepsilon}^{z_0+\varepsilon}\frac{\hat{p}}{\rho_0(U-c)^2}dz\,. \tag{2.28}$$

The right hand side of (2.28) vanishes provided either that $c_i \neq 0$ as $\varepsilon \to 0$ or if $c_i = 0$, then $U - c \neq 0$ within the interval of $z_0 - \varepsilon$ to $z_0 + \varepsilon$. Therefore, the second

matching condition becomes

$$\Delta\left(\frac{\phi}{U-c}\right)=0 \text{ at } z=z_0 . \tag{2.29}$$

Given the two matching conditions, Rayleigh's equation can be solved for a variety of piecewise linear profiles of U. Since in any linear velocity profile, $U''=0$, Rayleigh's equation reduces to $(U-c)(\phi''-k^2\phi)=0$. If we ignore the continuous part of the spectrum resulting from the singularity when $U=c$, then $\phi''-k^2\phi=0$. This second order linear differential equation with a constant coefficient has a general solution of the form

$$\phi(z)=Ae^{kz}+Be^{-kz} .$$

For the case where the piecewise linear profile has the form

$$U(z)=\begin{cases} u & (z>b \\ u\dfrac{2z-b}{b} & (0<z<b) \\ -u & (z<0 \end{cases} \tag{2.30}$$

it is convenient to take the following general solution form

$$\phi(z)=\begin{cases} Ae^{-k(z-b)} & (z>b \\ Be^{-k(z-b)}+Ce^{kz} & (0<z<b) \\ De^{kz} & (z<0) \end{cases} \tag{2.31}$$

after using the boundary conditions that $\phi\to 0$ at $\pm\infty$. Here, $A,B,C,$ and D are constants that need to be determined. From the first matching condition, using (2.31) yields

$$U'A+(U-c)kA=U'B+U'Ce^{kb}+k(U-c)B-k(U-c)Ce^{kb} \quad \text{at } z=b ,$$

then using (2.30) gives

$$k(u-c)A=\left[\frac{2u}{b}+k(u-c)\right]B+\left[\frac{2u}{b}-k(u-c)\right]e^{kb}C \tag{2.32}$$

At $z=0$,

$$U'Be^{kb}+U'C+(U-c)kBe^{kb}-(U-c)kC=U'D-(U-c)kD$$

again, using 2.30,

$$\left[\frac{2u}{b}+k(-u-c)\right]e^{kb}B+\left[\frac{2u}{b}-k(-u-c)\right]C=\left[\frac{2u}{b}-k(-u-c)\right]D \qquad (2.33)$$

The second matching condition (2.29) at $z=b$ gives

$$A=B+Ce^{kb} \qquad (2.34)$$

and at $z=0$ gives

$$Be^{kb}+C=D. \qquad (2.35)$$

By eliminating the four constants *A, B, C,* and *D* in (2.32) – (2.35), the eigenvalue relationship between the complex phase speed $c=c_r+ic_i$ and wave umber *k* may be derived. Equations (2.32)-(2.35) expressed in matrix form with the determinant set to zero, i.e.,

$$\begin{vmatrix} k(u-c) & -\left[\frac{2u}{b}+k(u-c)\right] & -\left[\frac{2u}{b}-k(u-c)\right]e^{kb} & 0 \\ 0 & \left[\frac{2u}{b}+k(-u-c)\right]e^{kb} & \left[\frac{2u}{b}-k(-u-c)\right] & \left[\frac{2u}{b-k(-u-c)}\right] \\ 1 & -1 & -e^{kb} & 0 \\ 0 & e^{kb} & 1 & -1 \end{vmatrix}=0$$

yields the resulting expression,

$$c^2=\frac{u^2}{b^2}\left[(kb-1)^2-e^{-2kb}\right]. \qquad (2.36)$$

The condition $c^2>0$ represents two stable waves that travel in opposite directions. Conversely, the condition $c^2<0$ represents two stationary waves where one wave is unstable and the other wave is stable. Setting $\left[(kb-1)^2-e^{-2kb}\right]=0$, we find that the shear layer with critical wavenumber $k=\frac{1.28}{b}$ is only unstable for wavenumbers $0<k<\frac{1.28}{b}$ and stable otherwise. Differentiating (2.32) with respect to k and setting the expression equal to zero yields the most-unstable wavenumber $k\approx\frac{0.8}{b}$. A plot of equation (2.36) is shown in Fig. 2.1.

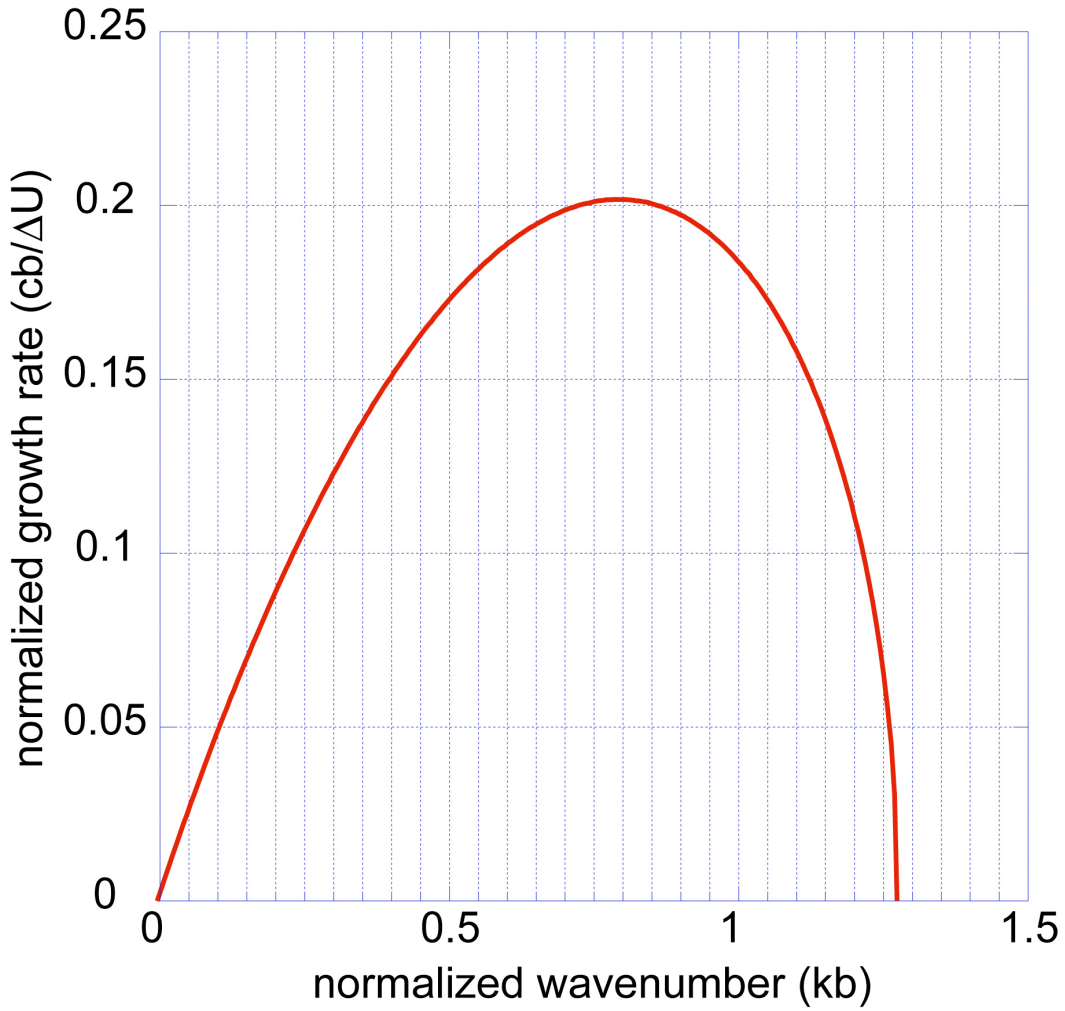

Figure 2.1. Normalized growth rate as a function of wavenumber as defined by eq. (2.36).

Chapter 3

Data analysis and model description

3.1. IHOP DATA

Radial velocities from multiple Doppler radars were used to synthesize the evolving 3-D BL airflow near surface-based mesoscale boundaries observed during IHOP (e.g. Buban et al. 2007; Ziegler et al. 2007). Using these wind fields, a Lagrangian analysis was performed to retrieve the evolving 3-D thermodynamic structure of the BL (Buban et al. 2007). The Lagrangian analysis advects in situ observations from mobile mesonets, aircraft, and mobile soundings, as well as pseudo-sounding grid point data both upstream and downstream along trajectories computed from the radar-synthesized wind fields (Ziegler et al. 2007). The Lagrangian data are then temporally and spatially weighted and objectively analyzed to the grid using a two-pass Barnes objective analysis scheme (Barnes 1973). Both the radar and Lagrangian analyses have a grid spacing of 500 m in the horizontal and 250 m in the vertical, with a total horizontal extent of 30 km and a vertical extent of 2.5 km (above which there is little or no Doppler velocity data). Examples of Lagrangian and multiple-Doppler wind analyses are shown in Fig. 3.1(c, d).

3.2. MODEL DESCRIPTION

3.2.1. Overview

The dryline-BL simulations in the present study are conducted using the Collaborative Model for Multiscale Atmospheric Simulation or COMMAS (Wicker and Wilhelmson 1995; Coniglio et al. 2006; Mansell et al. 2010; Buban et al. 2012, hereafter referred to as "B12"). COMMAS is a cloud-resolving and nonhydrostatic model, and it includes 5th-order advection (Wicker and Skamarock 2002) and a 1.5-

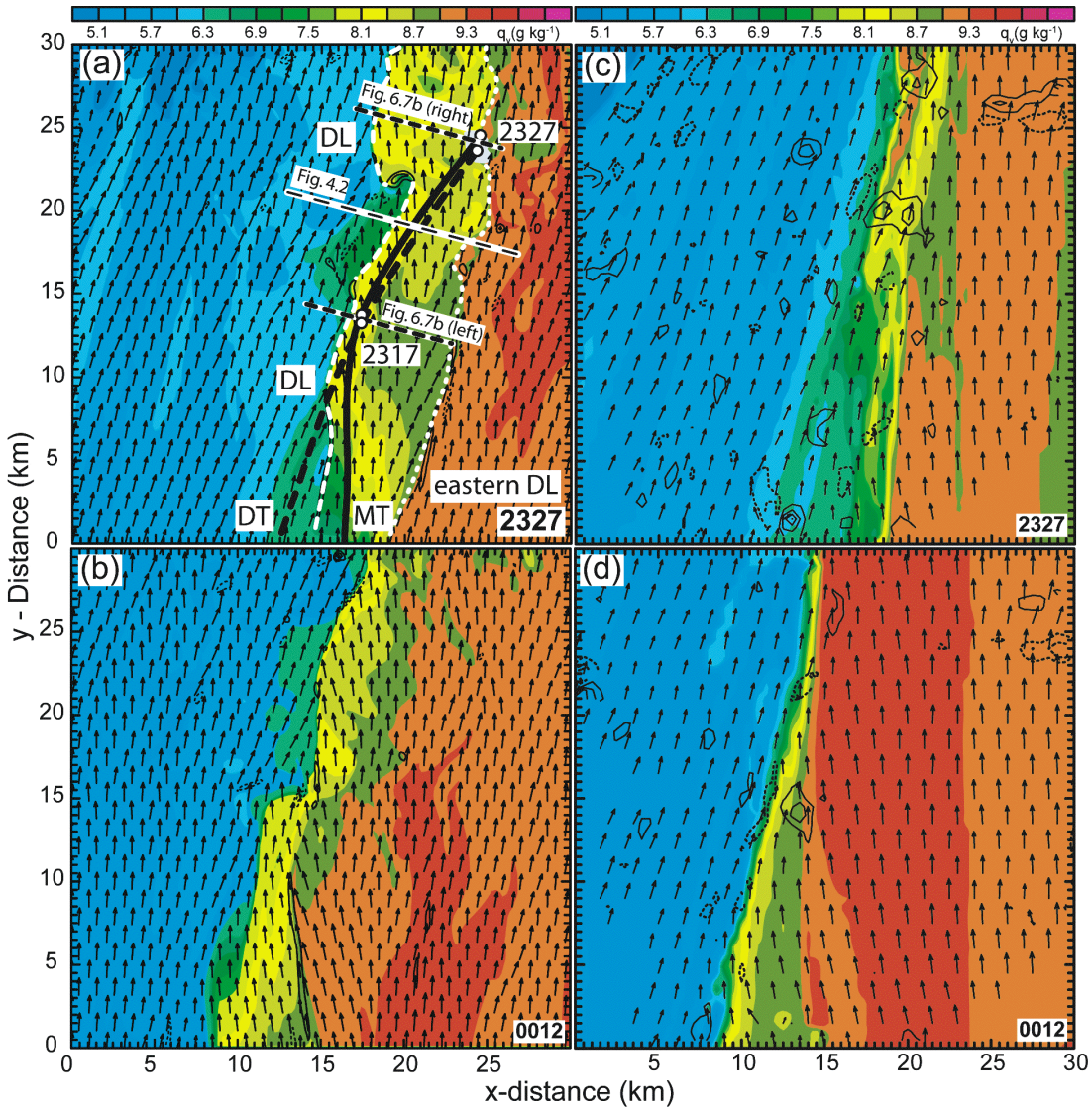

Figure 3.1. Water vapor mixing ratio (color filled), horizontal wind vectors (1 km = 20 m s^{-1}) and vertical vorticity every 20 x 10^{-3} starting at ±20 x 10^{-3} (Left) and 3 x 10^{-3} starting at ±3 x 10^{-3} (right), with positive values solid and negative values dashed. a) Simulation at 2327 UTC; b) simulation at 0012 UTC; c) Lagrangian analysis at 2327 UTC; d) Lagrangian analysis at 0012 UTC. The longer dashed line in panel (a) locates cross-sections shown in Fig. 4.2, while the shorter dashed lines in panel (a) locates cross-sections shown in Fig. 6.7. The vertical levels are at 20 m AGL (left) and ground level (right). The solid and dashed black curves denote the horizontal component of the moist (MT) and dry (DT) trajectories shown in Fig. 6.7. The short-dashed and dotted white curves denote the dryline and eastern dryline respectively.

order subgrid-scale turbulence parameterization. The lower boundary was treated as free-slip and the upper boundary as rigid. Since only shallow cumulus clouds are to be simulated, a simple Kessler warm-rain scheme was used to model the cloud microphysics. The dryline-BL modeling case is hereafter referred to as the "real data" case or simulation, since radar and Lagrangian analyses were used to initialize and provide time-dependent lateral inflow boundary conditions for the simulation as described below. The other two sets of simulations are the barotropic and baroclinic runs also described below.

3.2.1. Model description for real data case

Several new features were added to COMMAS to study BL circulations and misocyclones for the real data case (B12). Time-varying specified inflow boundary conditions were incorporated to allow nudging from the Lagrangian analyses. Since surface fluxes are important to BL structures in the dryline environment (Sun and Wu 1992; Ziegler et al. 1995; Ziegler et al. 1997), the model was also modified to include surface fluxes as calculated with a modified version of the Deardorff (1978) force-restore land surface/atmosphere exchange model (Peckham et al. 2004). Parameters of the surface physics scheme are listed in Table 1, while a comparison of modeled and observed surface fluxes for this case study are discussed in Appendix B. A surface shortwave and longwave radiation parameterization (Benjamin and Carlson 1986; Peckham et al. 2004) that includes the cloud-shadowing effect was also added.

The type of lateral boundary condition used is critically important to the model solution. Whether in smaller domains, or where the speed of meteorological features is such that the advective time-scale across the domain is small, the impact of the boundary conditions on the solution may be comparable to that of the initial conditions. As the initial conditions are advected out of the

domain, features introduced at the lateral boundaries and acted on by the model physics replace them. It is necessary to apply the lateral inflow boundary conditions with a fine enough temporal and spatial resolution to introduce misoscale features of interest into the domain, where they may subsequently evolve according to the fully nonlinear physics. For example, preliminary tests using 9-minute-interval multiple-Doppler wind analyses applied at the boundary proved too coarse, and no misocyclones developed in the model interior. Only when the 3-minute-interval analyses were used was the information communicated to the model interior fine enough for misocyclones to form. It is also important that, in conjunction with the specified inflow boundary conditions, lateral outflow boundaries (where the normal component of the wind is exiting the domain) are wave-radiating to allow for features to exit the domain with minimal feedback.

Parameter	Value
Surface temperature (i)	314.6 K
Soil temperature (i)	305 K
Soil moisture (upper layer) (i)	15 %
Soil moisture (lower layer) (i)	25 %
Canopy soil moisture (i)	0 %
Albedo (c)	0.20
Roughness length (c)	0.05 m
Vegetation coverage (c)	90 %

Table 1. Parameters for the surface physics scheme. The letter "i" corresponds to an initial condition (i.e., these quantities are subsequently predicted), while "c" represents a constant.

To resolve small-scale features, the model's horizontal grid spacing was set to 150 m. This resolution was chosen to adequately resolve small-scale forcing

mechanisms, yet coarse enough to be compatible with the spatial Lagrangian and multiple-Doppler radar analysis morphologies. In the vertical, the grid had a lowest layer thickness of 40 m at 20 m AGL. The model grid spacing is smaller than the Lagrangian analysis grid spacing of 500 m. Since BL structures were emphasized and only rather shallow cumuli were observed on 22 May, the upper boundary had a layer thickness of 200 m at 6 km AGL. The 30 km x 30 km x 6 km simulation model grid thus contains 201 x 201 x 61 grid points. The model was integrated with a time step of 2 sec. The model's base state profiles of pressure, potential temperature, vapor mixing ratio, and *u*- and *v*- wind components were prescribed from a mobile ground-based sounding (i.e., as depicted in Fig. 3c of Buban et al. 2007).

The initial conditions for the dryline simulation were provided by spatially interpolating the radar wind synthesis and Lagrangian analysis fields corresponding to the initial model time onto the model grid from the surface through 2.5 km AGL. The horizontally homogeneous initial model fields above 2.5 km were prescribed from the base state sounding. The initial pressure field was calculated by applying a hydrostatic balance constraint within each grid column.

The time-dependent lateral inflow boundary conditions for the dryline-BL simulation were obtained by spatially and temporally interpolating the 3-minute interval multiple-Doppler wind fields and 9-minute interval Lagrangian analyses via nudging to the (fixed, ground-relative) model grid at each time step. Above the 2.5 km level within the lateral inflow boundary surfaces, time-invariant and horizontally homogeneous fields were specified from the base state. Thus, observed fine-scale BL structures obtained from the radar and Lagrangian analyses were communicated into the model domain where they were subsequently forced by the nonlinear physics.

3.2.3. Model description for idealized simulations

For the idealized simulations, the base-state flow and the shear zone are assumed to be meridionally-oriented and centered within the model domain that takes the form of a meridionally extensive channel. In contrast to the real data dryline simulations, the idealized simulations instead assume periodic north-south boundary conditions and thus yield an essentially infinite-length channel.

The idealized simulation domain was configured with a 100 m grid spacing in both the horizontal and vertical directions. The domain size was 29.9 km in the meridional (along-stream) direction, 14.9 km in the zonal (cross-stream) direction, and 4 km in the vertical (i.e., 300 x 150 x 41 grid points). As inferred from simulation results to be presented, the chosen grid spacing is hypothesized to adequately resolve commonly observed features along drylines (e.g., shear zone width, vertical vorticity bands and isolated vortices, updrafts) as well as the physical instability mechanisms leading to misovortexgenesis. In addition, the expanded along-stream dimension was set up to better resolve the range of wavenumbers encountered in various model configurations.

The initial conditions for the idealized simulations were produced by parametrically prescribing model variables. A random *v*-component perturbation of 0.01 m s^{-1} was also added to the initial wind field. Additional simulations were run with different initial perturbations to test sensitivities to the results (Appendix C). The idealized simulations can be grouped into two categories, the barotropic simulations and the baroclinic simulations, which were both dry (i.e., no water vapor or cloud processes). For the simpler barotropic simulations, the initial potential temperature fields were horizontally homogeneous. The initial *u*- and *w*-wind components were assumed zero everywhere, while a horizontal shear in the *v*-wind component was prescribed. More specifically, the *v*-component wind was

prescribed with a constant value on the left side of the domain, a constant shear zone in the center of the domain, where the *v*-component increases linearly across the zone, followed by a constant value on the right side of the domain. This initial condition for the *v*-component corresponds to the piecewise-linear shear zone employed by Rayleigh (1880) and as reviewed in Chapter 2 and Appendix A. The piecewise-linear shear zone configuration consists of zero vorticity outside the shear zone, a constant vorticity inside the shear zone, and a vorticity discontinuity on each lateral boundary of the shear zone.

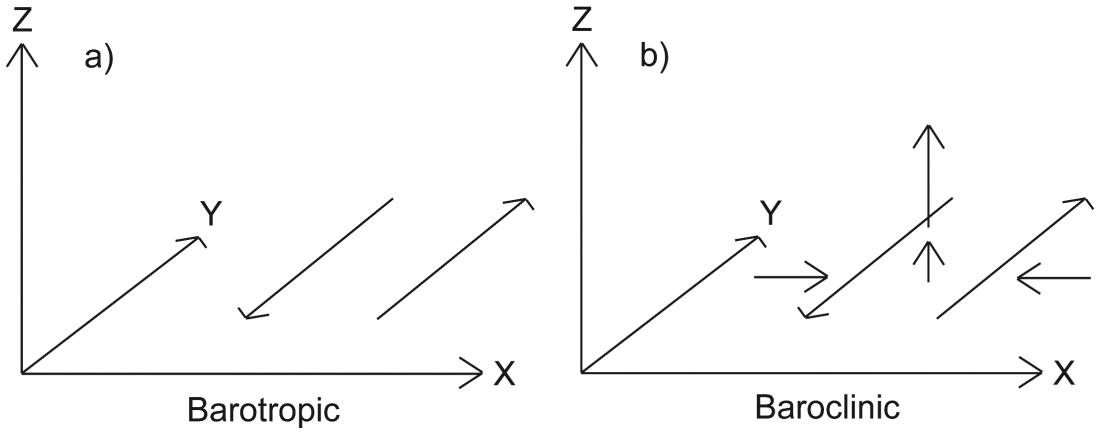

Figure 3.2. Schematic setups of the barotropic (a) and baroclinic (b) simulations.

shear width	6 m s^{-1}	8 m s^{-1}	12 m s^{-1}	16 m s^{-1}	20 m s^{-1}	24 m s^{-1}
400 m	4m6s	4m8s	4m12s	4m16s	4m20s	4m24s
500 m	5m6s	5m8s	5m12s	5m16s	5m20s	5m24s
600 m		6m8s	6m12s	6m16s	6m20s	6m24s
800 m			8m12s	8m16s	8m20s	8m24s
1000 m			10m12s	10m16s	10m20s	10m24s

Table 2. Acronyms for model run names as functions of shear zone width and shear magnitude for the various simulations. A prefix "bt" or "bc" is added to a given name in the text to indicate a barotropic (bt) or baroclinic (bc) run respectively

ζ (x 10^{-3} s^{-1})	6 m s^{-1}	8 m s^{-1}	12 m s^{-1}	16 m s^{-1}	20 m s^{-1}	24 m s^{-1}
400 m	15	20	30	40	50	60
500 m	12	16	24	32	40	48
600 m		13.3	20	26.7	33.3	40
800 m			15	20	25	30
1000 m			12	16	20	24

Table 3. Magnitude of the constant vertical vorticity within the shear zone for each simulation.

The *v*- wind component was also assumed to be constant with height. Therefore, the shear was purely due to the variation in north-south wind, and the initial vector vorticity everywhere was purely vertically oriented. The initial setup is detailed schematically in Fig. 3.2. To test the “barotropic instability mechanism” (Fig. 3.2a), a series of simulations were conducted by varying the width of the shear zone and the magnitude of the shear across the shear zone (Table 2) – thus varying

strength of the initial vorticity within the shear zone (Table 3).

For the dry baroclinic simulations (Fig. 3.2b), the *v*- and *w*-components were prescribed as in the dry barotropic runs. However, in the baroclinic cases, a horizontal potential temperature gradient was imposed within the shear zone. The shear parameters for each of the simulations were the same as in the barotropic cases. To simulate the dryline environment, a horizontal potential temperature difference of 0.5 *K* was prescribed with temperatures decreasing linearly eastward across the shear zone. The horizontal potential temperature gradient was only imposed from the surface up to 1.5 km. Above 1.5 km, the initial conditions were horizontally homogeneous in all variables except for v. Due to the inclusion of the horizontal potential temperature gradient (thus also a density gradient), a non-zero *u*- component was applied between the surface and 1.5 km AGL to the west of the dryline to maintain the horizontal position of the density gradient near the center of the domain. To counteract the intrinsic easterly density current phase speed, a westerly *u*-component was prescribed with a maximum value near the surface that linearly decreasing to zero at 1.5 km. The *u*-component takes the form:

$$U(z) = U_{sfc} - U_{sfc}\frac{z}{H},$$

where U_{sfc} is the velocity at the surface, z, is the height AGL, and H is the depth of the cold layer (1.5 km). The theoretical density current speed of magnitude U_{sfc} depends on the magnitude of the horizontal temperature gradient following the expression (Ziegler et al. 2010)

$$U_{sfc} = U_{dc} = bU_{env} - F\left[\frac{(gD\Delta\theta_v}{\theta_{v0}}\right]^{\frac{1}{2}}.$$

After a short period of initial dynamical adjustment in which the boundary width contracts via meridionally-uniform frontogenetic forcing, the basic flow structure follows the schematic in Fig. 3.2b.

The previously mentioned periodic north and south boundary conditions

allowed northward moving features to pass through the northern boundary and re-enter the southern boundary to continue their evolution. Wave-radiating boundary conditions were employed on the eastern and western lateral domain boundaries, while a free-slip boundary condition was employed at the surface. Parameterized friction, surface fluxes and radiation schemes were deactivated in the idealized simulations, since the goal of this study was to focus attention on horizontal shearing instability mechanisms.

3.3. SPECTRAL DENSITY ESTIMATION

To compare the idealized simulations to the results of linear theory (e.g., to compare the theoretical most-unstable wavenumber against the fastest growing wavenumber in the simulations), spectral density estimation was performed on spatial series in the meridional (downstream) direction. The spectral density estimation follows procedures described by Jenkins and Watts (1969, hereafter referred to as JW69).

Spatial series of variables (e.g., u, v, ζ) were output from the model at 30 s intervals along the entire downstream direction at every grid point residing in the initial meridionally-oriented shear zone. For example, for an initial 1000 m shear zone spanning NY spatial points in the y-coordinate direction of the simulation domain, 10 spatial series each containing NY = 300 grid points would be output for each variable every 30 s. For each spatial series the following procedure was performed. As verified by inspection, the time series of simulated variables in the shear zone were strongly forced by the constant, imposed larger-mesoscale background zonally-sheared meridional flow and thus did not require linear detrending. The mean was computed as

$$\overline{u} = \frac{1}{N}\sum_{i=1}^{N} u(y),$$

which was subsequently subtracted from each data point. For the remaining equations u is used as an example variable. The variance was then computed from

$$\sigma_u^2 = E\left[u(y)^2\right] = \frac{1}{N}\sum_{i=1}^{N} u(y)^2 .$$

Next the autocovariance function was computed, which takes the form

$$c_{uu}(d) = \frac{1}{N}\sum_{y=1}^{N-d} u_y u_{y+d} \quad 0 \le d \le N-1 ,$$

where c_{uu} is the autocovariance function of variable u and d is the lag distance in the y-direction.

To reduce the variance in the final spectral estimate, a lag window was calculated and applied to obtain the smoothed spectral estimate. According to this procedure, a Tukey window was used with the weights calculated by (JW69)

$$w(d) = \frac{1}{2}\left(1 + \cos\frac{\pi d}{M}\right),$$

where M is the truncation point. The truncation point was set to NY/3. The value of M controls the degree of smoothing of the spectral estimate. Smaller values of M produce smoother estimates, however may introduce larger biases in the estimate. Larger values of M retain more (possibly spurious) variance in the spectral estimate, however with smaller biases. (JW69). By trying various truncation points, it was concluded that the value of $M = NY/3 = 100$ provided the optimal spectral estimate via minimized bias and maximized smoothing to eliminate spurious peaks.

To demonstrate the effect of smoothing, several lag windows with varying truncation points were applied to the bt5m16s case (Table 2, Fig. 3.3). The larger values of M retain more amplitude in the critically-important peak of the spectrum, while also retaining more variance including possibly spurious sidelobes that may be related to the well-known Gibbs phenomenon (JW69). The small values of M eliminated most of the possibly spurious variance, but also underestimated the peak

amplitude and introduced bias by shifting the peak amplitude to smaller wavenumbers.

The smoothed spectral estimates were then computed from (JW69)

$$C_{uu}(k) = 2c_{uu}(0) + 4\sum_{d=1}^{M-1} w(d)c_{uu}(d)\cos\left(\frac{2\pi dk}{ny}\right) \quad 0 \le k \le \frac{ny}{2},$$

where k is the wavenumber. The smoothed spectral density estimates were then averaged over the shear zone in wavenumber-space.

$$\bar{C}_{uu}(k) = \frac{1}{N}\sum_{i=1}^{N} C_{uu_i}(k)$$

where N is the number of grid points across the shear zone (i.e. if the shear zone is 1 km, N=10). The averaged smooth spectral density estimates shows how the variance (or amplitude) of the spatial series is distributed over wavenumber. This variance is distributed over a continuous range of wavenumbers, so that on a plot of $\bar{C}_{uu}(k)$ vs. k, the area under the curve is equal to the percentage of the variance of the series explained by the wavenumbers in the range of

$$\bar{C}_{uu}(k) \text{ to } \bar{C}_{uu}(k + \Delta k).$$

Note that in all spectral estimate figures, the amplitude (square root of the variance) was plotted.

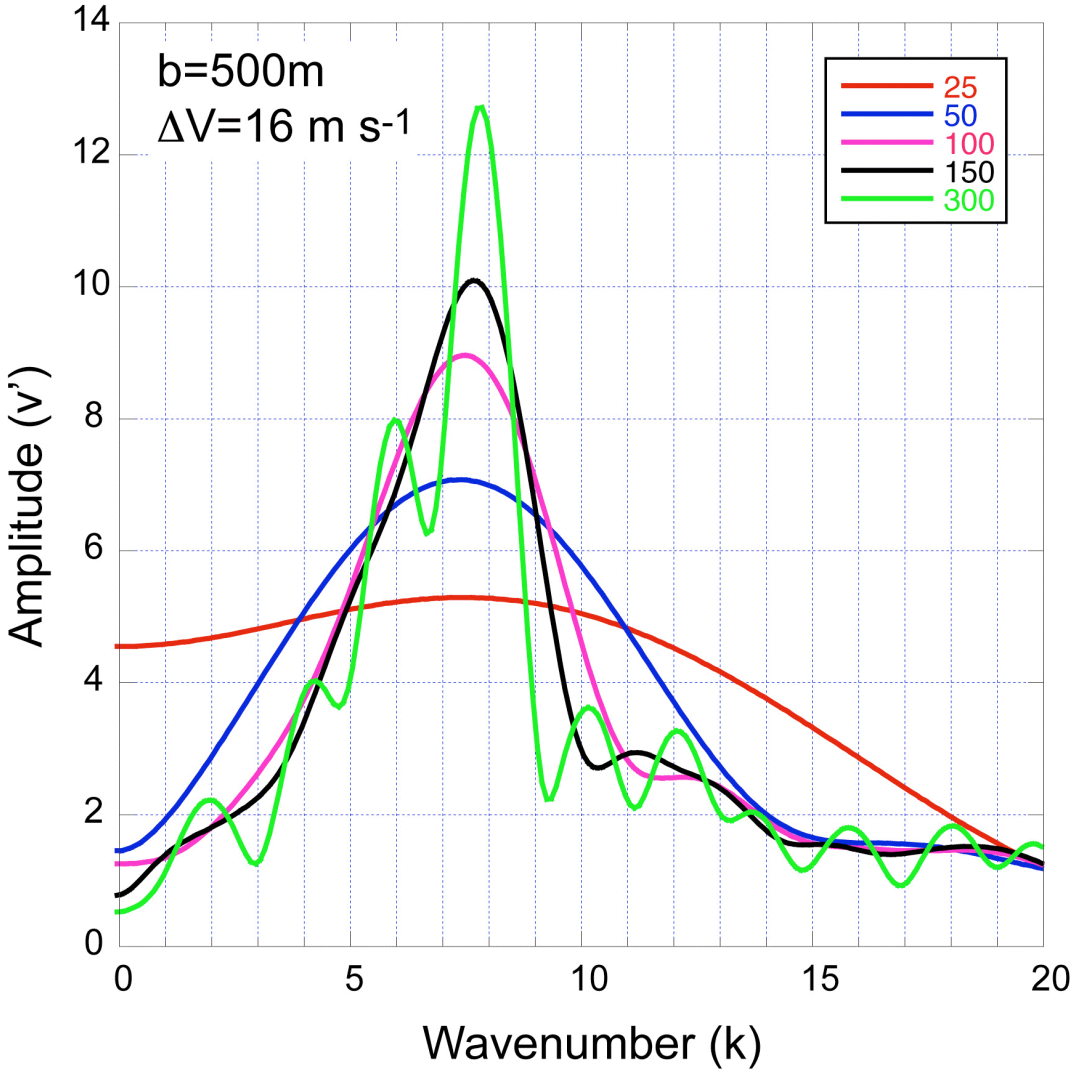

Figure 3.3. Spectral density estimates at 5 different truncation points for the idealized simulation case with a shear zone width of 500 m and a shear magnitude of 16 m s^{-1}. The value of the truncation point used in this study (100) corresponds to the magenta colored curve.

Chapter 4

Case study of dryline misocyclones on 22 May 2002

4.1. MESOSCALE DRYLINE ENVIRONMENT

The dryline and surrounding BL were simulated by B12 within an intensive observing region (IOR) where data were collected on 22 May 2002 during the International H_2O Project (IHOP). The fixed model domain had the same dimensions and location as the IOR, facilitating both data assimilation and model validation. The initial conditions were specified at 2242 UTC from the Lagrangian analysis for temperature and moisture and the multiple-Doppler radar analysis of horizontal velocity. The simulations were run for 90 minutes (2242-0012 UTC) corresponding to the time of the first and last Lagrangian analyses.

Both the analysis and the simulation contain a nearly north-south oriented dryline that vacillates initially before retrograding to the west later in the period (Fig. 3.1). The modeled and observed drylines are characterized by horizontal confluence and a strong moisture gradient (2-3 g kg^{-1} km^{-1}), as also evidenced by the individual mobile mesonet traverses (Buban et al. 2007). The modeled dryline has a tendency to form along vortex sheet segments indicative of concentrated across-dryline shear of the dryline-parallel wind component. Variability in the moisture fields is manifest as small undulations or ripples that move northward along the dryline at nearly the speed of the mean BL flow. Because the thermally forced BL circulations take on order 10 min to develop within the roughly 20 m s^{-1} southerly flow downstream from the inflow boundaries, analysis of the fully-formed misoscale BL structure is valid only within about the northern two-thirds of the domain. Hence, subsequent discussion of the local airflow perturbations (e.g., updrafts cells, misocyclones, etc.) will emphasize the portion of the domain from y = 10 km to 30 km.

The 2-D horizontal accumulation of a scalar gradient (analogous to the frontogenesis function for the rate of change of the potential temperature gradient), neglecting source, sink, and mixing terms, can be expressed in the form (Sanders 1955; Bluestein 1993; Ziegler et al. 1995; Grasso 2000; Buban et al. 2007; B12)

$$F = \frac{1}{|\nabla_H s|}\left[\frac{\partial s}{\partial x}\left(-\frac{\partial u}{\partial x}\frac{\partial s}{\partial x} - \frac{\partial v}{\partial x}\frac{\partial s}{\partial y}\right) + \frac{\partial s}{\partial y}\left(-\frac{\partial u}{\partial y}\frac{\partial s}{\partial x} - \frac{\partial v}{\partial y}\frac{\partial s}{\partial y}\right)\right], \qquad (3.1)$$

where $\nabla_H = (\partial/\partial x)\mathbf{i} + (\partial/\partial y)\mathbf{j}$ and the scalar s is either water vapor mixing ratio or virtual potential temperature in the present study. B12 showed that the simulated dryline is dominated by persistent accumulation of water vapor mixing ratio gradients and virtual potential temperature gradients at low levels (Fig. 4.1), as also shown from the observations and Lagrangian analysis reported by Buban et al. (2007, their Fig. 17). The quantity defined as accumulation (Saucier 1955) in the present study has been called frontogenesis in many previous dryline studies. A degree of localized along-dryline variability, however, exists in the structure of the accumulation field, especially during the early parts of the simulation. In the vertical, the dryline tends to have strong positive accumulation at low levels and negative accumulation at upper levels, consistent with convergence near the surface and divergence aloft as parcels exit the dryline updraft. This vertical structure of persisting airflow circulation and horizontal accumulation was also analyzed by Buban et al. (2007) and simulated in an earlier dryline case by Ziegler et al. (1995).

The vacillating dryline location is marked by a persistent, strong localized maximum of solenoidal forcing (via the horizontal vorticity equation) that collocates with the maximum updraft (Fig. 4.2). The persistent updraft core located at the dryline manifests the upward branch of a persistent secondary circulation that is maintained by persistent solenoidal forcing that is evident in the mean flow (B12;

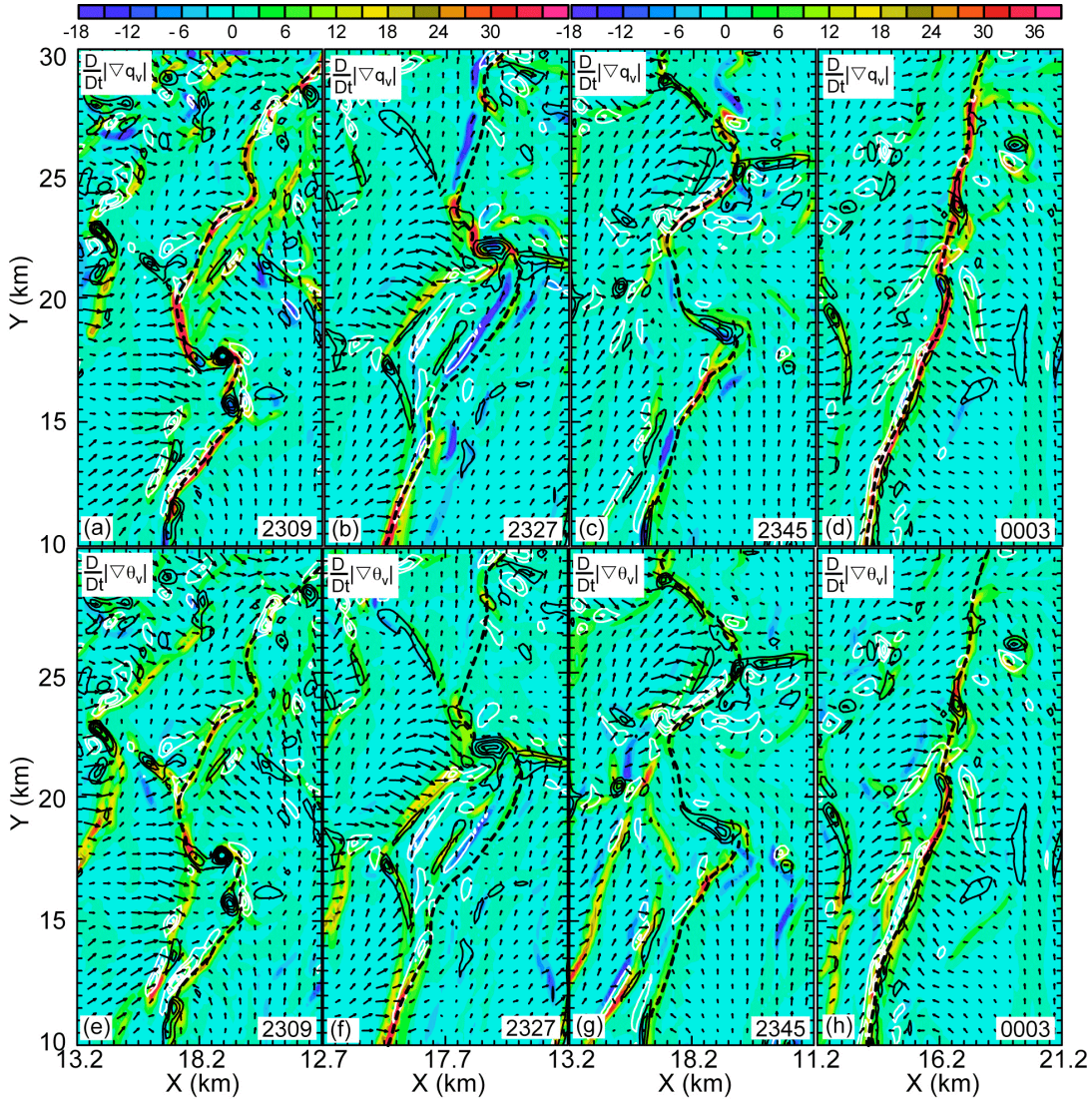

Figure 4.1. Simulated horizontal accumulation (color filled) of water vapor mixing ratio (a-d) and virtual potential temperature (e-h) at 250 m AGL and 2309-0003 UTC. Also shown are misocyclone-relative wind vectors (1 km = 5 m s^{-1}) calculated by subtracting a mean wind of 18 m s^{-1} at 190° from the total wind, and vertical vorticity every 5 x 10^{-3} starting at 5 x 10^{-3} (-5 x 10^{-3}), with positive values black and negative values white. The black dashed curves denote dryline locations.

see also Fig. 18 of Buban et al. 2007). The solenoidal secondary circulation assists in forming and maintaining the dryline by generating convergent, accumulative flow and vertical motion along the dryline. The solenoidal generation is a maximum at low levels and tilts downshear with height, as also shown in the Lagrangian analysis of Buban et al. (2007) and the modeling study of Ziegler et al. (1995). Wakimoto and Murphey (2009) analyzed the 22 May dryline on the mesoscale via dropsondes, and they documented the existence of a mesoscale virtual potential temperature gradient in the BL, which contributed via solenoidal forcing to a mesoscale secondary circulation with a maximum at low levels. Miao and Geerts (2007) list several other observed drylines that are all collocated with density gradients and secondary circulations. Schultz et al. (2007) discuss the relationship between the strength of the dryline gradient and the synoptic-scale confluence. From 2242 UTC through 0012 UTC, both the analysis and simulation maintain strong horizontal convergence and updraft speeds along the dryline, as also shown by Weiss et al. (2006).

Although the strongest vertical motion tends to develop along the dryline, comparably intense localized cells or bands of vertical motion are also seen to the east and west of the dryline (Figs. 4.2-4.3). The presence of HCRs, transverse rolls, and OCCs are noted to the west of the primary dryline (Fig. 4.3) resulting from unstable stratification via surface heating that forces a net upward sensible heat flux (B12). The simulated HCRs, transverse rolls, and OCCs have a similar structure to those features in the Lagrangian analyses (Buban et al. 2007, their Fig 5).

As localized updraft cells evolve, cumuli develop at times within deeper updrafts in the northern part of the domain (B12). Higher-based cumuli develop both along a secondary dryline to the west of the primary dryline and along stronger plumes associated with HCRs and OCC segments (Fig. 4.4). Lower-based

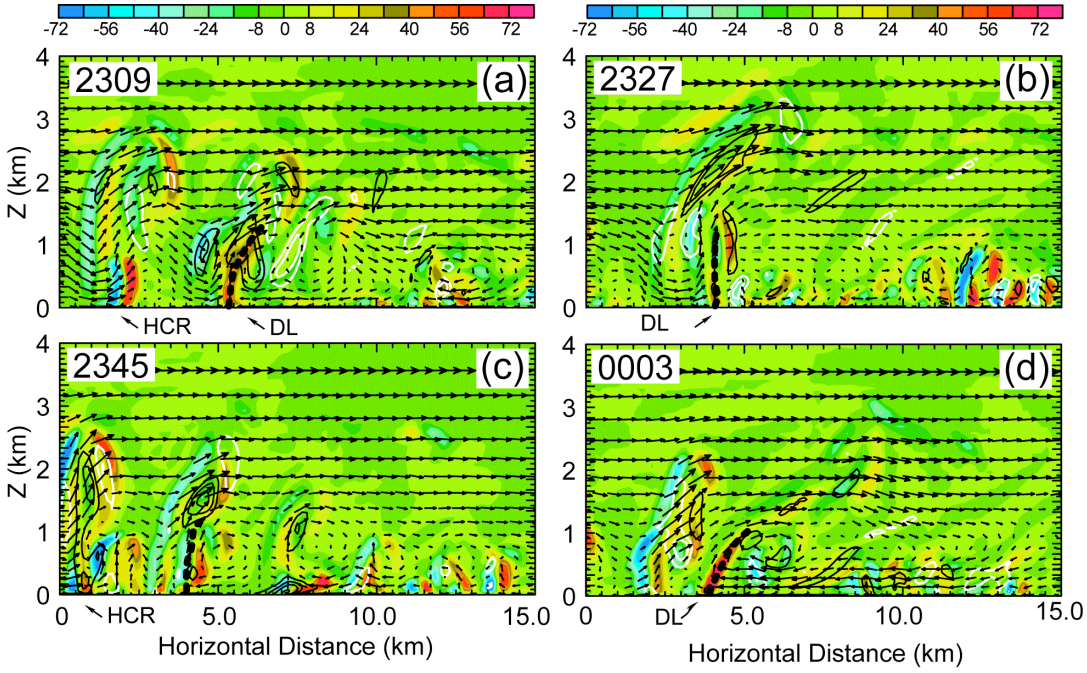

Figure 4.2. Vertical cross-sections of the simulated solenoidal generation (color-filled) of the along-dryline component of vorticity (x 10^{-6} s^{-2}). Also plotted are ground-relative wind vectors in the plane (1 km = 5 m s^{-1}) and vertical vorticity every 5 x 10^{-3} starting at 5 x 10^{-3} (-5 x 10^{-3}), with positive values black and negative values white. Also shown are the locations of the dryline (DL) and a horizontal convective roll (HCR). The cross-section locations are shown in Fig. 3.1.

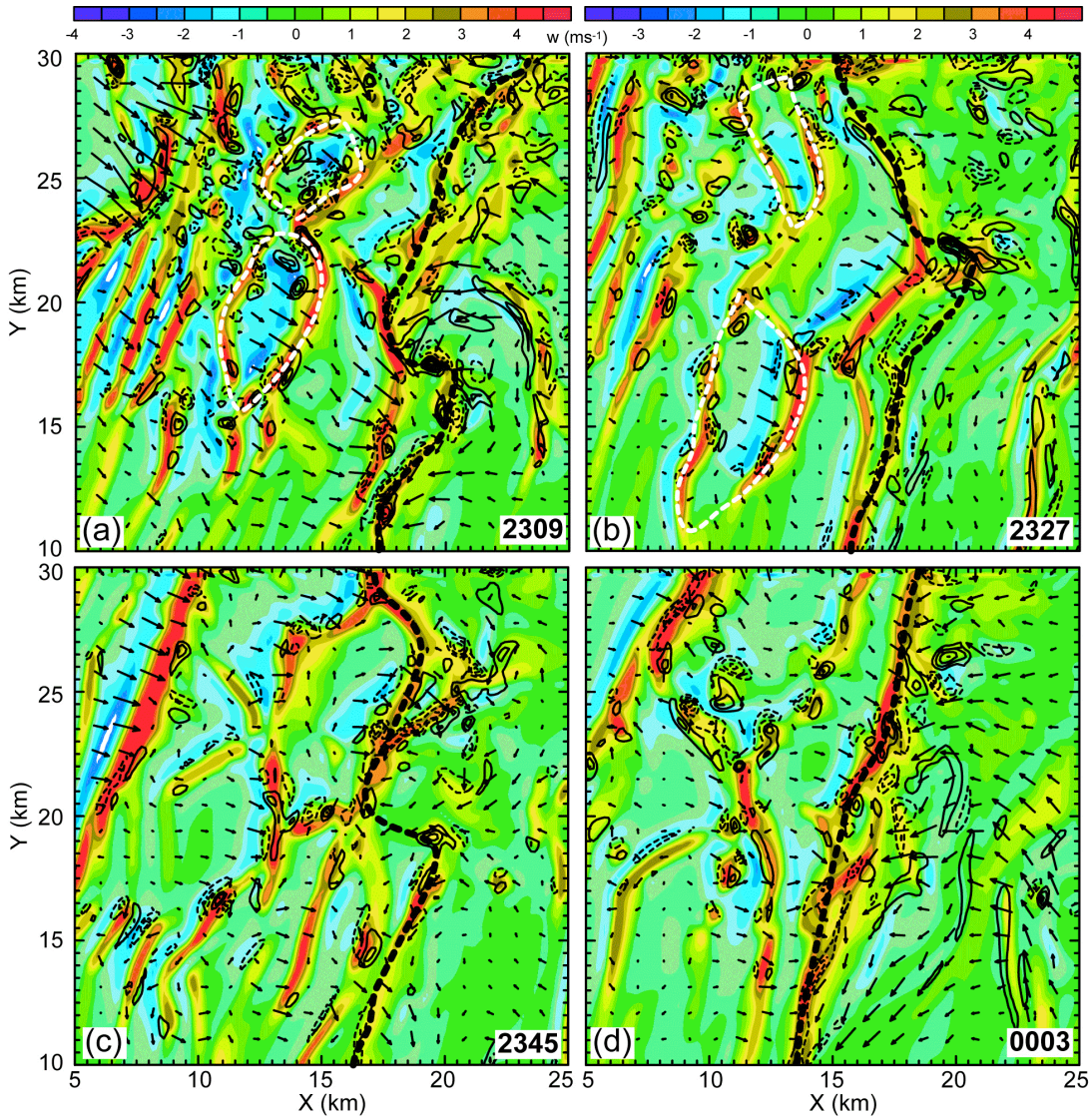

Figure 4.3. Simulated vertical velocity (color-filled) and misocyclone-relative wind at 500 m AGL (vectors) calculated by subtracting a mean wind of 18 m s^{-1} at 190° from the total wind, with a vector length of 1 km = 5 m s^{-1}. Also shown are contours of vertical vorticity at 5 x 10^{-3} intervals starting at 5 x 10^{-3} (-5 x 10^{-3}), with positive values solid and negative values dashed. The white dashed lines indicate OCCs. The dashed black curves denote the dryline locations.

cumuli develop to the east of the primary dryline where BL circulations have interacted with and crossed over the surface dryline location. Cumuli also develop along and east of the dryline where updrafts associated with solenoidal forcing locally lift a mixture of moist and dry air within a mesoscale updraft. As the simulation progresses toward early evening, the dryline retrogrades westward and BL convection west of the dryline weakens owing to the loss of surface heating as outgoing longwave radiation exceeds insolation.

4.2. DRYLINE MISOCYCLONES

The horizontal scale of the misocyclones on 22 May is generally about 1-3 km in the simulations (B12), somewhat smaller than in the radar analyses. This is likely a result of the grid spacing differences between the radar analyses (500 m) and the model (150 m). The vortical circulations in the simulations are able to contract in scale via persistent convergent forcing owing to the finer grid spacing, allowing them to match the scales inferred from the raw single-Doppler data. Conversely, the radar analysis of Buban et al. (2007) employed a 1-pass Barnes radar data interpolation, which in combination with the relatively coarse grid resulted in spatial smoothing of the objectively analyzed misocyclones (e.g., Majcen et al. 2008). The maximum vertical vorticity within the simulated misocyclones (~ 30 x 10^{-3} s^{-1}) is also stronger than the radar-synthesized misocyclones (~10 x 10^{-3} s^{-1}), again likely owing to the difference in grid resolution and radar analysis smoothing.

Observed airflow undulations and bands of concentrated *v*-component wind shear in the *x*-direction that coincide with the dryline are introduced at the southern model domain boundary via the time-dependent lateral inflow boundary conditions (B12). The radar-observed flow perturbations on the southern inflow boundary are prescribed from the input radar analyses (e.g., Fig. 4.5). In contrast, the *u*-

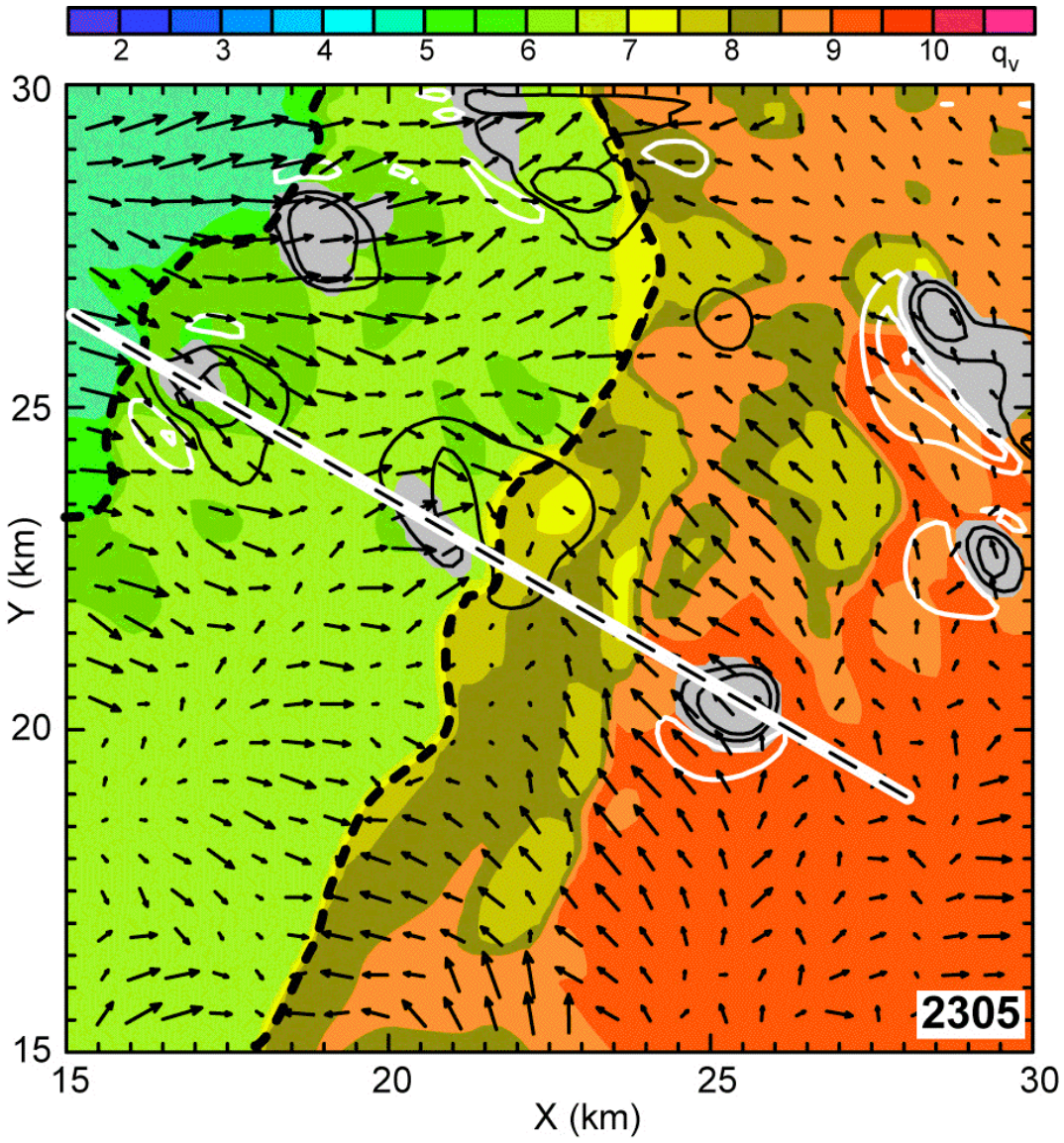

Figure 4.4. Simulated water vapor mixing ratio (color filled) at the lowest model level, cloud water mixing ratio > 0.05 g kg^{-1} (grey shaded) at ~3.5 km AGL, and misocyclone-relative wind vectors at the lowest model level calculated by subtracting a mean wind of 18 m s^{-1} at 190° from the total wind, with 1 km length equal to 5 m s^{-1}. Vertical velocity is contoured at 2 m s^{-1} intervals starting at 1 (-1) m s^{-1} with positive (negative) values black (white) and is shown at ~3.5 km AGL. The black dashed curves denote the dryline location. The black dashed line indicates the cross-section shown in Fig. 6.5.

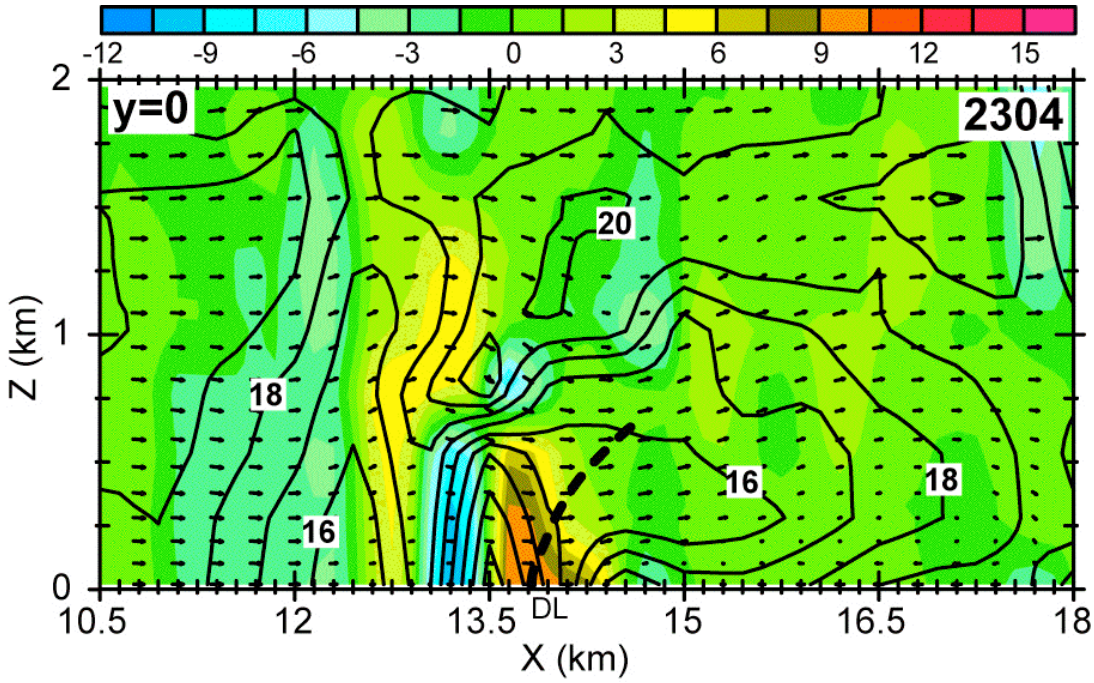

Figure 4.5. Vertical cross-section along the southern boundary with simulated vertical vorticity (color-filled x 10^{-3} s^{-1}), v-component of the wind (contoured), and plane-parallel ground-relative wind vectors (every other vector, with 1km length = 15 m s^{-1}). The black dashed curve denotes the dryline location. This vorticity perturbation amplifies into misocyclone M1 in Fig. 4.6.

component wind shear in the *y*-direction that is introduced at the southern boundary is about half as strong as the *v*-component shear. These wavelike perturbations, which have a horizontal length scale of about 10 km, subsequently collapse in scale and intensify to form misocyclones as they move downstream inside the model domain. The resulting misocyclones move north-northeastward along the dryline at 18 m s^{-1} (nearly the speed of the mean BL flow of 19.2 m s^{-1}). This speed estimate of a misocyclone was based on the movement of its vertical vorticity core at approximately 3-min intervals. The standard deviation of the speeds of all simulated misocyclones was 1.4 m s^{-1}, while the standard deviation of the wind speed from the mean BL state was 3.3 m s^{-1}. Although small differences exist in the structure of the various misocyclones, the main features common to the misocyclones can be presented by focusing on one particularly intense misocyclone (hereafter labeled "M1").

Growth of misocyclone M1 is illustrated in a Lagrangian, vortex-following sub-domain (B12), with the misocyclone-relative horizontal wind in the figures obtained by subtracting the misocyclone mean speed from the total wind (Fig. 4.6). An undulation introduced at the southern lateral boundary (Fig. 4.5) is initially manifest as a concentrated but elongated[1] region of enhanced positive vertical vorticity near the surface centered on the dryline (Fig. 4.6a). The maximum vertical vorticity associated with the initial shear zone introduced at the southern inflow boundary that subsequently amplifies into M1 has a magnitude of about 10 x 10^{-3} s^{-1} (Fig. 4.5). Additionally, an elongated enhanced region of negative vertical vorticity is present along a much weaker moisture gradient in the dry air west of the dryline.

[1] The introduction of persistent, slowly evolving radar-observed shear at the inflow boundary coupled with strong horizontal advection produces the elongated shear bands within the model domain.

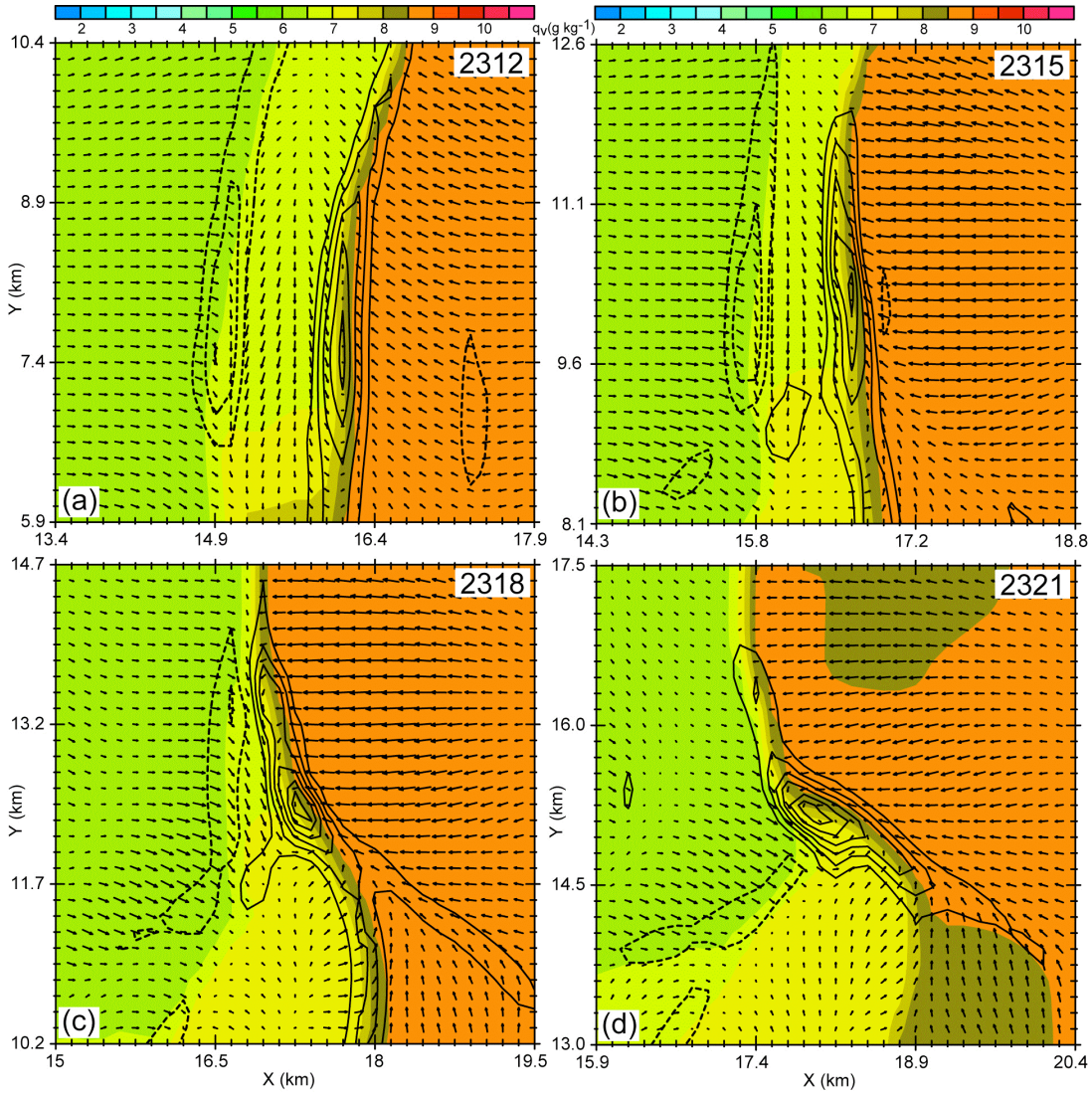

Figure 4.6. Simulated water vapor mixing ratio (color filled), horizontal winds, and vertical vorticity at (a) 2312, (b) 2315, (c) 2318, and (d) 2321 on 22 May 2002. Horizontal misocyclone-relative wind vectors (1 km = 5 m s^{-1}) are calculated by subtracting a mean wind of 18 m s^{-1} at 190° from the total wind. Vertical vorticity is contoured every 5 x 10^{-3} s^{-1} starting at 5 x 10^{-3} s^{-1} (-5 x 10^{-3} s^{-1}), with positive values solid and negative values dashed. All panels and fields are at the lowest model level (20 m AGL).

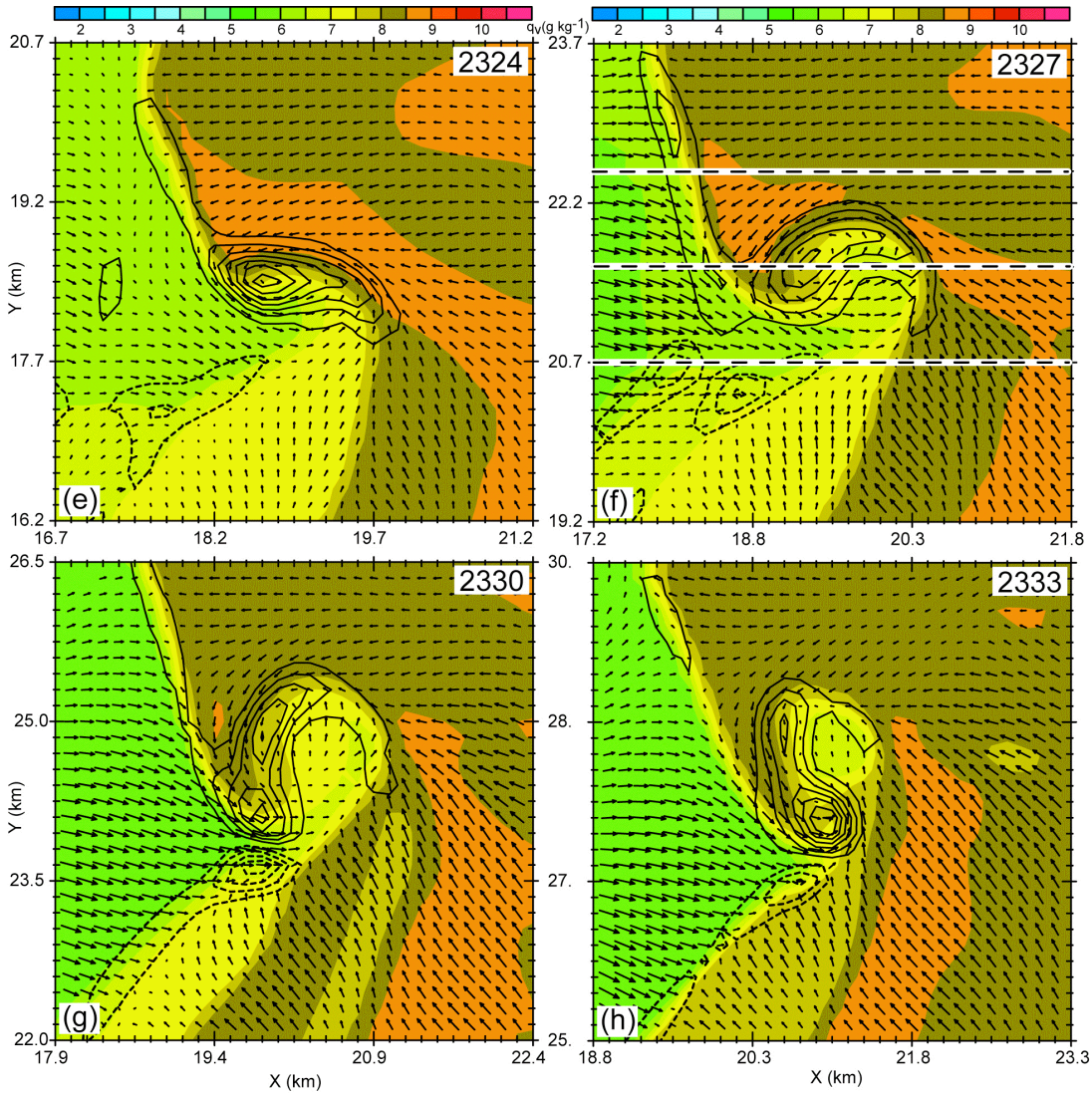

Figure 4.6, continued at (e) 2324, (f) 232327, (g) 2330, and (h) 2333 on 22 May 2002. The dashed black lines in panel f denote cross-section locations in Figs. 4.8 and 4.9.

Convergence along and north of the developing misocyclone causes the region between the dryline and western weak moisture gradient to contract, creating a stronger dryline segment (Figs. 4.6a-d). As this occurs, the region of negative vertical vorticity along the western moisture gradient weakens due to a decrease in convergence, and the maximum vorticity within the misocyclone increases to around its peak value exceeding 30 x 10^{-3} s^{-1}. The vorticity within the misocyclone at 2321 (Fig. 4.6d) is strongest near the surface and weakens with height (Figs. 4.7g-i). South and west of the misocyclone, a secondary moisture gradient associated with an HCR extends from the misocyclone center southwest into the dry air (Fig. 4.6d). The developing misocyclone takes on an elliptical shape with the major axis initially oriented north-south, with vortex tails on the northern and southern ends. The misocyclonic axis precesses counterclockwise as the dryline moisture gradient is rotated.

The genesis and roll-up of an elliptical vortex with vortex tails that subsequently precesses has been described by many studies (e.g., Goldstein 1931; Rosenhead 1931; Drazin and Reid 1981; Corcos and Sherman 1984; Pozrikidis and Higdon 1985). The most common explanation of the roll-up process of a shear band lying in a vertical plane is due to nonlinear Kelvin-Helmholtz instability. In the special case where density gradients are absent and the shear is in the horizontal plane, the term "horizontal shearing instability" is used (Rayleigh 1880; Miles and Howard 1964; Lee and Wilhelmson 1997). Periodic, small-amplitude disturbances along either a vortex sheet or a shear layer within some optimal range of width, shear magnitude, and vorticity are predicted to be unstable and subject to exponential initial growth according to linear theory. As nonlinear processes emerge, vorticity accumulates into localized elliptical cores, with the shear layer or vortex sheet stretched between the cores. These cores are connected to each other

by vorticity “tails” or “braids”, and they rotate or precess with nearly constant angular velocity. The misocyclone adjusts the moisture field along the dryline as it moves northward, bringing higher moisture westward preceding and drier air eastward after vortex passage. The wrap-up of a gradient in a scalar field by a vortex has been demonstrated and theoretically explained in several studies (Doswell 1984, 1985; Davies-Jones 1985).

A distinctive wrapping pattern of the moisture field associates with the real data simulated misocyclone (B12). As the simulated misocyclone approaches its mature phase or maximum vorticity, its major axis rotates more than 90° as moisture advects southward (i.e., relative to the vortex motion) to the west of the vortex (Fig. 4.6e). To the east of the misocyclone, dry air is simultaneously advected northward relative to the vortex motion. This process continues as the misocyclone migrates northward into the wrapping moist air (Fig. 4.6f). Eventually, moisture is wrapped completely around a sequestered pocket of dry air to the east of the misocyclone core. As this occurs, the misocyclone develops an “ inverted-U-shaped” asymmetry with the highest vorticity values residing on its southwest flank (Figs. 4.6g-h). As moisture wraps completely around the misocyclone center, a small region of negative vorticity moves northeast and strengthens just south of the strongest positive vorticity values on the south side of the misocyclone in association with a strengthening HCR (Fig. 4.6g). As the misocyclone interacts with the HCR, the southern part of the misocyclone reintensifies with vertical vorticity subsequently approaching its earlier peak value (Fig. 4.6h).

The vertical vorticity of the simulated misocyclone in the real data case is strongest near the surface and weakens as the center tilts downshear with height (B12). The strongest updrafts are initially collocated with the misocyclone and the dryline moisture gradient at 2321 UTC (i.e., when the vortex is farthest

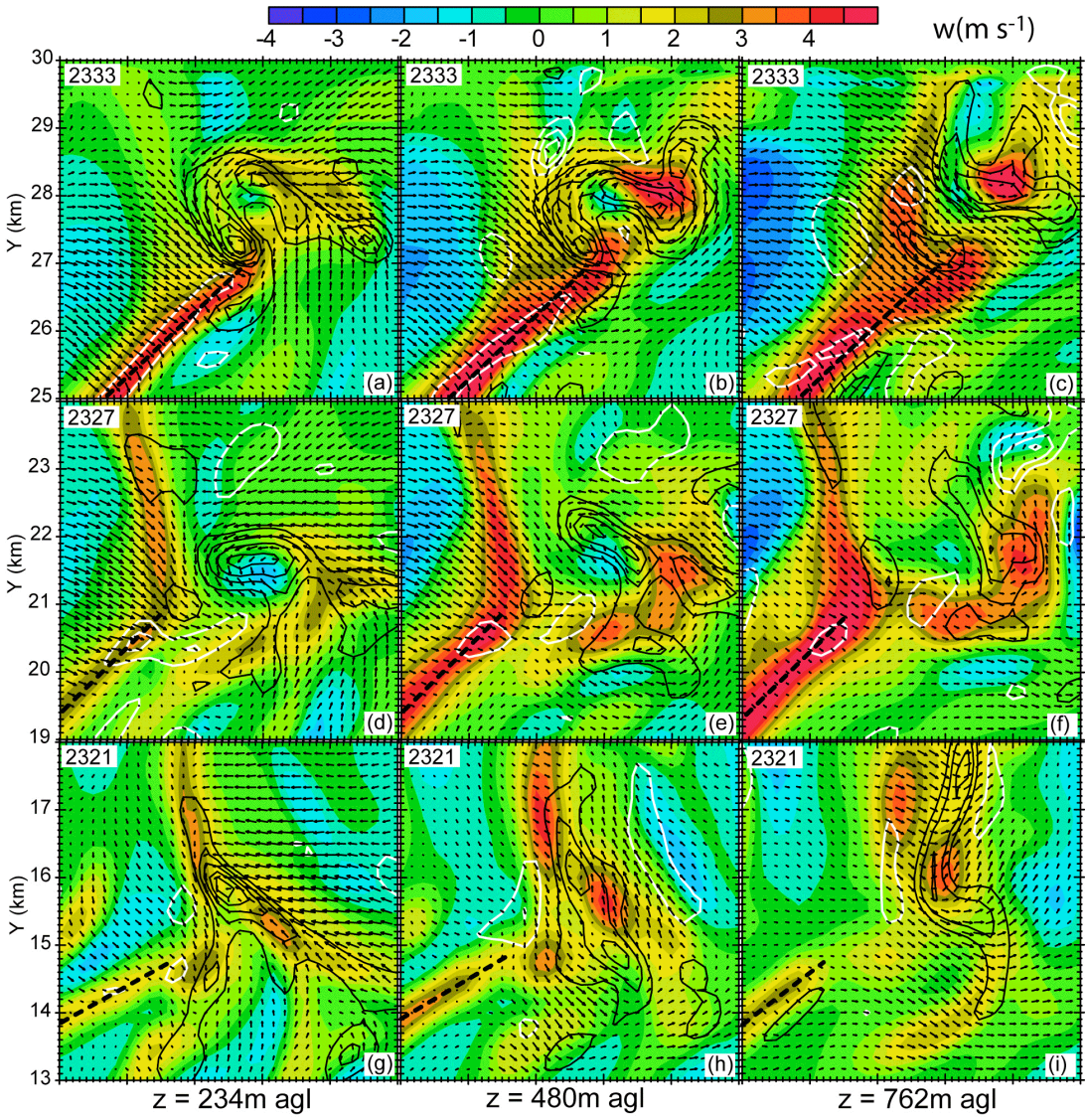

Figure 4.7. Simulated vertical velocity (color filled), horizontal misocyclone-relative wind vectors (1 km = 5 m s^{-1}) calculated by subtracting a mean wind of 18 m s^{-1} at 190° from the total wind, and vertical vorticity every 5 x 10^{-3} starting at 5 x 10^{-3} (-5 x 10^{-3}), with positive values black and negative values white. Vortex motion is from south to north (i.e., bottom to top). Heights are at 234 m AGL (left column), 480 m AGL (center column), and 763 AGL (right column). Each row is at the same horizontal location. The black dashed line indicates an HCR extending to the southwest of the misocyclone.

south), with enhanced updrafts along a developing HCR extending southwest into the dry air (Figs. 4.7g-i). As the misocyclone reaches a mature phase (2327 UTC), the updrafts on both the northern dryline segment and the HCR strengthen as a downdraft develops within the misocyclone center (Figs. 4.7d-f). A separate updraft core is located along the eastern edge of the misocyclone at 2327 UTC. As the misocyclone decays by 2333 UTC, the updraft on the eastern edge of the vortex is rotated and relocated along the northeast portion of the misocyclone (Figs. 4.7a-c). The strongest updraft at 2333 UTC extends to the southwest of the misocyclone along the merged dryline and HCR, with only a weak updraft along the northern dryline segment. The central downdraft now resides in an area of weaker vertical vorticity at the center of the "inverted-U-shaped" vortex, and the downdraft is flanked by regions of stronger vorticity on the northeast and southwest sides (Figs. 4.7a-c).

During the mature phase of the misocyclone, deep-layer convergence deepens the moist layer to the north of the vortex center (Fig. 4.8a). The dryline tilts eastward with height and remains associated with enhanced vertical vorticity due to across-dryline horizontal shears (Fig. 4.8a). An eastward surge of dry air to the south of the vortex effectively shifts the dryline eastward (Fig. 4.8c). The wrapping eastern and western drylines can be seen through the center of the misocyclone as dry air enters the misocyclone core during the wrap-up phase (Fig. 4.8b). Downdrafts associated with the dryline's secondary circulation depress the top of the moist BL to the northeast and southeast of the misocyclone center (Fig. 4.8a and Fig. 4.8c). For the most part, the virtual potential temperature fields tend to be negatively correlated with the water vapor mixing ratio fields. Relatively low θ_v values are collocated with higher q_v values, while relatively high θ_v values are collocated with lower q_v values (Figs. 4.8d-f versus Figs. 4.8a-c). However,

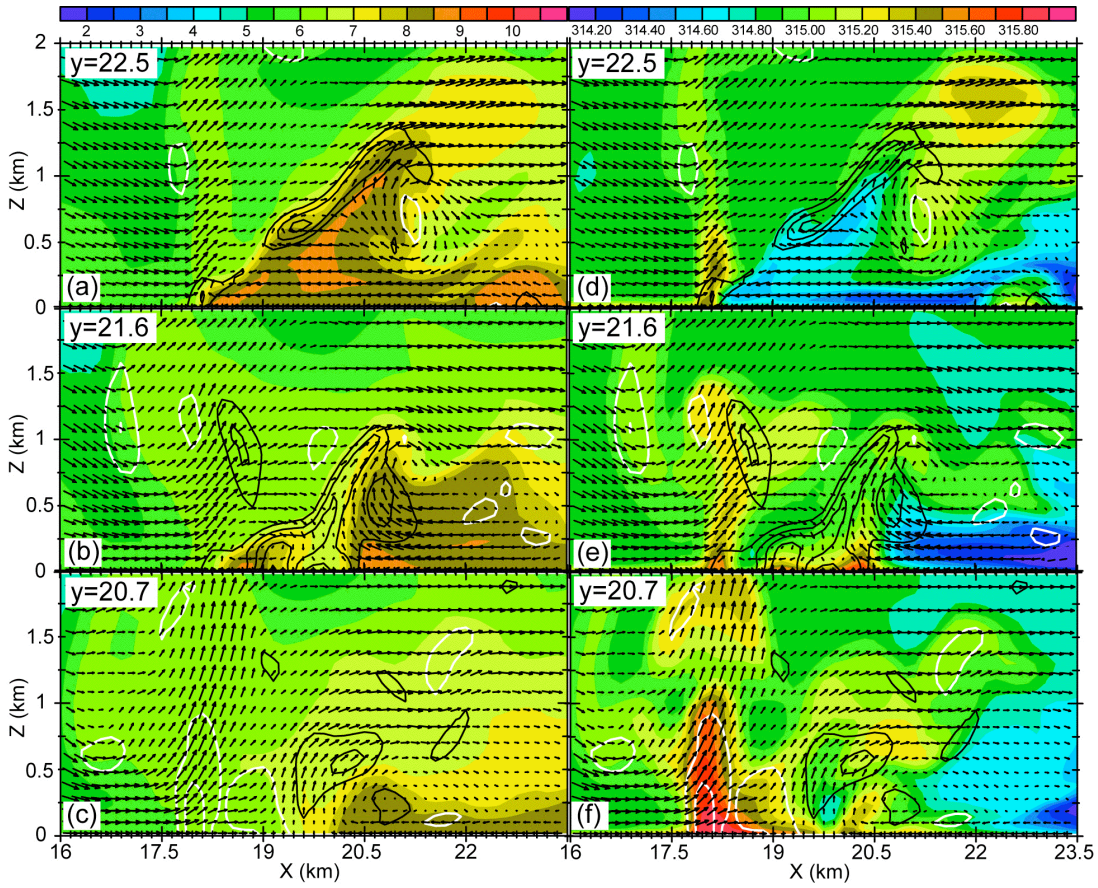

Figure 4.8. Vertical cross-sections of simulated water vapor mixing ratio (left column) and virtual potential temperature (right column) north, through the center, and to the south of a misocyclone at 2327 UTC. Also plotted are vortex-relative wind vectors (1 km = 15 m s^{-1}) and vertical vorticity every 5 x 10^{-3} starting at 5 x 10^{-3} (-5 x 10^{-3}), with positive values black and negative values white. Cross-section locations are shown in Fig. 4.6f.

isolated locations near the surface dryline location may have positively correlated temperature and moisture fields. As previously shown by Ziegler et al. (1997), the mesoscale BL circulations and updrafts associated with the dryline and HCR tend to transport the very warm, unstable lower-BL air into buoyant dry-convective plumes that may subsequently strengthen the mesoscale updrafts (Figs. 4.8d-f).

A pattern of 2-D horizontal q_v accumulation at lower levels and negative q_v accumulation at upper levels is seen to the north of the misocyclone along the dryline (Figs. 4.9a-c). A similar pattern is found in terms of 2-D horizontal θ_v accumulation, although the negative accumulation at upper levels is much weaker (Figs. 4.9d-f). The dryline and HCRs have intense accumulation in the lowest ~ 200-500 m AGL. Accumulation occurs along both dryline gradients through the center of a mature misocyclone. The dryline gradients accumulate to the south, however the accumulation zone is not as deep as to the north or along the eastern moisture gradient through the center of the misocyclone. It has been shown that accumulation (frontogenesis) is favored to the northwest and southeast of a cyclonically-rotating vortex as it deforms a scalar field characterized by initially north-south oriented isopleths associated with an east-west horizontal gradient (Doswell 1984, 1985; Davies-Jones 1985; Schultz et al. 1998). The updraft associated with the HCR contains pronounced θ_v accumulation due to locally strong thermal gradients in the dry BL.

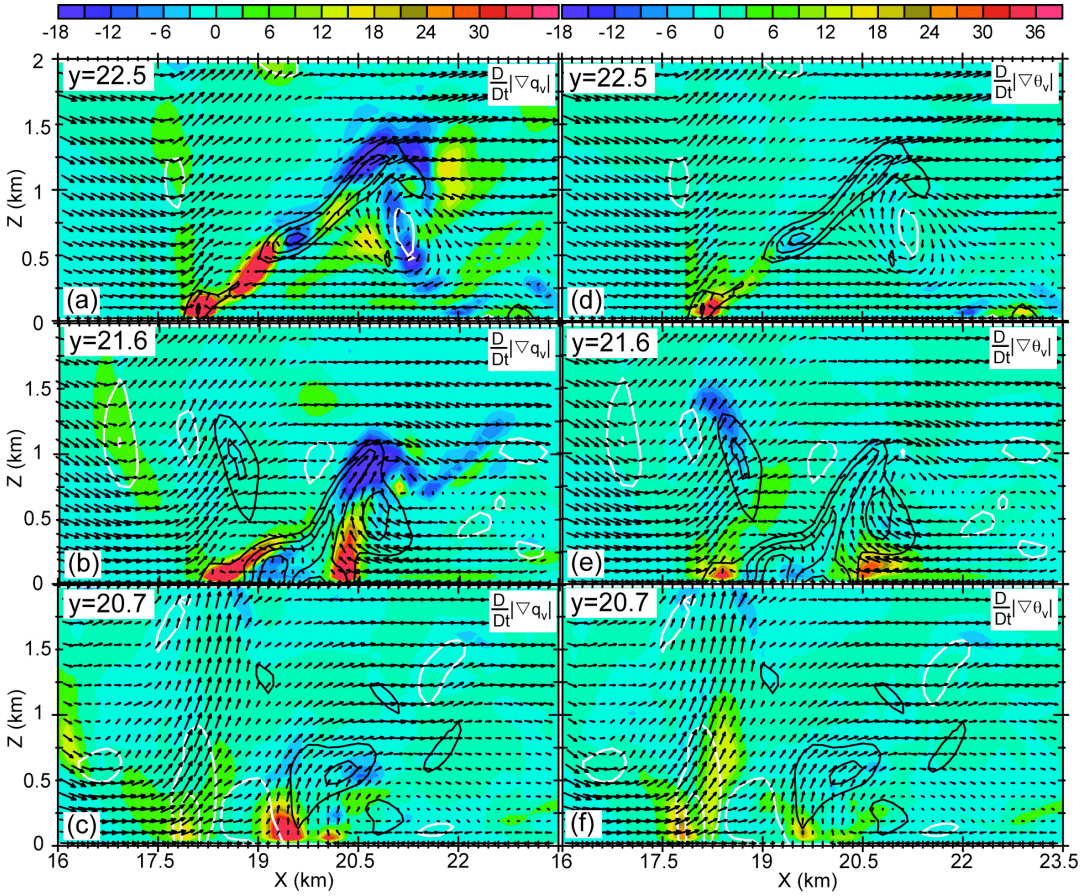

Figure 4.9. Vertical cross-sections of simulated accumulation of water vapor mixing ratio (left) and virtual potential temperature (right) north, through the center, and south of a misocyclone at 2327 UTC. Also plotted are vortex-relative wind vectors (1 km = 15 m s^{-1}) and vertical vorticity every 5 x 10^{-3} starting at 5 x 10^{-3} (-5 x 10^{-3}), with positive values black and negative values white. Cross-section locations are shown in Fig. 4.6f.

Chapter 5

Idealized simulations

5.1. BAROTROPIC SIMULATIONS

A series of idealized simulations were performed for the barotropic case (i.e., approximating a free shear layer between two infinite fluids of equal density). Each simulation is identical in configuration except for the two varied parameters of shear zone width and shear magnitude (thus vorticity). The parameters for the series of simulations are shown in Tables (2-3). The simulations were initialized with a random *v*-component perturbation of 0.01 m s^{-1} over the entire domain. All simulations have a similar evolution. The initial north-south oriented shear zone remains stationary and of constant width equal to the initial width for some time before periodic disturbances grow and distort the shear zone in a wave-like manner. The resulting waves roll-up into discrete vortices that persist for a brief time before nonlinear processes lead to vortex mergers and evolution into turbulence. Although the behavior of the simulations is consistent from one simulation to the next, there are differences, for example, in the growth rates and number of vortices, for a given simulation, in accordance with linear theory.

5.1.1. Evolution of shear zones

Four simulations with various shear zone widths and magnitudes of shear are shown in detail to represent typical behavior manifest generally in all simulations. Evolution of the *v*-component wind from the emergence of small-amplitude waves into the non-linear regime is shown for the bt4m12s case in Fig. 5.1. At 1440 s into the simulation (Fig. 5.1a), waves are beginning to emerge along the shear zone. By this time, it has been documented using the spectral analysis method described in Ch. 3.3 (not shown) that the perturbations along the shear zone have grown by 2-3

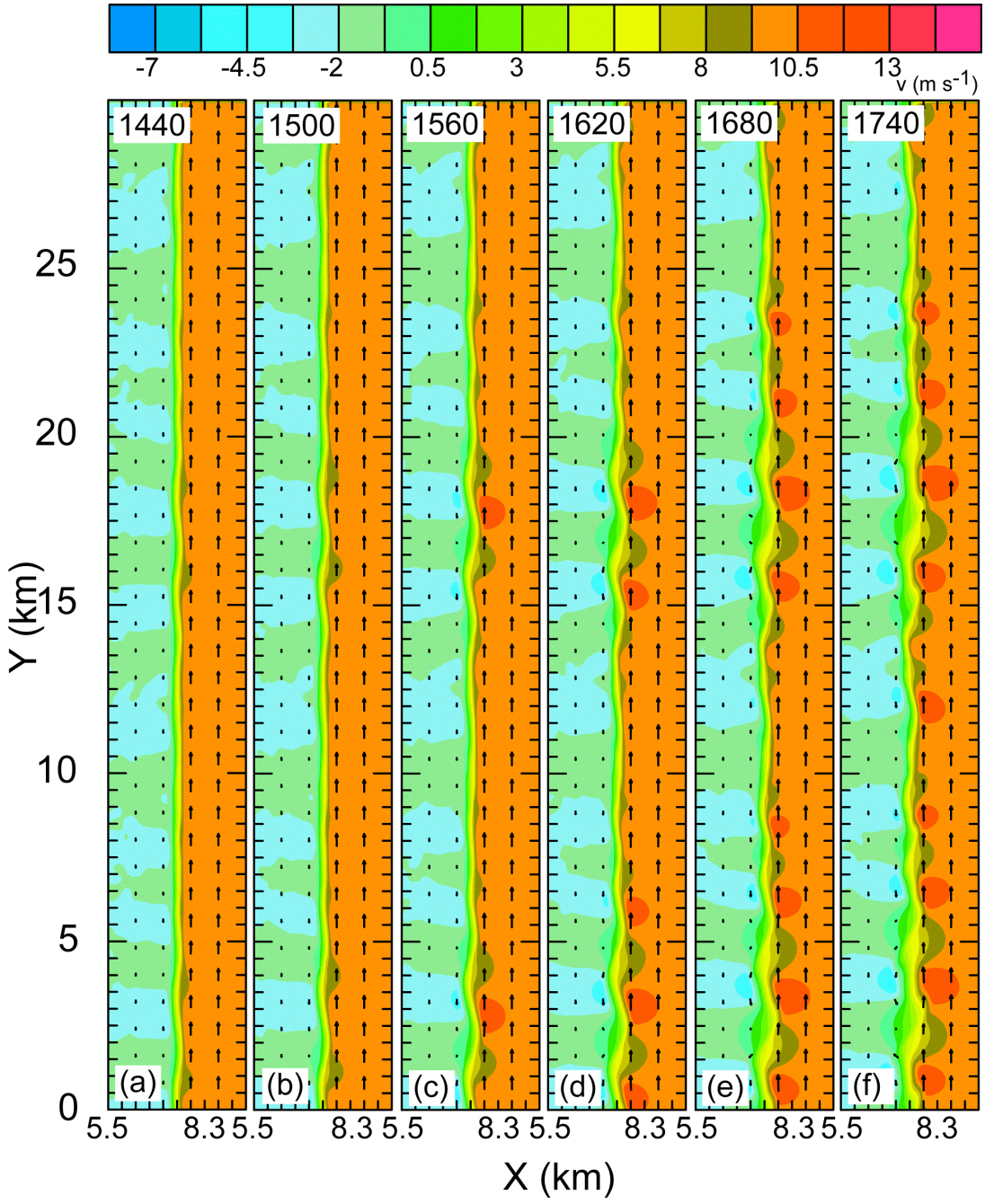

Figure 5.1. *v*-component wind (color filled) and horizontal wind vectors (500 m = 10 m s^{-1}) through the center of the simulation domain (z = 2.0 km) for the bt4m12s case.

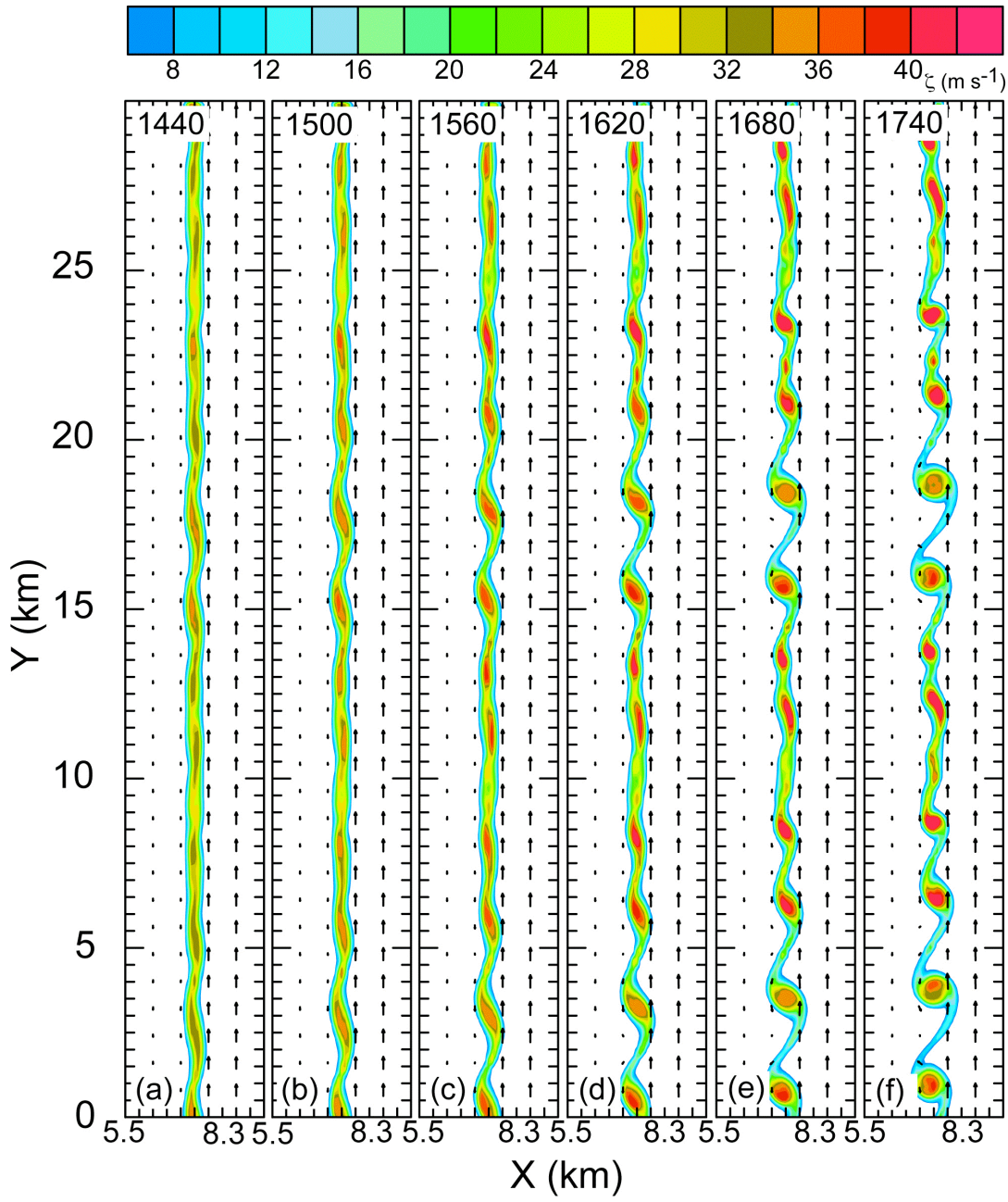

Figure 5.2. Vertical vorticity (color filled) and horizontal wind vectors (500 m = 10 m s^{-1}) for the bt4m12s case through the center of the domain (z = 2.0 km).

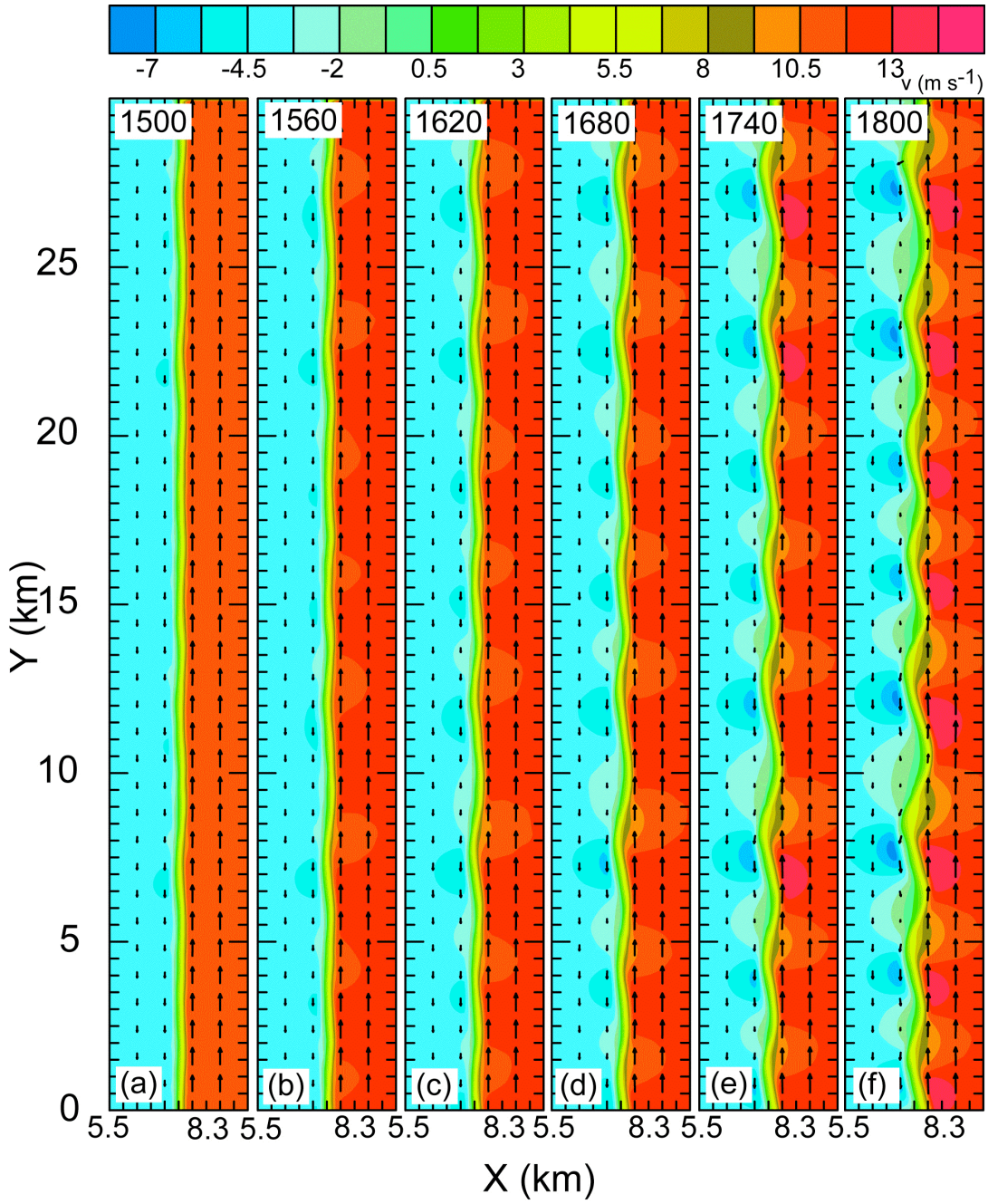

Figure 5.3. As in Fig. 5.1, except for the bt5m16s case.

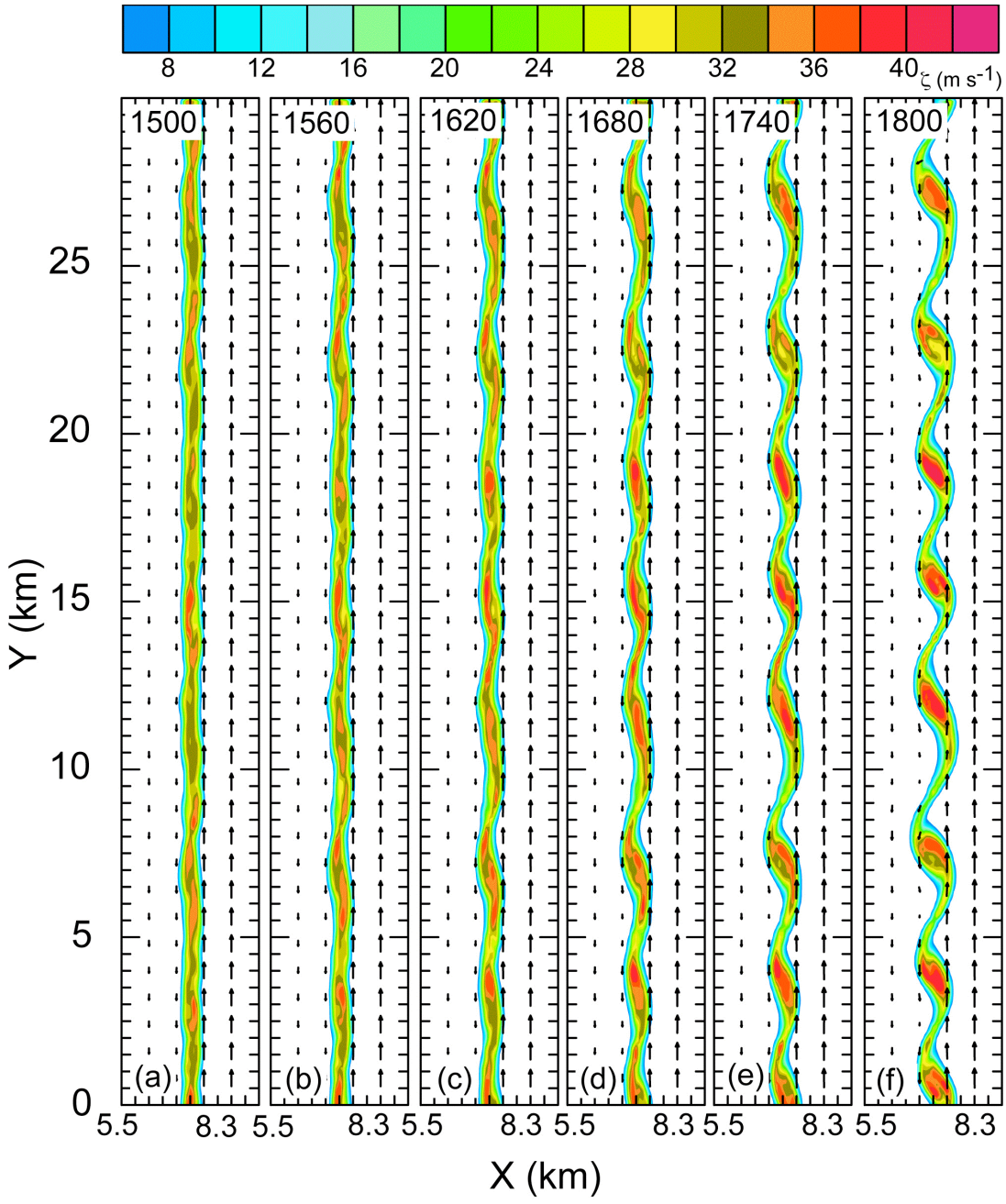

Figure 5.4. As in Fig. 5.2, except for the bt5m16s case.

orders of magnitude from the initial random perturbation. As time progresses, a periodic series of nearly equally spaced waves continues to grow exponentially as quantified by spectral analysis (shown later). In addition to the dominant wavenumber around 10, additional structure around wavenumber 2 is also seen. As the simulation proceeds toward the nonlinear regime from 1440 through 1740 s (Figs. 5.1b-f), the perturbations continue to grow and begin to roll up into discrete vortices. This process can be better visualized in the vertical vorticity fields (Fig. 5.2). Initially, wavelike vorticity perturbations emerge and grow exponentially in time. The wavelike vorticity perturbations begin to contract into cores and increase in magnitude as the discrete vortices start to form. As in the *v*-component wind fields, the periodicities around wavenumber 10 and wavenumber 2 are evident in the vorticity structure.

Series of *v*-component wind fields for the bt5m16s case are shown in Fig. 5.3. As in the bt4m12s case, the shear zone is characterized by the emergence of small-amplitude waves by ~1500s (Fig. 5.3a). These waves continue to grow in amplitude and eventually roll up into discrete vortices between 1560 and ~ 1800 s (Figs. 5.3b-f). The vorticity fields also behave similarly in the bt5m16s and bt4m12s cases, with wavelike perturbations in the shear zone and isolated pockets of enhanced vorticity by ~1500s (Fig. 5.4a). These wavelike perturbations grow exponentially as vorticity is concentrated into discrete cores between 1560 and ~ 1800 s (Figs. 5.4b-f). Unlike the bt4m12s case, where there was a dominant wavenumber in the shear zone structure, with a secondary smaller wavenumber component, in the bt5m16s case only one dominant wavenumber (~8) is seen.

The fields of *v*-component velocity for the bt8m20s case are shown in Fig. 5.5. A similar pattern as in the previous two cases develops. Early on, small-amplitude waves emerge within the shear zone, continue to amplify exponentially,

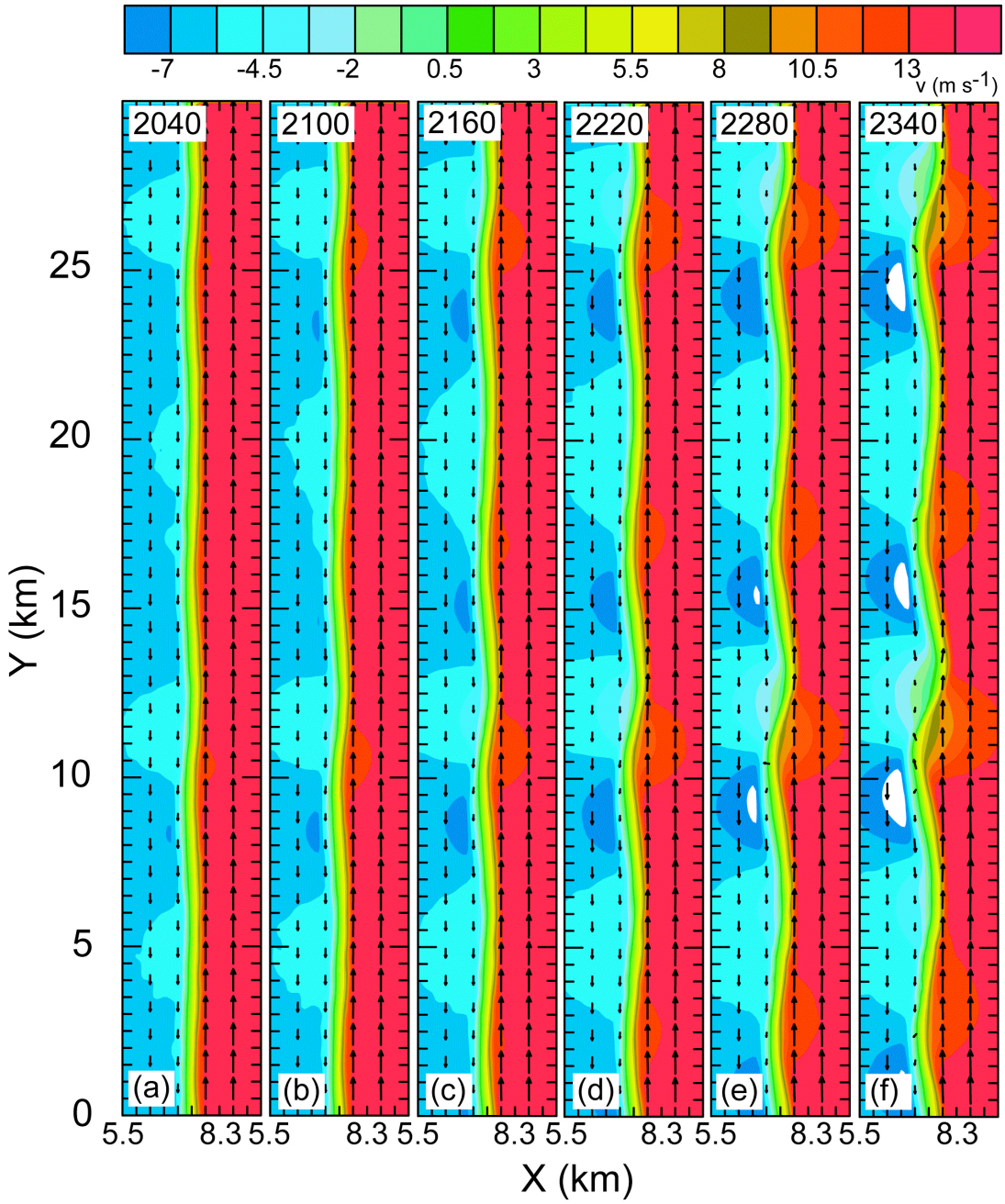

Figure 5.5. As in Fig. 5.1, except for the bt8m20s case.

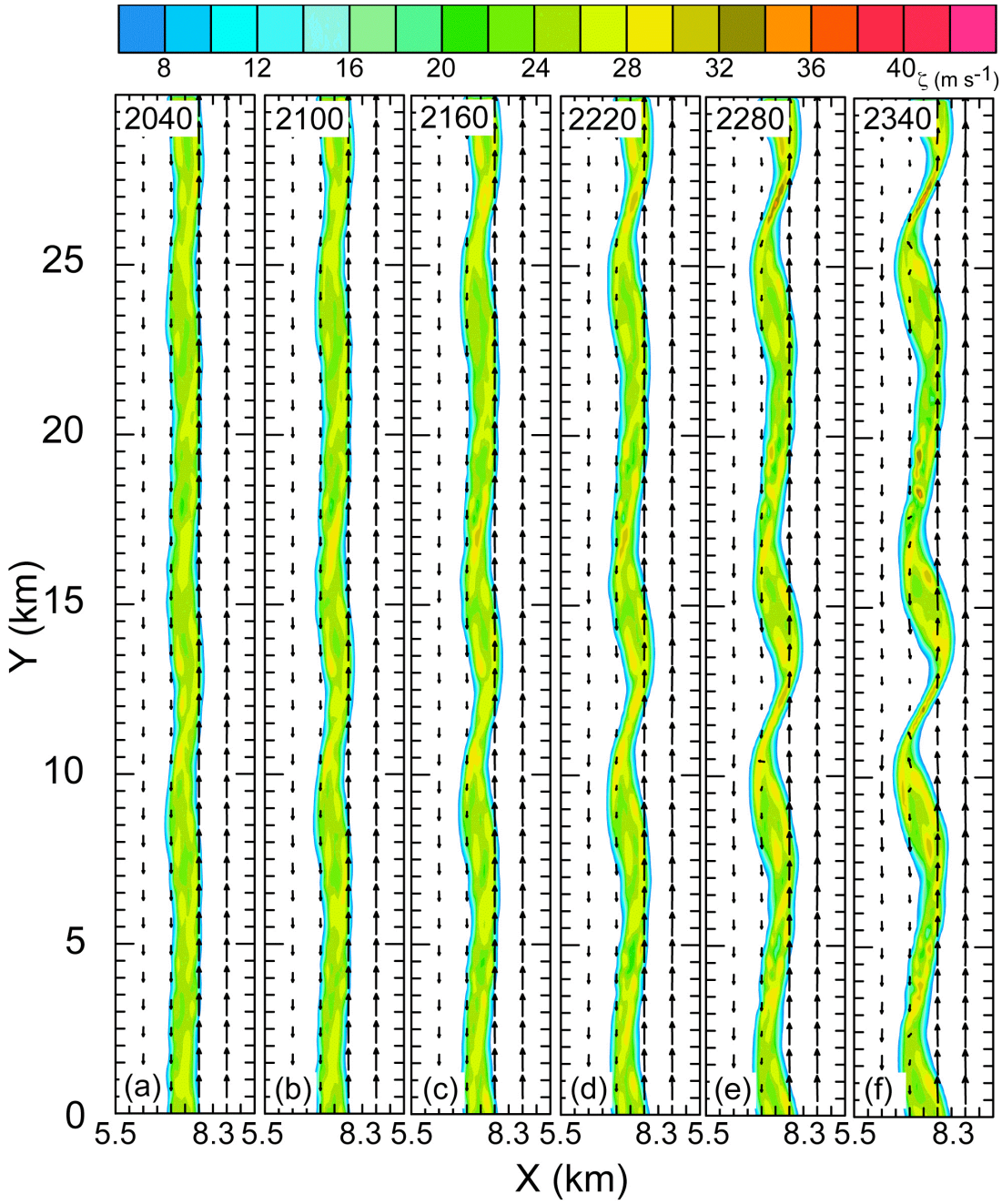

Figure 5.6. As in Fig. 5.2, except for the bt8m20s case.

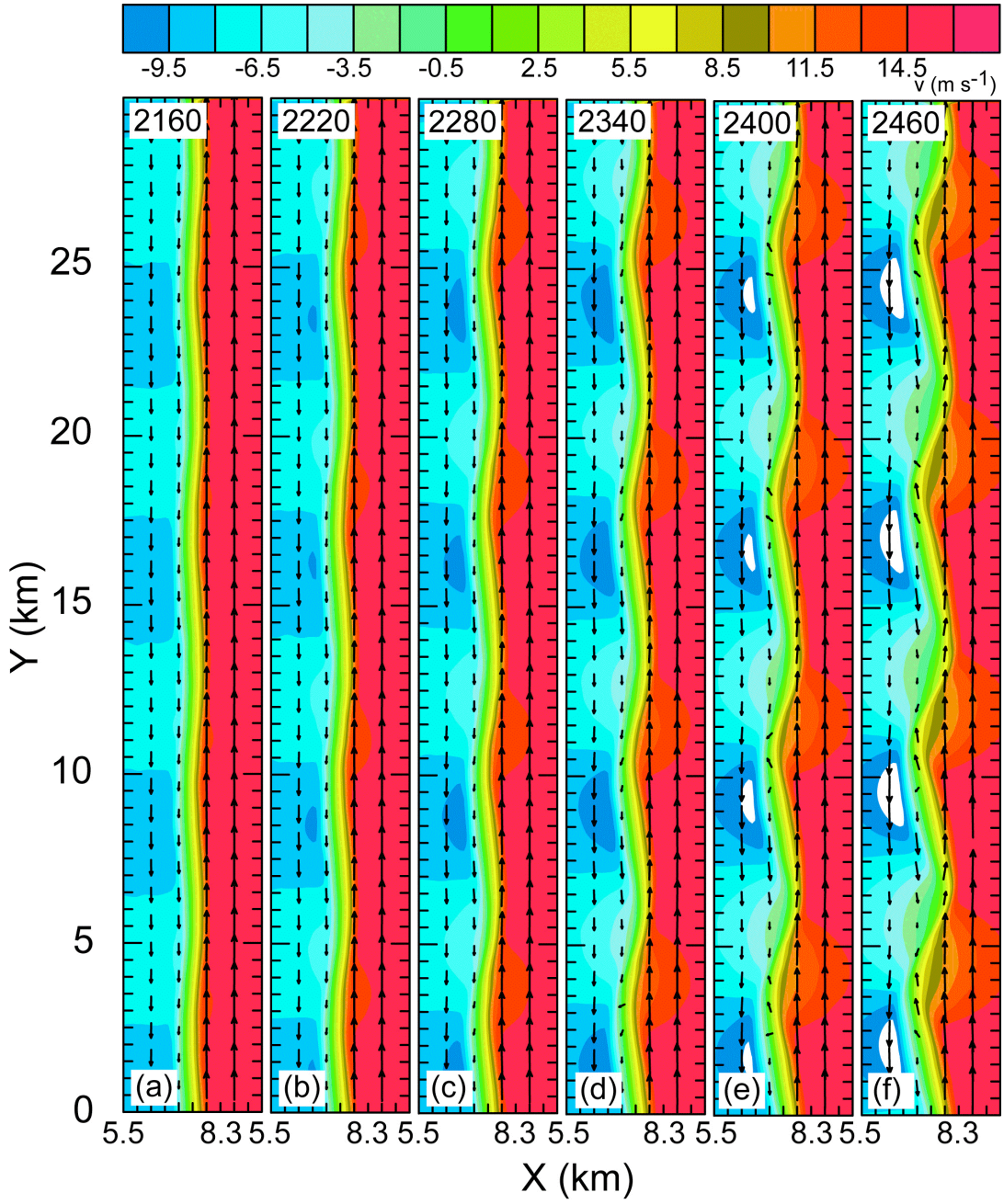

Figure 5.7. As in Fig. 5.1, except for the bt10m24s case.

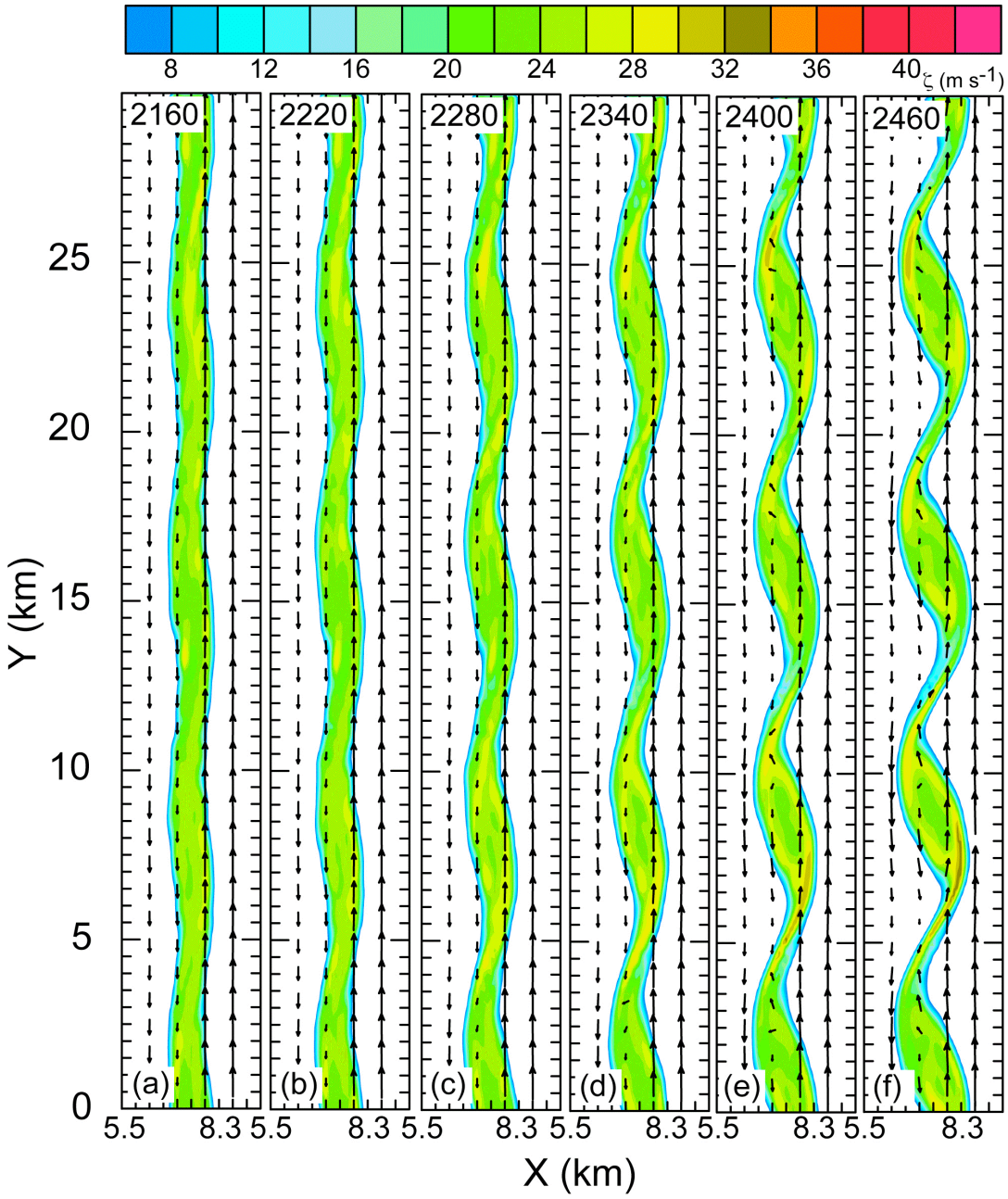

Figure 5.8. As in Fig. 5.2, except for the bt10m24s case.

and with time, roll up into discrete vortices (Figs, 5.5, 5.6). In this latter case, however, the process proceeds more slowly due to the smaller value of initial vorticity within the shear zone. Also, the perturbations emerge with a dominant wavenumber around 4, although some variability is seen in the wave spacing

For the bt10m24s case, the v-component wind and vorticity fields are shown in Figs. 5.7, and 5.8 respectively. Again, the evolution of the shear zone is as in the previous cases. The dominant wavenumber in the bt10m24s case is around 4, and is highly periodic throughout the domain. Note that as the width of the shear zone increases from 400 m – 1000 m, the dominant wavenumber that emerges decreases and the resulting vortices that develop increase in size. In addition, especially in the bt8m20s and bt10m24s cases, more variability in the vorticity structure within the shear zone is seen.

5.1.2. Perturbation wavelengths

Linear theory predicts the most unstable wavenumber (k) to be ~0.8/b or a most unstable wavelength (l=2π/k) of ~7.9b, where b is the width of the shear zone[2]. Therefore, with time, an arbitrary exponentially growing initial disturbance should become dominated by a wavelength close to that of the most-unstable mode, as long as the disturbance amplitudes are small enough for linear theory to be valid. Spectral density estimates at successive times show the perturbation amplitude evolution as a function of wavenumber for the bt4m12s case (Fig. 5.9). For this shear zone width, linear theory predicts the most-unstable wavenumber to be 9.5 (λ= 3160 m).

---

[2] Note that in all subsequent references, we will be discussing a domain-relative wavenumber $\kappa = \frac{kL}{2\pi}$, and wavelength $\lambda = \frac{2\pi}{\kappa}$, where L = 29,900 m is the north-south domain length. For example, a wavenumber of 5 refers to 5 waves of length 5980 m that span the north-south domain.

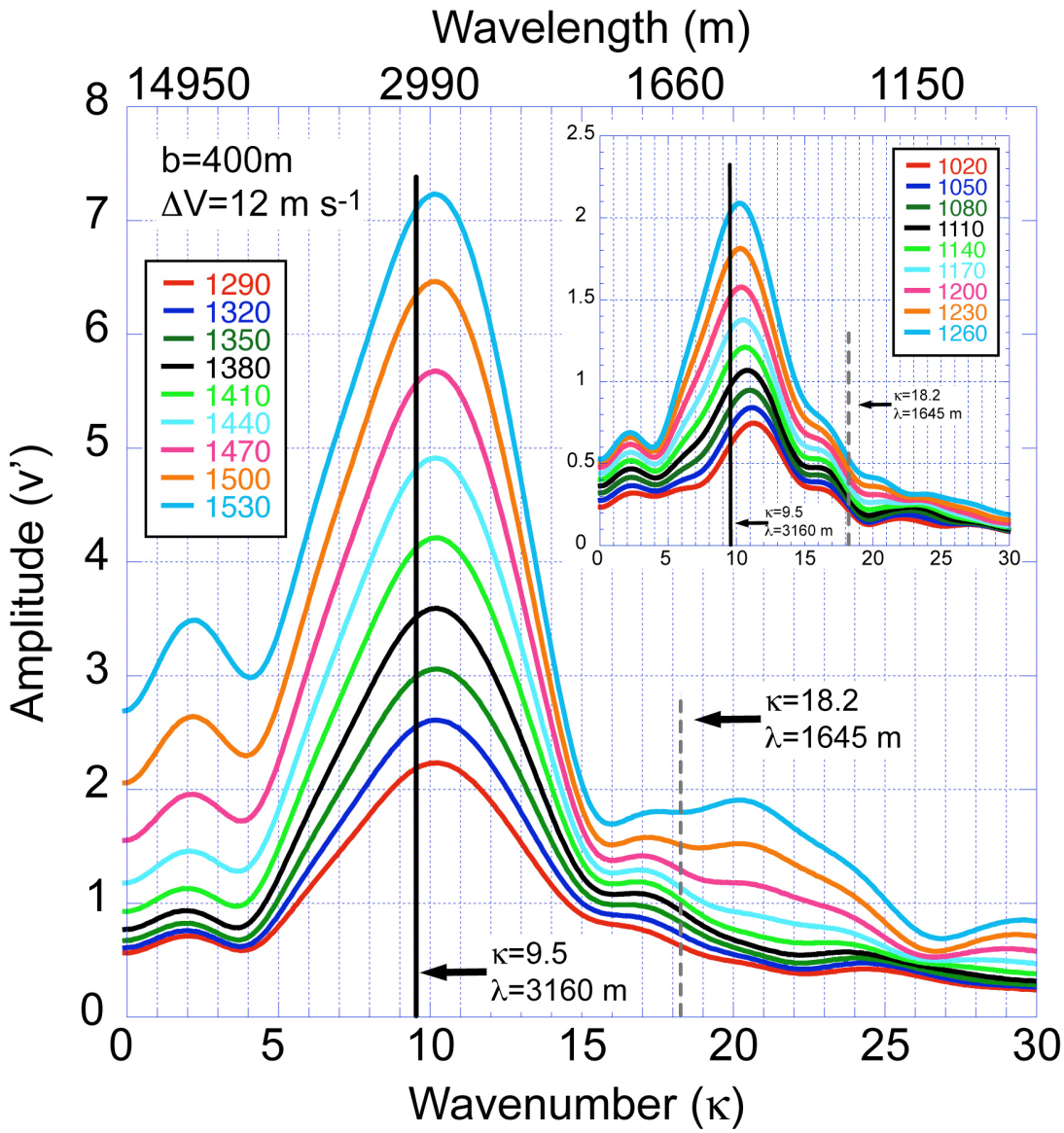

Figure 5.9. Spectral density estimates of the v-component perturbation wind amplitude (m s^{-1}) as a function of wavenumber during the periods 1290-1530 s and 1020-1260 s (inset) after the start of simulation bt4m12s. The vertical black line denotes the most-unstable wavenumber (9.5) and the gray dashed line denotes the neutral wavenumber predicted by linear theory (18.2).

From the start of the simulation, all wavenumbers begin to grow and there is very little difference in the amplitudes among the wavenumbers. By 1020s into the simulation, structure in the spectral density estimate begins to emerge, with a maximum amplitude in the 11-12 wavenumber range. This peak in amplitude subsequently shifts to around wavenumber 10.1 and strongly amplifies during the exponential growth phase. This peak in amplitude (κ = 10.1, λ = 2970 m) is close to the peak in amplitude expected to emerge by growth of the theoretical most-unstable mode (κ = 9.5, λ = 3160 m). In addition to the primary peak, a secondary local maximum in amplitude occurs around wavenumber 2 (λ = 14950 m). This secondary peak can also be seen in the horizontal fields of *v*-component velocity (Fig. 5.1) and vertical vorticity (Fig. 5.2). The exponential growth can be inferred by noting that the change in amplitude from one period to the next increases as time increases.

Note that the spectra are only plotted out to wavenumber 30 in Fig. 5.9 and all subsequent cases. This was done to capture the wavenumbers that were substantially growing. Growth rates are observed to monotonically decrease with increasing wavenumber in all cases so that at large wavenumbers the spectra asymptotically approach the spectra of white noise with an amplitude equal to the magnitude of the initial perturbation. Thus the wavenumber 0-30 band isolates the significant growth across all cases.

In all simulations transient initial growth is seen across all wavenumbers. Later, even at wavenumbers larger than the theoretical neutral wavenumber where linear theory predicts stability, some growth is seen. One limitation of linear theory is that it ignores any non-exponential (i.e. algebraic) growth, which is possible in real fluids (Pedlosky 1987). It appears that some non-exponential growth is occurring in these simulations. However, it is the exponential growth that with time

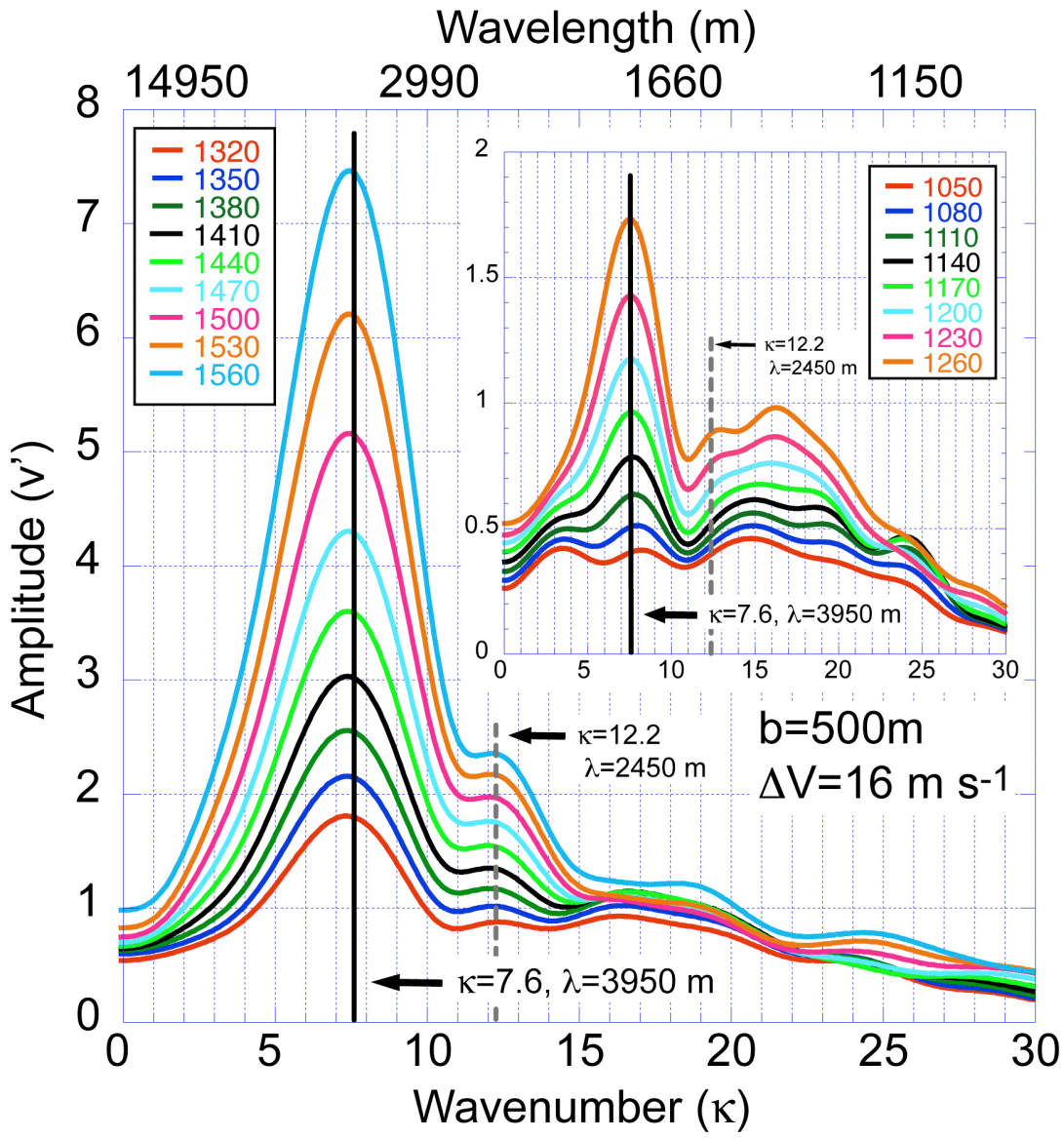

Figure 5.10. Spectral density estimates of the v-component perturbation wind amplitude (m s^{-1}) as a function of wavenumber during the periods 1320-1560 s and 1050-1260 s (inset) after the start of simulation bt5m16s. The vertical black line denotes the most-unstable wavenumber (7.6) and the gray dashed line denotes the neutral wavenumber predicted by linear theory (12.2).

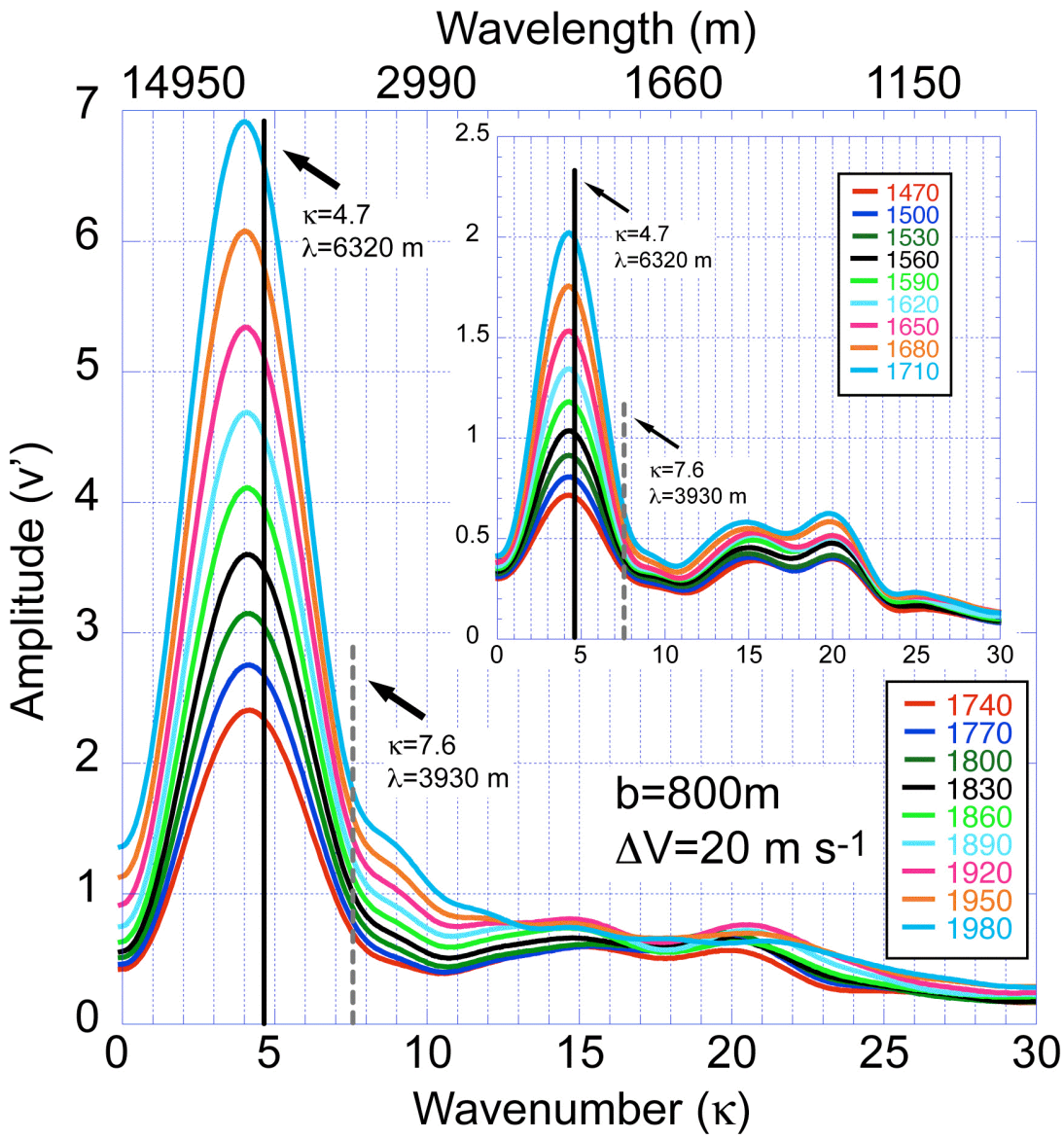

Figure 5.11. Spectral density estimates of the v-component perturbation wind amplitude (m s^{-1}) as a function of wavenumber during the periods 1740-1980 s and 1470-1710 s (inset) after the start of simulation bt8m20s. The vertical black line denotes the most-unstable wavenumber (4.7) and the gray dashed line denotes the neutral wavenumber predicted by linear theory (7.6).

will dominate the spectrum, thus describing the emerging structure at later times.

Spectral density estimates as in Fig. 5.9 are shown for the bt5m16s case in Fig. 5.10. It is seen that as in the bt4m12s case, growth occurs at nearly all wavenumbers at all times. Initially, a weakly defined triple peak emerges by around 1050 s around wavenumbers 3, and 16, transitioning to a single strong peak at wavenumber 7.5 (λ = 4000 m) between 1320-1560 s. This wavenumber is very close to the theoretically predicted most unstable wavenumber of 7.6 (λ = 3950 m). Unlike the bt4m12s case, a secondary peak at lower wavenumber is not evident.

Spectral density estimates are shown for the bt8m20s case in Fig. 5.11. Again, as in the previous cases, growth occurs at nearly all wavenumbers at all times, and like the bt5m16s case, a weakly-defined triple peak occurs initially, although later at ~1500 s and around wavenumbers 4 and 15, and 20. With time, the spectral density estimate transitions to having a single strong peak at wavenumber 4.0 (λ = 4775 m) between 1740-1980 s. This wavenumber is somewhat smaller than the theoretically predicted most unstable wavenumber of 4.7 (λ = 6320 m).

Fig. 5.12 shows the time evolution of the spectral density estimates for the bt10m24s case. Here, a consistent pattern of growth at nearly all wavenumbers is again seen. By 1560 s into the simulation, a peak in amplitude begins to emerge around wavenumber s3-4. This peak gradually shifts to wavenumber 3.9 (λ = 7670 m) by 1830-2070 s into the simulation and is very close to the theoretical most-unstable wavenumber of 3.8 (λ = 7900 m) predicted by linear theory. As in the bt4m12s case, a secondary peak in amplitude also occurs although at higher wavenumbers (~ 9). Additionally, there is some evidence of a possible tertiary peak around wavenumber 12. However in comparison to the primary peak, the secondary peak is about one order of magnitude smaller while the tertiary peak is two orders of magnitude smaller. The tertiary peak in particular may not be physical due to its

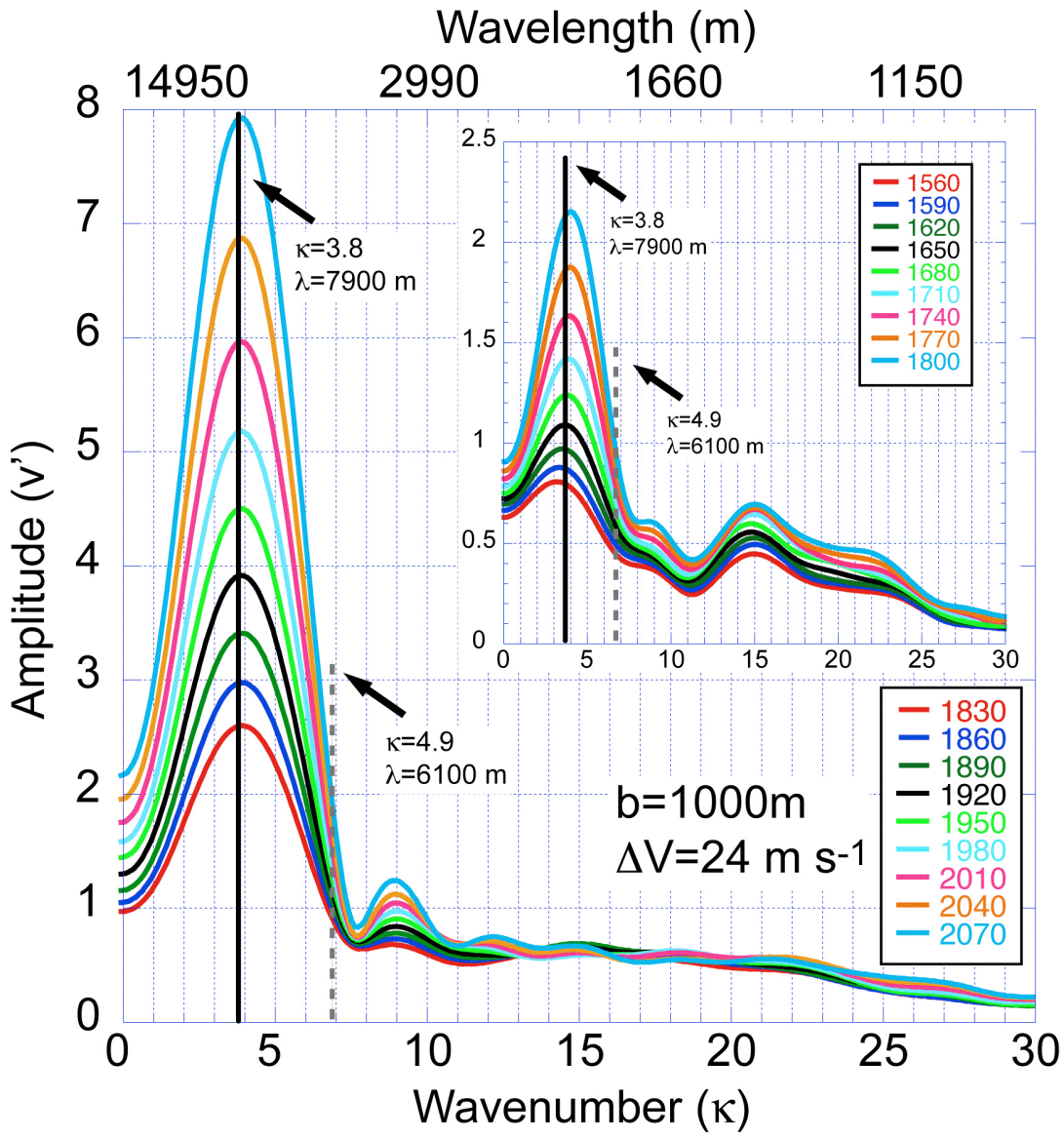

Figure 5.12. Spectral density estimates of the v-component perturbation wind amplitude (m s^{-1}) as a function of wavenumber during the periods of 1830-2070 s and 1560-1800 s (inset) after the start of simulation bt10m24s. The vertical black line denotes the most-unstable wavenumber (3.8) and the gray dashed line denotes the neutral wavenumber predicted by linear theory (6.9).

possible forcing via a Gibbs oscillation owing to the strong primary peak (e.g., JW69).

The barotropic simulations all behave similarly across the range of shear zone widths and shear magnitudes in terms of the peak amplitude in the spectral density estimates at the later stages of exponential growth when perturbation amplitudes are relatively high and linear theory is still valid (Fig. 5.13). The actual wavenumbers of maximum perturbation amplitude are close to the theoretical most-unstable wavenumber across the range of simulations. For a given shear zone width, the differences in wavenumber are small across the various shear magnitudes, ranging from 0.1 for the 800 m cases, to 0.5 for the 400 m cases (although this corresponds to a wavelength of about 150 m in both). However, there is a small high bias in the 400 m and 1000 m simulations, and a small low bias in the 800 m runs compared to the theoretical values. By normalizing the wavenumbers according to shear zone width, the simulations can be compared to one another and to the theoretical most-unstable wavenumber (Fig. 5.14). It is seen that the actual wavenumbers are close to the theoretical wavenumber (0.8), with the biases mentioned above.

As predicted by linear theory, the most-unstable wavelength is approximately 7.9*b* (i.e., a slope of 7.9 as plotted as wavelength vs. shear zone width graph). Plotting the simulated maximum amplitudes as a function of shear zone width yields a best-fit line with a slope of ~8.4, or very close to the theoretical slope (Fig. 5.15). Although the previously discussed biases are again evident, the high correlation coefficient (R = .977) shows only a relatively small variance among the data relative to the best-fit line.

Although linear theory predicts the most-unstable wavenumber (i.e., fastest growing mode), and transient growth is possible, given enough time while within

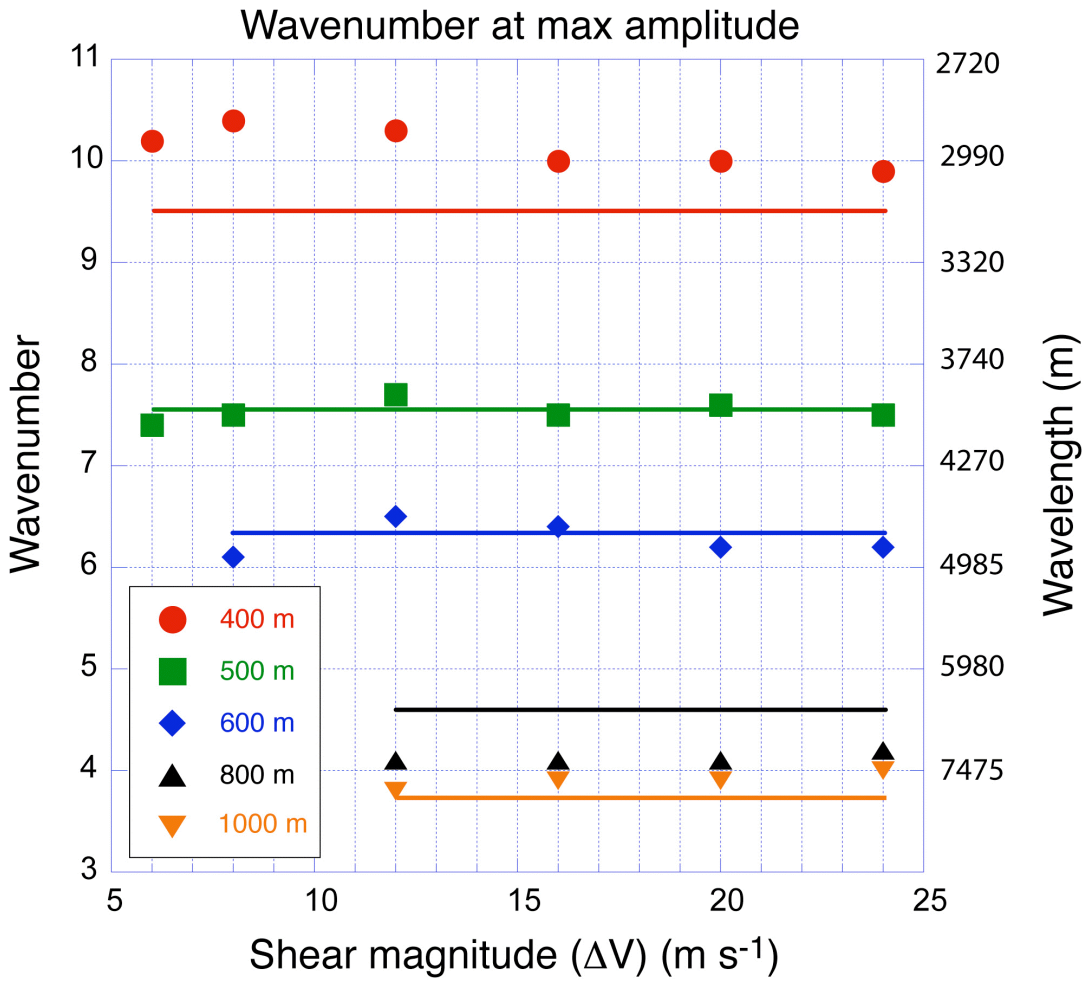

Figure 5.13. Wavenumber (wavelength) of maximum amplitude of the perturbation spectral density estimate for all barotropic simulations (markers) during the later phase of exponential growth (i.e., peak in curve at latest time in Figs. 5.9-5.12). The horizontal lines indicate the theoretical most unstable wavelength for a given shear zone width (color).

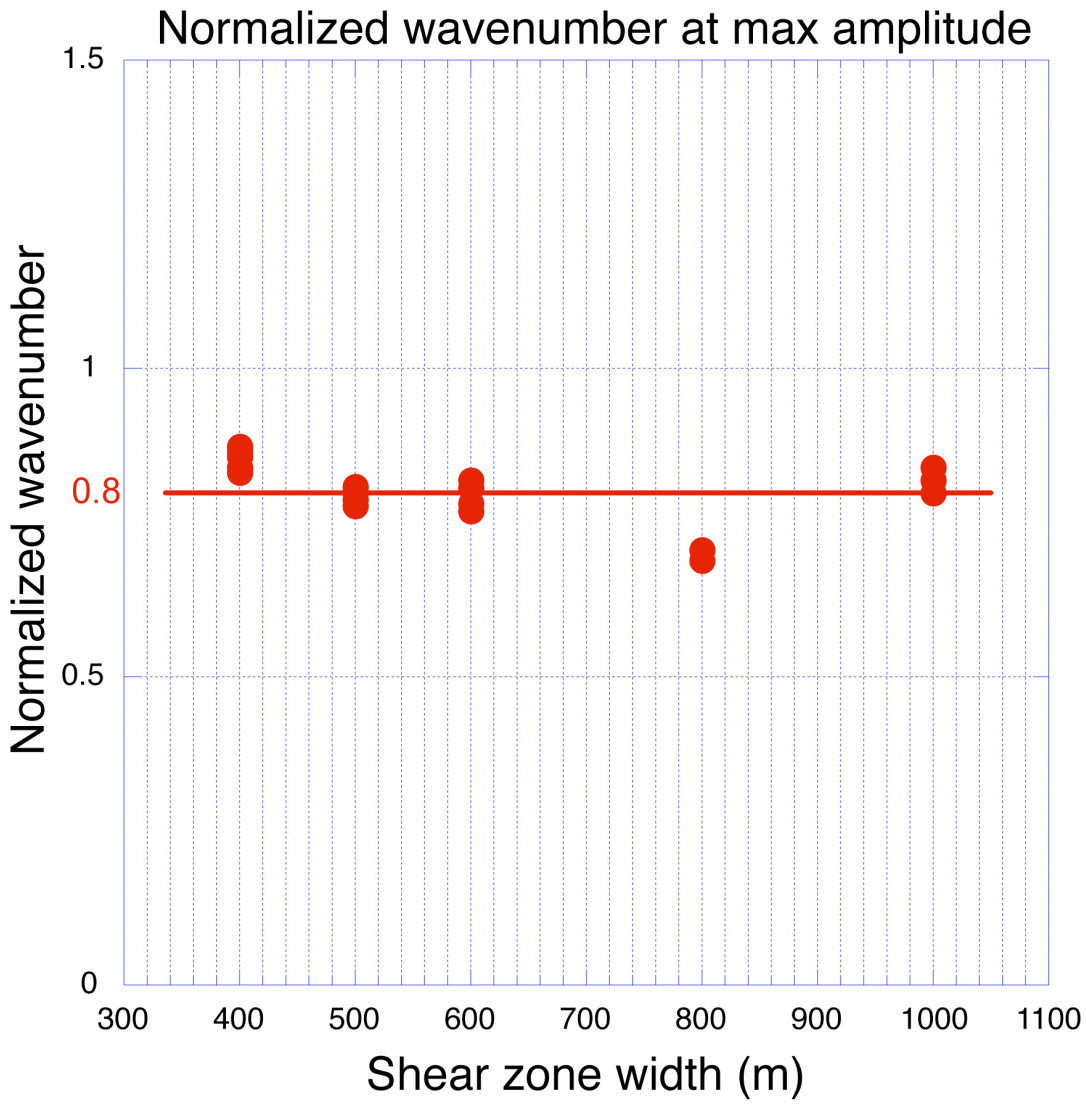

Figure 5.14. As in Figure 5.13, however data values were normalized by the shear zone width and domain length via the relation $\kappa = 2\pi k/L$. The horizontal red line is the theoretical most-unstable normalized wavenumber.

the constraints that linear theory is still valid, it is expected that the fastest growing mode will emerge as the dominant mode. It is therefore valid to compare the theoretical fastest growing wavenumber to the maximum amplitude wavenumber in the model simulations. Growth rates obtained from the spectral density estimates may be computed and compared directly with linear theory. However, the growth rates near the expected wavenumber of maximum growth rate vary across wavenumber and magnitude within the exponential growth rate regime predicted by linear theory. It is therefore difficult to determine which wavenumber to compare with linear theory. In fact, no objective way was found that produced consistent results.

The following results for the maximum growth rates were therefore obtained subjectively by analyzing the data from each simulation. Although the subjectivity can lead to slight differences in the results and their interpretation, the following are presented to supplement the results obtained by analyzing the peak amplitudes (which were easily obtained objectively). It will be shown in the next subsection, that any errors in identifying the wavenumber of maximum growth does not preclude the comparison of the actual growth rates to that of linear theory, as the differences in growth rates between the maximum wavenumber and the theoretical maximum wavenumber are negligible. Results across all barotropic simulations of wavenumber of maximum growth rate at the later stages of exponential growth (i.e. when perturbation amplitudes are relatively high and linear theory is still valid) are shown in Fig. 5.16. It is seen that the simulated wavenumber of maximum growth rate are close to the theoretical wavenumbers of maximum growth rate, although with more variance than in the wavenumber of peak amplitude. There is still a low bias at 800 m and a high bias at 1000 m, however, the high bias at 400 m is not seen.

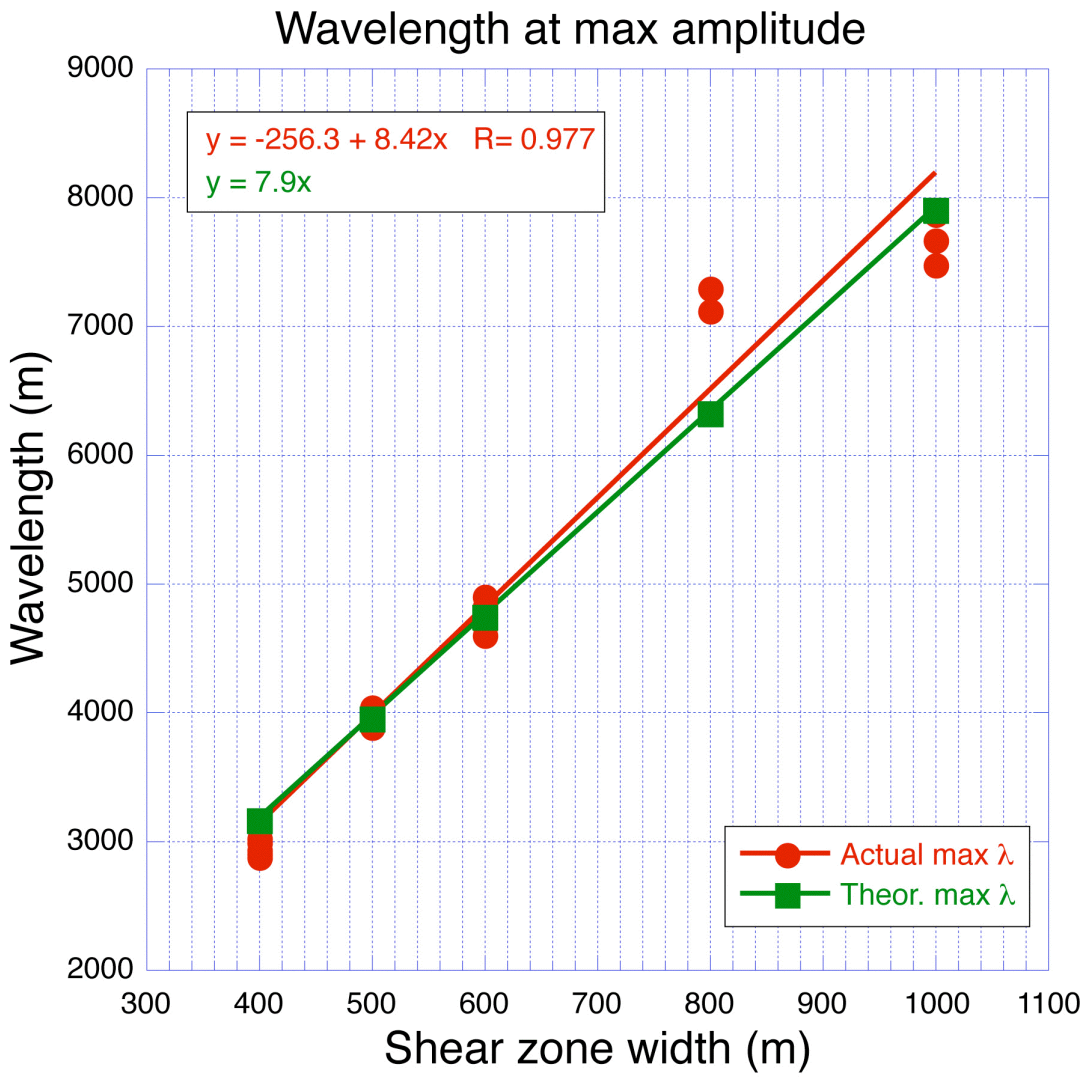

Figure 5.15. Wavenumber (wavelength) of maximum amplitude of the perturbation spectral density estimate for all barotropic simulations (red circles) during the later phase of exponential growth (i.e., peak in curve at latest time in Figs. 5.9-5.12), and the theoretical most-unstable wavelength (green squares). The best-fit lines are shown along with their equations.

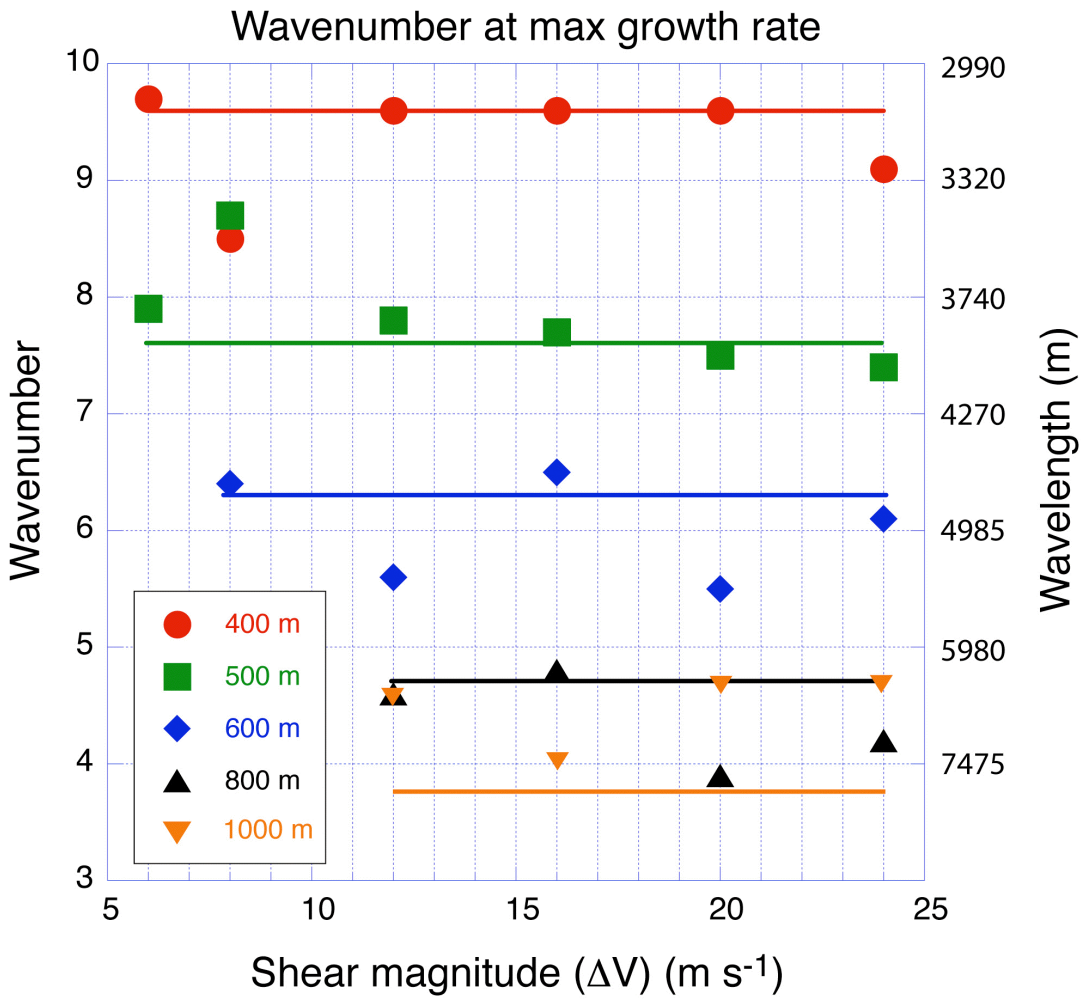

Figure 5.16. As in Fig. 5.13, except markers denote wavenumber (wavelength) at the maximum growth rate.

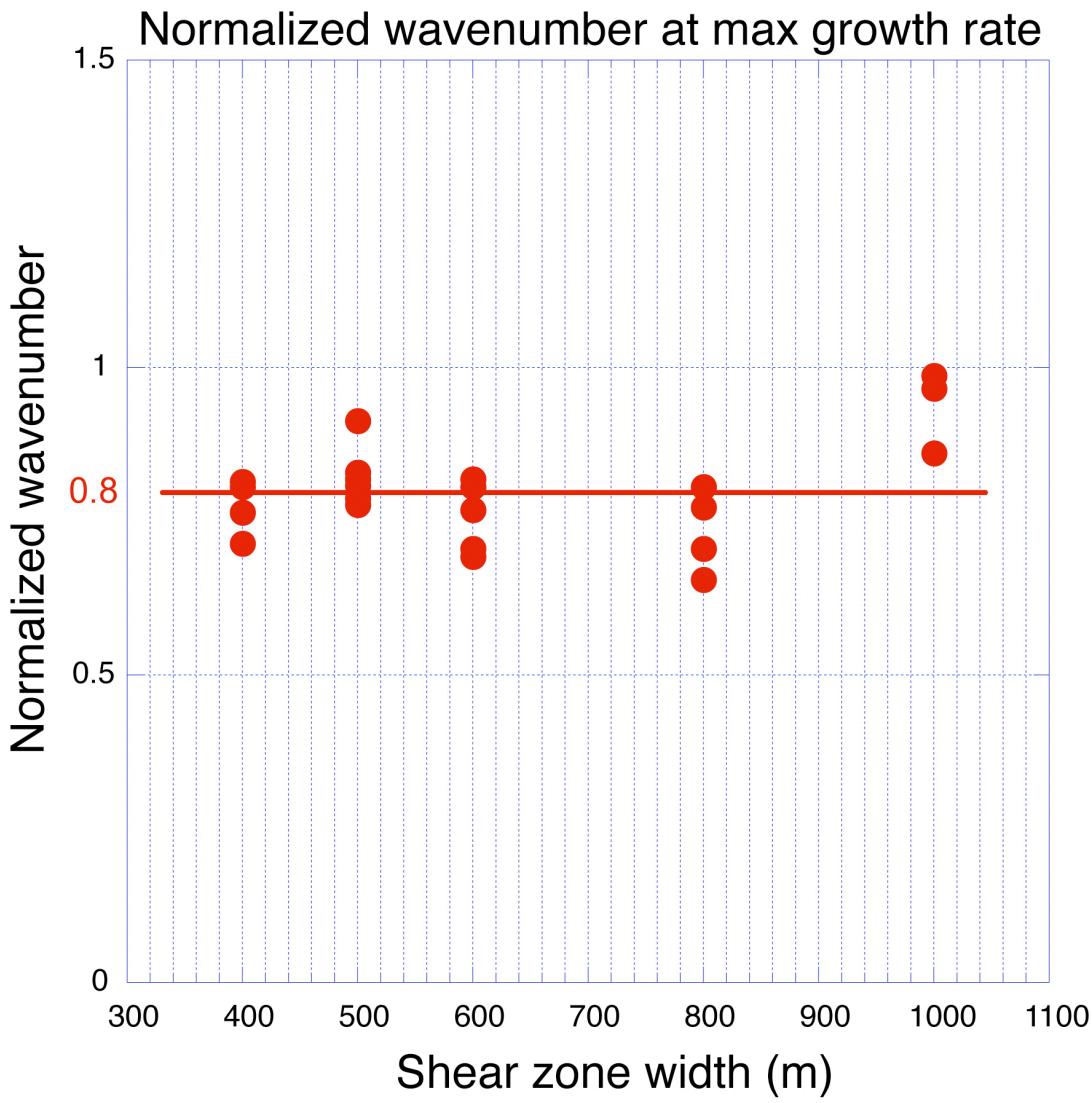

Figure 5.17. As in Fig. 5.14 except red circles represent wavenumber at maximum growth rate.

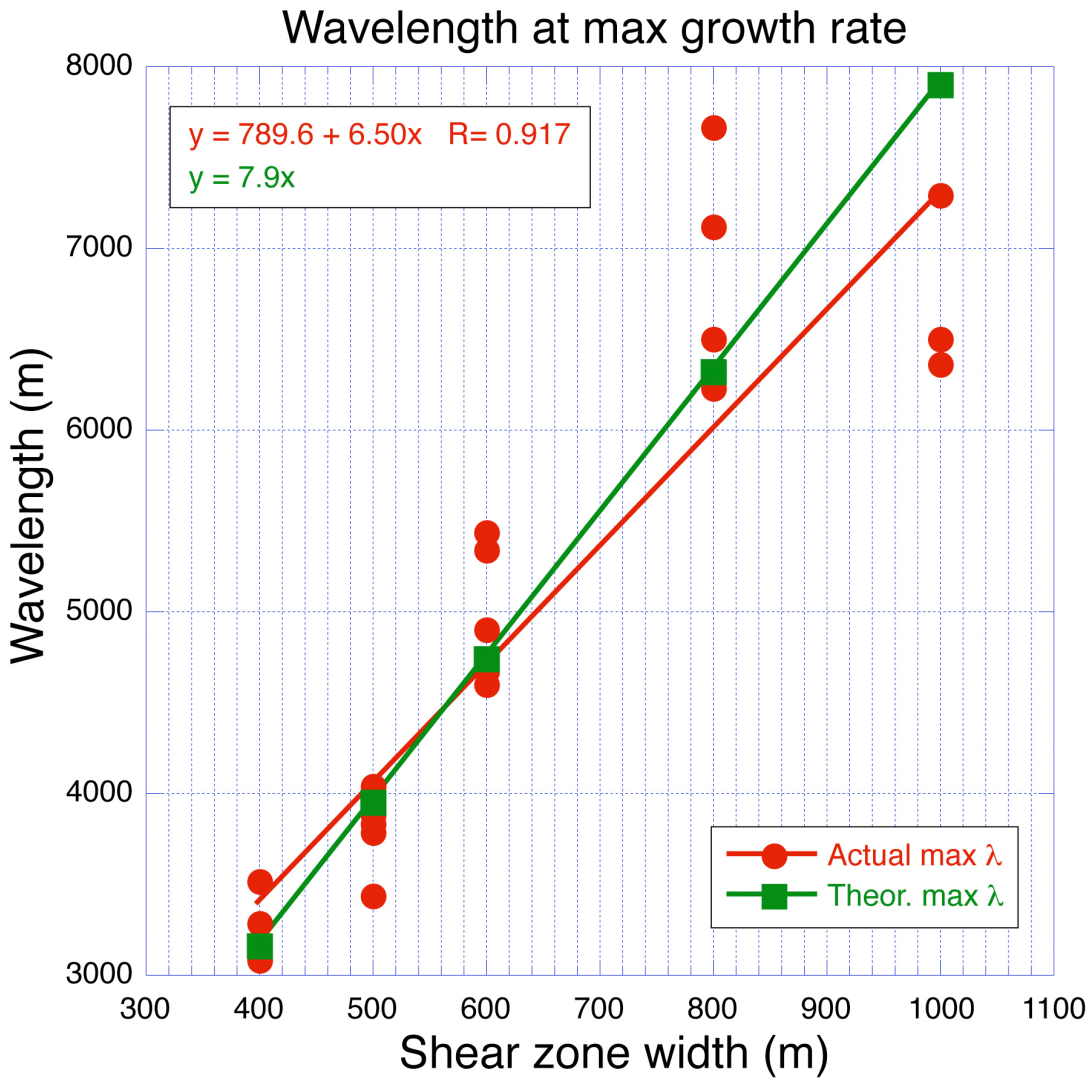

Figure 5.18. As in Fig. 5.15 except red circles represent wavenumber at maximum growth rate.

If the barotropic runs are compared in terms of the normalized wavenumber (as in Fig. 5.14), we see similar results to the wavenumber of maximum amplitude (Fig. 5.17). However, again we see more variance among the simulations as compared to the wavenumber of maximum amplitude. Finally, plotting the wavenumber of maximum growth rate as a function of shear zone width (Fig. 5.18), we find a slope of the best-fit line to be ~6.5 compared with a slope of ~8.4 for the wavelength of maximum amplitude and the theoretical most unstable wavenumber slope of 7.9. Also, more variation among the simulations is seen with a correlation coefficient (R = .917), which is slightly less than that for the wavenumber of maximum amplitude results (R = .977).

5.1.3. Perturbation growth rates

The growth rates are computed from the spectral density estimates as follows. First, by plotting the perturbation amplitude as a function of time on a semi-log graph, the times during which the amplitudes were growing exponentially can be identified by where the data points form straight lines segments. From these line segments, the (exponential) growth rates were found by the computing the slope of the line.

Figure 5.19 shows the amplitudes as a function of time for 5 different wavenumbers for the bt4m12s case. Note that the largest growth rate is around the theoretical maximum ($\kappa = 9.5$), and that for all wavenumbers (except wavenumber 3) the correlation coefficient of the fitted line is greater than 0.99, indicating nearly perfect exponential growth. The magnitude of the growth rate (.00572) is also close to the value predicted from linear theory (.00604). An additional example is shown in for the bt5m16s case (Fig. 5.20), with similar results to the bt4m12s case, with a maximum growth rate at the theoretical maximum ($\kappa = 7.6$), and all wavenumbers showing excellent fits to an exponential curves. For case bt5m12s, the magnitude of

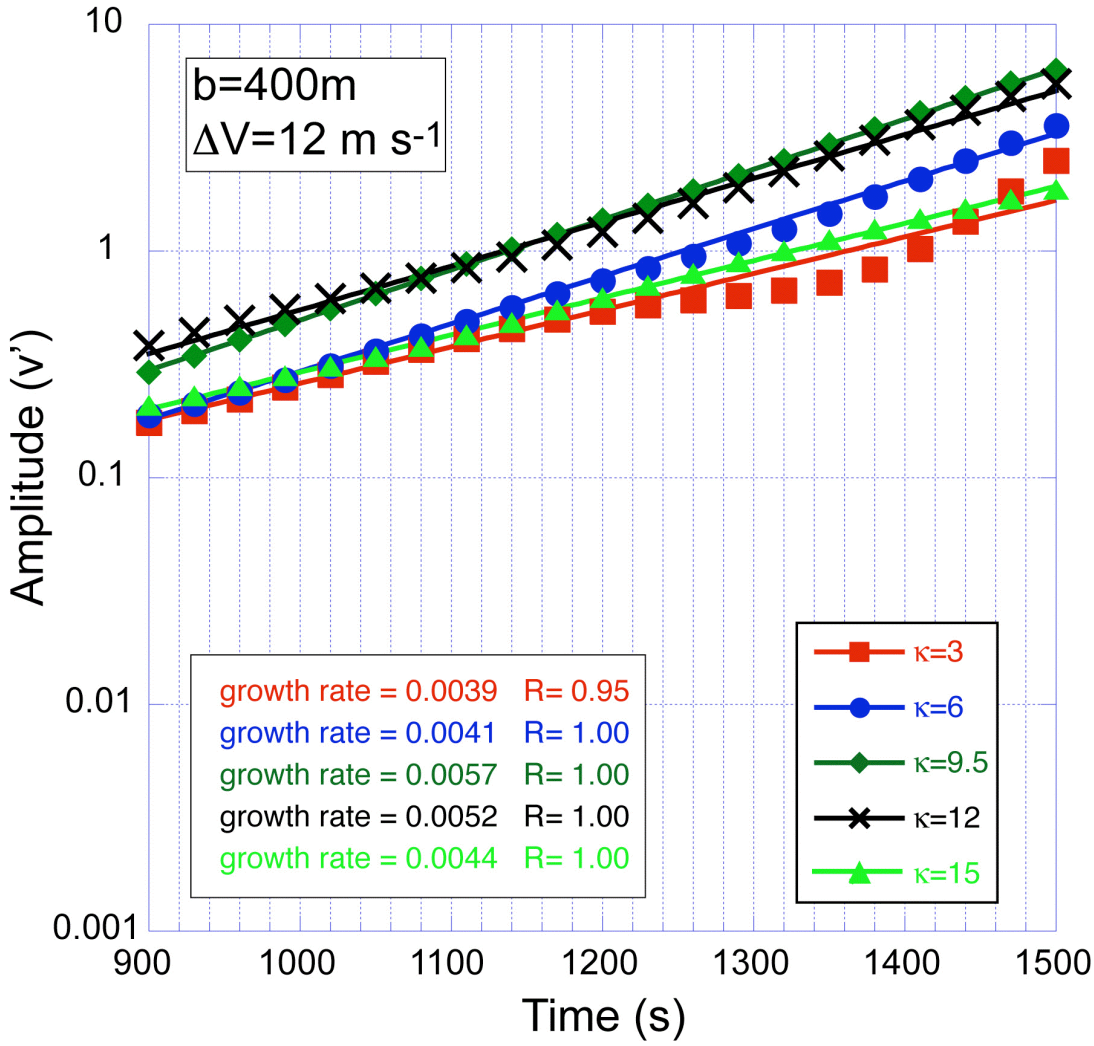

Figure 5.19. Amplitudes as a function of time (markers) at different wavenumbers (colors) for the bt4m12s case. Also shown are best-fit lines, their slopes (growth rates), and correlation coefficients.

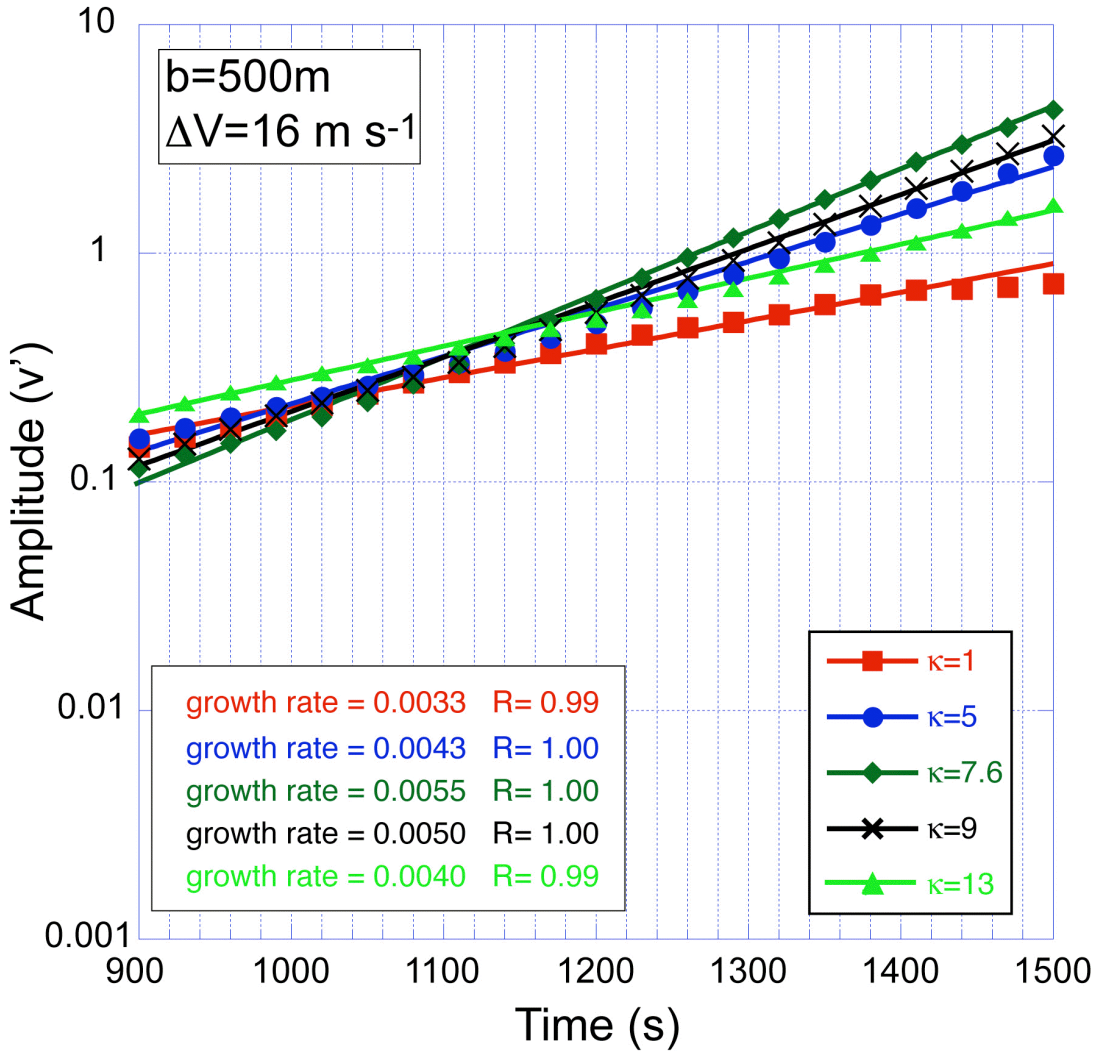

Figure 5.20. As in Fig. 5.19, except for the bt5m16s case.

the growth rate (.00552) is somewhat lower than that predicted from linear theory (.00643).

The actual wavenumber where the maximum growth rate occurs for a given simulation is not always at the predicted maximum wavenumber, however it is always close. This is due to the shape of the growth rate curve (i.e., growth rate vs. wavenumber), which is fairly flat near the peak. Therefore, we can look at two statistics, the wavenumber where the actual maximum growth rate occurs, and the growth rate at the theoretical peak wavenumber, and compare these to the predicted growth rates. It is seen that that these two growth rates are nearly identical. For example in the 400 m shear zone case (Fig. 5.16), this would correspond to comparing the growth rates calculated at the red circles (actual max) and the growth rates calculated at points on the red line (theoretical max) to the predicted values. These growth rates are plotted in Fig. 5.21, where each panel corresponds to a given shear zone width, and the growth rates are plotted as a function of shear magnitude. For the all cases, there is a strong linear relationship between the magnitude of the shear and the growth rates, with larger growth rates corresponding to larger shear values (Fig. 5.21). The linear correlation between the growth rate and shear magnitude is high for the 800 m shear zone widths ($R \sim 0.98$), even higher for the 600 m and 500 m widths ($R > 0.99$) and is essentially exact for the 400 m case ($R = 1.0$) to the degree of precision of the calculations (5 decimal places). Note that the growth rates for any given simulation are nearly identical whether they are computed at the actual maximum wavenumber or at the theoretical maximum wavenumber.

The computed growth rates from the simulations are smaller than the growth rates predicted by linear theory, however this bias tends to decrease at smaller shear zone widths. In terms of the functional relationship between shear magnitude and

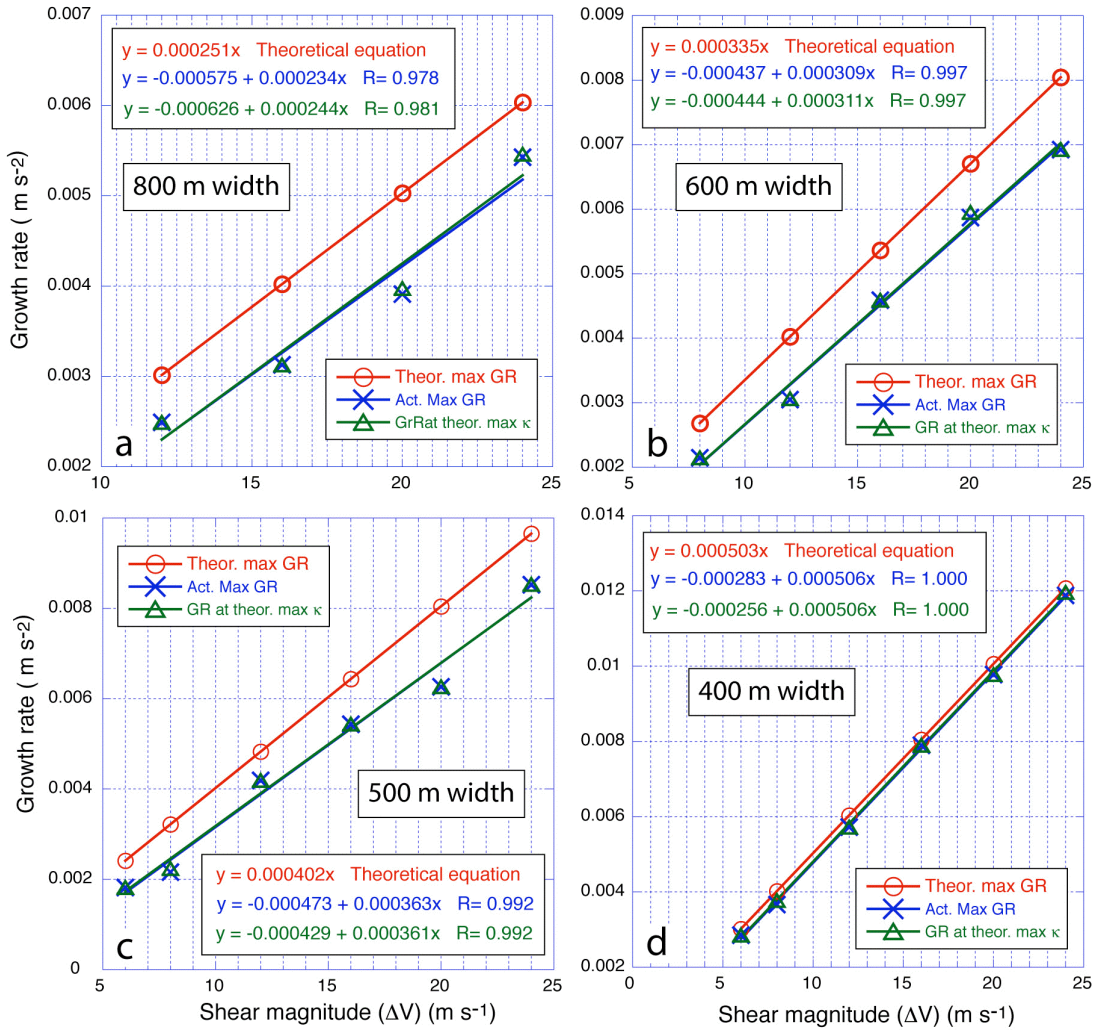

Figure 5.21. Maximum growth rates (blue) and growth rates at the theoretical maximum (green) plotted as a function of shear magnitude for four different shear zone widths. Also plotted in red are the theoretical maximum growth rates. Lines indicate linear least squares fits to the data points. Also shown are the least squares line equation and the correlation coefficient of these fitted lines.

growth rate for a given shear zone width, the theoretical and simulated results are in excellent agreement (Fig. 5.21).

Linear theory predicts that the maximum growth rate varies as a function of the shear zone vorticity. Combining the 4 panels in Fig. 5.21, we can plot the growth rates as a function of shear zone vorticity (Fig. 5.22). There is a strong linear dependence of growth rate on the shear zone vorticity across all simulations as a whole (R = .989). Note that this linear relationship is essentially the same whether we look at the growth rate at the actual maximum or the theoretical maximum. Therefore, we will only discuss the actual maximum growth rate and imply that this is the growth rate at the theoretical maximum wavenumber, neglecting any extremely small differences. The actual functional relationship between shear zone vorticity and growth rates (i.e., the slope of the curves in Fig. 5.22) in the simulations agrees with linear theory to better than one percent (i.e., simulated slope of 0.1997 vs. theoretical slope of 0.2012). Therefore, although the spatial structure of the evolving shear layer depends only on the shear zone width, the dynamics that govern the temporal growth depends only on the vorticity magnitude and not on the shear zone width or shear magnitude independently.

5.1.4. Phase shift and initial length

Wave interaction theory (WIT) predicts that the growth of instabilities occurs once the two vorticity waves propagating along the shear zone vorticity discontinuities become phase-locked (i.e. Heifetz et al. 1999; Heifetz and Methven 2005; Carpenter et al. 2012; Guha et al. 2013). Phase-locking occurs when the phase shift between the two waves promote exponential growth of each wave. From linear theory, this phase shift is predicted to be $\phi = \cos^{-1}\left[\left(1-2\alpha_n\right)e^{2\alpha_n}\right]$, where α_n is the normalized wavenumber of maximum growth. A series of phase shifts were calculated for each case by examining the vorticity fields (e.g., Fig. 5.2) during

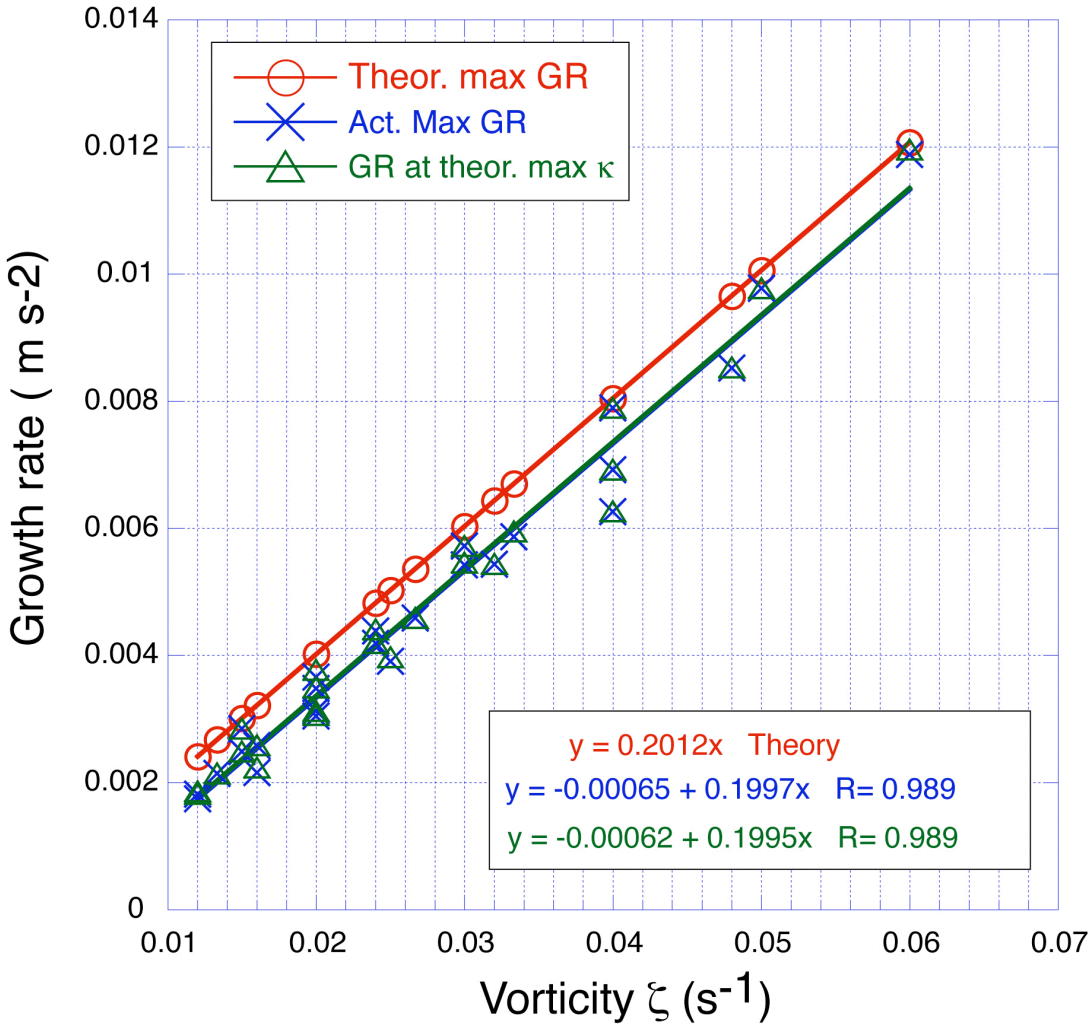

Figure 5.22. Maximum growth rates (blue) and growth rates at the theoretical maximum (green) plotted as a function of vorticity for all barotropic simulations. Also plotted in red are the theoretical maximum growth rates. Lines indicate linear least squares fits to the data points. Also shown are the least squares line equation and the correlation coefficient of these fitted lines.

Phase shift	4m12s	5m16s	8m20s	10m24s
1	0.37π	0.36π	0.29π	0.34π
2	0.33π	0.40π	0.27π	0.38π
3	0.31π	0.32π	0.31π	0.41π
4	0.36π	0.39π	0.32π	0.39π
5	0.41π	0.39π	0.29π	0.40π
6	0.32π	0.30π	0.30π	0.39π
7	0.38π	0.38π	0.33π	0.34π
8	0.38π	0.37π	0.31π	0.36π
Average	**0.36π**	**0.36π**	**0.30π**	**0.38π**
Linear theory	0.35π	0.35π	0.35π	0.35π
Actual Max. wavenumber	0.38π	0.35π	0.28π	0.38π

Table 4. Calculated phase shifts from four simulations, including eight individual developing waves per simulation. Also shown are the averages for each case, the predictions of linear theory, and the phase shifts computed from the actual maximum wavenumber.

the emergence of well-defined vortices. A total of eight individual waves were examined in each case, with results of the following calculations listed in Table 4. The most-unstable wavenumber predicted by linear theory corresponds to a theoretical phase shift of 0.35π. The phase shifts calculated from the simulations are close to the predicted values (ranging from 0.30π - 0.38π). We can also calculate the theoretical phase shift corresponding to the wavenumber of actual maximum growth rate. The calculated phase shifts are closer to these values, indicating that the wavenumber that eventually emerges has an actual phase shift in accord with WIT. Knowing the phase shift, we can calculate the initial length of

Initial length (m)	4m12s	5m16s	8m20s	10m24s
1	1840	2700	4640	4730
2	1730	2160	4000	5170
3	1620	2480	4110	4730
4	1730	2810	3890	4950
5	1730	2480	3890	5280
6	1620	2380	3890	4840
7	1890	2700	4750	4730
8	1890	2270	4000	4840
Average	**1760**	**2500**	**4150**	**4910**
Linear theory	2130	2660	4300	5320
Actual Max. wavenumber	2040	2680	4780	5060

Table 5. As in Table 4, except for initial lengths.

what will eventually become the resulting vortex core as $l_{init} = \left(1 + \frac{\phi}{\pi}\right)\frac{\lambda}{2}$, where λ is the normalized wavelength, corresponding to the most-unstable mode. Table 5 shows the values of initial length calculated from the simulations. Again, the values are consistent with the initial lengths corresponding to the most-unstable wavenumber predicted by linear theory, and with the initial lengths corresponding to the actual most-unstable mode. However, the initial lengths had a low bias in all four simulations.

5.1.5. Nonlinear evolution

Although it is beyond the scope of this research to study the fully nonlinear dynamics of the resulting vortices, some aspects of the roll-up of vortices may be

described and compared to observed and other simulated vortices. Continuation of Fig. 5.3 is shown in Fig. 5.23 for the bt5m16s case. As the shear zone continues to roll-up into discrete vortices, the flow saturates (i.e., perturbations reach a maximum) around 1920 s into the simulation (Fig. 5.23a-b). At this time, there is a maximum perturbation in the positive (negative) v-component velocity on the east (west) sides of the circulation and a positive (negative) u-component velocity on the south (north) side corresponding to a velocity couplet and a vortex with a positive sign of vertical vorticity (Fig. 5.24). Nonlinear effects eventually dominate as the vortices continue to evolve in the period 1980 - 2160 s (Fig. 5.23c-f, Fig. 5.24c-f).

In terms of vorticity structure (Fig. 5.24), nearly equally spaced elliptical vortex cores develop which are separated by bands or braids of vorticity. With time, these braids become elongated and begin to completely wrap around the central vortex core. The elliptical vortex core itself rotates at constant angular velocity. The core also nutates; that is, the core aspect ratio (the ratio of the major and minor axis of the ellipse) undergoes a periodic oscillation. Once the core reaches saturation, the vorticity within the core evolves in a somewhat complicated manner. In all vortices, there is a slight decrease with time of the magnitude of the central vorticity, although in some vortices this relative weakness is in the center whereas in others it is displaced to one side. As the vortices evolve, vertical motion fields develop with maximum amplitudes of about ~2-3 m s^{-1}. Although the strongest vertical motion fields are near the vortex core, weaker vertical motions develop along the braids. There appear to be 3 types of vertical motion structures associated with the mature vortices. The first is characterized by a couplet of upward/downward motion with centers on either side of the vortex, the second with weak downward motion within the vortex and no exterior updraft, and the third with an updraft surrounding the vortex and a downdraft in the center.

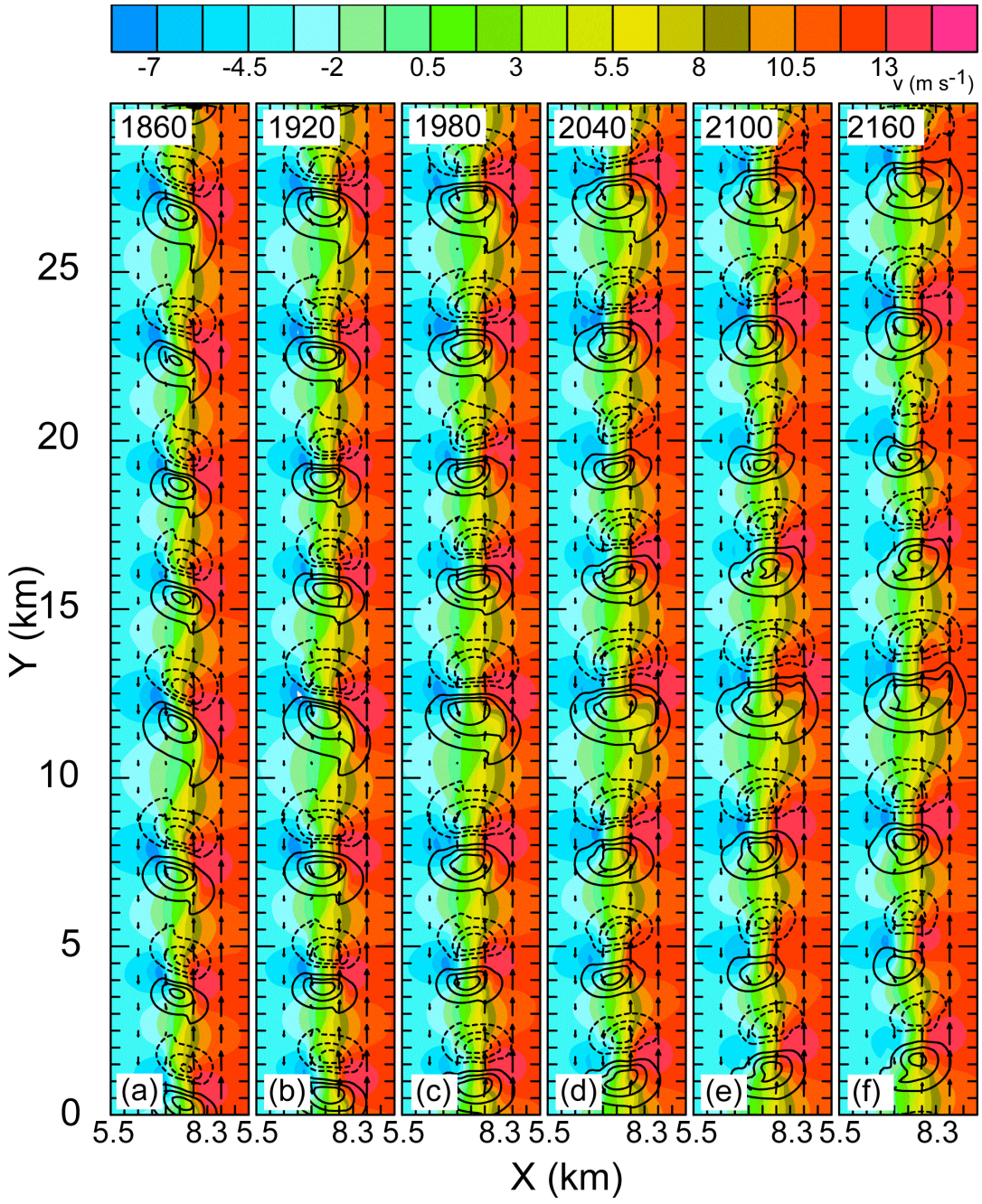

Figure 5.23. *v*-component wind (color filled) and horizontal wind vectors (500 m = 10 m s^{-1}) through the center of the simulation domain (z = 2.0 km) for the bt5m16s case with solid (dashed) contours denoting westerly (easterly) flow at 1 m s^{-1} intervals starting at 1 (-1) m s^{-1}.

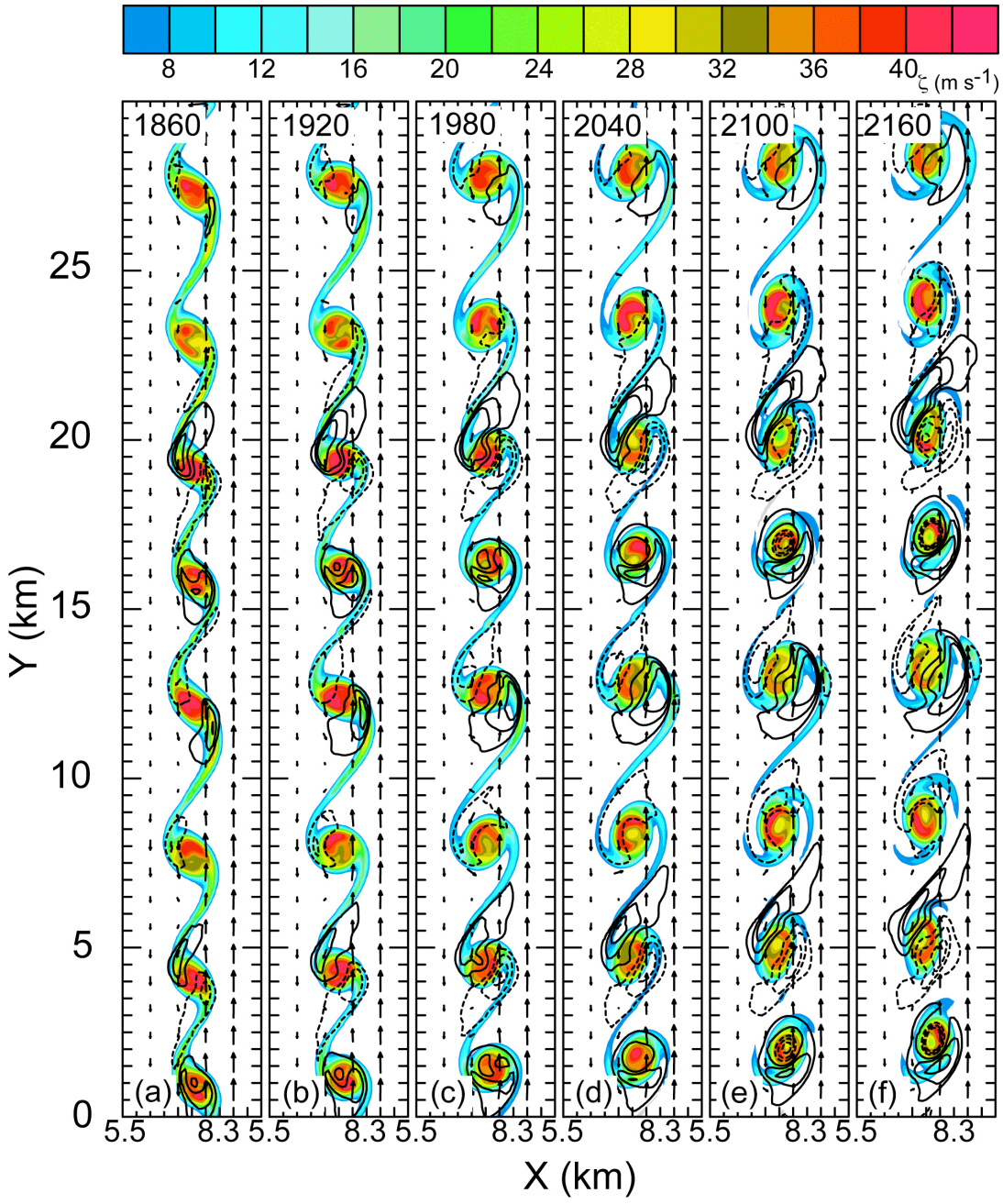

Figure 5.24. Vertical vorticity at z = 2.0 km for the bt5m16s case, with the solid (dashed) black contours denoting positive (negative) vertical velocity at 1 m s^{-1} intervals starting at 1 (-1) m s^{-1}. Also shown are the horizontal wind vectors (500 m = 10 m s^{-1}).

The structures of the pressure fields are consistent among all vortices, with a pressure perturbation minimum in the center of each vortex and a local pressure perturbation maximum between each vortex in the braid regions (Fig. 5.25). Away from the vortex cores, the pressure perturbation field remains fairly constant with both the local maximum and minimum elliptical regions featuring a nearly east-west oriented major axis. In the vortex cores, however, the major axis of the pressure minimum rotates with an angular velocity near that of the vortex itself.

The vertical structure of the vorticity and vertical velocity fields following one particular vortex is shown in Figs. 5.26 and 5.27. By 1860s into the simulation, the maximum in vertical vorticity is tilted from south to north with height (the core) with the weaker braids tilting from north to south with height (Fig. 5.26a-c). An updraft exists on the western part of the core and also tilts and increases from south to north with height. On the eastern flank of the core, a downdraft is seen which also tilts from south to north with height, but decreases in strength. This pattern of "wrapping" updrafts and downdrafts along with the vorticity cores and braids is common to many of the simulated vortices.

As the vortex continues to evolve, the magnitude of the vorticity in the braid north of the vortex weakens slightly (Fig. 5.26d,g), whereas the maximum vorticity in the southern part of the vortex core deepens (Fig. 5.26f,i). Through the center of the core, the peak vorticity remains nearly constant. Some variability in the vertical structure is noted both in the vortex core and in the braid region. By about 2040, the western updraft and eastern downdraft reach a maximum, which persists (Fig. 5.27). The vertical structure of the updraft remains similar throughout the 1860-2160 time frame. By 2040, the braids begin wrapping around the vortex core (Fig. 5.27). Also by this time, a relative weakness in the vertical vorticity develops through the center of the vortex in the middle levels associated with the downdraft.

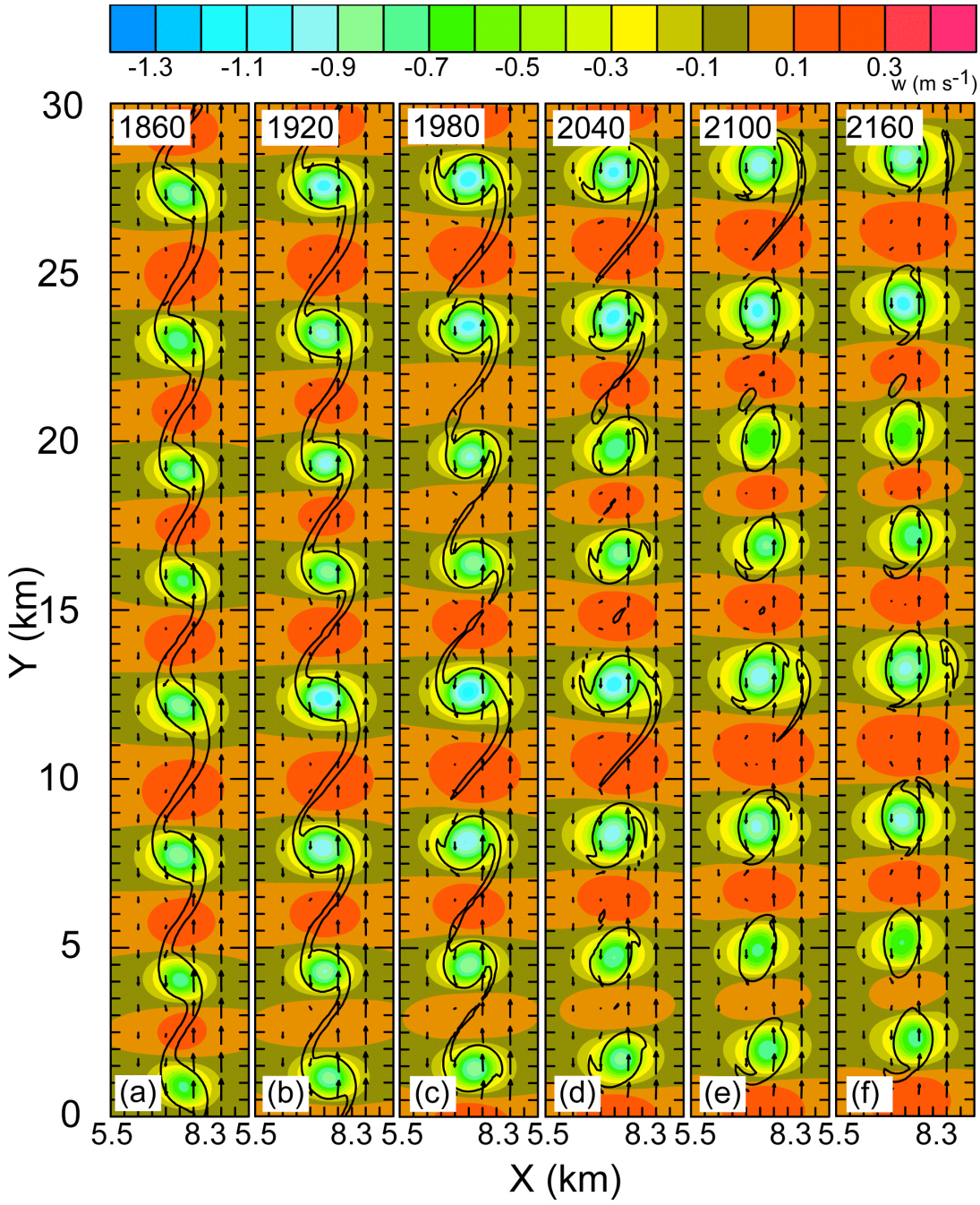

Figure 5.25. Perturbation pressure in hPa (color-filled) and the 10 x 10^{-3} s^{-1} vertical vorticity contour (black) for the bt5m16s case. Also shown are the horizontal wind vectors (500 m = 10 m s^{-1})

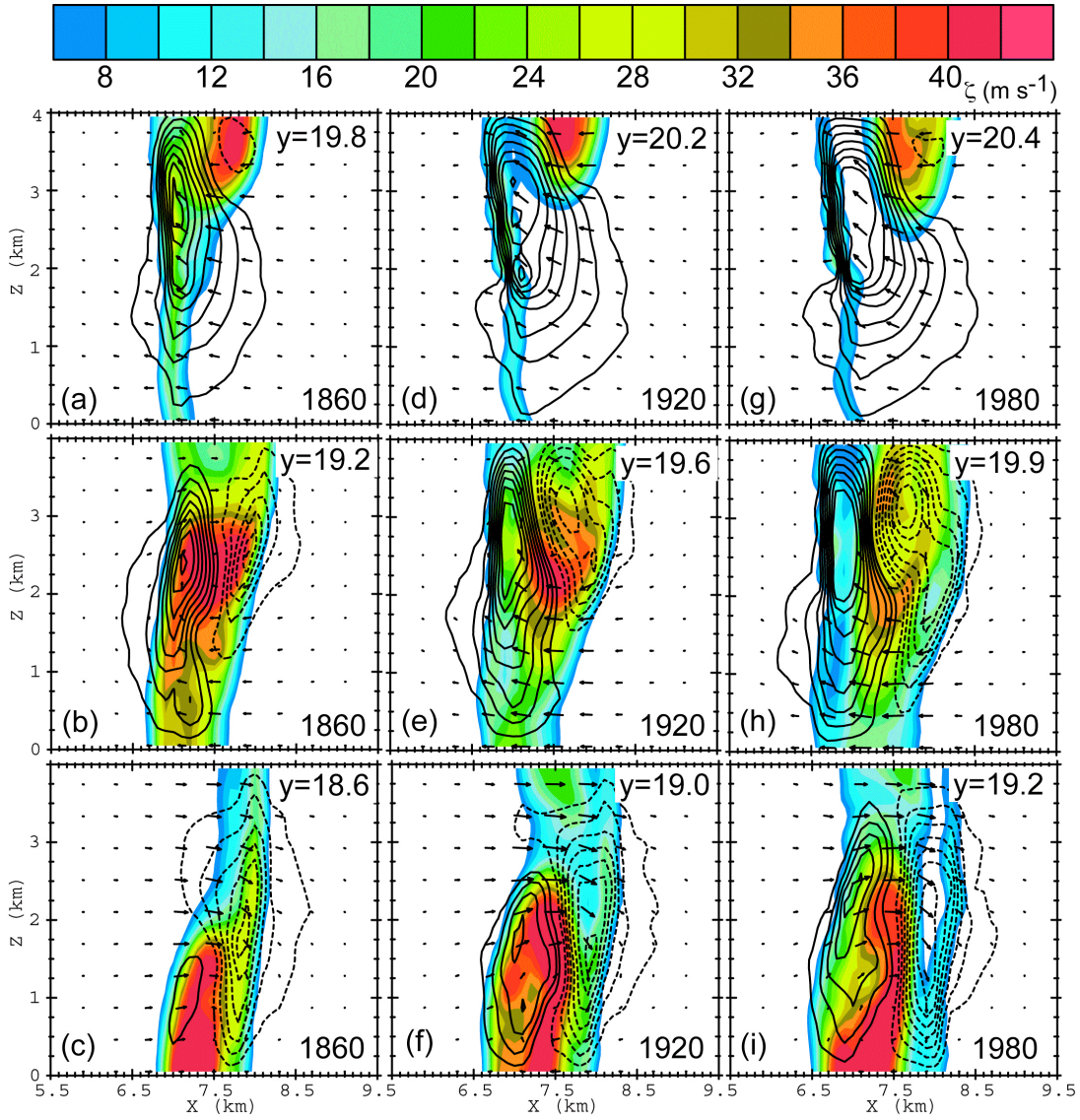

Figure 5.26. Vertical vorticity (color filled) and vertical velocity with solid (dashed) black contours denoting positive (negative) vertical velocity at 1 m s^{-1} intervals starting at 1 (-1) m s^{-1} for the bt5m16s case. The top panels are just north of the vortex core, the middle panels through the center of the vortex, and the bottom panels just south of the vortex cores. Each column represents a different times increasing to the right.

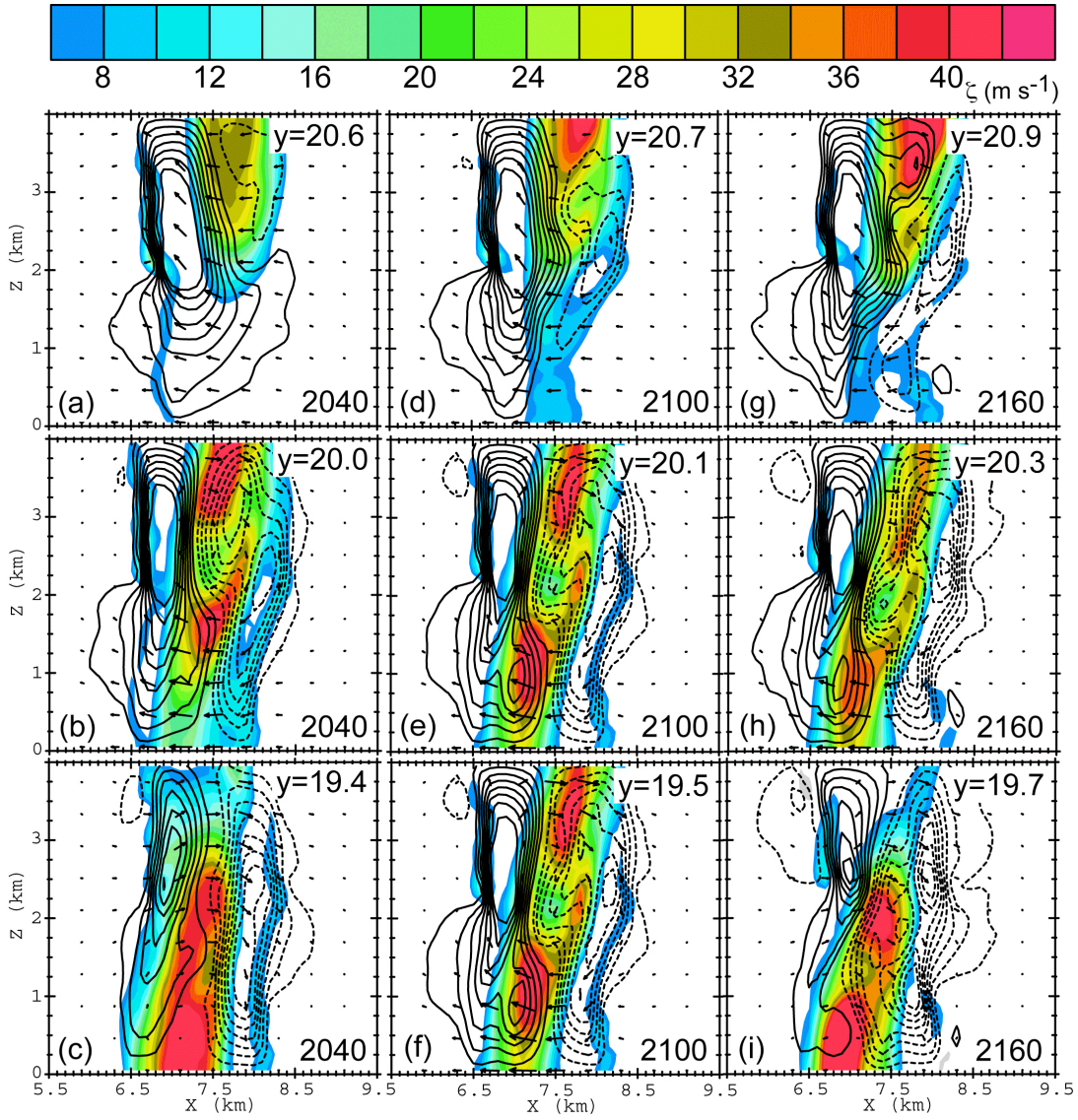

Figure 5.27. As in Fig. 5.26 but at later times.

A north-south cross-section through the middle of a series of vortices is shown in Fig. 5.28. There appear to be four "types" of vortices in terms of their vorticity and vertical motion fields. The first type of vortex (the left-most or southern-most) is characterized by a nearly vertical column of vertical vorticity that initially contains a deep updraft. With time, a central downdraft develops from top down and is associated with a local weakness in the vertical vorticity. As this occurs, the vortex becomes narrower near the surface and wider aloft.

The next type of vortex slopes slightly downstream with height and flanked by a downdraft on the southern side and updraft on the northern side. These vertical motions increase with time, with the updraft increasing with height and downdraft decreasing with height. In addition, a local weakness in the vertical vorticity is seen within the central part of the vortex.

The third vortex type slopes very slightly upstream with height and initially contains very weak upward vertical motions that transition to very weak downward vertical motions. Just north of the vortex core, a downdraft updraft couplet develops and intensifies along a kink in the braid. Again, a local weakness in the vorticity fields is seen in the vortex center.

The last type of vortex is characterized by an updraft on the southern side of the vortex. This vortex also tilts upstream with height and contains a local minimum in vorticity within the vortex center. Also, a downdraft develops along and north of the vortex core with time. In general, with time, the size of the vortices increases and the size and magnitude of the vorticity in the braids between the vortices decreases. Also, every fourth vortex, the vortex type is repeated. That is, there is a wavenumber two component to the series of vortices (i.e., each vortex type is repeated twice in the simulation domain). Note that as the mature vortex begins to saturate, the localized updraft maximum also begin to reach a nearly

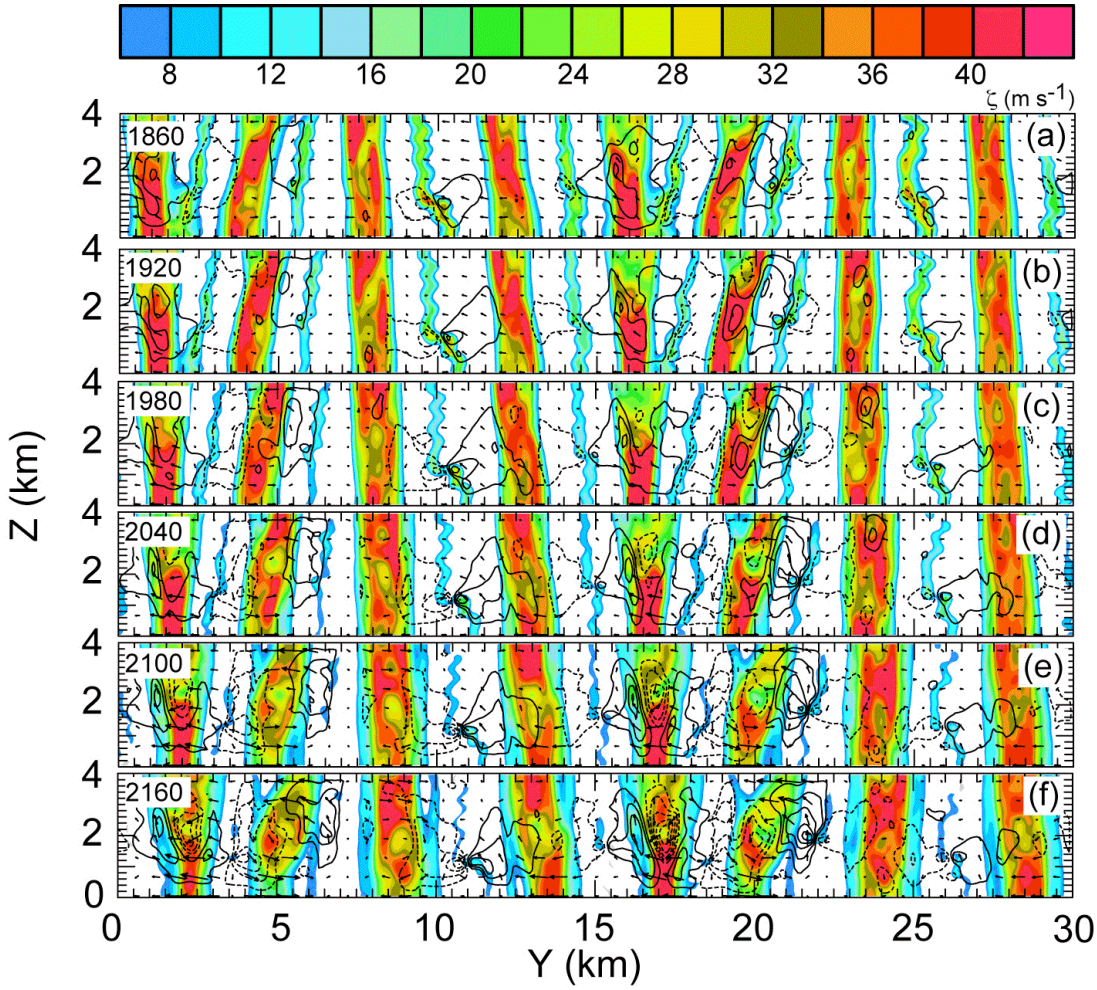

Figure 5.28. Vertical cross-sections (y increasing northward) of vertical vorticity (color filled) and vertical velocity at (a) 1860, (b) 1920, (c) 1980, (d) 2040, (e) 2100, and (f) 2160. The solid (dashed) black contours denote positive (negative) vertical velocity at 1 m s^{-1} intervals starting at 1 (-1) m s^{-1} for the bt5m16s case. Also shown are the wind vectors in the plane (500 m = 10 m s^{-1}).

constant average value (Figs. 5.24, 5.26-5.28). Although the detailed evolution of the nonlinear stage of evolution has been shown for only one case, we can compute the average local maxima in vertical motion as each case reaches vortex saturation and compare the results (Fig. 5.29).

For a given shear zone width, as the magnitude of the shear increases, the average local vertical motion maximum also increases. Across each shear zone width series, the correlation between the magnitude of the maximum vertical motion and the magnitude of the shear is very high ($R \sim 0.978$-$.999$). Also, across the series of shear zone widths, the slope of the best-fit lines is also similar, but generally features a decrease in slope with increasing width. This decrease is most pronounced between the 600m and the 800m cases. Note that the 1000m cases (not shown) also have a slope that is smaller than the 800m cases.

Since for a given magnitude of shear, as the shear zone increases the shear zone vorticity decreases, the decrease in the slope of the lines in Fig. 5.29 as the shear zone with increases might be due to the effects of shear zone width on the vorticity. Since the growth rate and subsequent vortex strength is proportional to the shear zone vorticity, the relationship between maximum vertical motion and shear zone vorticity is shown in Fig. 5.30. Across all barotropic simulations, as the shear zone vorticity increases, the resulting localized updraft maxima also increase, with a fairly high degree of correlation ($R = 0.89$). This suggests that given a known magnitude of the initial shear zone vorticity, the magnitude of the subsequent local vertical motion maximum associated with mature vortices can be diagnosed.

5.1.6. Cumulus formation

An additional four equivalent-barotropic simulations were performed (all with different shear zone widths and shear magnitudes) with moisture added while

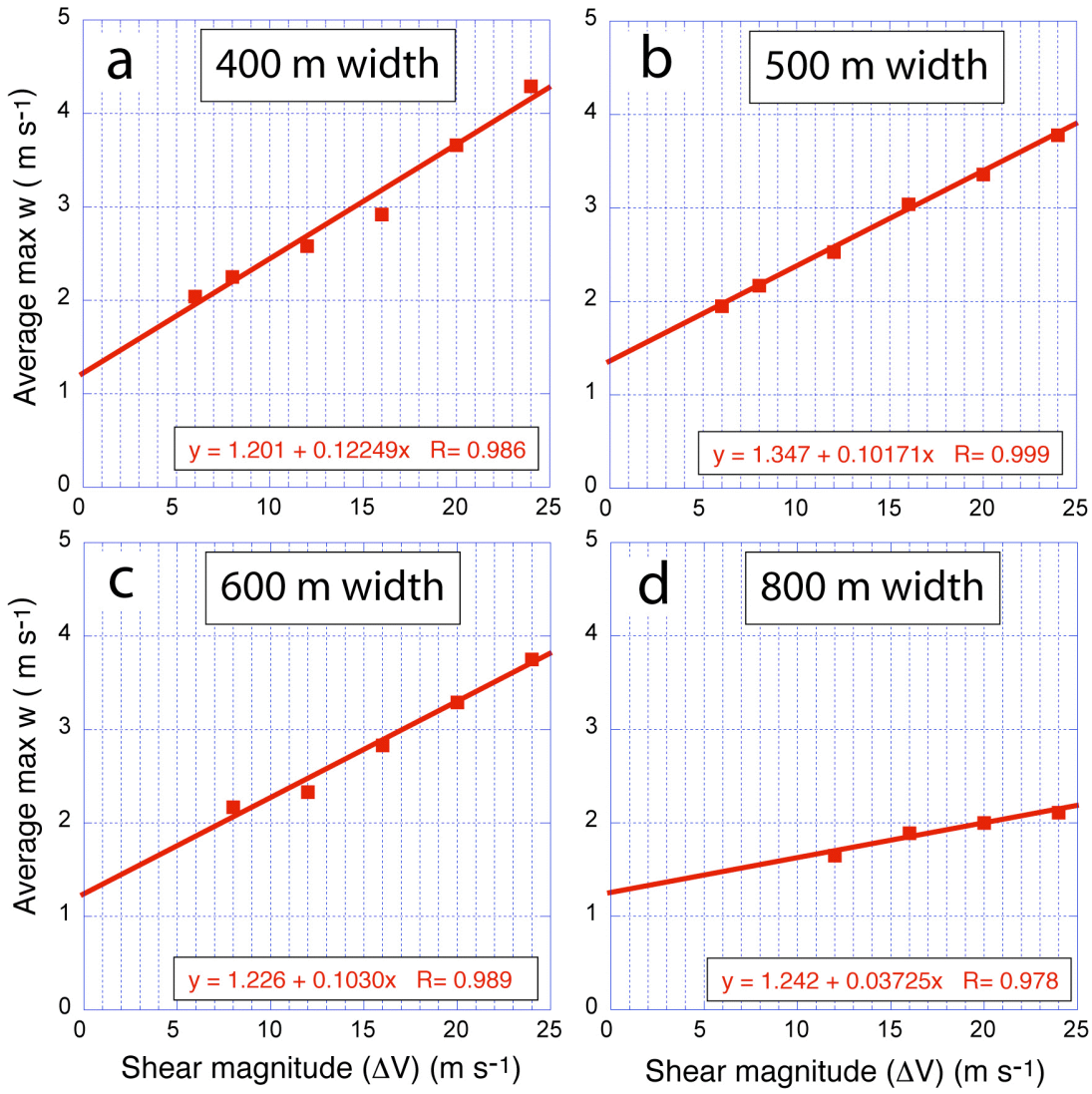

Figure 5.29. Average maximum upward vertical motion (red squares) and the linear least-squares fit (red line) for barotropic simulations with four shear zone widths as a function of shear magnitude.

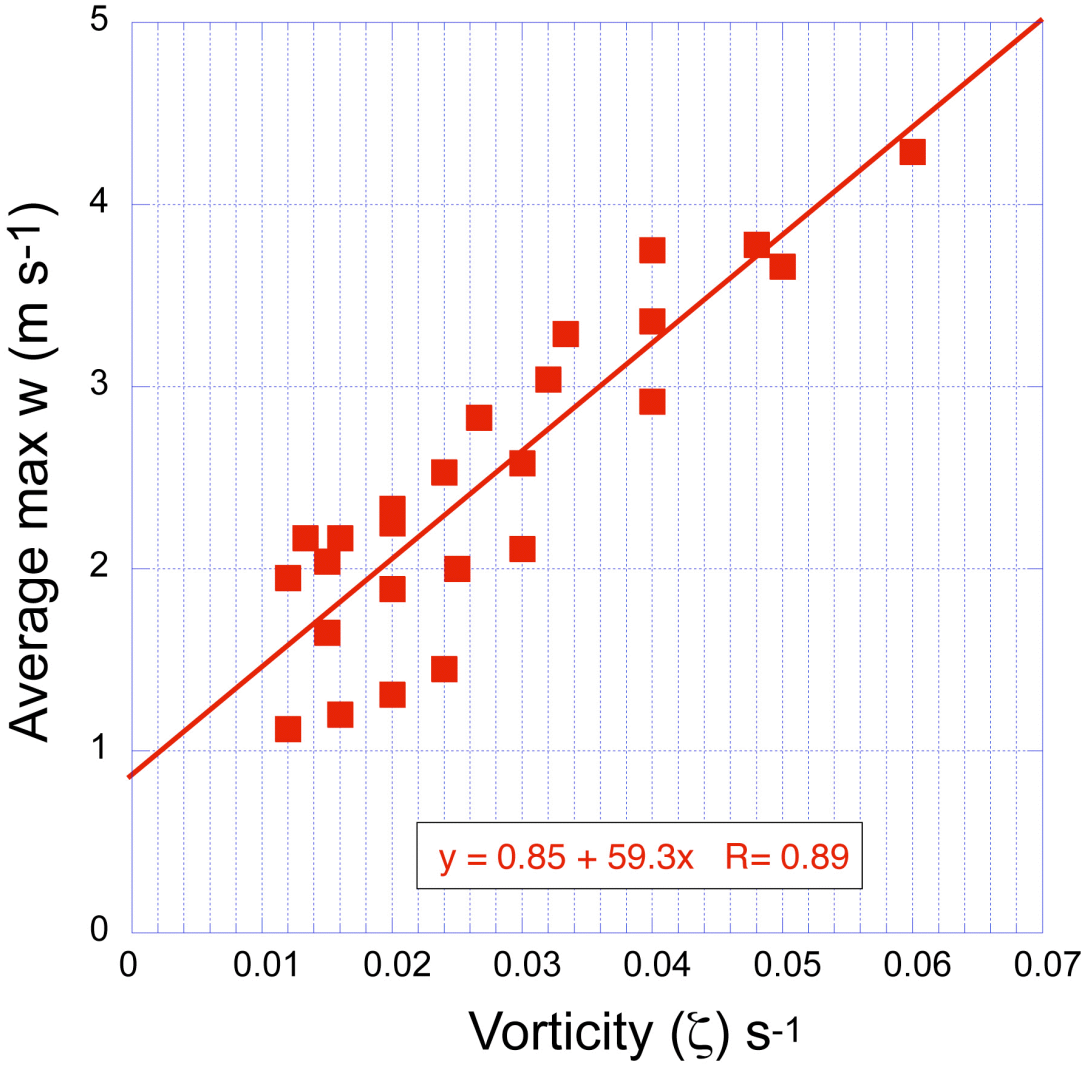

Figure 5.30. Average maximum upward vertical motion for each barotropic simulation (red squares) and the linear least-squares fit (red line) as a function of shear zone vorticity.

maintaining homogeneity in virtual potential temperature to assess preferred locations of cumulus formation. The moist equivalent-barotropic runs are denoted by a suffix "mbt" preceding the run name shown in Table 2. To produce the moist equivalent-barotropic simulations, moisture was prescribed throughout the entire domain, with higher values east of the shear zone, lower values west of the shear zone, and values increasing linearly from west to east across the shear zone. Prescribed moisture values also decreased linearly with height everywhere, while prescribed potential temperature increased slightly with height. The resulting potential temperatures were adjusted such that the virtual potential temperature was horizontally homogeneous (thus preserving the barotropic base state) and increased slightly with height (providing a small static stability).

Evolution of the vorticity and cloud-water mixing ratio at 3 km for the mbt5m16s are shown in Fig. 5.31. Clouds have formed by about 1980 s between the wrapping braid region and the core west of several mature vortices. Also, the developing cumuli grow larger with time. Note again the wavenumber two modulation of the vorticity fields and the resulting cloud pattern. Of the eight discrete vortices, two contain the largest developing cumuli of roughly the same size and shape, two contain smaller cumuli of roughly the same size and shape, and four do not develop cumuli.

The moisture fields associated with the evolving vortices display the classic Kelvin-Helmholtz (KH) billow wave pattern (although most previous KH billow examples involve waves in a vertical plane), with moist and dry air wrapping around the vortex center (Fig. 5.32). The modeled cumuli are associated with the stronger updrafts, with the deepest, strongest updrafts producing the largest cumuli. Note that although the peak in each local updraft is centered on the moisture gradient on the west edge of the core, nevertheless the modeled cumuli form to the west of the

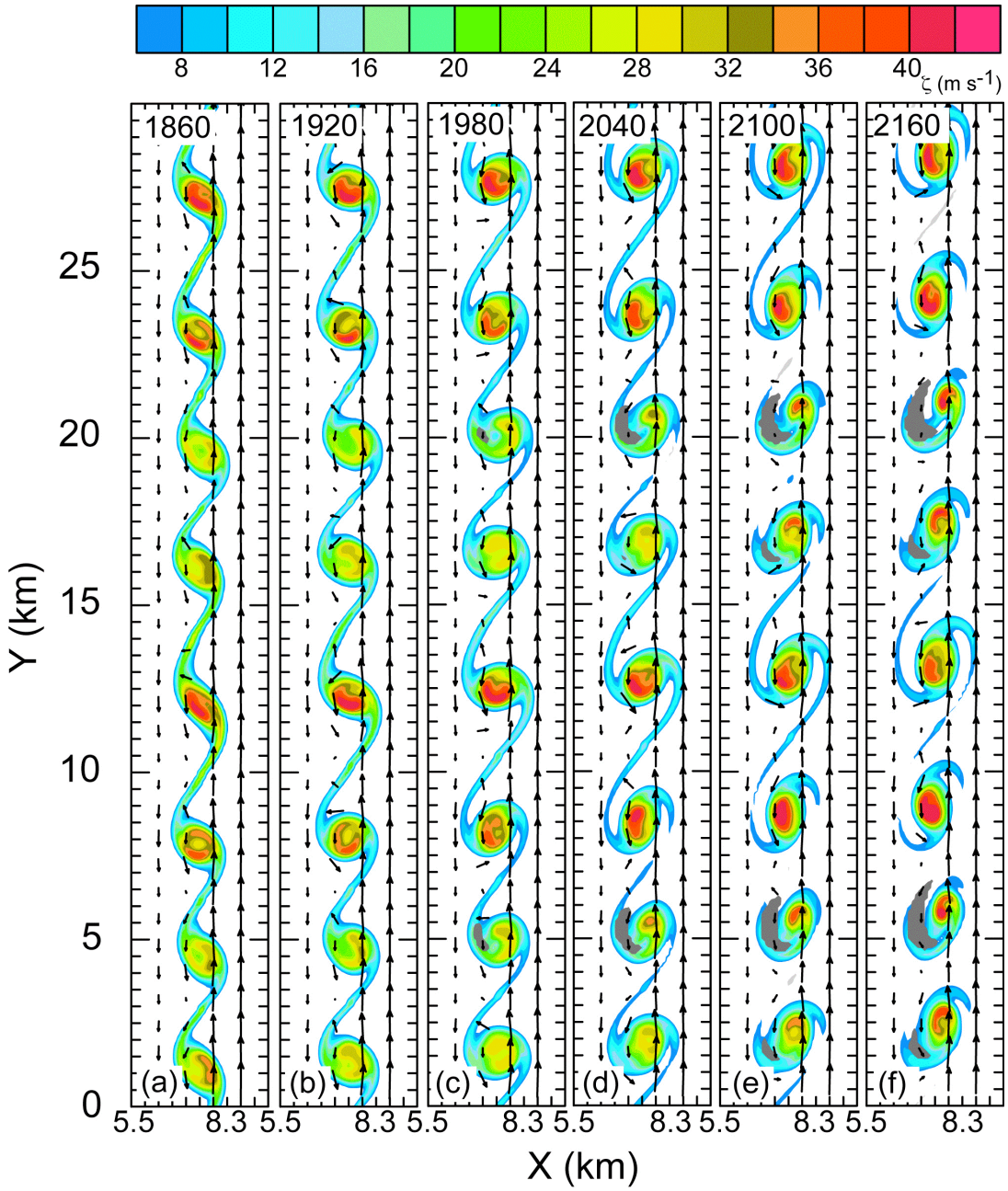

Figure 5.31. Vertical vorticity at z = 3.0 km, with the solid gray shading denoting cloud water mixing ratio greater than 0.01 g kg^{-1} for the mbt5m16s case. Also shown are the horizontal wind vectors (500 m = 8 m s^{-1}).

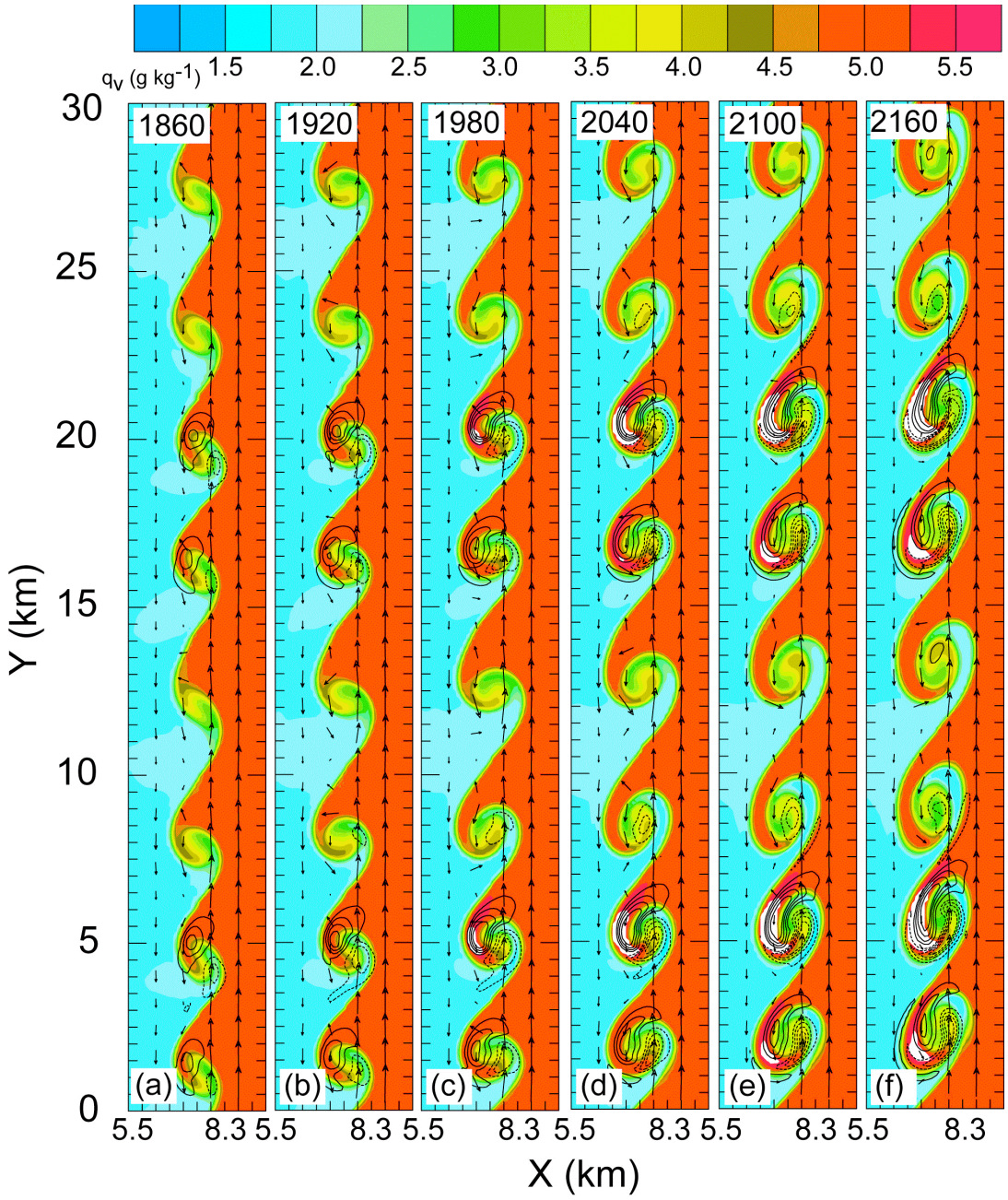

Figure 5.32. Water vapor mixing ratio (color filled) at 3.0 km for the mbt5m16s case. The solid (dashed) black contours denote positive (negative) vertical velocity at 1 m s^{-1} intervals starting at 1 (-1) m s^{-1}. Also shown are the horizontal wind vectors (500 m = 8 m s^{-1}). The white shaded regions denote cloud water mixing ratio greater than 0.01 g kg^{-1}.

maximum updraft. In other words, cumulus formation is forced within weaker (but still locally strong) updrafts that are juxtaposed with higher moisture values in the region between the vortex core and adjoining braid to the west. Although only one moist simulation is shown, the locations of developing cumuli (in relation to the vortex) were identical in all moist simulations.

5.2. BAROCLINIC SIMULATIONS

A series of idealized dry simulations were performed for the baroclinic case in which a coincident shear layer and a horizontal density gradient were imposed between two infinite fluids. Each simulation is identical in configuration except for the two varied parameters of shear zone width and shear magnitude (thus vorticity and magnitude of the density gradient). The magnitude of the temperature perturbation in the cold air was set to 0.5 K and was prescribed from the surface up to 1.5 km in height. The parameters for the series of simulations are shown in Tables (2-3).

All simulations have a similar evolution. The initial north-south-oriented shear zone begins moving eastward briefly before slowing and becoming quasi-stationary near the center of the domain. In addition, the shear zone width for all cases collapses to about twice the grid spacing before periodic disturbances grow and distort the shear zone in a wave-like manner. The resulting waves roll-up into discrete vortices that persist for a brief time before nonlinear processes lead to vortex mergers and evolution into turbulence. Although the behavior of the simulations is consistent from one simulation to the next, there are differences, for example, in the growth rates, number of vortices, and how fast the shear zone collapses for any given simulation. Despite the transient behavior of the initial shear zones in the baroclinic cases, the results can usefully be generalized in similar fashion to the barotropic cases in which the initial shear zone was steady.

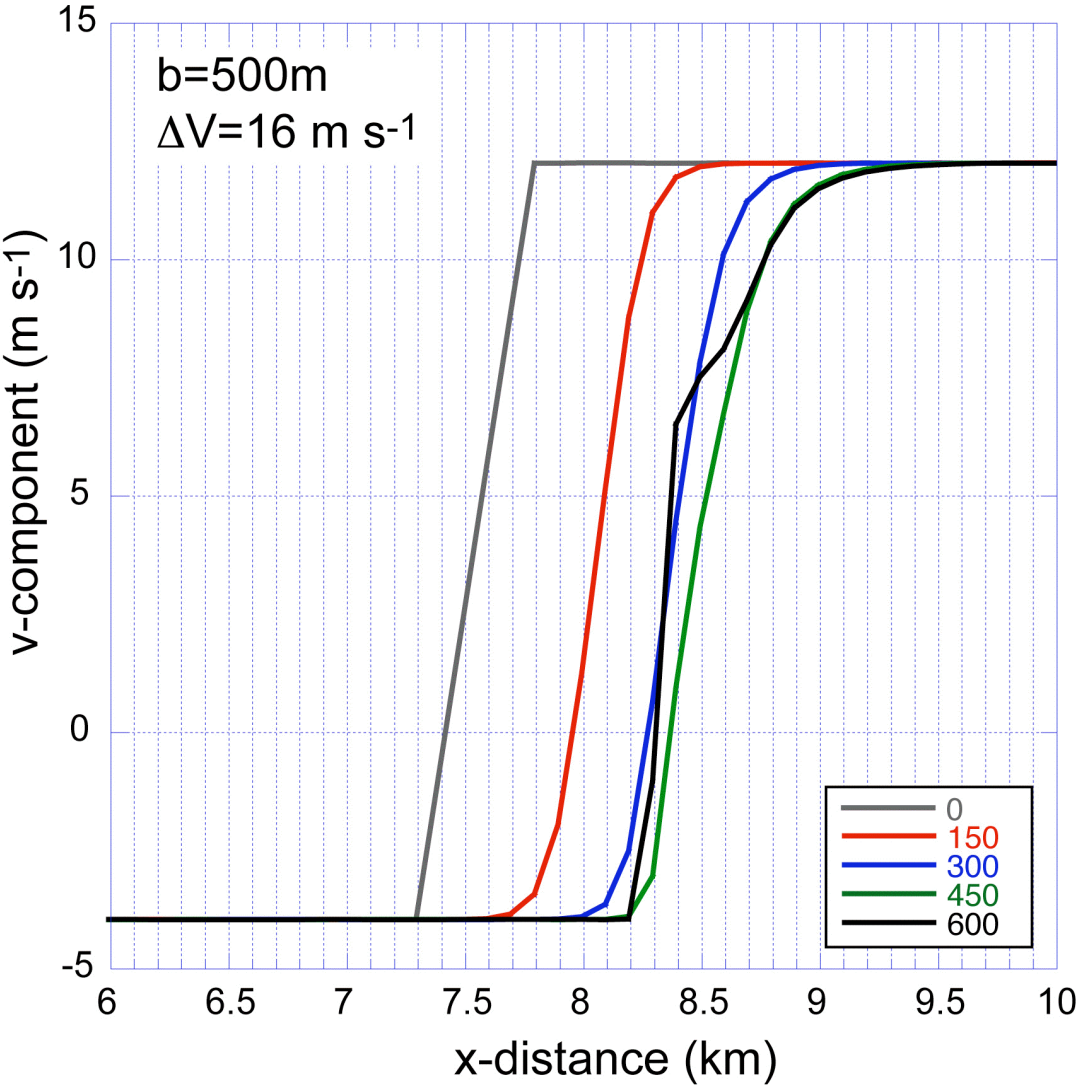

Figure 5.33. North-south averaged v-component velocity profiles for the bc5m16s case. Different color curves indicate different times.

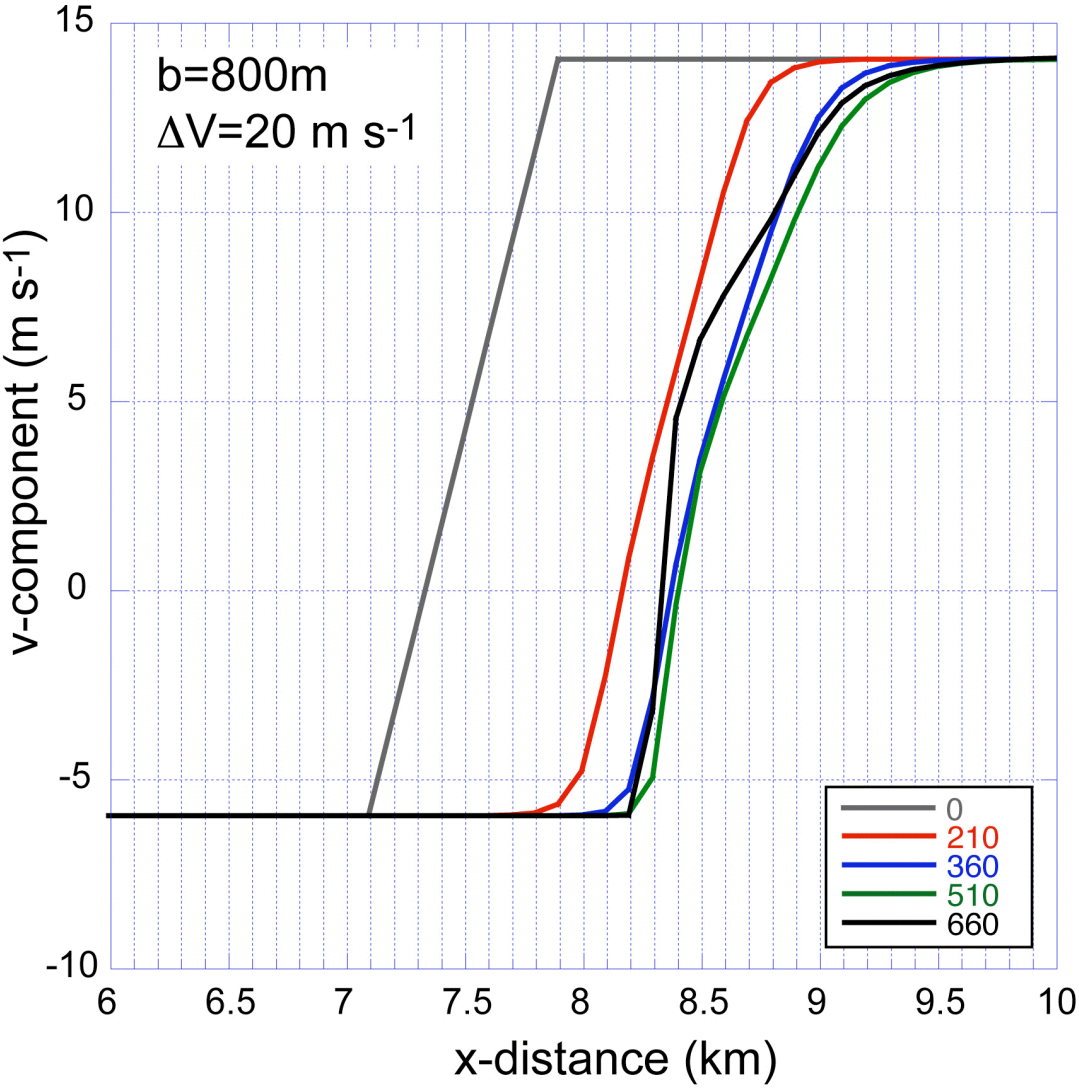

Figure 5.34. As in Fig. 5.33, except for the bc8m20s case.

5.2.1. Evolution of shear zones

The initial collapse of the shear layers in the baroclinic simulations may be visualized via the evolving *v*-component velocity profiles at several times prior to the emergence of discrete vortices. The *v*-component velocity profiles are shown in Figs. 5.33 and 5.34 for the bc5m16s and bc8m20s cases, respectively. The shear layer behaves similarly in both cases, with an initial eastward motion before slowing and becoming essentially stationary. As this occurs, the width of the shear zone collapses, however the collapse is greater on the western side of the shear zone than on the eastern side. Immediately prior to the emergence of the vortices, approximately 75% of the shear is located within 2Δ on the western edge of the shear zone. For the bc8m20s case, the boundary collapse took slightly longer due to the wider initial shear zone. The evolution of the vorticity profile for bc5m16s and bc8m20s cases are shown in Figs. 5.35 and 5.36 respectively. For the bc5m16s case, as the shear zone begins to collapse, the peak vorticity values don't change much, however the distance containing the higher vorticity values decreases.

During shear zone contraction, the distance containing lower vorticity values actually increases. As time progresses, the peak vorticity values begin to increase, and the distance containing these higher values also decreases (i.e., evolving from a top hat profile to a steep single-peak profile). The vorticity gradient is also largest on the western side of the shear zone, and gradually weakens from west to east. The bc8m20s case follows a similar evolution, however the exponential increase in peak vorticity is more readily seen. In both cases, the vorticity profile just before the appearance of discrete vortices is characterized by a rapid increase in vorticity on the western shear zone edge, followed by a peak in vorticity and a gradual exponential-like decrease in vorticity continuing to the east.

The evolution of the peak vorticity within the initially contracting shear zone

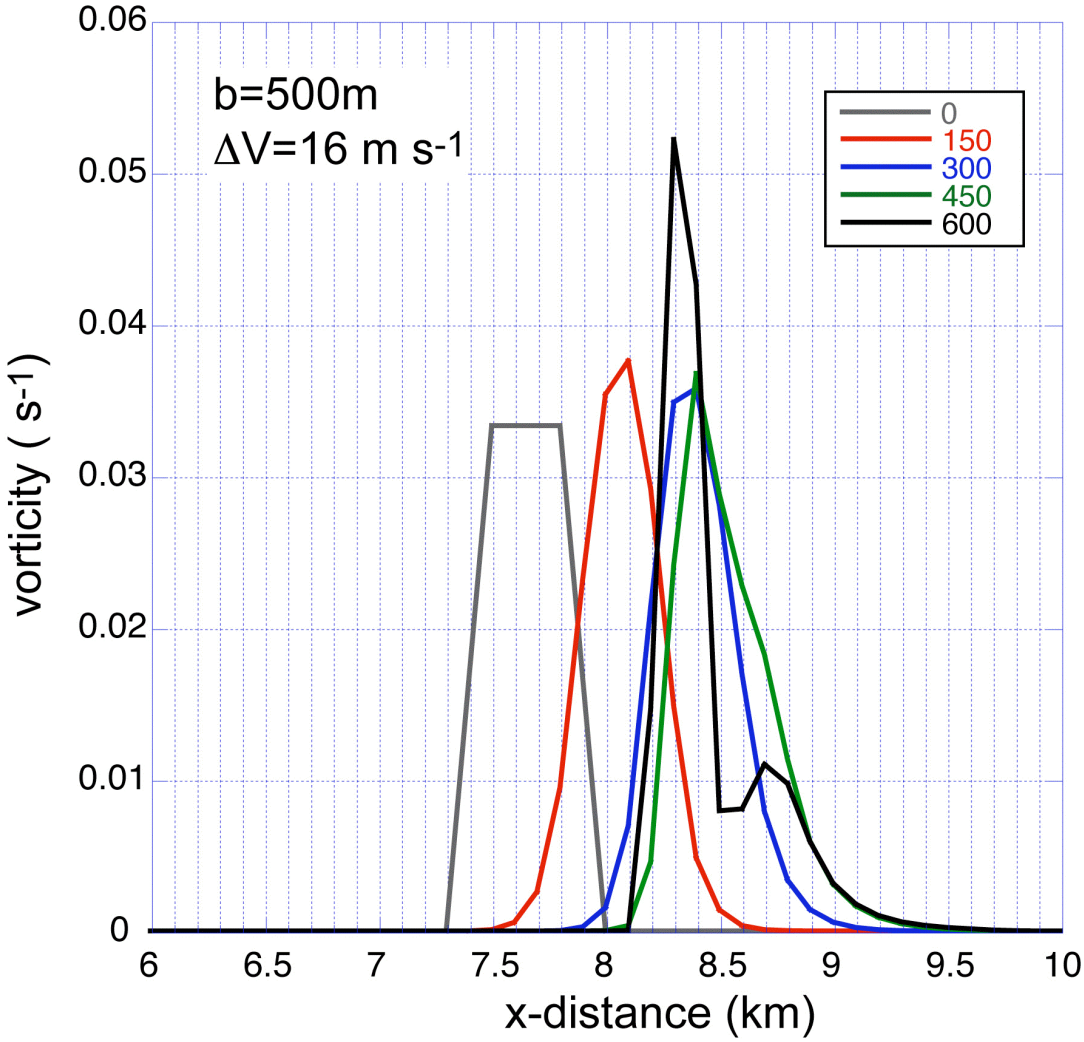

Figure 5.35. North-south averaged vertical vorticity profiles for the bc5m16s case. Different colored curves denote different times.

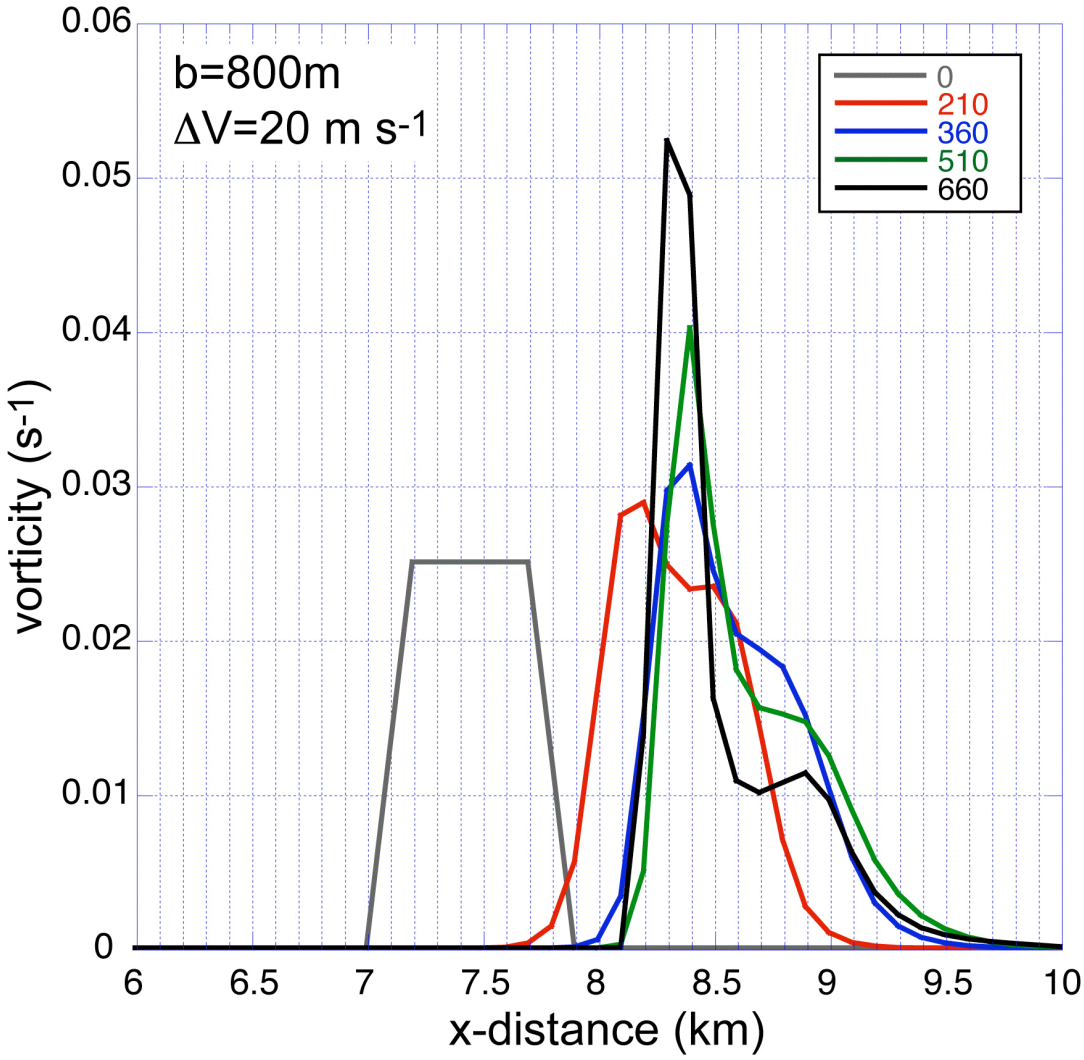

Figure 5.36. As in Fig. 5.35 except for the bc8m20s case.

can usefully be approximated in terms of the predominant vorticity tendencies due to stretching and tilting. Because the shear zone is contracting, one would expect the magnitude of the peak vorticity to increase due to stretching. Neglecting *y*-variations of variables, the vertical vorticity equation can be written in the form

$$\frac{D\zeta}{Dt} = -\zeta \frac{\partial u}{\partial x} - \frac{\partial v}{\partial z}\frac{\partial w}{\partial x} \tag{5.1}$$

where ζ is the vertical vorticity and the effects of friction and the earth's rotation have been neglected. The first term on the right hand side is the vorticity tendency stretching term, while the second term is that due to tilting. From the simulation, we can take north-south averages of the vorticity in each column, then pick out the maximum average vorticity in the east west direction (i.e. the peak in the curves in Fig. 5.35) at each time. We can then estimate what peak vorticity value we would expect, given an initial vorticity value (constant barotropic value) plus a change due to the presence of stretching and tilting. For example for the stretching term, we find the peak vorticity value at some time, then using that value of vorticity (ζ) at that point and a calculated divergence at that point ($\frac{\partial u}{\partial x}$), compute a vorticity tendency. This is also done for the tilting term.

The evolution of individual tendencies is shown in Fig. 5.37. Both the stretching and tilting terms are very small to begin as the model is adjusting to the initial conditions. Eventually the stretching term begins to increase exponentially, with positive values indicating increasing vorticity tendency. The tilting term increases slowly, initially with positive tendency values, then decreases more rapidly with negative values ensuing at later times. To see the net effect on the resulting vorticity evolution, we take the tendency values and multiply them by the time interval between calculations, and add them to the previous estimated vorticity

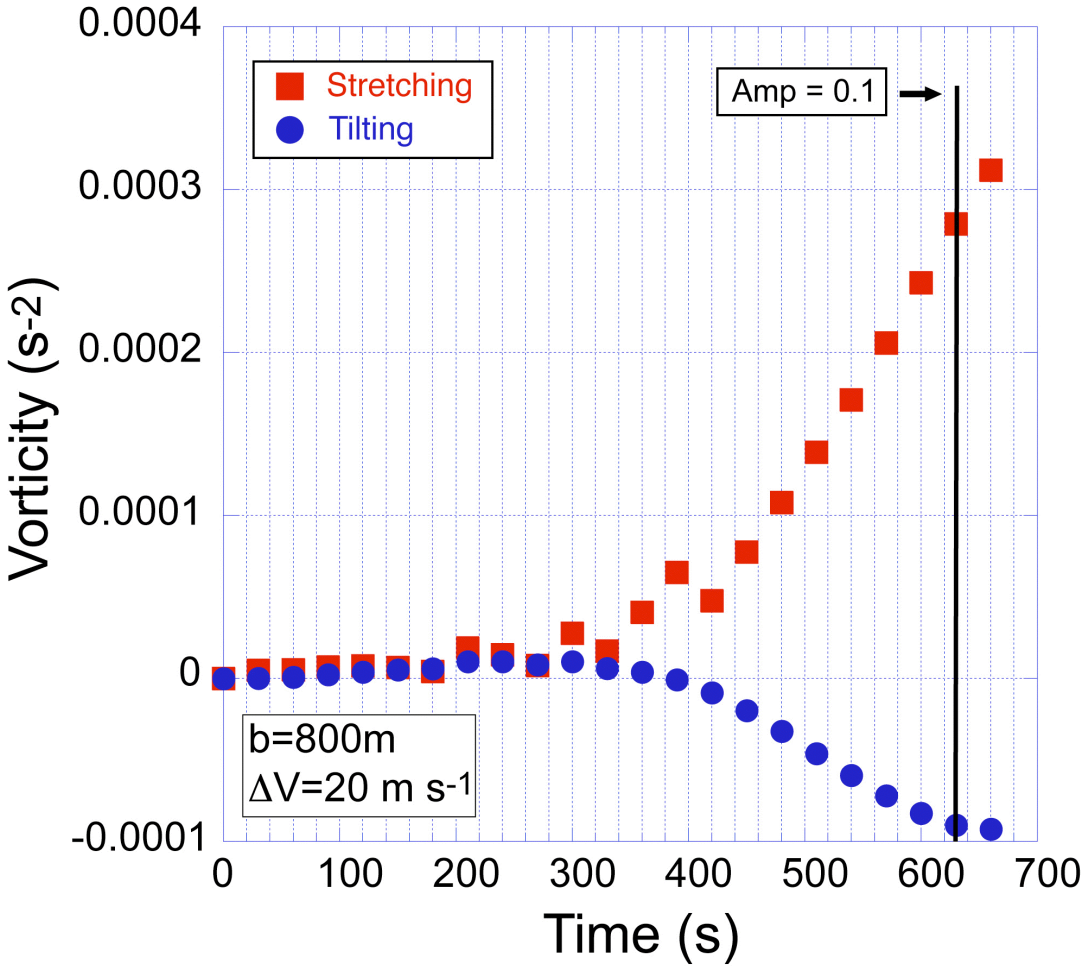

Figure 5.37. Instantaneous stretching vertical vorticity tendency (red squares) and tilting vertical vorticity tendency (blue circles) at various times in the bc8m20s case.

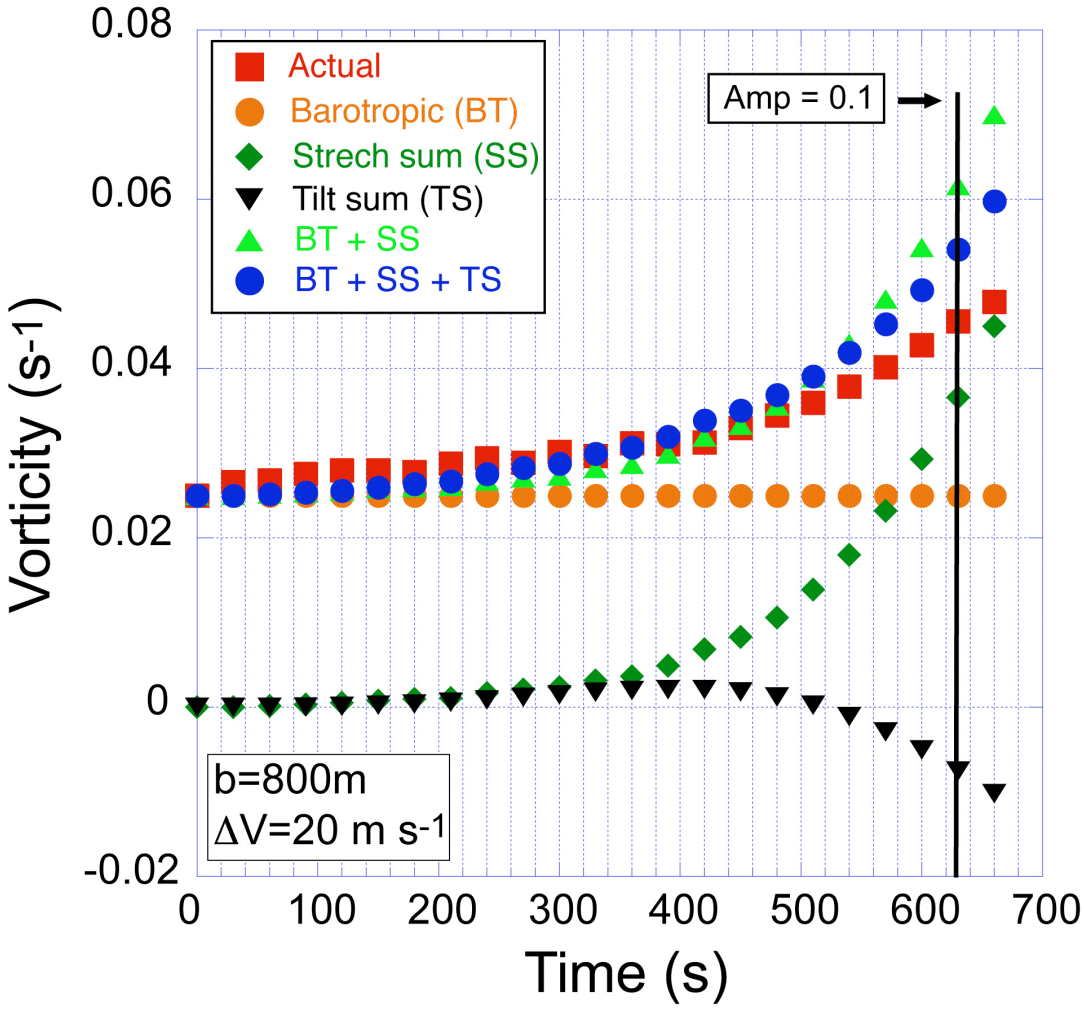

Figure 5.38. Vertical vorticity values at various times for the bc8m20s case. Actual vorticity from the simulation (red squares), initial vorticity (orange line), integrated stretching component to the total vorticity (green diamond), integrated tilting component to the total vorticity (black triangle), the sum of the initial and stretching integrated vorticity (green triangle), and sum of the initial, stretching, and tilting integrated vorticity (blue circles).

values. In this way we are "integrating" the vorticity equation from some initial time to some later time. The results are shown in Fig. 5.38. We see that the net result is exponential increases in the estimated vertical vorticity, with values that are close to what was output from the simulations, although the actual simulated values are slightly higher at early times and somewhat lower at later times. If we looked at just the initial vorticity and the stretching term (green triangle in Fig. 5.38) we would see that the estimated vorticity overestimates the actual vorticity. The tilting term however, compensates for this by redistributing vertical vorticity into horizontal vorticity at later times. The sum of the tilting and stretching terms added to the initial vorticity gives a good estimate of the vorticity at early times. Note that at later times, the estimated and actual vorticities begin to diverge with the estimated values greater than actual values. At these later times, the shear zone width is nearing 2-3 times the grid spacing, implying that the simulation is unable to increase the vorticity as fast as the calculated stretching and tilting terms would suggest.

Evolution of the *v*-component wind from the emergence of small-amplitude waves into the discrete vortices is shown for the bc5m16s case in Fig. 5.39. At 840 s into the simulation (Fig. 5.39a), waves are beginning to emerge along the nearly stationary shear zone. By this time, the perturbations along the shear zone have grown by 2-3 orders of magnitude from the initial random perturbation. As time progresses, a series of waves continue to grow exponentially, however unlike in the barotropic cases, the waves are not equally spaced and have north-south variation in their amplitudes. As the simulation proceeds into the non-linear regime, the perturbations continue to grow and begin to roll up into discrete vortices with varying sizes and spacing. This process can more readily be seen in the vertical vorticity fields (Fig. 5.40). Initially, wavelike vorticity perturbations emerge and grow exponentially in time. The wavelike vorticity perturbations begin

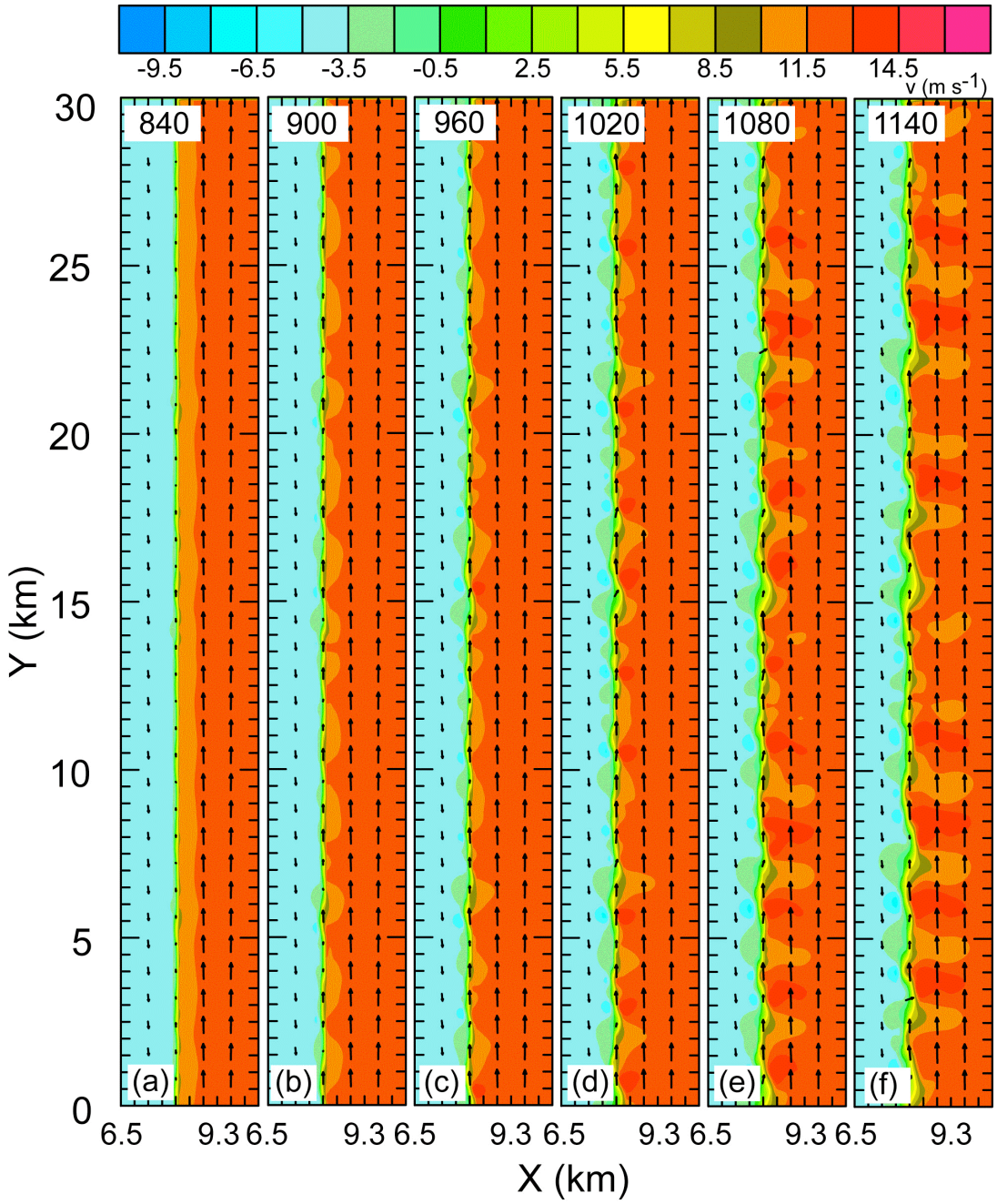

Figure 5.39. Fields of v-component wind (color filled) and horizontal wind vectors (500 m = 8 m s^{-1}) at the second model level (z = 150 m) for the bc5m16s case.

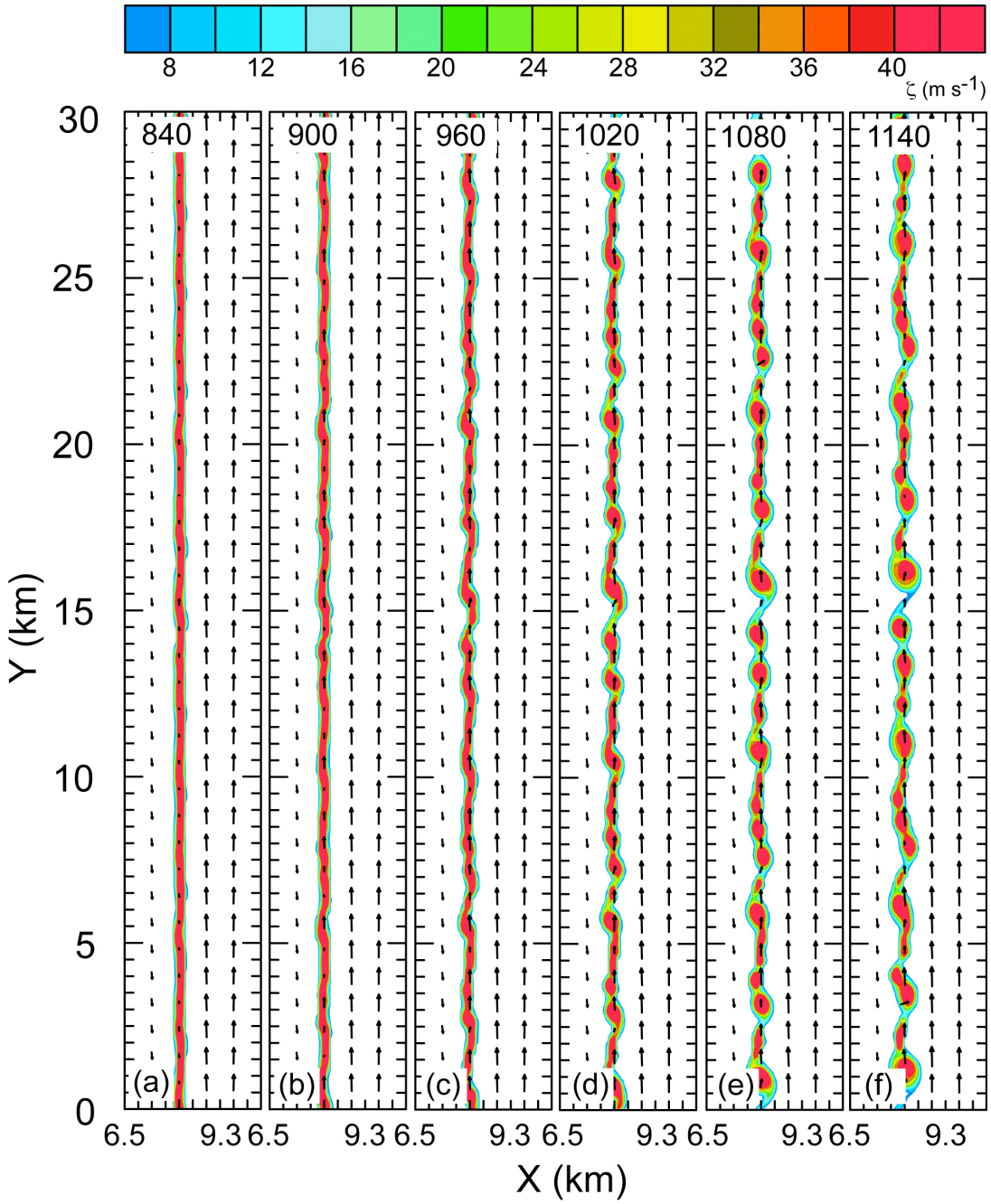

Figure 5.40. Vertical vorticity (color filled) and horizontal wind vectors (500 m = 8 m s^{-1}) for the bc5m16s case at the second model level (z = 150 m).

to contract into cores and increase in magnitude as the discrete vortices start to form. As in the v-component wind fields, a complex structure is seen with evidence of vortex mergers by 1140 s into the simulation.

Series of *v*-component wind fields for the bc8m20s case are shown in Fig. 5.41. Like in the bc5m16s case, the shear zone is characterized by the emergence of small-amplitude waves by ~1080 s (Fig. 5.41a) into the simulation. These waves continue to grow in amplitude and eventually roll up into discrete vortices with various wavelengths and amplitudes by ~ 1200 s. The vorticity fields also behave similarly in the bc8m20s case as in the bc5m16s case, with wavelike perturbations evolving into discrete vortices with varying amplitudes and wavelengths that begin merging by ~1320 s (Fig. 5.42).

5.2.2. Perturbation wavelengths

For the baroclinic cases, the predictions of linear theory are not valid. Unlike the barotropic cases, there is a background u-component wind, horizontal convergence and a time-dependent width of the resulting shear zone. In fact, in all baroclinic simulations, the shear zone width collapses to around ~2-3 times the grid spacing prior to the emergence of significant wave amplitudes. Perhaps it could be expected that at least some component of the resulting growth rates would reside around the wavelength at which linear theory would predict the maximum to occur given an initial shear zone width of ~2-3Δ.

Spectral density estimates at successive times show the perturbation amplitude evolution as a function of wavenumber for the bc5m16s case (Fig. 5.43). Assuming a shear zone width of 2-3Δ, linear theory predicts the most-unstable wavenumbers to be in the range of 12.6 - 19 (λ= 2370 - 1580 m). From the start of the simulation, all wavenumbers begin to grow and there is very little difference in the amplitudes among the wavenumbers. By 600s into the simulation, structure in

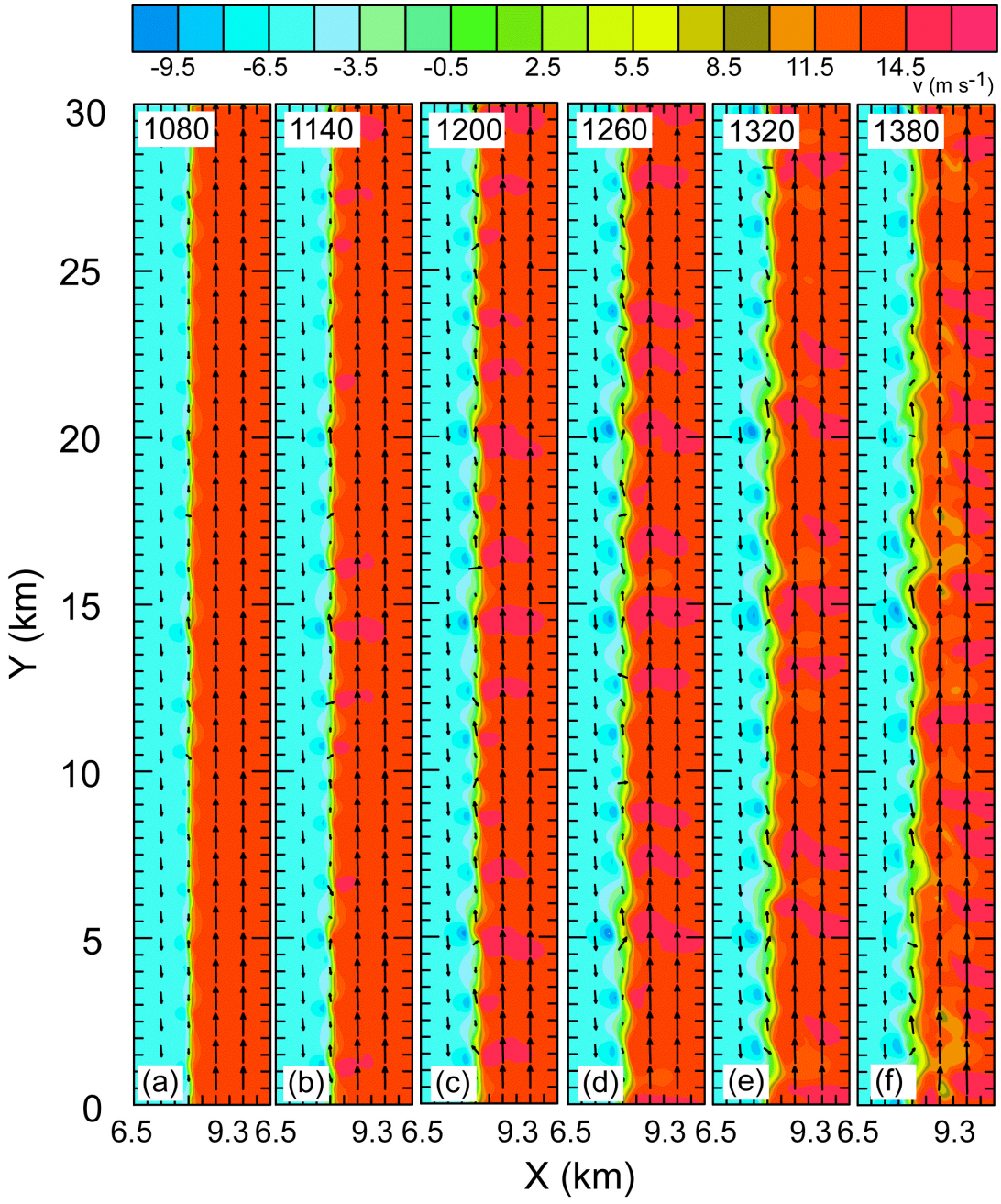

Figure 5.41. Fields of v-component wind (color filled) and horizontal wind vectors (500 m = 8 m s^{-1}) at the second model level (z = 150 m) for the bc8m20s case.

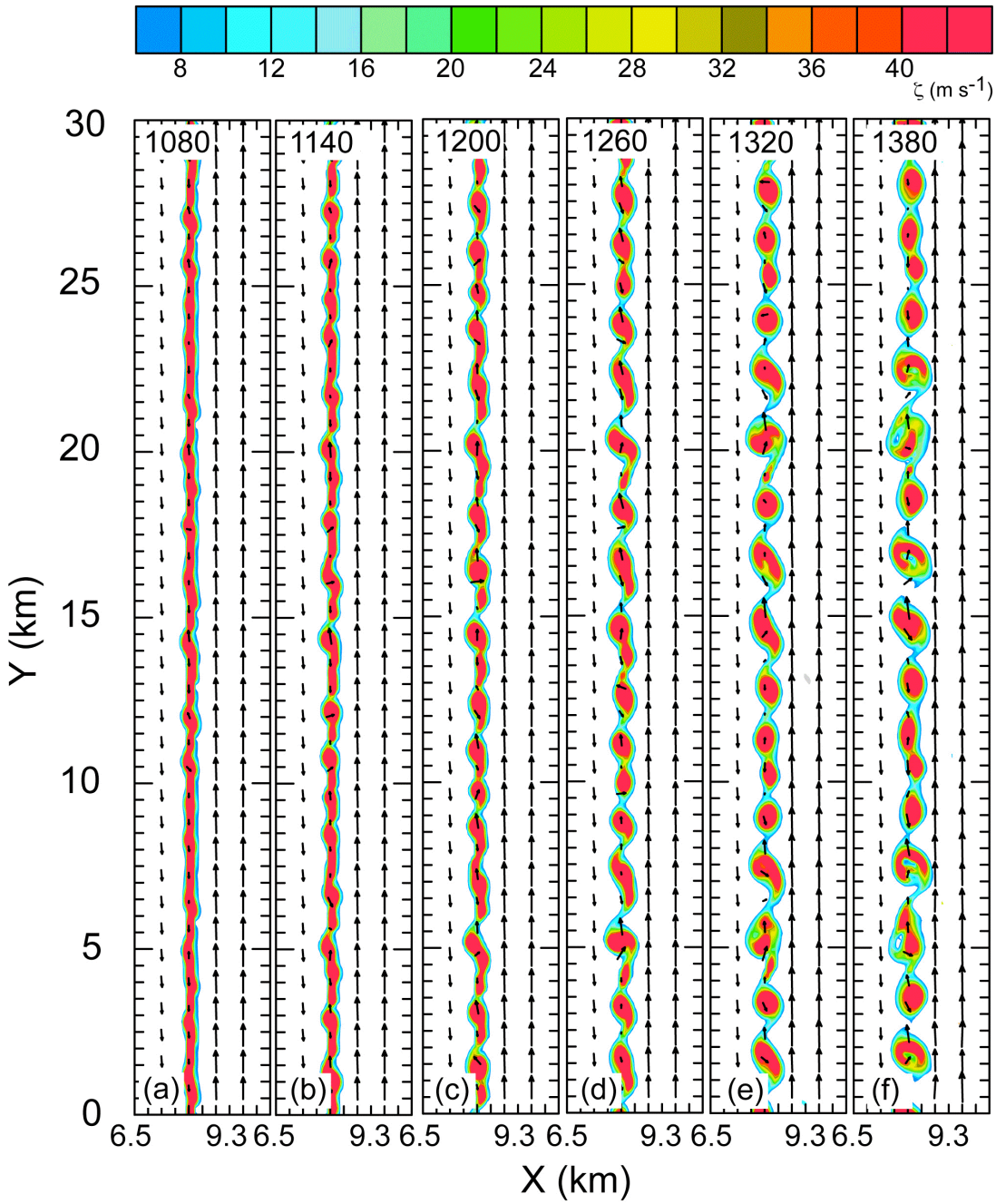

Figure 5.42. Vertical vorticity (color filled) and horizontal wind vectors (500 m = 8 m s^{-1}) for the bc8m20s case at the second model level (z = 150 m).

the spectral density estimate begins to emerge, with a maximum in amplitude around wavenumber 12. This peak in amplitude grows exponentially and remains the peak as discrete vortices begin to emerge. Unlike the barotropic cases that are primarily dominated by one main peak in the spectrum, the bc5m16s case features a main peak and additional secondary peak in the spectrum. The main peak in amplitude (κ = 12.0, λ= 2490 m) is close to the peak in amplitude expected to emerge by growth of the theoretical most unstable mode assuming an initial shear zone of ~3Δ (κ = 12.6, λ= 2370 m). In addition to the primary peak, a secondary maximum occurs around wavenumbers 6-7 (, λ= 4980-4270 m) and 24-26 (λ = 1150-1250), The additional peaks occurs at nearly one half and twice the wavenumber of the primary peak in amplitude, suggesting that a possible resonant interaction is modulating the magnitudes of the secondary peaks.

For the bc8m20s (Fig. 5.44), the main peak in the spectrum is found around wavenumber 16 (λ= 1870). This peak in amplitude is close to the peak in amplitude expected to emerge by growth of the theoretical most unstable mode assuming an initial shear zone of ~2.4Δ. Like the bc5m16s case, there is a main peak in amplitude as well as two smaller secondary peaks in amplitude around wavenumbers 25-26 (λ= 1200- 1150) and wavenumbers 10-11 (λ= 2990-2720).

5.2.3. Perturbation growth rates

As in the barotropic cases, the growth rates in the baroclinic cases can also be computed from the spectral density estimates. However, the growth rates are not constant in the baroclinic cases, but instead increase with time as the shear zone contracts. By plotting the perturbation amplitude as a function of time on a semi-log graph, it is seen that unlike in the barotropic cases where the time-series were straight lines (i.e., constant exponential growth), the time-series for the baroclinic cases curve upward slightly (i.e., increasing exponential growth) with time. Fig.

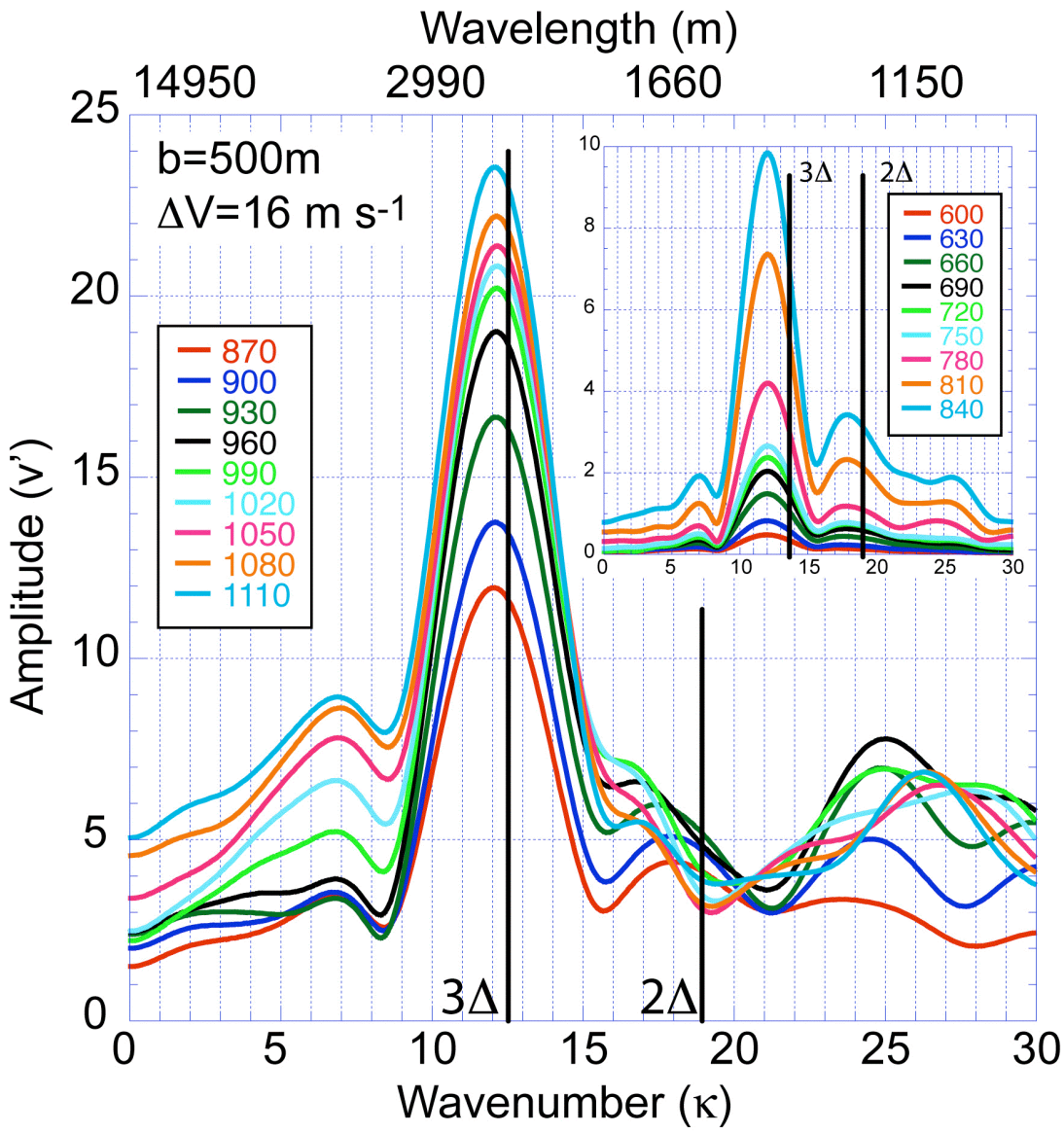

Figure 5.43. Spectral density estimates of the v-component perturbation wind amplitude (m s^{-1}) as a function of wavenumber during the periods 870-1110 s and 600-840 s (inset) after the start of simulation bc8m80s. The vertical black lines denote the most-unstable wavenumbers predicted by linear theory for a shear zone width of 2Δ and 3Δ.

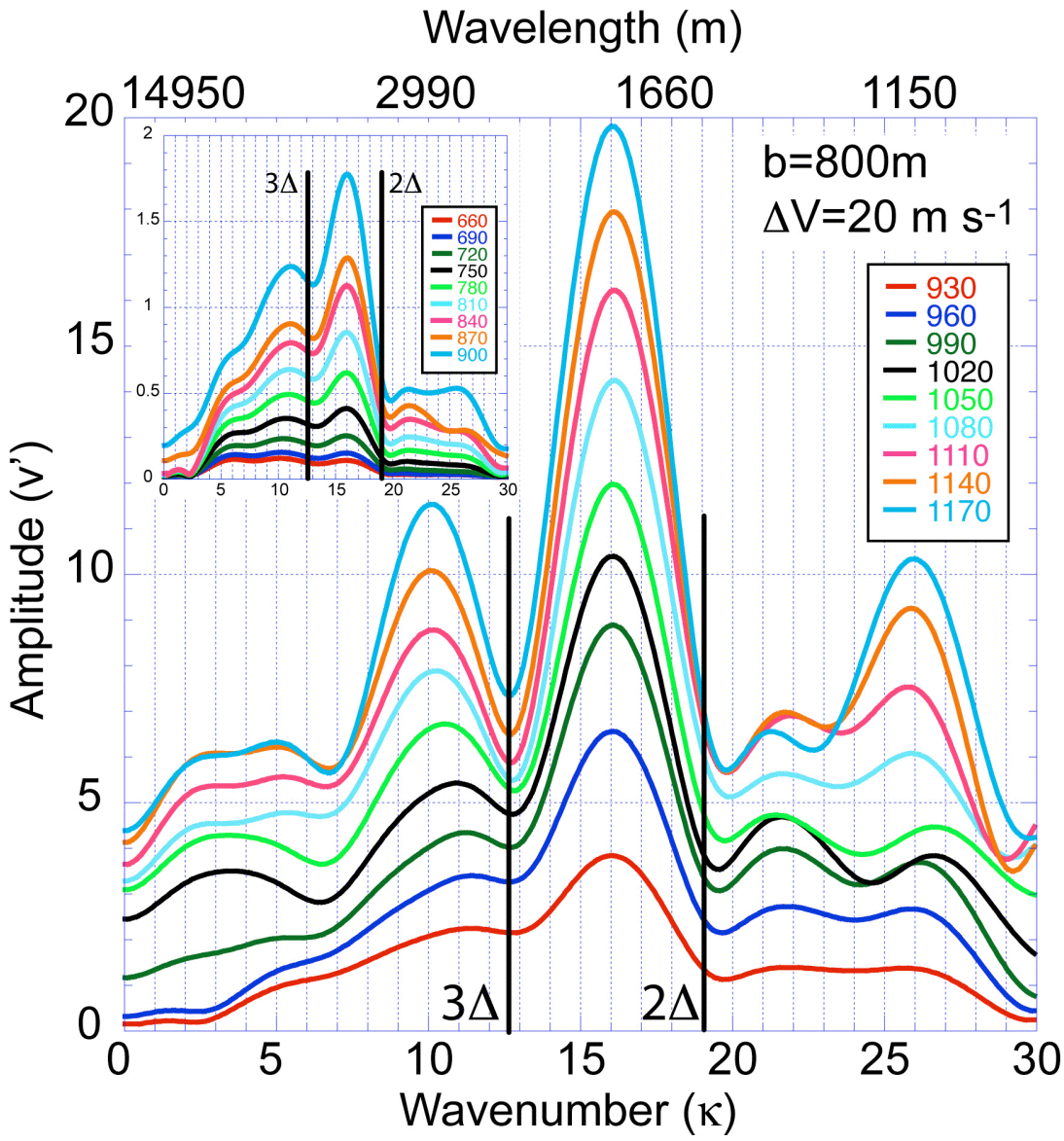

Figure 5.44. Spectral density estimates of the v-component perturbation wind amplitude (m s^{-1}) as a function of wavenumber during the periods 930-1170 s and 660-900 s (inset) after the start of simulation bc8m80s. The vertical black lines denote the most-unstable wavenumbers predicted by linear theory for a shear zone width of 2Δ and 3Δ.

5.45 shows the amplitudes as a function of time for five different wavenumbers for the bc5m16s case. As time increases, all wavenumbers experience an increase in growth rate (slope). The greatest amplitude and the largest average growth rate occur at wavenumber 12 ($\lambda = 2490$), corresponding to the peak in amplitude seen in Fig. 5.43. Likewise, the bc8m20s case also features an increase in growth rate with time (Fig. 5.46), albeit with a somewhat lesser extent. The greatest amplitude and largest growth rate occurs at wavenumber 16 ($\lambda = 1870$), corresponding to the peak in amplitude in Fig. 5.44.

It is useful to determine if linear theory may be applied to the baroclinic cases despite the complication imposed by the time-varying initial shear zone width. The evolution of the shear zone width may be parametrically approximated by computing the maximum shear zone vorticity as proxy for the shear zone width via the relationship $b = \Delta U/\zeta$ (where ΔU is nearly constant). The modeled shear zone vorticity evolution closely conforms to a tanh function in time (Fig 5.47). The tanh function is of the form

$$\xi = a\tanh(rt + m) + d \ ,$$

where a is the vorticity amplitude, r is the shape parameter, and m and d are displacements in the x- and y-dimensions. An example of a tanh function as derived by fitting to the model-output vorticity is shown in Fig. 5.47. The tanh curve very closely follows the model output, thus providing an excellent parametric estimate of the vorticity and hence also the shear zone width at any given time. Fitted tanh parameter values for the various idealized baroclinic simulations are listed in Table 6.

The growth rate from linear theory is proportional to the vorticity in the shear layer, which is typically assumed to be a constant as appropriate for the conventional barotropic base state (e.g., Rayleigh 1880; see also Appendix A).

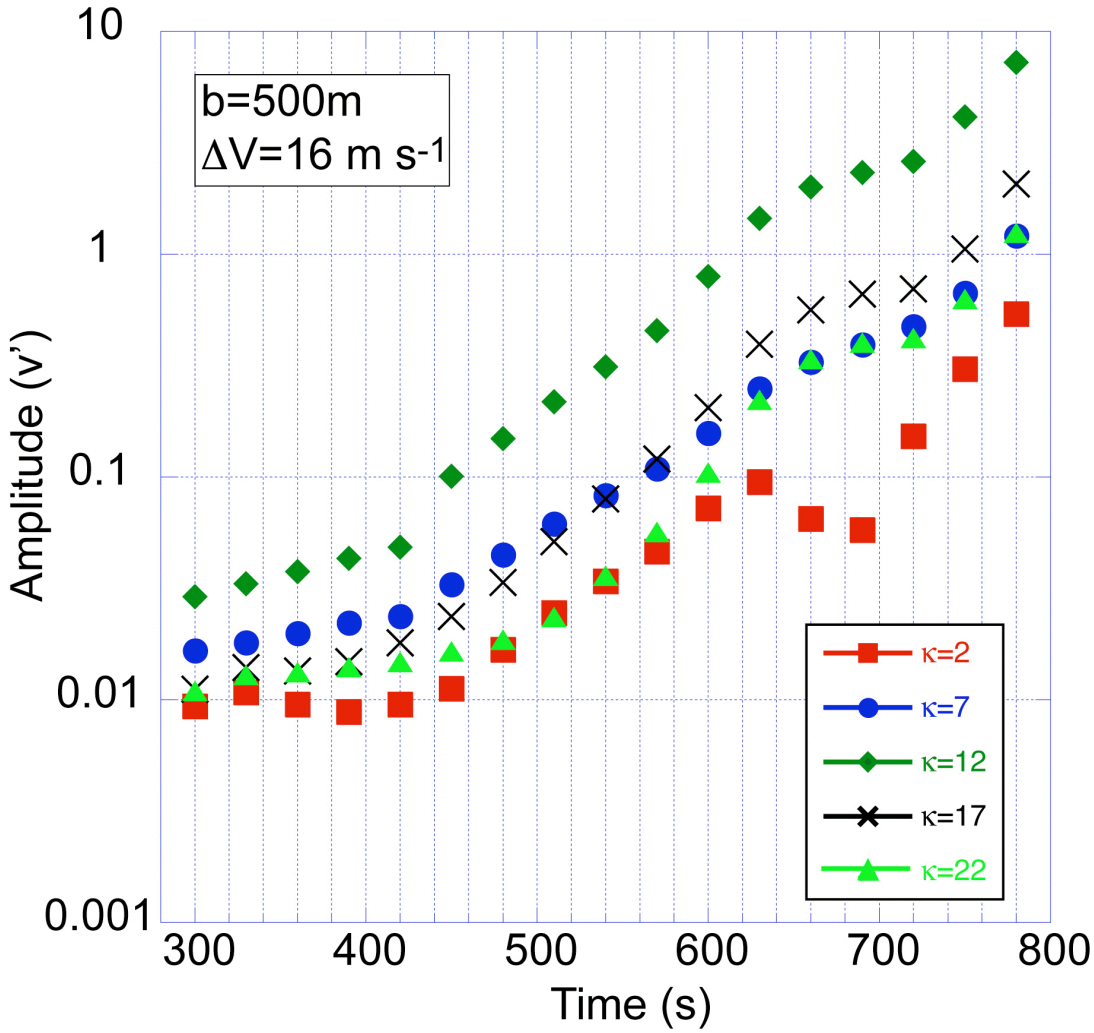

Figure 5.45. Wave (vortex) amplitudes as a function of time (markers) at different wavenumbers for the bc5m16s case. Colored markers in the key at lower right denote the different wavenumbers.

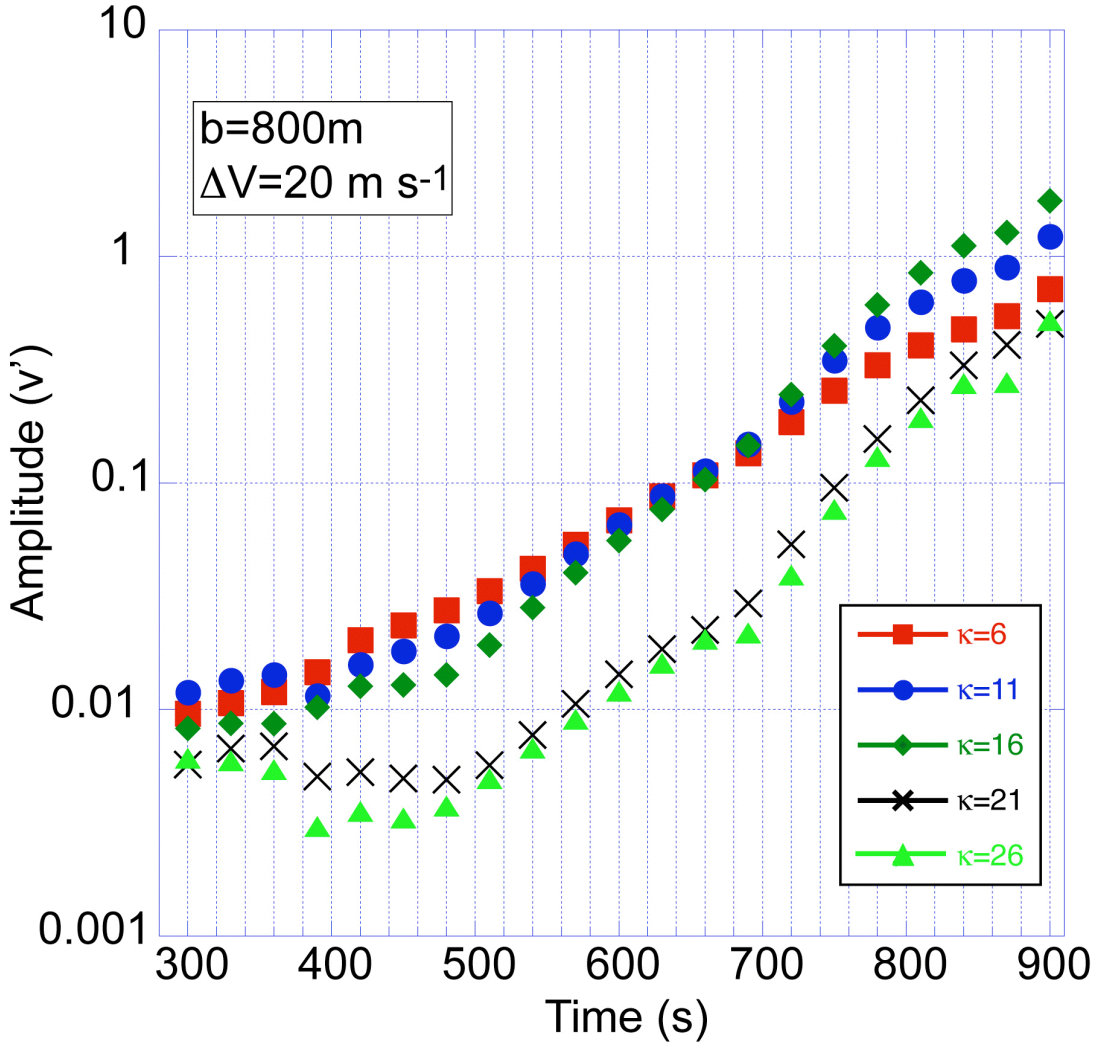

Figure 5.46. Amplitudes as a function of time (markers) at different wavenumbers for the bc8m20s case.

Substituting a time-varying vorticity function into the expression for the linear growth rate (eq. 2.36) allows us to model the total growth rate for the baroclinic cases. The maximum vorticity of each simulation is computed at each output time and a hyperbolic-tangent function is then fitted to the maximum vorticity data using the Levenberg-Marquardt algorithm as implemented in the SciPy software package. Substituting the above analytic tanh functional expression for the vorticity into the linear growth rate equation 2.36 yields the complex phase speed

$$c(t) = \frac{a}{2}\left[\tanh(rt+m)+d\right]\left[\left(\frac{2kU}{a\tanh(rt+m)+d}-1\right)^2 - \exp\left(\frac{-4kU}{a\tanh(rt+m)+d}\right)\right]^{\frac{1}{2}}. \quad (5.2)$$

We can then compute an average growth rate integrated over some time interval and compare this to the simulation data. The theoretical model for the average growth rate becomes

$$c_{avg} = \frac{1}{N}\sum_{i=1}^{N} c_i \quad (5.3)$$

where N is the number of output time intervals. To compute the corresponding average growth rate for the simulated shear zones, we first compute the local growth rate between two neighboring output intervals (in all simulations, the output interval was 30 s),

$$c(t) = \frac{1}{\Delta t}\ln\left(\frac{C_{uu}(t)}{C_{uu}(t-1)}\right). \quad (5.4)$$

where C is the spectral density estimate. Then the average growth rate is then computed as in equation (5.3), where N is the same in the simulation calculations and the theoretical model calculations.

Results from the computed average growth rates for simulations with four shear zone widths along with values computed from equations (5.2)-(5.3) are shown in Fig. 5.48. For the 1000 m runs, (Fig. 5.48a), the growth rates are in good agreement between the theoretical model and the calculated values from the

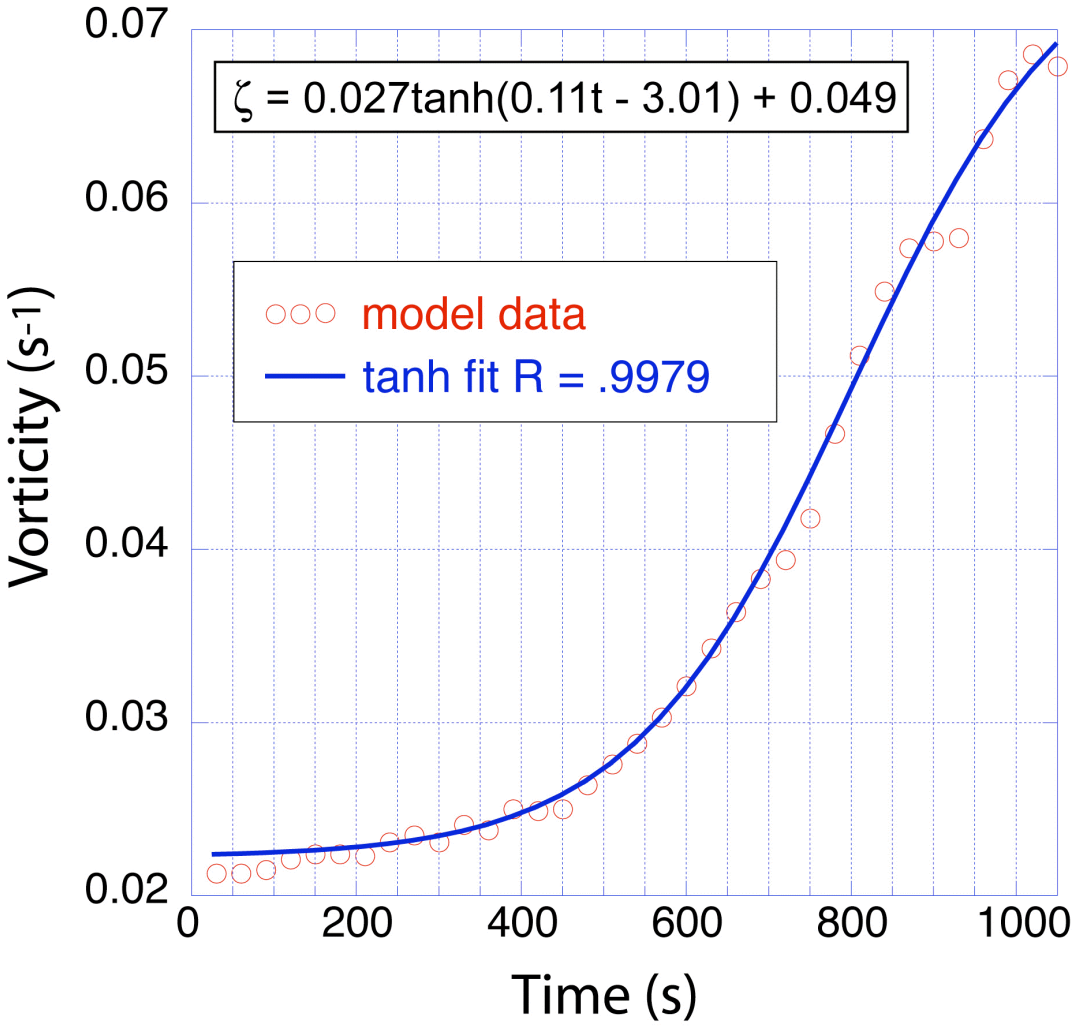

Figure 5.47. Peak north-south averaged vorticity as a function of time for the bc8m16s case (red circles) and tanh function fit (blue curve).

Simulation	*a*	*r*	*m*	*d*
bc5m6s	-.00725	-.2038	4.525	.0208
bc5m8s	-.00974	-.2007	4.426	.0275
bc5m12s	.01387	.2257	-4.491	.0407
bc5m16s	.01728	.2578	-5.527	.0533
bc5m20s	-.01747	-.3538	7.228	.06226
bc5m24s	-.02350	-.3137	6.620	.07803
bc6m8s	.01121	.1657	-3.784	.02566
bc6m12s	.01660	.1702	-3.885	.03851
bc6m16s	-.02062	-.1929	4.319	.05016
bc6m20s	.02246	.2412	-5.219	.05985
bc6m24s	-.02713	-.2278	4.927	.07163
bc8m12s	-.01872	-.1243	3.246	.03564
bc8m16s	.02741	.1127	-3.019	.04924
bc8m20s	.03175	.1199	-3.145	.05969
bc8m24s	.03467	.1275	-3.236	.06816
bc10m12s	.02752	.06683	-2.194	.03941
bc10m16s	.03717	.06593	-2.177	.05294
bc10m20s	.03773	.07586	-2.299	.05831
bc10m24s	.03730	.08746	-2.245	.06284

Table 6. Parameters for the tanh function $\xi = a\tanh(rt+m)+d$ in the various idealized baroclinic simulations.

simulation output. The results are in even better agreement for the 800 m, 600 m, and 500 m runs (Fig. 5.48b-d). In all cases for a given shear zone width, there is a nearly linear increase in average growth rate as the shear (hence vorticity) is increased. The growth rates calculated from the simulations are slightly low-biased relative to the theoretical model predictions except in the 500 m runs, with the latter characterized by a slight high bias. With few exceptions, there is very close agreement of the magnitude of the average growth rate between the theoretical model and the calculations from the simulations.

The average growth rates across all baroclinic simulations are plotted as a

function of the initial shear zone vorticity to convey the overall rate of growth in an aggregate sense (Fig. 5.49). There is a very good linear relationship between the average growth rate and the initial shear zone vorticity, both for the theoretical model and for the simulation calculations. Also, there is a very good agreement between the theoretical model and the simulation calculations. However, there is some spread due to the nature of the collapsing shear zone and the increase in averaged vorticity with time. That is, for a given initial vorticity, the average growth rates are larger for larger shear zone widths. Larger shear zone widths can collapse to a greater degree than smaller widths, thus allowing for larger vorticity values at later times, hence a larger average growth rate. For example, an initial vorticity of 0.02 s^{-1} experiences growth rates of 0.0057, 0.0060, and 0.0063 for the 600 m, 800 m, and 1000 m cases respectively.

5.2.4. Emergence of discrete vortices

As the baroclinic simulations progress, instability leads to the emergence of discrete vortices as also noted in the barotropic cases. Since the baroclinic shear zones collapse and the vorticity within them increases, the growth rates are higher and discrete vortices emerge earlier than in the corresponding barotropic cases with the same initial shear zone width and shear magnitude (corresponding to the same initial vorticity). By the time the vortices begin to emerge and the shear zone has fully collapsed, the shear zone vorticity has achieved its maximum value (e.g., the initial shear zone vorticity was 0.032 s^{-1} and the vorticity within the emerging vortices is ~ 0.07 s^{-1}, or more than double the initial value for the bc5m16s case).

Although the entire shear zone is characterized by upward vertical motions due to the pronounced secondary circulation associated with the zonal density gradient, localized regions of enhanced upward vertical velocity are nevertheless noted by 900 - 960 s in case bc5m16s (Fig. 5.50a-b). As the upward vertical

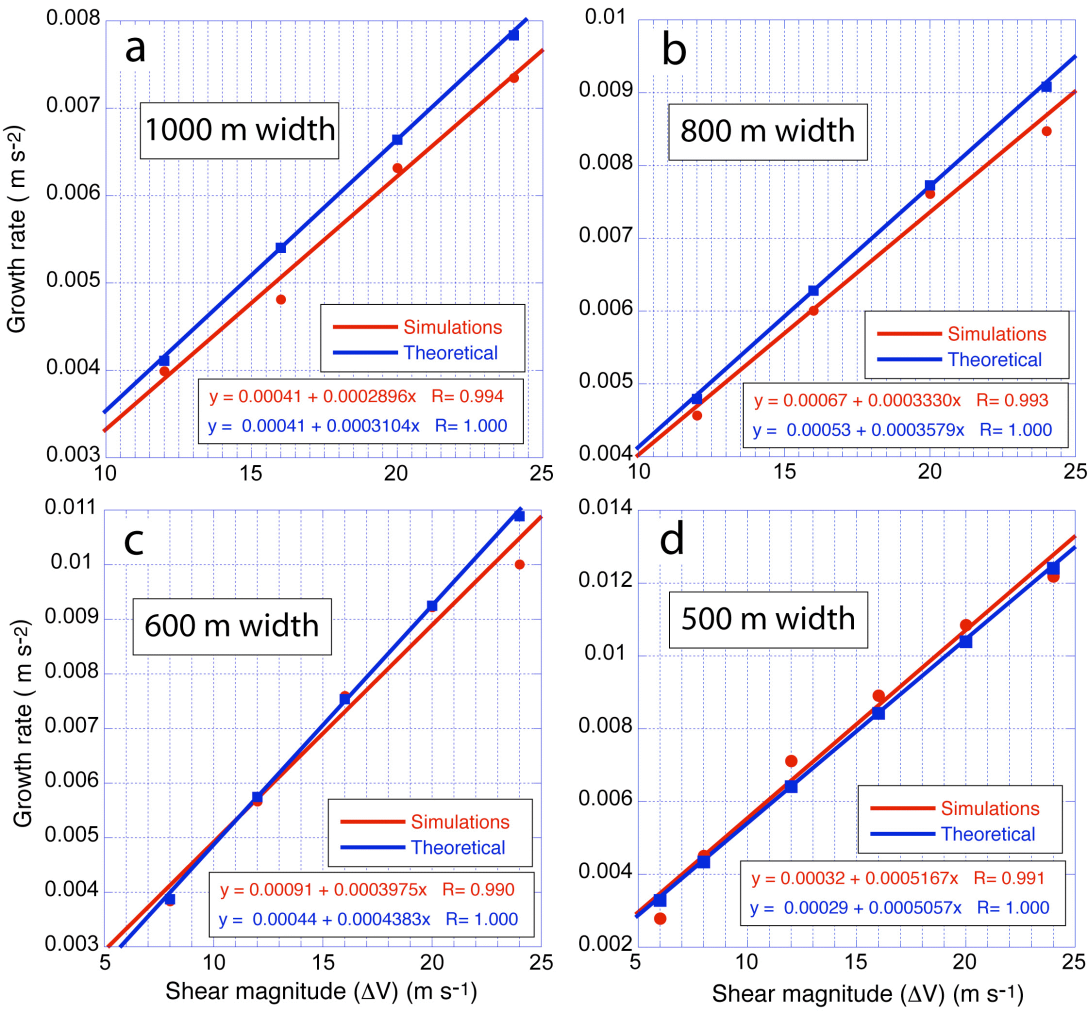

Figure 5.48. Maximum average growth rates (red dots) plotted as a function of shear magnitude for four different shear zone widths. The maximum average growth rates as predicted by the parameterized growth rate eq. (5.2) and described in the text ("theoretical") are denoted by blue dots. The red and blue lines indicate linear least squares fits to the respective data points. Also shown are the least squares linear fitting equations and the correlation coefficients of the fitted lines.

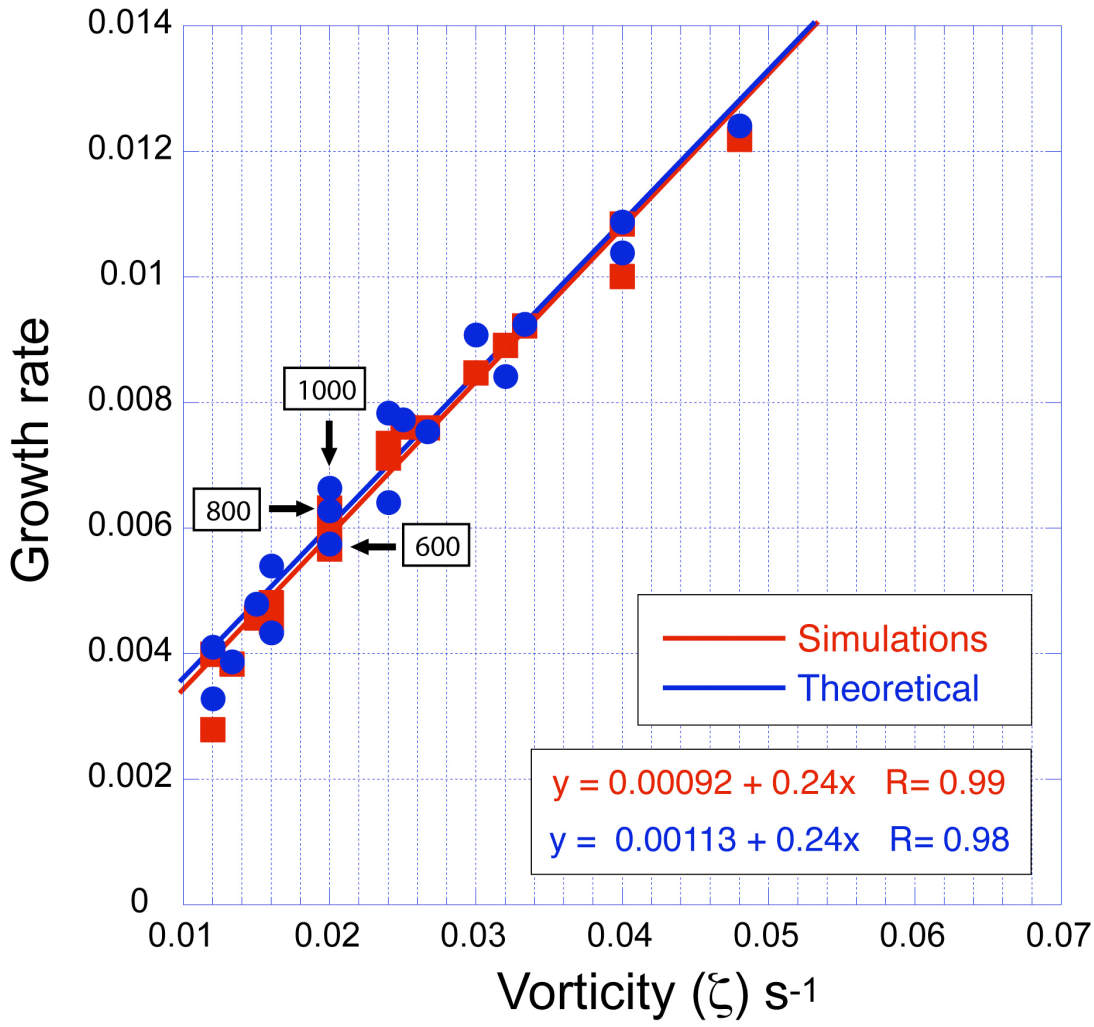

Figure 5.49. Average maximum growth rates as a function of initial shear zone vorticity for all baroclinic simulations. Red squares represent simulation values, while blue circles are parameterized growth rate equation values.

velocity increases within localized regions, discrete regions of localized vertical vorticity maxima also emerge. By 1020 s (Fig. 5.50c), downdrafts have begun to form in the centers of most of the discrete vortices, although significant nonlinear evolution has already begun. The updrafts and downdrafts continue to intensify from 1080 s through 1200 s (Fig. 5.50d-f) and achieve saturation after 1200 s (Fig. 5.50f). The remaining vortices that eventually begin to pair and coalesce into larger vortices (not shown) are generally characterized by central downdrafts flanked by updrafts between vortices.

Compared to the nonlinear evolution of this case's barotropic counterpart (bt5m16s), several commonalities and differences exist. First, in the baroclinic case the vortices are spaced closer together than in the barotropic case. This is to be expected as the wavenumber of maximum growth increases (i.e., wavelength decreases) as the shear zone width collapses. Further, as the collapsing shear zone contains increasingly larger vorticity values, the growth rates are larger and the vortices emerge earlier and stronger in the baroclinic case. Also, there is much more variability in the spatial structure of the baroclinic vortices compared to the barotropic. Whereas the barotropic vortices are all nearly the same shape and size, the baroclinic vortices take on a range of shapes and sizes. Also, although the emerging vortices go through some degree of nutation, it is less in the baroclinic case than in the barotropic case, since the vortices tend to be more circular, and are perhaps somewhat constrained by the background east-west convergence within the shear zone.

As in the barotropic case, there seems to be a wavenumber 2 modulation of the vorticity fields (i.e., as manifest as a structural resemblance in regions spaced 15 km apart in the periodic domain). Again as in the barotropic case, at later times there is generally a downdraft near the vortex center with flanking updrafts although

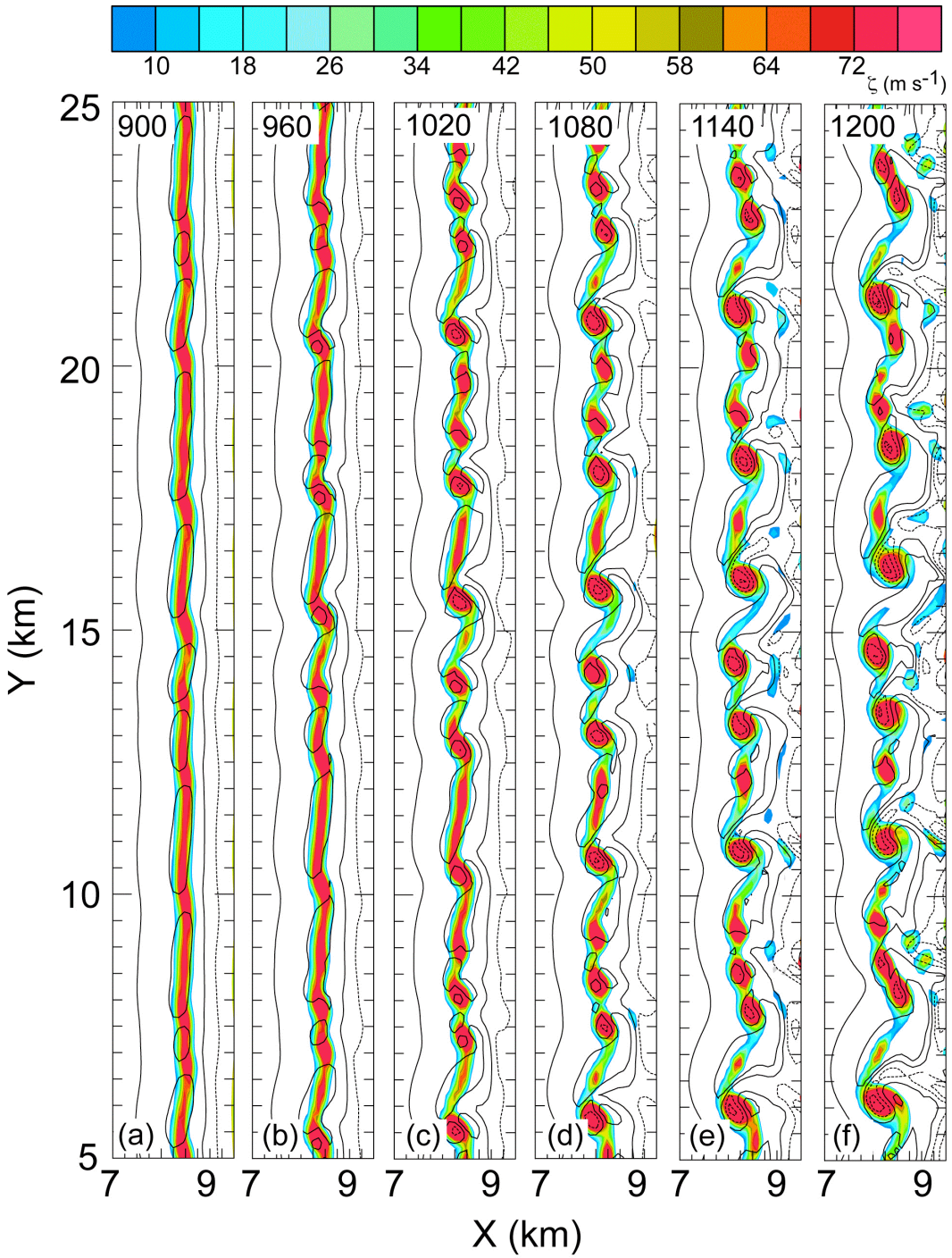

Figure 5.50. Vertical vorticity (color filled) at z = 550 m for the bc5m16s case. The solid (dashed) black contours denoting positive (negative) vertical velocity at 2 m s^{-1} intervals starting at 1 (-1) m s^{-1}.

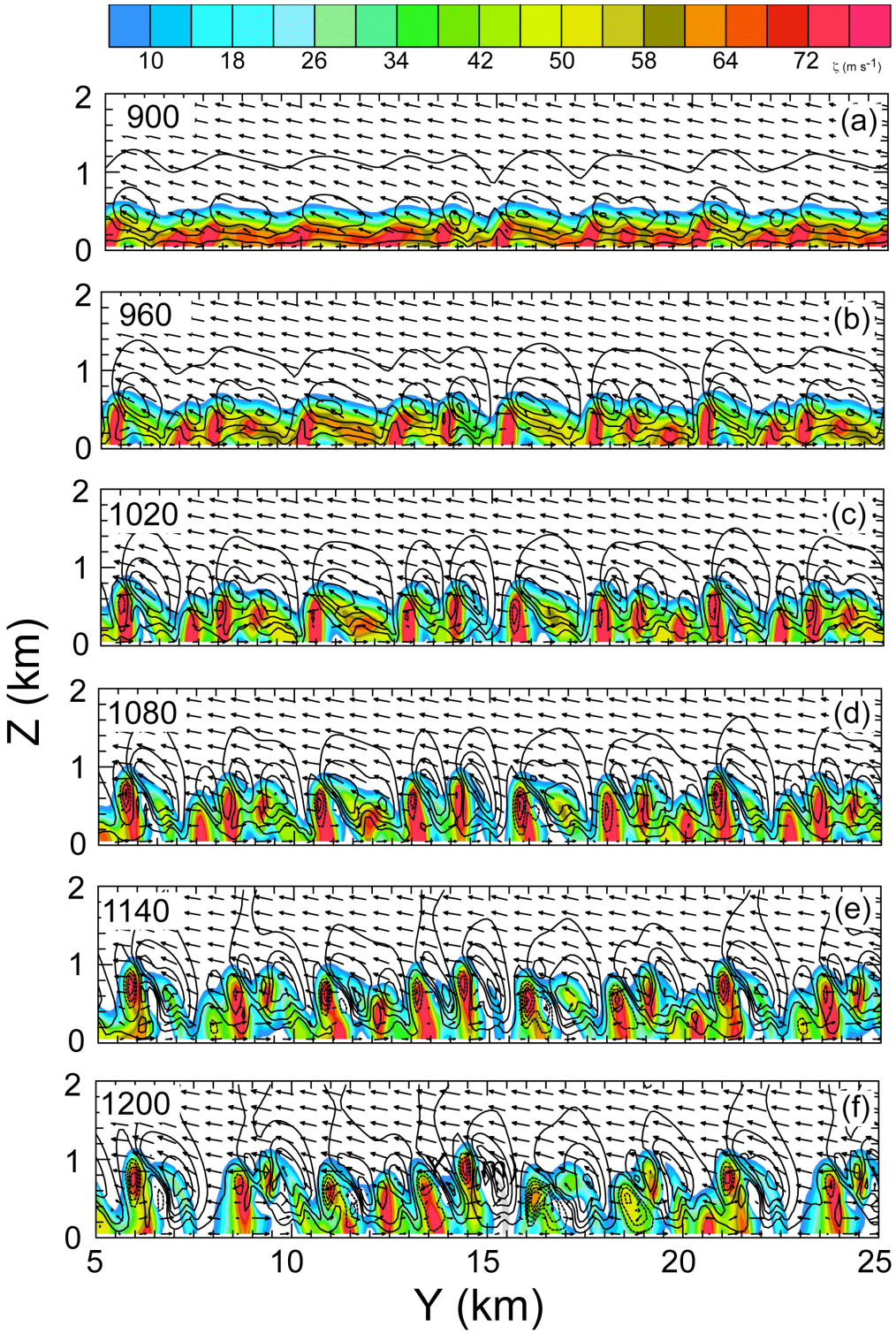

Figure 5.51. North-south cross-sections through the shear zone for the bc5m16s case. Vertical vorticity is color-filled and solid (dashed) curves denote upward (downward) vertical motion with an interval of 1 m s^{-1}, starting at 1 (-1) m s^{-1}. Note that the vertical axis has been stretched by a factor of 2.

the downdrafts seemed to be more centered in the baroclinic case (Figs 5.50, 5.51). Although the vertical velocity structure tends to be fairly symmetric in the barotropic case, in the baroclinic case there is a greater degree of spatial variability.

Chapter 6

Discussion and synthesis of results

6.1. 22 MAY 2002 DRYLINE

6.1.1. Comparison of simulated misocyclones in the real data case with observed misocyclones

Several of the simulated misocyclones in the real data case have a similar structure and evolution to M1, which was previously discussed in Chapter 4.2 (see also B12). These simulated misocyclones all intensify within a zone of convergence, concentrated shear, updrafts, and vertical vorticity that is located along or just east of the dryline moisture gradient (e.g., Fig. 6.1). As misocyclones M1, M2, and M4 continue to intensify, their major axes precess counterclockwise to form a characteristic "S-shaped" gradient (Fig. 6.2a,b,d). In contrast, misocyclone M3 develops a more circular structure and does not precess significantly as it moves downstream (Fig. 6.2c). Misocyclones M1, M2, and M4 reach a maximum intensity after precessing about 90°. As each misocyclone reaches the mature phase, an axial downdraft develops as updrafts persist in convergent regions to the north and south of the circulation centers. Continued advection around the misocyclone eventually leads to a seclusion, wherein moisture wraps completely around the vortex and closes off a pocket of dry air.

Several notable features of the simulated misocyclones (Fig. 4.6, Fig. 6.2) are consistent with observed misocyclones (e.g. Pietrycha and Rasmussen 2004; Arnott et al. 2006; Marquis et al. 2007). The misocyclonic structure, which is characterized by an absolute maximum in vertical vorticity near the surface and a relative maximum, that decreases and slopes downshear with height, is similar in both the simulation and the observations (Fig. 4.6; Buban et al. 2007, their Fig 19). Both the simulated and observed misocyclones are centered and remain along the

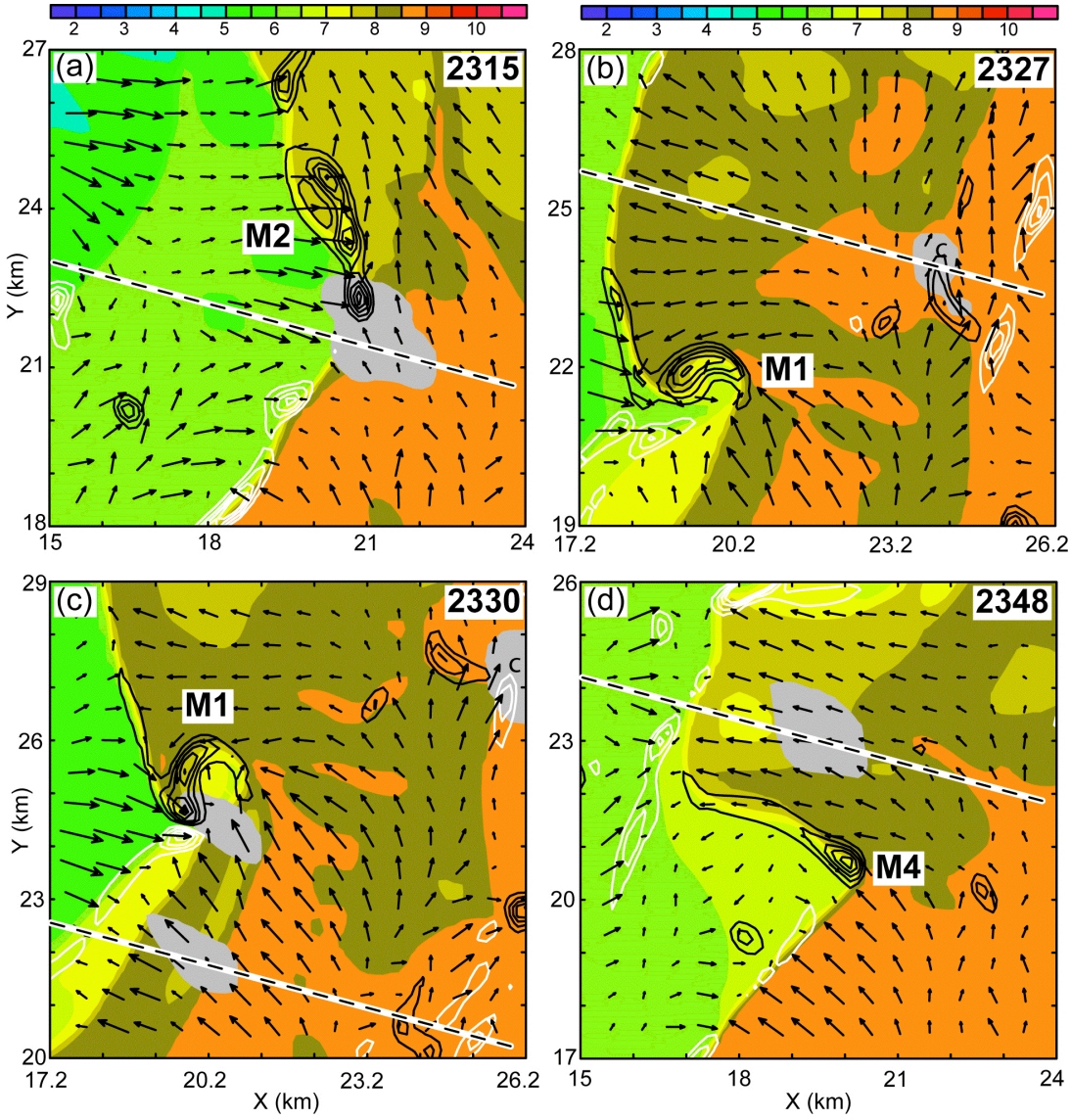

Figure 6.1. Simulated water vapor mixing ratio (color filled) and vertical vorticity (contoured every 5 x 10^{-3} s^{-1} starting at 5 x 10^{-3} s^{-1}) at the lowest model level, with positive values black and negative values white and cloud water mixing ratio > 0.05 g kg^{-1} (grey shaded) at ~3.5 km AGL. Also shown are the misocyclone-relative wind vectors at the lowest model level (1 km = 5 m s^{-1}) calculated by subtracting a mean wind of 18 m s^{-1} at 190° from the total wind, with 1 km length equal to 5 m s^{-1}. The letter c in panels b and c indicate the same cumulus cloud. The black dashed lines indicate cross-section locations shown in Fig. 6.7.

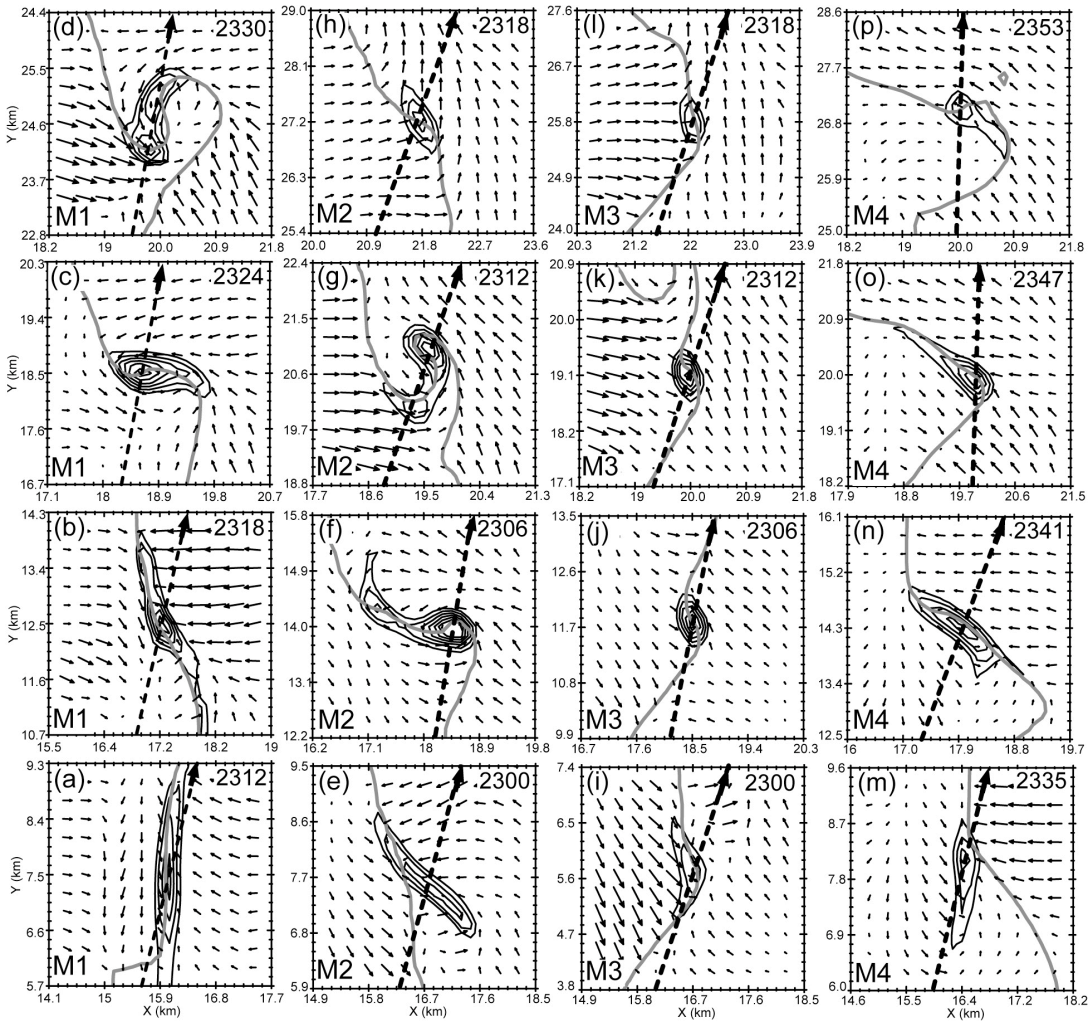

Figure 6.2. Evolution of four simulated misocyclones (M1-M4) at a 6-minute intervals from the simulation. Shown are the lowest model level positive vertical vorticity values (contoured) every 5 x 10^{-3} s^{-1} starting at 5 x 10^{-3} s^{-1} and horizontal vortex-relative wind vectors. Also shown is the 7.5 g kg^{-1} mixing ratio isopleth along the dryline (grey curve) at the lowest model level and estimated motion (black dashed line).

dryline gradient through most of their life cycles. The simulated and observed misocyclones also tend to be elliptically shaped. The major axes of elliptical misocyclones are oriented along the dryline gradient and precess counterclockwise with time. The observed and simulated misocyclones are initially collocated with an updraft that extends both north and south along the dryline, with the strongest updraft cores located north of the misocyclones. The central updraft subsequently weakens in both the simulated and observed misocyclones, and a downdraft eventually replaces the weakening updraft in the simulation of M1. Development of pressure minima in the simulated misocyclones (e.g., as in the idealized simulation case in Fig. 5.25) with collocated central downdrafts is consistent with a downward-directed perturbation pressure gradient force owing to the low-level vertical vorticity maximum combined with a cyclostrophically-forced central pressure minimum $\Delta p' \sim -\zeta^2$ that decreases with height (e.g., by analogy to supercell occlusion downdrafts reported by Brandes 1984). The limited period of radar measurements on 22 May has precluded radar observation of a central downdraft by Buban et al. (2007). However, central downdrafts have been observed in other dryline misocyclones (Marquis et al. 2007). At later times, the updraft to the north of the misocyclone weakens while the updraft to the south of the misocyclone strengthens.

In both the simulations and the Lagrangian analyses, the misocyclones force dryline waves by advecting moist air westward to the north of the vortex (i.e., leading the northward-moving vortex) and advecting dry air eastward to the south of the vortex. The resultant wrapping pattern of moist and dry air around the simulated misocyclones (e.g., as described in Chapter 4.2, Fig. 4.6) is similar to radar-analyzed trajectories and Lagrangian analyses perturbed by observed misocyclones (Marquis et al. 2007; Buban et al. 2007, their Figs. 19-20). Although the general

effects of the misocyclones on the moisture fields are similar in both the Lagrangian analyses and the simulations, much more detail is seen in the simulations owing to both the finer grid resolutions and filtering in the radar and Lagrangian analyses (Ziegler et al. 2007). The misocyclones were not observed long enough to visualize the decay process, and therefore cannot be compared to the simulations in the latter aspect.

6.1.2. Misocyclone dynamics

Given the very similar morphology and evolution of several simulated and observed misocyclones, it is likely that the simulations are collectively resolving a consistent underlying dynamical evolution process. The formation of observed and simulated misocyclones occurs along dryline segments distinguished by convergence, shear, updrafts, and bands of vertical vorticity, suggesting that an essentially barotropic horizontal shearing instability dominates the initial stages of the misocyclogenesis process (see previous discussion in Chapter 5). However, documenting all sources of instability from which misocyclones may eventually grow to and past maturity is beyond the scope of this study. Nevertheless, the real data simulation provides a high-resolution dataset from which subsequent misocyclone evolution and several significant dynamical forcing processes may be identified.

Using the anelastic approximation of the momentum equations, the vertical vorticity equation may be written in the form

$$\frac{\partial \zeta}{\partial t} = -V_H \cdot \nabla_H \zeta - w\frac{\partial \zeta}{\partial z} + \left(\frac{\partial u}{\partial z}\frac{\partial w}{\partial y} - \frac{\partial v}{\partial z}\frac{\partial w}{\partial x}\right) - \zeta\left(\frac{\partial u}{\partial x} + \frac{\partial v}{\partial y}\right) \qquad (6.1)$$

where ζ is the vertical vorticity and the effects of friction and the earth's rotation have been neglected (Shapiro et al. 2009). The baroclinic term has also been omitted from eq. (6.1), as it is several orders of magnitude smaller than the remaining calculated terms (not shown). Thus, the local vertical vorticity tendency

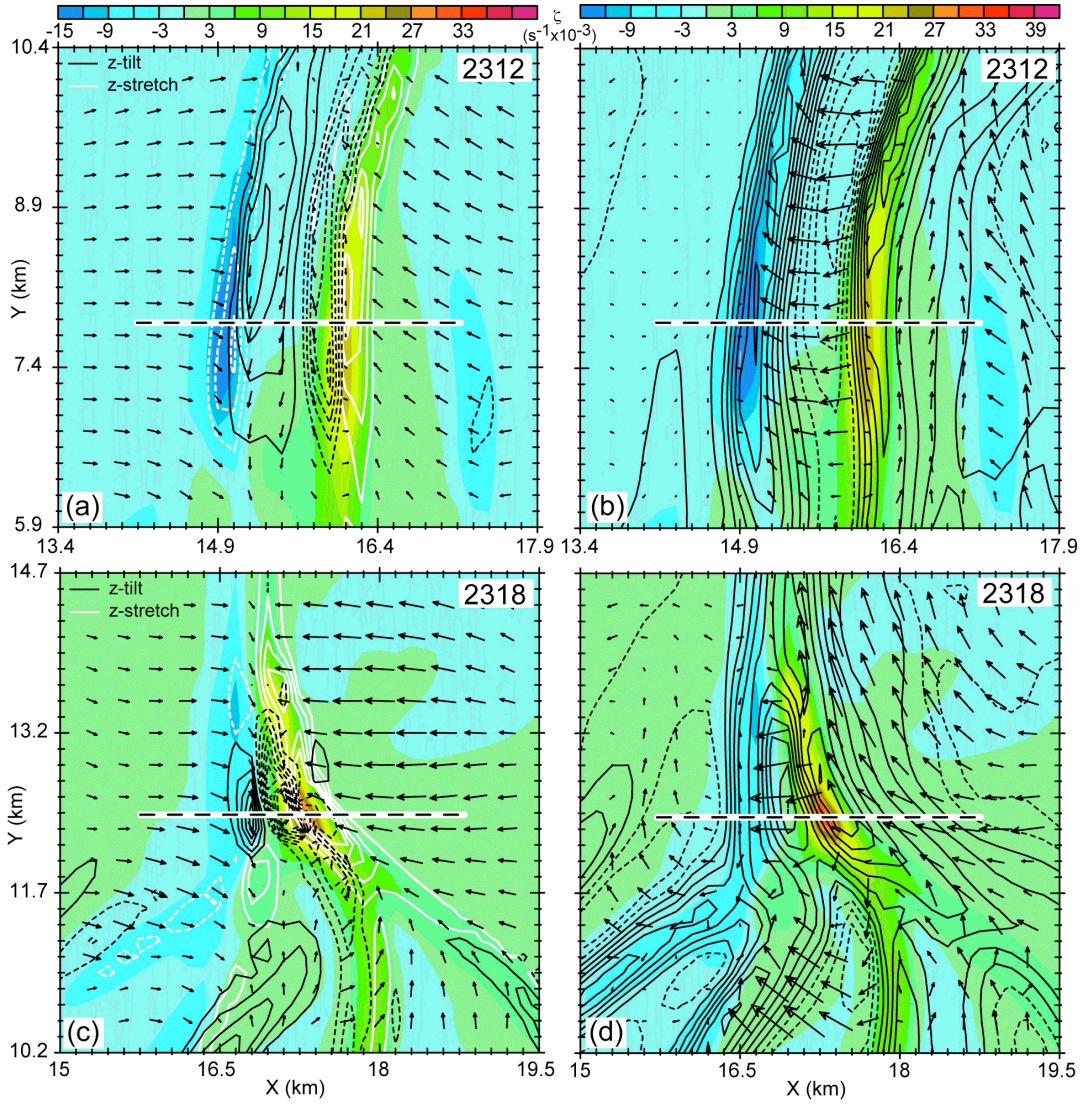

Figure 6.3. Simulated vertical vorticity at the lowest model level (color-filled) with other overlay fields at 2312-2330 UTC for misocyclone M1. Left: Tilting production of vertical vorticity (contoured in black every 50 x 10^{-6} s^{-2} starting at 50 x 10^{-6} s^{-2}), with positive values solid and negative values dashed, and stretching of vertical vorticity contoured in white every 50 x 10^{-6} s^{-1} starting at 50 x 10^{-6} s^{-1}), with positive values solid and negative values dashed. Also shown are the misocyclone-relative wind vectors at the lowest model level (1 km = 5 m s^{-1}) calculated by subtracting a mean wind of 18 m s^{-1} at 190° from the total wind. Right: Vertical velocity contoured in black every 0.5 m s^{-1} starting at 0.5 m s^{-1}) with positive values solid and negative values dashed, and horizontal vorticity vectors with 1 km length equal to 15 x 10^{-3} s^{-1}. Black dashed lines indicate cross-section locations in Fig. 6.4.

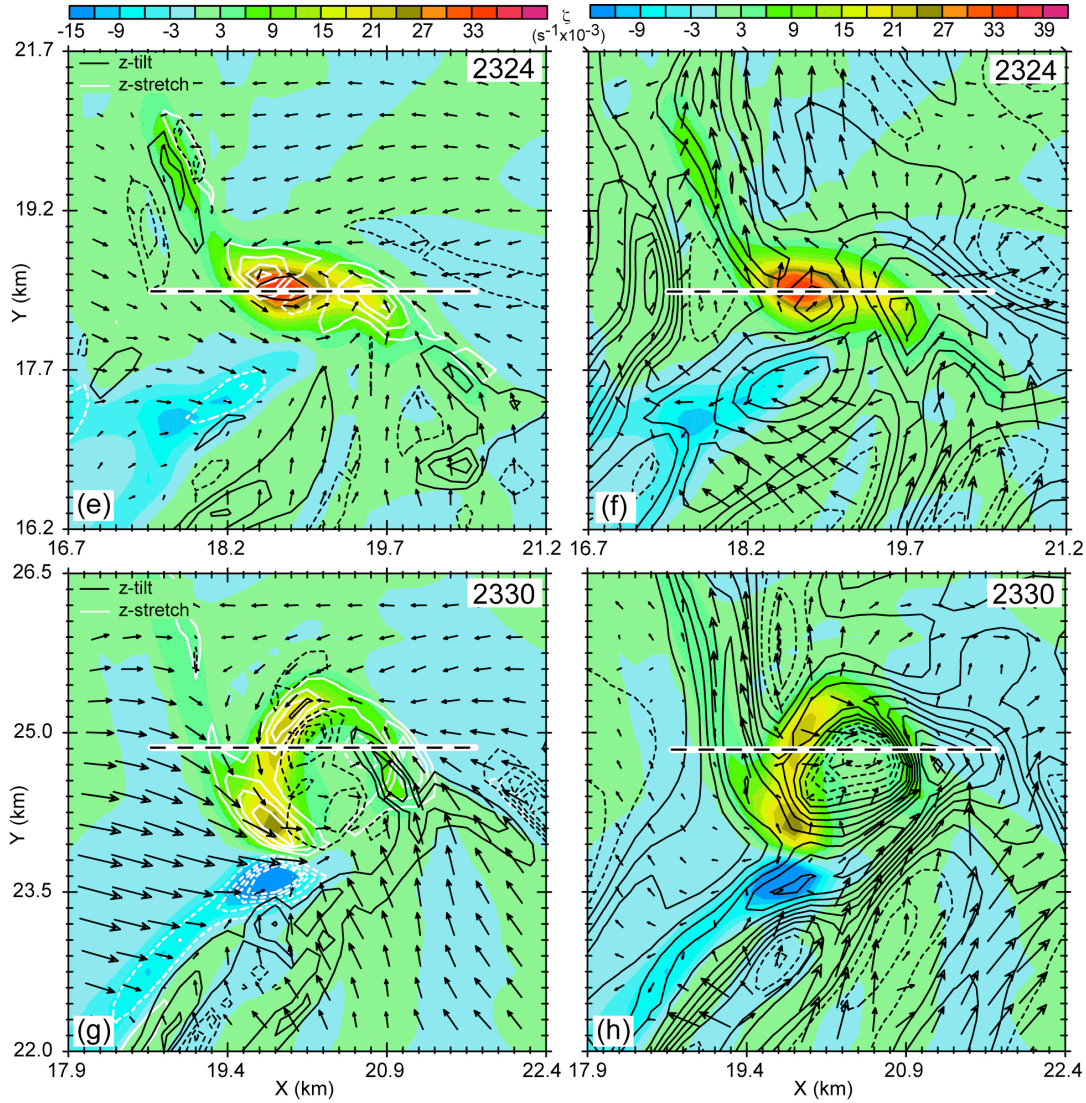

Figure 6.3. Continued.

is due to the four right-hand-side terms that are respectively the tendencies due to the horizontal advection of ζ, the vertical advection of ζ, the tilting of the horizontal vorticity into the vertical axis, and the stretching of ζ. Since we are interested in the change in intensity following the vortex, the horizontal wind components in eq. (6.1) are misocyclone-relative. The dynamics of the misocyclone can be described in terms of vorticity tendencies as it evolves through three distinct phases.

During the *initial growth phase* (~2306-2312 UTC), the development of the misocyclone is primarily due to the stretching of vertical vorticity (B12). During this phase the stretching mainly occurs along and east of the updraft core (Figs. 6.3a, 6.4a-d, bullet 1). West of the updraft core the vorticity tendency is primarily negative (Figs. 6.3a, 6.4a-d, bullets 2-3) and due to the tilting of westward-directed horizontal vorticity vectors downward (i.e., $\frac{\partial v}{\partial z} > 0$, $\frac{\partial w}{\partial x} > 0$, $-\frac{\partial v}{\partial z}\frac{\partial w}{\partial x} < 0$). Weak negative advection of vertical vorticity into the misocyclone is present at this stage (i.e., the vertical vorticity is a local maximum in the misocyclone and the flow is convergent), while positive vertical advection of vertical vorticity is also acting through the top of the misocyclone (not shown).

During the ensuing *rapid growth phase* (~2312-2324 UTC; refer to figures at 2318 UTC), the stretching of vertical vorticity intensifies as convergence and vertical motion increase within the misocyclone (B12). Thus, during the rapid growth phase w increases with height more rapidly since w vanishes at the lower boundary. As increasing $\frac{\partial w}{\partial z}$ becomes located over increasing ζ, stretching $\left(\zeta\frac{\partial w}{\partial z}\right)$ intensifies along the updraft core (Figs. 6.3c-d, 6.4e-f, bullet 4). The vertical vorticity tendency west of the updraft core is negative and remains dominated by the tilting of westward-directed horizontal vorticity vectors downward (Figs. 6.3c-d, 6.4e-f, bullet 5). Although there is negative horizontal vertical vorticity advection, the strong stretching allows the misocyclone to grow in both intensity

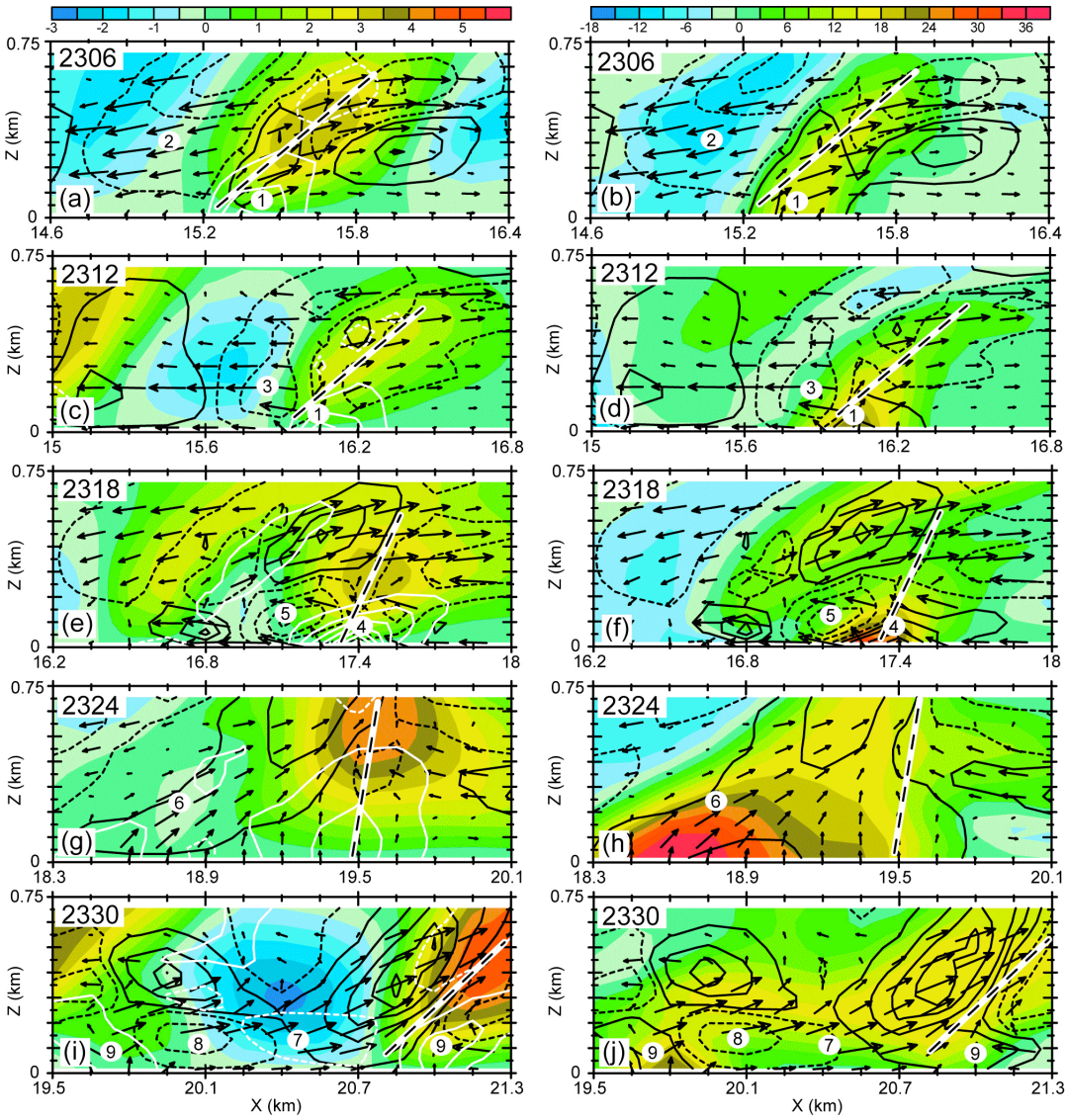

Figure 6.4. Vorticity vectors in the plane of the cross-section (150 m length equal to 15 x 10^{-3} s^{-1}) with kinematic fields at 2306-2330 UTC. Left: Vertical velocity (color-filled), vertical tilting of horizontal vorticity (contoured in black every 200 x 10^{-6} s^{-2} starting at 50 x 10^{-6} s^{-2}), with positive values solid and negative values dashed, and stretching of vertical vorticity contoured in white every 100 x 10^{-6} s^{-2} starting at 50 x 10^{-6} s^{-2}, with positive values solid and negative values dashed. Right: vertical vorticity (color-filled), the sum of tilting plus stretching of vertical vorticity tendency (contoured in black every 200 x 10^{-6} s^{-2} starting at 50 x 10^{-6} s^{-2}), with positive values solid and negative values dashed. The black dashed line indicates the axis of the updraft core. Numbered white dots locate vorticity forcing features described in the text. Cross-section locations for panels c-j are located in Fig. 6.3.

and diameter (Figs 6.3c-f, 6.4e-f). Strong vertical advection of vertical vorticity also contributes to the deepening of the misocyclone through 2324 UTC. The misocyclone reaches its maximum intensity during this phase.

The onset of the *decay phase* is marked by simultaneous weakening of the tilting and stretching tendency terms (B12). At the onset of misovortex decay, the horizontal and vertical advection terms are balanced with the tilting and stretching terms. From the initiation through the growth phase, the pressure within the misocyclone center falls as a cyclostrophic balance between the pressure and angular momentum is rapidly achieved and subsequently sustained. That is, the simulation rapidly adjusts the pressure in response to the circulation to remain dynamically balanced. In fact, calculations confirm that the pressure perturbation near the surface within the misocyclone is almost exactly what would be expected for the misocyclone to be in cyclostrophic balance given the misocyclone-relative horizontal velocity field (not shown). As the misocyclone continues to strengthen, the pressure continues to fall in the center. Since the misocyclonic vorticity decreases with height, there is a net downward-directed perturbation pressure gradient force. As the perturbation pressure gradient strengthens, the updraft weakens and subsequently transitions to a central downdraft (Figs. 6.4g-h, bullet 6).

As previously discussed in section 6.1.1., the transition process from axial updraft to axial downdraft in a misocyclone is similar to the development of an occlusion downdraft in the intensifying low-level mesocyclone of a supercell storm (e.g., Brandes 1984). This process limits the extent of misocyclone growth and initiates the onset of the decay phase. With the downdraft continuing to strengthen, the misocyclonic vertical vorticity weakens from the center outward. During this phase, compression of vortex tubes (Figs. 6.3g-h, 6.4i-j, bullet 7) along with negative tilting of eastward-directed vorticity vectors (Fig. 6.4i-j, bullet 8) lead to

negative vertical vorticity tendency in the center of the misocyclone. Along the periphery of the central downdraft, areas of updraft and positive vertical vorticity stretching persist (Figs. 6.3g-h, 6.4i-j, bullet 9). Thus, the decaying misocyclone takes the form of an ("inverted U-shaped") arc of enhanced vorticity along the western edge of the broader circulation (Figs. 6.3g-h). As the misocyclone continues to decay, the remaining vertical vorticity weakens by 2330 UTC except for a residual vortex at the southern edge of the broader circulation (Figs. 6.3g-h). The weakening broader misocyclone subsequently moves out of the model domain.

6.1.3. Cumulus formation

Shallow cumuli have been observed both visually and by satellite within the IOR on 22 May (Buban et al. 2007). The Lagrangian analyses are unable to represent cumuli in the 22 May case, since the cloud base is higher than the top of the analysis domain. Cumuli develop in the real data simulation (B12), thus providing a high-resolution dataset with which to demonstrate the transportive nature of the cumulus formation process.

Ziegler and Rasmussen (1998) have proposed a "parcel continuity principle" which states that a cumulus cloud will form only if air parcels reach their LCL prior to exiting the mesoscale updraft that provides the lift needed to achieve water saturation. That is, the time required for an air parcel to cross and eventually exit the updraft (defined as $w > 0$) horizontally must equal or exceed the time required for the parcel to rise from its entrainment level to its LCL (Ziegler et al. 2007, Ziegler and Rasmussen 1998). Depending on the saturation point level of the source region of air and the time duration and intensity of lifting, only a rather small subset of all BL updraft air parcels would normally achieve their LCLs (Ziegler et al. 2007). The BL air that eventually formed simulated cumuli was hot and dry (θ_v ~315 K and q_v~5 g kg^{-1}), thus requiring strong, sustained lifting t hrough a rather

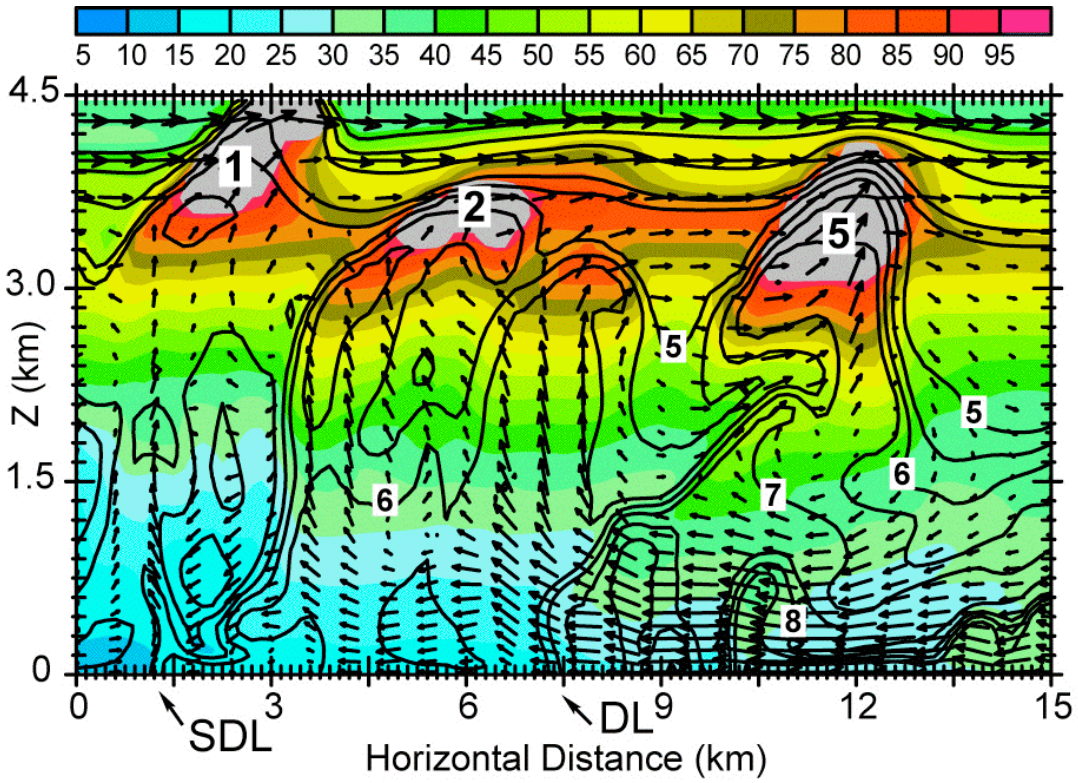

Figure 6.5. Real-data-simulated relative humidity (color-filled), water vapor mixing ratio (black contours at 0.5 g kg^{-1} interval), cloud water mixing ratio greater than 0.01 g kg^{-1} (gray shading), and plane-parallel wind vectors with 1 km = 5 m s^{-1} in a dryline-normal cross-section at 2305 UTC (denoted by the black dashed line in Fig. 4.4). Also shown are dryline (DL) and secondary dryline (SDL). The numbers within each cumulus cloud indicate regions in Fig. 6.6.

deep layer that contained potentially inhibitive vertical wind shear to reach the LCL height of ~3.0-3.5 km (B12). The latter conditions are achieved in several areas within the northeastern quadrant of the simulation domain (Fig. 4.4).

High-based cumuli develop to the west of the dryline within stronger updrafts associated with a weak secondary dryline, HCRs, and OCCs (B12, Fig. 4.4). Lower-based cumuli also develop within strong updraft bands along the dryline as well as where HCR or OCC segments have moved from southwest to northeast across the dryline (Fig. 4.4). Measurement of thirty individual updraft cores yielded a mean horizontal updraft speed of 19.0 m s^{-1} with a standard deviation of 1.1 m s^{-1}. Updraft cores thus tend to move near the mean BL velocity (19.2 m s^{-1}), allowing air parcels to spend a sufficient amount of time within the updraft to reach their LCLs.

Simulated cloud-base heights tend to decrease from west to east across the dryline as a result of the differing origins and saturation points of rising air (B12), as previously inferred from aircraft in situ observations and a photogrammetric analysis by Ziegler and Rasmussen (1998). The range of simulated cloud-base heights are ~2.9 - 3.2 km AGL along and east of the dryline, ~3.30 - 3.35 km AGL just west of the dryline, and ~3.35 - 3.5 km AGL along the western secondary dryline (Figs. 6.5 - 6.6). These LCL heights are broadly consistent with an LCL height of ~3.4 km estimated from mobile soundings launched west of the dryline (Buban et al. 2007). The detailed differences in cloud-base height are a manifestation of the differing thermodynamic characteristics of the air parcels that subsequently reach cloud base as discriminated by their originating BL airmasses.

The simulated cumuli reported by B12 can be organized into five groups according to individual cloud base heights and locations (Fig. 6.6). Backward air trajectories calculated from cumuli in the first group (not shown) with the highest

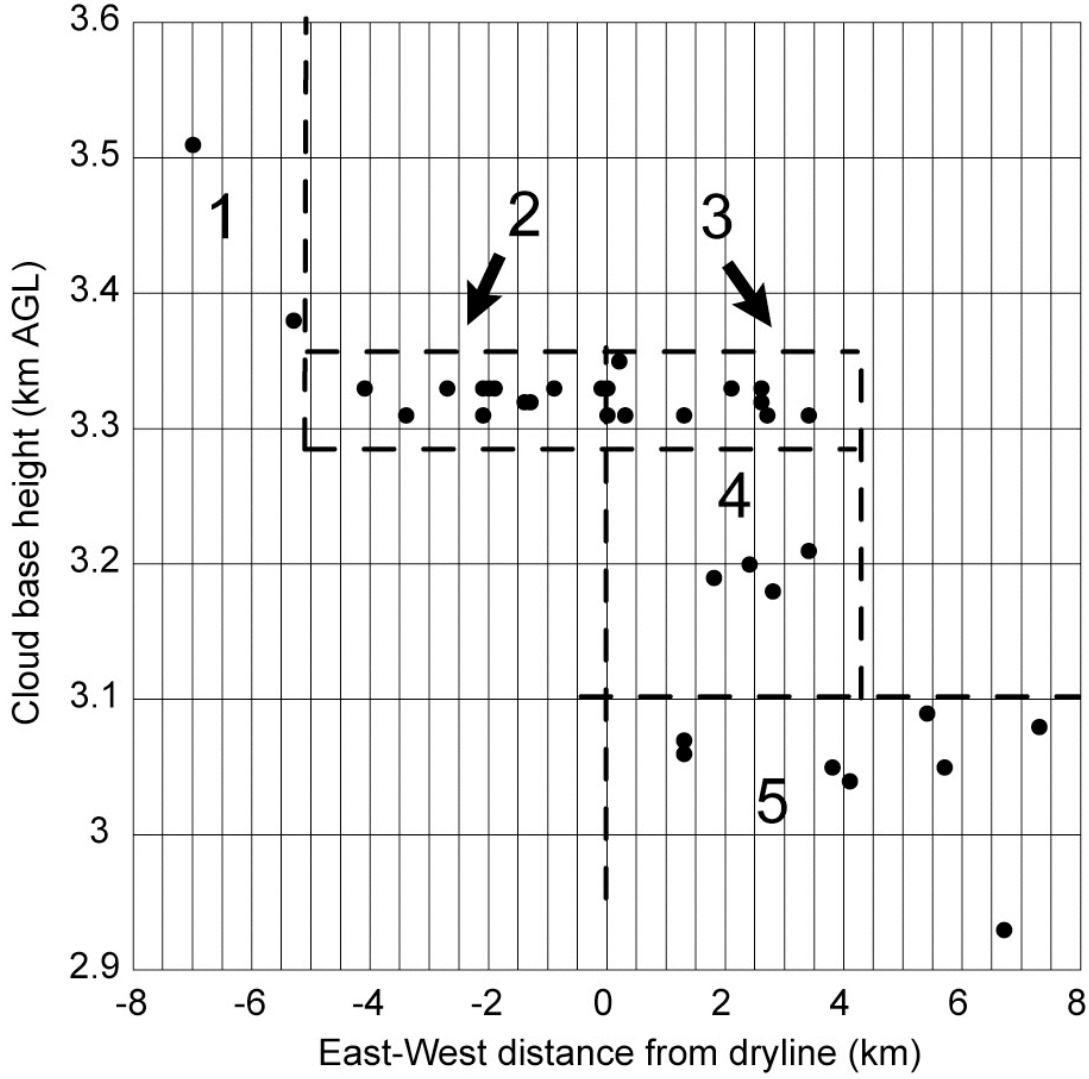

Figure 6.6. Cloud base height (km AGL) as a function of east-west distance relative to the dryline (km). 1) Cumuli formed from air lifted along secondary dryline; 2) cumuli formed from dry air lifted west of the dryline; 3) cumuli formed from dry air lifted over the dryline; 4) cumuli formed from a mixture of dry and moist air within the dryline; 5) cumuli formed from a mixture of dry and more moist air lifted just east of the dryline.

cloud base (~ 3.5 km) reveal that parcels eventually reaching their LCL originate in the middle to upper BL, and are lifted gradually while traversing the updraft along the secondary dryline. All air trajectories described in the present study are calculated using three iterations of a quadratic Runge-Kutta predictor-corrector scheme (McCalla 1967). In the second group, somewhat lower-based cumuli with cloud bases around 3.3 km form within locally stronger updrafts along HCR and OCC segments between the secondary and primary drylines. Air that reaches the LCL in this latter area has a source region in the lower to middle BL. Both higher-based and lower-based cumuli form along and just east of the dryline. The higher-based cumuli comprise the third group and form along HCR and OCC segments that have crossed over the dryline. These latter cumuli have similar cloud base heights and parcel source regions to the cumuli formed along HCR and OCC segments that have not crossed over the dryline. Air within these higher-based cumuli originates at various levels within the lower to middle BL west of the dryline. In the fourth group, lower-based cumuli form within the dryline updraft and consist of a mixture of parcels originating within the dryline moisture gradient at very low levels and drier air in the middle BL west of the dryline. These cumuli have bases ~ 3.2 km. Those cumuli farthest east with the lowest cloud base comprise the fifth group, consisting of a mixture of moist air at low levels within the dryline gradient and dry air west of the dryline in the middle BL, however those low level parcels arise from the moist side of the dryline gradient.

Backward air trajectories illustrate parcel source regions (e.g., Fig. 3.1a, Fig. 6.7b) for a cumulus cloud east of the dryline (B12). Air parcels that subsequently enter the cumulus cloud originate at the southern boundary from both the moist side of the dryline gradient and about 4 km west of the dryline (Fig. 3.1a). As these air parcels of differing saturation points enter the dryline updraft and are brought into

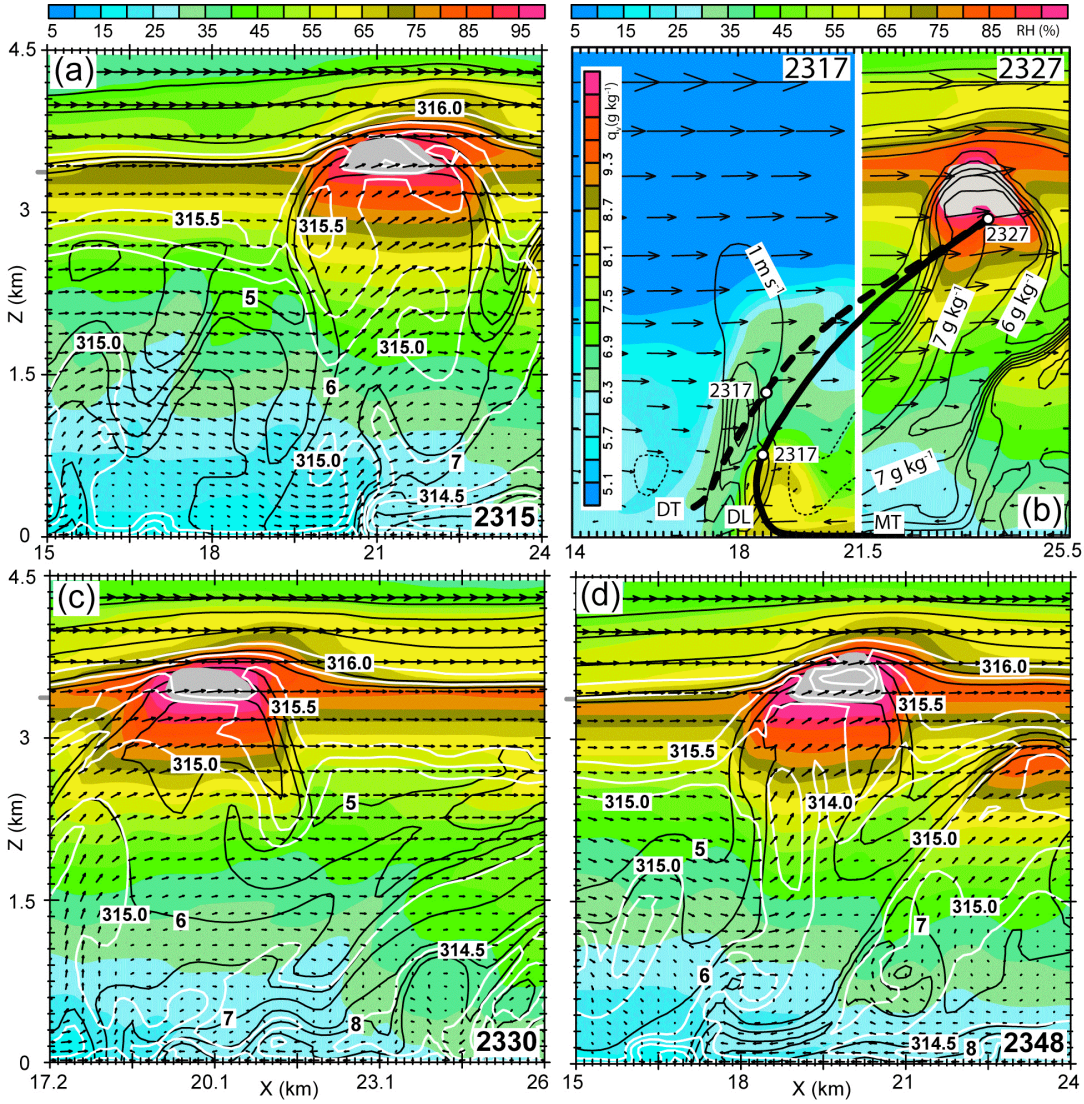

Figure 6.7. Panels (a), (c), (d): relative humidity (color-filled), water vapor mixing ratio (black contours at 0.5 g kg^{-1} intervals), virtual potential temperature (white contours at 0.25 K interval), cloud water mixing ratio greater than 0.01 g kg^{-1} (gray shading), and plane-parallel wind vectors with 1 km = 15 m s^{-1}. Panel b (left): water vapor mixing ratio (color filled) and vertical velocity (every 1 m s^{-1} starting at ±1 m s^{-1}) with positive (negative) values indicated by the solid (dashed) black contours. Also shown are plane-parallel wind vectors with 1 km = 20 m s^{-1}. Panel b (right): as in (a) but omitting temperature. Also shown are plane-parallel wind vectors with 1 km = 20 m s^{-1}. In panel b, the thick black solid and dashed curves are the plane projections of the trajectories shown in Fig. 3.1.

closer proximity by convergence (Fig. 6.7b), they mix as they are accelerated upward (not shown). In fact, due to the helical nature of the flow, these two air parcels actually twist around one another as they approach the LCL (Fig. 3.1a, Fig. 6.7b), with the eastern and lower air parcel eventually becoming farther west and higher than the other parcel. It is found that the simulated cumuli all form from a mixture of air from differing source regions, that these source regions are spaced much farther apart than the scale of the individual clouds, and that air travels a considerable horizontal distance (~20 km) within the updraft prior to reaching the LCL.

The simulated cumuli both east and west of the dryline are small in horizontal extent (Fig. 6.1) and rather shallow (Fig. 6.5, Fig. 6.7). These characteristics are consistent with photographic images of cumuli on 22 May (Buban et al. 2007, their Fig. 5.4c?). Cumuli formed by a strengthening HCR west of the dryline (Fig. 6.1c, Fig. 6.7c) and cumuli formed from HCR segments that have moved over the dryline (Figs. 6.1a,d; Figs. 6.7a,d) have nearly the same cloud-base height, reside within a larger area of higher relative humidity, and are forced by a rather erect updraft plume associated with the parent HCR. A significant distinction between these cumuli is that the plumes that develop cumuli to the east of the dryline are no longer connected to their near-surface updrafts due to the stratification introduced by the virtually cooler moist BL. Cumuli formed by a mixture of dry air from west of the dryline and moist air within the dryline zone have a lower cloud base (Fig. 6.1b, Fig. 6.7b) and are forced by the along-dryline updraft whose enhanced tilt is a consequence of the solenoidally forced secondary circulation that also enhances westerly shear.

Several cumuli develop near misocyclones in the simulations (Fig. 6.1). Although some appear to be a result of previously hypothesized processes (e.g.,

deepening of the moist layer and enhanced convergence north of the misocyclone due to the misocyclone's interaction with the dryline), the number of cumuli associated with misocyclones is small compared to the total number of cumuli. Furthermore, cumuli do not develop within the vicinity of several misocyclones. Therefore, little inference can be drawn from the real data simulation regarding the influence of misocyclones on cumulus formation on 22 May 2002.

6.2. COMPARISON OF THE IDEALIZED BAROTROPIC AND BAROCLINIC SIMULATIONS

6.2.1. Evolution of shear zones

All of the barotropic simulations have a similar evolution. From the initial state, characterized by a region of constant vorticity bordered on the east and west by regions of zero vorticity, the simulations progress by maintaining a nearly homogeneous, constant vorticity, constant width vorticity layer for a considerable time. As the simulations start, there is a spin-up period (roughly ~ 200 s) where small perturbations are damped, followed by exponential growth of preferred wavenumbers consistent with predictions of linear theory. Eventually, as the initial perturbations have grown by about 2 orders of magnitude, wavelike features emerge along the shear zone. These wavelike features continue to amplify and eventually develop into discrete vortices.

All of the baroclinic simulations also have a similar evolution to each other, but different from the barotropic simulations. The initial state is characterized by a region of constant vorticity bordered on the east and west by regions of zero vorticity. Along the shear zone and below 1.5 km a vertically homogeneous east-to-west temperature gradient is imposed embedded in a westerly shear. As the simulations spin up, the horizontal density gradient induces a secondary circulation. Therefore, the shear zone initially moves eastward before slowing and becoming nearly stationary. During this time, the shear zone undergoes collapse and the

vorticity within the zone increases. It has been shown that the increase in vorticity is primarily due to stretching of vorticity, opposed slightly by tilting of the vertical vorticity by the secondary circulation. As the simulation spins up, like in the barotropic cases, the small random perturbations are initially damped. Eventually, as the initial perturbations have grown by about two orders of magnitude, wavelike features emerge along the shear zone. These wavelike features continue to amplify and eventually develop into discrete vortices.

6.2.2. Linear theory

Linear theory is only applicable when the magnitude of the perturbations is "small" compared to the characteristic velocity of the shear. Although there is no well-defined cutoff for the transition from the linear to the nonlinear regime, one metric to assess the degree of linearity (i.e., the extent to which products of perturbations can be neglected compared to some measure of the mean flow), is to compare the amplitude of the perturbation in the *v*-component wind to the *v*-component shear across the shear zone (i.e., peaks in the curves in Fig. 5.9). If v' is the amplitude, then the ratio $L = \frac{2v'}{\Delta V}$ is a measure of the percentage of the mean flow contained in the perturbation. In all the barotropic simulations, it appears that the growth described by linear theory holds well up through rather large values of *L*. Small-amplitude wavelike features first become visible in the momentum fields after *L* achieves order 10%. The perturbations continue to grow exponentially at the same rate and peak wavenumber up through $L \sim 50\%$ or more. Thus it appears that the predictions of linear theory may be extended into the nonlinear regime.

Even before visible waves can be seen in the simulations (about the time when the validity of linear theory weakens), spectral density estimates and growth rates can be computed. Therefore even from the beginning, the behavior of the

simulations can be compared to linear theory with regard to the growth of random perturbations. Note that even though there isn't a theoretical analytic result applicable for the baroclinic cases, we can still identify a "linear regime" for these cases, with the interpretation that this is the period where the initial random perturbations are small compared to the initial flow (i.e. $L \leq 10\%$).

For the barotropic cases, initially there is a spin-up period, where perturbations either do not grow exponentially or else are damped, followed by a period of exponential growth. This behavior is seen across all barotropic simulations and was also reported in a simulation of fluctuation growth along a frontogenetic oceanic front (McWilliams et al. 2009). After the spin-up period the growth rates are essentially exponential (as evidenced by the high linear correlation on the semi-log plots in Figs. 5.19 and 5.20). Also, the actual growth rates and wavenumbers of maximum growth are very close to those predicted by linear theory. As the width of the shear zone increases, the most-unstable wavelength also increases, remaining about 7.9 times the width of the shear zone, and this is independent of the magnitude of the shear across the zone. The growth rates of these maxima, however, are dependent on the magnitude of the vorticity in the layer, thus both the magnitude of the shear and the shear zone width. The larger the vorticity values, the larger the growth rates. Therefore, simulations with higher initial vorticity values have the emergence of wavelike structures and eventually discrete vortices sooner than simulations with weaker initial vorticity values, since all simulations are initialized with the same random perturbation (= 0.01 m s^{-1}).

For the baroclinic cases (as in the barotropic cases), initially there is a spin-up period wherein perturbations either do not grow exponentially or else are damped. After, a period of super-exponential growth develops as the growth rates are increasing due to shear zone contraction (as evidenced by the slight upward

curvature on the semi-log plots in Figs. 5.45 and 5.46). This behavior is seen across all barotropic simulations. To try to extend the theoretical analytic results of linear theory applicable to the barotropic cases to the baroclinic cases, the analytic theory was modified to allow for an evolving shear zone width. The modified linear theory equation applied to the baroclinic simulations yields excellent agreement between the new theory and "observed" growth rates from the simulations. The resulting growth rates are larger in the baroclinic cases than the barotropic cases for the same initial shear zone vorticity, since the growth rates are still a function of the vorticity, and the vorticity increases due to shear zone collapse. This result is consistent with McWilliams et al. (2009), who found that baroclinic frontogenesis enhanced the growth of 3-D fluctuations along a simulated oceanic front. As in the barotropic simulations, there is a high degree of correlation between the growth rates and the initial shear zone vorticity, with larger vorticity values leading to larger growth rates and earlier emergence of the wavelike structures and resultant discrete vortices.

Although the linear theory only holds while the growing perturbations are small (i.e., on the order of 0.1-1.0 m s^{-1} in the simulations), the discrete vortices that eventually form, albeit well into the nonlinear regime, possess wavelengths and spacings consistent with that predicted from linear theory in the barotropic cases. It therefore seems that linear theory can be extended to some degree into the nonlinear regime for these cases, or that the initial exponential growth "fixes" the structure of the later emerging vortices. The results suggest in either way a degree of predictive value, in the sense that the spacing of discrete vortices can be determined prior to their emergence given an initial shear zone width. Also, if some estimate of the magnitude of the shear across the shear zone is known (hence vorticity), some estimate of the growth rates of the emerging vortices can also be estimated.

For the baroclinic cases, although some estimate of an initial shear zone vorticity and some estimate of the nature of the shear zone collapse could allow some estimate of the resulting growth rates, it would seem to be more difficult than in the barotropic cases. In addition, once the wavelike structures and discrete vortices emerge in the baroclinic cases, they are farther along into the nonlinear regime and exhibit a more complicated structure than the barotropic cases. In the baroclinic cases, there is nothing to prevent the shear zone from continuing to collapse other than grid resolution. In all cases, the shear zones collapse to around twice the grid spacing before the emergence of the wavelike structures, and the resulting structures have wavelengths consistent with what would be predicted by a barotropic linear theory with a shear zone width of around 2Δ. Regardless of the actual resolution employed, it seems that the model will always try to collapse the gradient to around 2Δ. This tendency has also been shown in other simulations of frontal zones (e.g., Gall et al. 1987; Garner 1989). In nature, we find that actual boundaries (fronts, drylines, etc.) tend not to collapse to arbitrarily small scales. Eventually, turbulent diffusion would tend to limit the magnitudes of gradients across boundaries; however, there might be other processes that also limit these gradients (Hoskins 2003). For example, McWilliams and Molemaker (2011) suggest that growing frontal instabilities can actually have a frontolytic effect. Therefore, in nature, although the baroclinic simulations may initially be more appropriate, eventually, any collapsing shear zone would tend toward the barotropic configurations of a nearly constant shear zone width.

6.2.3. Evolution of discrete vortices

Once past the linear growth regime, discrete vortices develop nonlinearly. A common structure is seen across all barotropic simulations and is typified by the bt5m16s case shown. The nearly equally spaced vortices are elliptically shaped,

grow in size, and are connected by thinning braid regions. As the vortices evolve, they rotate with a nearly constant angular velocity and eventually the braid regions wrap completely around the cores. This structure and evolution has been seen frequently in many observational and numerical studies (e.g. Freymouth 1966; Thorpe 1971; Brown and Roshko 1974; Winant and Browand 1974; Cantwell 1981; Corcos and Sherman 1984; Pozrikidis and Higdon 1985; Basak and Sarkar 2006; Guha et al. 2013). The evolving vortices also undergo nutation wherein the ratio of the major to minor axis length oscillates, another common feature of vortices under a variety of conditions (e.g. Kida 1981; Basak and Sarkar 2006; Guha et al 2013). Eventually, the nonlinear interaction among the vortices leads to vortex-pairing and mergers (e.g., Winant and Browand 1974; Basak and Sakar 2006; Marquis et al. 2007).

The behavior of the vortices that develop in the baroclinic simulations is similar to those in the barotropic simulations, with a few notable differences. In the baroclinic simulations, the emerging vortices are not as equally spaced, and have differing sizes compared to the barotropic cases. The greater degree of variability is likely due to the modulation of the dominant wavenumber by other less dominant wavenumbers (i.e., see minor peak in the spectral density estimates in Figs. 5.43 and 5.44). The resulting vortices also develop cores and connecting braids but with a more complicated structure. These cores also rotate and nutate, however to a lesser degree than in the barotropic simulations, perhaps because the baroclinic vortices tend to be more circular than elliptical. As in the barotropic cases, the vortices in the baroclinic cases eventually pair and merge at later times.

6.2.4. Vertical motions in vortices

Once the vortices have developed into discrete cores with connecting braids, relatively strong vertical motions fields also develop. To the author's knowledge,

no previous barotropic theoretical or numerical study has analyzed the velocity field along the direction of the vorticity within a shear zone (i.e., the vertical velocity component in the present study). Presumably, this is due to the vast majority of the studies either being two-dimensional (where no such velocity component exists) or that the orientation of the shear layer is such that the shear is in the vertical (i.e., the classic Kelvin-Helmholtz instability problem). In the present study the vertical velocity component is important, since simulations are interpreted as replicating real atmospheric boundaries and thus since vertical motions can lead to CI and subsequent storm development. In the barotropic simulations, the stronger updrafts tend to occur where the braids attach to the cores. The strongest downdrafts tend to occur either along the braid regions, or in the center of vortices. Note that in the simulations, there is also a wavenumber 2 modulation of the fields, such that not all vortices within a simulation have updrafts or downdrafts in the same location, however pairs of vortices spaced one half of a domain apart (15 km) do appear to have similar structure. In the center of all vortices a local pressure perturbation minimum develops, and vortices have a tendency to develop central downdrafts. Although not all vortices develop central downdrafts, those without central downdrafts also contain only weak updrafts.

Prior to the emergence of vortices, the baroclinic simulations are characterized by strong updrafts along the entire shear zone due to the secondary circulation associated with the density gradient within the zone. As the discrete vortices develop, stronger updrafts tend to develop between vortices, with downdrafts developing within the vortex cores. Unlike in the barotropic cases, nearly every distinct vortex core in the baroclinic cases develops a central downdraft. These vertical motion characteristics are consistent with those found along a baroclinic shear zone in Lee and Wilhelmson (1997). Subjective analysis of

several observational studies broadly conform to the updraft structure in both the barotropic and baroclinic simulations, that is, generally strongest updrafts between or just north of vortex cores, weaker updrafts just south of vortex cores, and either the weakest updrafts or else downdrafts along the vortex axis (e.g. Wilson et al. 1992; Kawashima and Fujiyoshi 2005; Arnott et al. 2006; Marquis et al. 2007; Campbell et al. 2014).

It has been shown that for the barotropic simulations, average maximum updrafts that develop are highly correlated with the vorticity within the shear zone, with the stronger updrafts associated with higher vorticity values. Several previous studies have been reviewed to see if a similar correlation had been seen prior. Both observational and modeling studies were examined, and with the exception of one high-resolution modeling study (Lee and Wilhelmson 1997) there was only a small range in the strength of simulated or observed misocyclones. Most had vorticity

Study	Description	maximum vorticity ($\times 10^{-3}$ s^{-1})	maximum updraft ($m\ s^{-1}$)
Kawashima and Fujiyoshi 2005	radar observations	10	3-4
Lee and Wilhelmson 1997	100 m resolution simulation	70-80	8-9
Arnott et al. 2006	radar observations	8	2-3
Wilson et al. 1992	1 km resolution simulation	10	3-4
Campbell et al. 2014	1 km resolution simulation	8	2
Kawashima 2011	500 m resolution simulation	10	3-4
Buban et al. 2007	radar observations	8	3

Table 7. List of several other studies containing misocyclones, with their description, maximum vertical motion and maximum updraft.

values around 8-10 x 10^{-3} s^{-1} and they were associated with vertical velocities of 2-4 m s^{-1} (Table 7). There is generally an increase in vertical velocity with increasing vorticity in these studies. Note that in the present study, the lowest initial shear zone vorticity values were 10 x 10^{-3} s^{-1} and the updrafts associated these values were around 1-2 m s^{-1}. However, these were the *average* maximum vertical velocities in the domain, therefore the simulation did have local updrafts greater than the average.

6.3. COMPARISON OF THE 22 MAY 2002 CASE WITH IDEALIZED SIMULATIONS

6.3.1. Vortex evolution

Several misocyclones were identified in the real data simulations. These misocyclones were forced by perturbations introduced at the southern lateral boundary and allowed to evolve according to the dry-convective airflow dynamics within the domain interior. These misocyclones have features similar to vortices produced by both the barotropic and the baroclinic simulations. Four simulated misocyclones from the real data case show a range in variability (Fig. 6.2). Initially, each misocyclone is oriented in a north-south or northwest-southeast direction along the near-surface shear zone and takes on an elliptical shape, similar to the shape of the emerging misocyclones in the barotropic and baroclinic simulations, however, the variability is more like that seen in the barotropic simulations.

The misocyclones move downstream and nearly the speed of the mean shear-layer wind as do the barotropic and baroclinic simulated vortices. As they move down stream, all simulated vortices rotate counterclockwise, however in both the baroclinic and real data simulations, some vortices are more circular and thus the rotation is less pronounced. Although some misocyclones in the real data case have "tails" extending from the vortex core, they don't have fully connected braids as in the barotropic and baroclinic simulations. Since the misocyclones are spaced farther

apart, and there is fully formed mesoscale turbulence and friction, it seems the real data simulations would be unable to preserve they very thin features. Eventually, the real data simulated misocyclones begin to weaken as the move out of the domain. In both the barotropic and baroclinic simulations, the vortices eventually merge to form complicated, more turbulent structures. In the real data case, it appears that the spacing of the misocyclones is too large to allow for vortex mergers, and once they reach a maximum, they begin to decay.

Another aspect of the several real data simulated misocyclones is the presence of a central downdraft, a feature seen in both the barotropic and baroclinic simulated misocyclones. As the central downdraft develops, vertical vorticity in the center is weakened, and this eventually leads to the decay of the misocyclones in the real data cases. In both the barotropic and baroclinic simulations, weakening in the center occurs, but vortex mergers occur before much weakening of individual vortices is seen.

A detailed analysis of one misocyclone (M1) has been discussed in Chapter 4. Since this misocyclone is situated along a dryline that is characterized by a shear zone collocated with a moisture gradient, the effect of the misocyclone on the moisture gradient may be determined. It is seen that the misocyclone reorients the moisture gradient initially by wrapping moist air west and dry air east. With time, the moisture gradient wraps completely around the misocyclone thus closing off a pocket of dry air near the vortex center. From the mbt5m16s simulation shown (Fig. 5.32), there is a similar evolution. Moist and dry air parcels are wrapped around the evolving vortex in a classic "spiral billows" effect conventionally associated with the presence of Kelvin-Helmholtz instabilities.

6.3.2. Cumulus formation

The advection of the moisture fields and the vertical motions within these types of vortices can have an effect on possible cumulus formation. Given that relatively strong vertical motions develop in the barotropic simulations, several tests are run with moisture added to determine preferred regions of cloud development. All simulations with moisture produce clouds in preferred regions. As the vortex cores rotate and the braids wrap around the cores, moist and dry air regions are also rotated around the vortex center. Clouds form between the core and the braid region to the west of the core, where the strongest updrafts are collocated with the highest moisture values. Not all vortices have clouds and the extent of the clouds varies, however vortices one-half of a domain apart do have similar cloud structure. Within each vortex, the moisture structure is very similar, however the vertical motion fields are more variable. The regions with the strongest updrafts produced the largest (and deepest) clouds, with small (shallower) clouds in the weaker updrafts, and no clouds in the weakest updrafts. Note that in the mbt5m16s case, clouds develop even to the southwest of the vortex core (Fig. 5.32) in a region where updrafts generally have not been documented in previous studies. In the mbt5m16s case, by the time the clouds have formed the vortex is mature, and the updraft has wrapped a considerable way around the core. Hence in a vortex-relative sense, the updraft is in a position consistent with other studies (e.g., starting from the initial development of the vortex the updraft remains in the right front quadrant of the system).

Since the strongest updrafts are associated with the highest values of shear zone vorticity, one would expect the largest and deepest developing clouds to also be associated with those shear zones with the highest vorticity values. Therefore, assessing the vorticity associated with a given shear zone (dryline, frontal zone, etc.)

could yield some information about the potential for parcels to reach their LCLs and subsequent LFCs to trigger CI.

On 22 May 2002, several shallow high-based cumuli were observed in the IOR, and cumuli were simulated in the real data case. The observed and simulated cumuli were associated with various BL structures including HCRs, mesoscale dryline updrafts, and misocyclones. Moist, equivalent-barotropic simulations were configured to determine preferred cumulus development with respect to developing vortices. Since the moist equivalent-barotropic simulations do not contain the fully 3-D, dry-convective BL circulations that are allowed to develop in the real data case, only the relationship between cumulus formation and vortices can be compared in the real data and equivalent-barotropic simulations.

Cumuli develop coincidently with several misocyclones in the real data simulation (Fig. 6.1). Although not all misocyclones in the real data case are associated with developing cumuli, those misocyclones that have coincident cumuli generally experience cumulus development either in the northern/northeastern quadrants or the southeast quadrant. Those cumuli that develop to the north of the misocyclone are embedded within deep moist convective plumes that tilt significantly eastward with height. Those cumuli that develop to the south of the misocyclone are embedded within more erect updrafts and thus remain closer to the surface position of the dryline than in the case of northern cumuli. These preferred northern and southern locations for cumulus formation coincide with the locations of the strongest vertical motions in the moist barotropic simulations.

Chapter 7

Conclusions

This study presents a series of simulations that attempt to replicate the dynamics of the dryline and surrounding BL with special emphasis on misocyclones. The first simulation is a real data case, initialized and forced through time-dependent lateral boundary conditions via analyses of temperature, moisture, and momentum from the 22 May 2002 IHOP dataset. The second series of simulations are the barotropic runs, initialized with a north-south oriented constant vorticity shear zone and north-south periodic boundary conditions. The third series of simulations are baroclinic, wherein the shear zone also contains an east-west temperature gradient. The barotropic and baroclinic simulations have varying magnitudes of shear and differing shear zone widths (corresponding to differing initial vorticity values) across the runs. The barotropic and baroclinic runs each contain a series of twenty-five different runs, with each baroclinic simulation and a corresponding barotropic simulation having the same shear zone width and shear magnitude. Additionally, several equivalent-barotropic simulations are rerun with moisture included under the constraint of horizontally homogeneous virtual potential temperature to assess preferred cumulus cloud formation areas.

The real data simulation reproduces the dryline, misocyclones, and convective BL features such as HCRs and OCCs, with similar structures to observed features of equivalent scale. However, some differences in the details exist. The dryline is simulated as a nearly north-south oriented zone marked by q_v and θ_v gradients of about 2-3 g kg^{-1} km^{-1} and 1 K km^{-1} respectively. The dryline is persistently convergent with accumulation in lower levels, and maintains a persistent solenoidally-driven secondary circulation. These characteristics of the dryline have also been observed, albeit weaker in the observational analyses than

the simulations mainly due to coarser grid spacing and necessary analysis filtering. These characteristics are also consistent with both observed and simulated drylines in other past studies. Features on the dry and moist sides of the simulated dryline (e.g. moisture plumes, HCRs, OCCs) also have higher amplitudes and more detailed structure than in the analyses as a result of the finer model grid resolution.

Simulated cumuli in the real data case have similar characteristics to observed cumuli. High-based simulated cumuli develop along a weak secondary dryline west of the primary dryline and contain a mixture of air originating from the middle and upper BL. Somewhat lower-based cumuli develop along stronger plumes associated with HCRs and OCCs between the primary and secondary dryline, and consist of a mixture of air with source regions in the lower and middle BL. Cumuli also develop east of the dryline and have similar cloud-base height and air source regions as those between the primary and secondary drylines. These cumuli arise within updrafts associated with HCR and OCC segments from the west that move over the dryline. Lower-based cumuli also develop within the dryline updraft east of the surface dryline position. These cumuli contain a mixture of dry air from the middle BL west of the dryline and varying degrees of moist air from very low levels within the dryline gradient. All simulated cumuli contain at least some dry air from west of the dryline. Furthermore, all cumuli form from a mixture of air from more than one source region and thus air with a range of water vapor mixing ratios and saturation point. The cumulus source regions are spaced much farther apart than the scale of the individual clouds while air travels a considerable horizontal distance prior to reaching its LCL. Orientation of HCR and dryline updrafts along the mean wind vector allows lifted parcels to spend a sufficient amount of time within the updraft to reach their LCL.

It has been hypothesized that the misocyclones that are observed along

atmosphere boundaries such as drylines or fronts may arise due to a horizontal shearing instability (HSI). To address the development of vortices with characteristic scales comparable to observed misocyclones to a purely HSI process, the series of barotropic simulations have been performed across a range of shear magnitudes and shear zone widths that are comparable to those of observed boundaries. Linear theory provides analytic expressions for the growth rates and wavenumbers of maximum growth rate as a function of shear zone magnitude and shear zone width for the piecewise linear shear zones in the barotropic series of runs. A comparison between linear theory and the barotropic simulations shows excellent agreement between the wavenumber (wavelength) of maximum growth. This wavelength is approximately equal to $7.9b$. Additionally, an excellent agreement between the predicted growth rates and the simulated growth rates is also found. This growth rate is dependent on the vorticity within the layer, as opposed to the shear zone width and magnitude of the shear independently. From the barotropic simulations, linear HSI theory adequately explains the growth of small perturbations at observed dryline scales.

As a way to better understand the physical mechanism by which vortices emerge from the initial shear zone, a Wave Interaction Theory (WIT) interpretation has been developed. Within this framework, a shear zone consists of two or more density or vorticity discontinuities that can support two or more density or vorticity waves. The interaction of these waves can produce the instability if each interfacial wave amplifies the other. This theoretical interpretation predicts the initial wavelength and phase shift of the corresponding most-unstable mode predicted by linear theory. In the series of barotropic simulations, the results of the calculated initial phase shifts and wavelengths are consistent with the WIT interpretation of the horizontal shearing instability.

Although linear HSI theory is only strictly valid for perturbations that are small compared to the background flow (i.e., <10% shear magnitude), the structure of the unstable perturbations beyond the linear regime nevertheless resemble the structure within the linear regime. As the barotropic shearing instability continues into the nonlinear regime, discrete vortices eventually form. The resulting vortices have a spacing very close to the predicted wavenumber (wavelength) of maximum growth (i.e., if linear theory predicts a wavelength of maximum growth of 4 km, the resulting discrete vortices will be spaced around 4 km apart). Also, those shear zones with larger growth rates develop discrete vortices faster than those with smaller growth rates. Therefore, linear HSI theory appears to extend into the nonlinear regime in the sense that the fastest growing HSI mode will continue to grow fastest and eventually emerge as the dominant mode well within the nonlinear regime.

In many observed boundaries such as fronts and drylines, a horizontal density gradient exists across the shear zone. To see what effects a horizontal density gradient would have on the otherwise purely barotropic shearing instability mechanism, a series of baroclinic simulations have been performed. The baroclinic simulations are similar to the barotropic simulations with several notable differences. First, although the barotropic simulations feature a quasi-steady shear zone as the small initial perturbations are growing, the baroclinic simulations rapidly develop a secondary circulation due to the imposed horizontal density gradient. Convergence along the shear zone associated with the developing solenoidally-forced secondary vertical circulation induces an accumulative shear zone contraction down to about twice the horizontal grid spacing of the simulation. The contracting shear zone width is accompanied by an increase in shear zone horizontal circulation and vertical vorticity, owing primarily to stretching though

somewhat offset by tilting of the vertical vorticity into the horizontal by the secondary circulation. The vertical vorticity increase due to the contracting shear zone leads to a larger growth rate for a given baroclinic run compared to its barotropic counterpart with the same initial shear zone width and shear magnitude. Additionally, contraction of the shear zone to scales barely resolvable by the grid resolutions leads to emerging vortices with much shorter wavelengths than the barotropic runs.

Although it is well understood why the baroclinic simulations tend to collapse frontal zones down to minimally resolvable scale (especially in this case with a free-slip lower boundary condition and no friction), real atmospheric boundaries do not collapse down in scale beyond some point. Due to turbulence or other mechanisms, real boundaries that are collapsing eventually reach a state where the across-boundary scale would hypothetically achieve a fairly steady state. Therefore, it is hypothesized that aspects of both the barotropic and baroclinic simulations may describe various real boundaries at various stages of their individual evolutions.

Although the very early growth of misocyclones has not been simulated in the real data case, the emergence of a simulated misocyclone from an elongated area of shear has been examined in some detail. The simulated misocyclone in the real data case contains very similar structures to the discrete vortices in the idealized simulations. In the real data and idealized simulations, vortices become elliptically shaped, grow in size, and rotate counterclockwise with a nearly constant angular velocity. In the idealized simulations, the vortices are connected by thinning braid regions. These braids are not seen in the real data simulations, but only "tails" along the major axis, likely due to the effects of lower spatial resolution combined with the simulated vortices in the real data case being relatively more isolated than

in the idealized simulations. The misocyclones in both the real data and idealized simulations also develop a pressure minimum in the vortex core and a tendency to develop a central downdraft. The vertical motion fields generally feature the weakest updrafts or downdrafts in the vortex core, with stronger updrafts along the braids or edges of the vortex core. The common structure and evolution of the simulated vortices has been seen frequently in many previous observational and numerical studies.

The moist barotropic simulations have been conducted to determine preferred regions of cumulus formation relative to the ambient shear zone and misocyclones. In all moist simulations, cumuli develop in the region where a core connects to a braid generally in the front-left vortex-relative quadrant. The front-left vortex-relative quadrant contains the strongest updrafts in collocation with regions of larger water vapor mixing ratio values in a deeper layer, with the stronger updrafts producing the largest and deepest clouds. It is also found that the average local maximum in updraft increases with increasing vorticity in the barotropic runs. Thus, shear zones with higher initial vertical vorticity values would be expected to develop more and /or larger cumuli. In the real data case, cumulus formation tends to occur either north or south of the vortex core along and east of the dryline. The latter cumulus locations in the real data case are consistent with those in the barotropic runs.

In summary, a barotropic HSI mechanism adequately describes the growth of perturbations along shear zones with horizontal and vertical length and velocity scales that are characteristic of drylines and fronts. In the barotropic runs, linear theory may be extended into the nonlinear regime to anticipate the characteristic spacing, size, and growth rate parameters of discrete vortices with structures similar to observed atmospheric vortices. These characteristic parameters include a spacing

of about 7.9 times the shear zone width, a growth rate proportional to the shear zone vertical vorticity, and a size proportional to the shear zone width. The baroclinic simulations show that horizontally contracting shear zones feature larger growth rates, smaller vortex spacings, and smaller vortex sizes than shear zones that do not undergo collapse with the same initial vertical vorticity. It has been hypothesized that some real atmospheric boundaries that may experience an initial frontogenetic contraction associated with density gradients (thus behaving like the baroclinic simulations) eventually attain a steady state wherein contraction has ceased (thus behaving like the barotropic simulations). It is further speculated that the extent to which individual real boundaries behave more like either the barotropic or else the baroclinic simulations likely varies both with boundary type and time.

To summarize these results hypothetically in terms of sensible weather such as cumulus formation, CI potential, and storm evolution, it has been found that simulated cumuli tend to form in preferred locations that are removed from misocyclone cores and are either in between or on the edges of vortex cores. Since boundaries with higher vertical vorticity values are associated with stronger updraft cores, and stronger updraft cores are associated with larger and deeper cumuli, those boundaries with higher vorticity would tend to offer a higher probability of cumulus formation and resultant CI. Also, since misocyclone spacing (therefore updraft spacing) is larger for larger shear zone widths, cumuli development would tend to be sparser for boundaries of larger width. Thus for a given shear magnitude, it is hypothesized that increasing shear zone width should increase updraft spacing and decrease updraft strength and thus reduce the potential for cumulus formation and CI. In environments supporting severe thunderstorm development, it is further hypothesized that relatively wide and weakly sheared boundaries would tend to support widely scattered isolated severe storms. In hypothetical contrast, narrow

and strongly sheared boundaries would tend to promote more numerous, closely spaced storms and perhaps rapid upscale growth to form quasi-linear mesoscale convective systems.

References

Arnott, N. R., Y. P. Richardson, J. M. Wurman, and E. M. Rasmussen, 2006: Relationship between a weakening cold front, misocyclones, and cloud development on 10 June 2002 during IHOP. *Mon. Wea. Rev.*, **134**, 311–335.

Atkins, N. T., R. M. Wakimoto, and T. M. Weckwerth, 1995: Observations of the sea-breeze front during CaPE. Part II: Dual-Doppler and aircraft analysis. *Mon. Wea. Rev*., **123**, 944–969.

Atkins, N. T., R. M. Wakimoto, and C. L. Ziegler, 1998: Observations of the finescale structure of the dryline during VORTEX 95. *Mon. Wea. Rev.*, **126**, 525–549.

Barnes, S. L., 1973: Mesoscale objective analysis using weighted time-series observations. NOAA Tech. Memo. ERL NSSL-62, National Severe Storms Laboratory, 60 pp.

Basak, S. and S. Sarkar, 2006: Dynamics of a stratified shear layer with horizontal shear. *J. Fluid. Mech.* **568**, 19–54.

Benjamin, S. G., and T. N. Carlson, 1986: Some effects of surface heating and topography on the regional severe storm environment. Part I: Three-dimensional simulations. *Mon. Wea. Rev.* **114**, 307-329.

Betchov, R. and A. Szewczyk, 1963: Stability of a shear layer between parallel streams. *Phys. Fluids*, **6**, 1391-1396.

Bluestein, H., 1993: *Synoptic-dynamic meteorology in midlatitudes Volume II*. Oxford, 594.

Brandes, E. A., 1984: Relationships between radar-derived thermodynamic variables and tornadogenesis. *Mon. Wea. Rev.*, **112**, 1033–1052.

Browand, F. K., 1966: An experimental investigation of the instability of an incompressible separated shear layer. *J. Fluid Mech.* **26**, 281-307

Brown, G. L. and A. Roshko, 1974: On density effects and large structures in turbulent mixing layers. *J. Fluid Mech.* **64**, 775–816.

Buban, M. S., C. L. Ziegler, E. N. Rasmussen, and Y. P. Richardson, 2007: The dryline on 22 May 2002 during IHOP: Ground-radar and in situ data analyses of the dryline and boundary layer evolution. *Mon. Wea. Rev.*, **135**, 2473–2505.

Buban, M. S., C. L. Ziegler, E. R. Mansell, and Y. P. Richardson, 2012: Simulation of dryline misovortex dynamics and cumulus formation. *Mon. Wea. Rev.*, **140**,

3525–3551.

Cantwell, B. J., 1981: Organized motion in turbulent flow. *Ann. Rev. Fluid Mech.* **13**, 457–515.

Carbone, R. E., 1982: A severe frontal rainband. Part I. Stormwide hydrodynamic structure. *J. Atmos. Sci.*, **39**, 258–279.

Carbone, R. E., 1983: A severe frontal rainband. Part II. Tornado parent vortex circulation. *J. Atmos. Sci.*, **40**, 2639–2654.

Carpenter, J. R., E. W. Tedford, E. Heifetz, and G. A. Lawrence, 2013: Instability in stratified shear flow: Review of a physical interpretation based on interacting waves. *Appl. Mech. Rev.* **64**, 061001-1-17.

Coniglio, M. C., D. J. Stensrud, and L. J. Wicker, 2006: Effects of upper-level shear on the structure and maintenance of strong quasi-linear mesoscale convective systems. *J. Atmos. Sci.,* **63**, 1231–1252.

Conzemius, R. J., and E. Fedorovich, 2008: A case study of convective boundary layer development during IHOP_2002: Numerical simulations compared to observations. *Mon. Wea. Rev.*, **136**, 2305–2320.

Corcos, G. M., and F. S. Sherman, 1984: The mixing layer: deterministic models of a turbulent flow. Part 1. Introduction and the two-dimensional flow. *J. Fluid Mech.* **139**, 29–65.

Crook, N. A., T. L. Clark, and M. W. Moncrieff, 1991: The Denver cyclone. Part II: Interaction with the convective boundary layer. *J. Atmos. Sci*., **48**, 2109–2126.

Davies-Jones, R. P., 1985: Comments on "A kinematic analysis of frontogenesis associated with a nondivergent vortex. *J. Atmos. Sci.***42**, 2073-2075.

Deardorff, J. W., 1978: Efficient prediction of ground surface temperature and moisture, with inclusion of a layer of vegetation. *J. Geoph. Res.* **83**, 1889–1903.

Doswell, C. A., III., 1984: A kinematic analysis of frontogenesis associated with a nondivergent vortex. *J. Atmos. Sci.*, **41**, 1242–1248.

Doswell, C. A., III, 1985: Reply. *J. Atmos. Sci.*, **42**, 2076–2079.

Drazin, P. G., and L. N. Howard, 1962: The instability to long waves of unbounded parallel inviscid flow. *J. Fluid Mech.*, **14**, 257–283.

Drazin, P. G. and Reid, W. H., 1981: *Hydrodynamic Stability*. Cambridge University Press, 525 pp.

Esch, R. E., 1957: The instability of a shear layer between two parallel streams. *J. Fluid Mech.*, **3**, 289–303.

Freymuth, P., 1966: On the transition in a separated laminar boundary layer. *J. Fluid Mech.* **25**, 683–704.

Fujita, T. T., 1981: Tornadoes and downbursts in the context of generalized planetary scales. *J. Atmos. Sci.*, **38**, 1511–1534.

Gall, R. L., R. T. Williams, and T. L. Clark, 1987: ON the minimum scale of fronts. *J. Atmos. Sci.*, **44**, 2562–2574.

Garner, S. T., 1989: Fully Lagrangian numerical solutions of unbalanced frontogenesis and frontal collapse. *J. Atmos. Sci.* **46**, 717–739.

Gaster, M., 1965: On the generation of spatially growing waves in a boundary layer. *J. Fluid Mech.*, **22**, 433-441.

Guha, A., M. Rahmani, and G. A. Lawrence, 2013: Evolution of a barotropic shear layer into elliptical vortices. *Phys. Rev. E.* **87**, 013020.

Goldstein, S., 1931: On the stability of superposed streams of fluids of different densities. *Proc. Roy. Soc. Lon.* **132**, 524–548.

Grasso, L. D., 2000: A numerical simulation of dryline sensitivity to soil moisture. *Mon. Wea. Rev.*, **128**, 2816–2834.

Hazel, P., 1972: Numerical studies of the stability of inviscid stratified shear flows. *J. Fluid Mech.* **51**, 39-61.

Heifetz, E., C. H. Bishop, and P. Alpert, 1999: Counter-propagating Rossby waves in the barotropic Rayleigh model of shear instability. *Quart. J. Roy. Meteor. Soc.* **125**., 2835-2853.

Heifetz E., and J. Methven, 2005: Relating optimal growth to counter-propogating Rossby waves in shear instability. *Phys. Fuids.* **17**, 064107-1-14.

Hoskins, B. J., 2003: Back to frontogenesis. *A Half Century of Progress in Meteorogogy: A Tribute to Richard Reed, Meteor. Monogr.*, No 31. Amer. Meteor. Soc., 49–59.

Jenkins, G. M., and D. G. Watts, 1969: *Spectral analysis and its applications*. Holden-Day, 525 pp.

Kanak, K. M., 2008: Vortical structures in convective boundary layers and implications for the initiation of deep convection. Preprints, 24th AMS Conference

on Severe Local Storms, Savannah, GA.

Kanak, K. M., Lilly, D. K., and Snow, J. T., 2000: The formation of vertical vortices in the convective boundary layer. *Quart. J. Roy. Meteor. Soc.*, **126A**, 2789-2810

Kawashima, M., and Y. Fujiyoshi, 2005: Shear instability wave along a snowband: Instability structure, evolution, and energetics derived from dual-Doppler radar data. *J. Atmos. Sci.,* **62**, 351–370.

Kida, S., 1981: Motion of an elliptic vortex in a uniform shear flow. *J. Phys. Soc. Jpn.* **50**, 3517–3520.

Lee, B. D., and R. B. Wilhelmson, 1997a: The numerical simulation of non-supercell tornadogenesis. Part I: Initiation and evolution of pretornadic misocyclone circulations along a dry outflow boundary. *J. Atmos. Sci.*, **54**, 32–60.

Lee, B. D., and R. B. Wilhelmson, 1997b: The numerical simulation of non-supercell tornadogenesis. Part II: Evolution of a family of tornadoes along a weak outflow boundary. *J. Atmos. Sci.*, **54**, 2387-2415.

Lee, B. D., C. A. Finley, and R. B. Wilhelmson, 2000: Simulating deep convection initiation by misocyclones. Preprints, 20th AMS Conference on Severe Local Storms, Orlando, FL.

Lessen, M., 1950: On the stability of free laminar boundary layer between parallel streams. *Nat. Adv. Comm. Aero., Wash.,* no. 979.

Lessen, M. and J. A. Fox, 1955: 50 Jahre Grenzschichtforschung, pp. 122-126. Braunschweig: Friedr. Vieweg.

Mansell, E. R., C. L. Ziegler, and E. C. Bruning, 2010: Simulated electrification of a small thunderstorm with two-moment bulk microphysics. *J. Atmos. Sci.*, **67**, 171–194.

Marquis, J., Y. P. Richardson, and J. M. Wurman, 2007: Kinematic observations of misocyclones along boundaries during IHOP. *Mon. Wea. Rev.*, 135, 1749–1768.

McCalla, T. R., 1967: *Introduction to Numerical Methods and FORTRAN Programming*. Wiley, 359 pp.

McWilliams, J. C. and M. J. Molemaker, 2009: Linear fluctuation growth during frontogenesis. *J. Phys. Oceanogr.* **39**, 3111–3129.

McWilliams, J. C. and M. J. Molemaker, 2011: Baroclinic frontal arrest: A sequel to unstable frontogenesis. *J. Phys. Oceanogr.*, **41**, 601–619.

Miao, Q. and B. Geerts, 2007: Finescale vertical structure and dynamics of some dryline boundaries observed in IHOP. *Mon. Wea. Rev.*, **135**, 4161–4184.

Michalke, A., 1965b: On spatially growing disturbances in an inviscid shear layer. *J. Fluid. Mech.* **23**, 521-544.

Michalke, A. and R. Wille, 1966: Stromungsvorgange im laminar-turbulenten Ubergangsbereich von Freistrahlgrenzschichten. *Proc. 11th Intern. Cong. Appl. Mech., Munich*, 1964 (ed. H. Gortler). Berlin: Springer-Verlag.

Miles, J. W., 1961: On the stability of heterogeneous shear flows. *J. Fluid Mech.* **10** 496–508.

Miles, J. W., and L. N. Howard, 1964: Note on a heterogeneous shear flow. *J. Fluid Mech.*, **20**, 331–336.

Murphey, H. V., R. M. Wakimoto, C. Flamant, and D. E. Kingsmill, 2006: Dryline on 19 June 2002 during IHOP. Part I: airborne Doppler and LEANDRE II analyses of the thin line structure and convection initiation. *Mon. Wea. Rev.,* **134**, 406–430.

Peckham, S. E., R. B. Wilhelmson, L. J. Wicker, and C. L. Ziegler, 2004: Numerical simulation of the interaction between the dryline and horizontal convective rolls. *Mon. Wea. Rev.*, **132**, 1792–1812.

Pedlosky, J., 1987: *Geophysical fluid dynamics.* Springer-Verlag, 710 pp.

Pietrycha, A. E., and E. N. Rasmussen. 2004: Finescale surface observations of the dryline: A mobile mesonet perspective. *Wea. Forecasting*, **19**, 1075–1088.

Pozrikidis, C. and J. J. L. Higdon, 1985: Nonlinear Kelvin-Helmholtz instability of a finite vortex layer. *J. Fluid Mech.***, 157**, 225–263.

Rayleigh, L., 1880: On the stability, or instability, of certain fluid motions. *Proc. Lond. Math. Soc.*, **Xi,** 57-70.

Rosenhead, L., 1931: The formation of vortices from a surface of discontinuity. *Proc. Roy. Soc. Lon.* **134**, 170–192.

Sanders, F., 1955: An investigation of the structure and dynamics of an intense frontal zone. *J. Meteor.*, **12**, 542–552.

Sato, H., 1959: Further investigation on the transition of two-dimensional separated layer at subsonic speeds. *J. Physical Soc. Jap.* **12**, 1797-1810.

Sato, H., 1960: The stability and transition of a two-dimensional jet. *J. Fluid Mech.*, **7**, 53-80.

Saucier, W. J., 1955: *Principles of meteorological analysis*. Dover Publications, Inc., 438 pp.

Schade, H. and A. Michalke, 1962: Aur hydrodynamischen Stabilitatstheorie ebener und freien Grenzschicht. *Z. Flugweiss*., **10**, 147.

Schultz, D. M., D. Keyser, and L. F. Bosart, 1998: The effect of large-scale flow on low-level frontal structure and evolution in midlatitude cyclones. *Mon. Wea. Rev.*, **126**, 1767-1791.

Schultz, D. M., C. C. Weiss, and P. M. Hoffman, 2007: The synoptic regulation of dryline intensity. *Mon. Wea. Rev.*, **135**, 1699–1709.

Scotti, R. S., and G. M. Corcos, 1972: An experiment on the stability of small disturbances in a stratified free shear layer. *J. Fluid Mech.* **52**, 499–528.

Shapiro, A., C. K. Potvin, and G. Jidong, 2009: Use of a vertical vorticity equation in variational dual-Doppler wind analysis. *J. Atmos. Oceanic Technol.*, **26**, 2089–2106.

Sun, W., and C. Wu., 1992: Formation and diurnal variation of the dryline. *J. Atmos. Sci.*, **49**, 1606–1619.

Tatsumi, T., and T. Kakutani, 1958: The stability of a two-dimensional laminar jet. *J. Fluid Mech.* **4**, 261–275.

Thorpe, S. A., 1971: Experiments on the instability of stratified shear flows: miscible fluids. *J. Fluid Mech.*, **46**, 299–319.

Wakimoto, R. M., and J. W. Wilson, 1989: Non-supercell tornadoes. *Mon. Wea. Rev*., **117**, 1113–1140.

Wakimoto, R. M., and N. T. Atkins, 1996: Observations on the origins of rotation: The Newcastle tornado during VORTEX 94. *Mon. Wea. Rev*., **124**, 384–407.

Wakimoto, R. M., C. Liu, and H. Cai, 1998: The Garden City, Kansas, storm during VORTEX 95. Part I: Overview of the storm's life cycle and mesocyclogenesis. *Mon. Wea. Rev*., **126**, 372–392.

Wakimoto, R. M., and H. V. Murphey, 2009: Analysis of a dryline during IHOP: Implications for convection initiation. *Mon. Wea. Rev.*, **137**, 912–936.

Wang, Y., 1975: An experimental study of the instability of a stably stratified free shear layer. *J. Fluid Mech.*, **71**, 563–575.

Warner, T. T., R. A. Peterson, and R. E. Treadon, 1997: A tutorial on lateral

boundary conditions as a basic and potentially serious limitation to regional numerical weather prediction. *Bull. Amer. Meteor. Soc.*, **78**, 2599–2617.

Wicker, L. J., and W. Skamarock, 2002: Time-splitting methods for elastic models using forward time schemes. *Mon. Wea. Rev.*, **130**, 2088–2097.

Wicker, L. J., and R. B. Wilhelmson, 1995: Simulation and analysis of tornado development and decay within a three-dimensional supercell thunderstorm. *J. Atmos. Sci.,* **52**, 2675–2703.

Winant, C. D., and F. K. Browand, 1974: Vortex pairing: the mechanism of turbulent mixing-layer growth at moderate Reynolds number. *J. Fluid. Mech.*, **63**, 237-255.

Weiss, C. C., H. B. Bluestein, and A. L. Pazmany, 2006: Finescale radar observations of the 22 May 2002 dryline during the International H2O project (IHOP). *Mon. Wea. Rev.*, **134**, 273–293.

Ziegler, C. L., W. J. Martin, R. A. Pielke and R. L. Walko, 1995: A modeling study of the dryline. *J. Atmos. Sci.,* **52**, 263–285.

Ziegler, C. L., T. J. Lee, and R. A. Pielke Sr., 1997: Convective initiation at the dryline: A modeling study. *Mon. Wea. Rev.*, **125**, 1001–1026.

Ziegler, C. L., and E. N. Rasmussen, 1998: The initiation of moist convection at the dryline: Forecasting issues from a case study perspective. *Wea. Forecasting.*, **13**, 1106-1131.

Ziegler, C. L., E. N. Rasmussen, T. R. Shepherd, A. I. Watson, and J. M. Straka, 2001: The evolution of low-level rotation in the 29 May 1994 Newcastle–Graham, Texas,
storm complex during VORTEX. *Mon. Wea. Rev.,* **129**, 1339-1368.

Ziegler, C. L., M. S. Buban, and E. N. Rasmussen, 2007: A Lagrangian objective analysis technique for assimilating in situ observations with multiple-radar-derived airflow. *Mon. Wea. Rev.,* **135**, 2417-2442.

Ziegler, C. L., E. R. Mansell, J. M. Straka, D. R. MacGorman, and D. W. Burgess, 2010: The impact of spatial variations of low-level stability on the life cycle of a simulated supercell storm. *Mon. Wea. Rev*., **138**, 1738–1766.

Appendix A: Derivation of Rayleigh shearing instability

The purpose of this Appendix is to rederive the expression for shearing instability as previously obtained by Rayleigh (1880). The current rederivation usefully includes a more detailed explanation of Rayleigh's method via current mathematical and meteorological notation as well as an illustration of various quantities that are employed in the solution. Appendix A.1 contains the expression for motion of a point vortex, which is employed in the Rayleigh (1880) solution as rederived in Appendix A.2. Appendix A.3 contains additional useful details of the derivation of the growth rate of the most-unstable mode.

A.1. Motion induced by a point vortex

Assuming 2-D incompressible flow, a streamfunction can be introduced such that in cylindrical coordinates,

$$u_r = \frac{1}{r}\frac{\partial \psi}{\partial \theta}, \quad u_\theta = -\frac{\partial \psi}{\partial r} \ .$$

Also assume that the flow is irrotational everywhere except at the origin where the vorticity is infinite. Therefore, $\nabla \, x \, u = 0$ everywhere except at $r = 0$, so that

$$\frac{1}{r}\frac{\partial}{\partial r}\left[r\left(-\frac{\partial \psi}{\partial r}\right)\right] - \frac{1}{r}\frac{\partial}{\partial \theta}\left[\frac{1}{r}\frac{\partial \psi}{\partial \theta}\right] = \Gamma\delta(r - r_0),$$

which is Laplace's equation in cylindrical coordinates. Here δ is the Dirac delta function and Γ is the circulation strength.

A solution is sought for which the induced velocity due to the point vortex is axisymmetric and purely tangential, so the above reduces to

$$\frac{1}{r}\frac{\partial}{\partial r}\left[r\left(-\frac{\partial \psi}{\partial r}\right)\right] = \Gamma\delta(r - r_0).$$

The circulation $\Gamma = \zeta A$, is finite in any arbitrary area including the singularity and its strength is equal to the strength of the point vortex. Integrating the above and using Stoke's theorem, $\iint_A \nabla \, x \, u \, dA = \oint_C u \cdot dl$, where the curve c includes the singularity, the above reduces to

$$\int_c -\frac{\partial \psi}{\partial r}\, dl = \int_0^{2\pi} -\frac{\partial \psi}{\partial r} r\, d\theta = -2\pi r \frac{\partial \psi}{\partial r} = \zeta \mathrm{A} = \Gamma,$$

$$u_\theta = -\frac{\Gamma}{2\pi r}.$$

That is, a source of vorticity at a point will induce tangential velocity everywhere in a fluid, with a magnitude proportional to the strength of the vorticity, and inversely proportional to the distance from the point.

A.2. Rayleigh (1880) solution

The Rayleigh (1880) solution assumes constant vorticity $\zeta = \left(\frac{\partial v}{\partial x} - \frac{\partial u}{\partial y}\right)$ in a finite shear layer that is bounded by an upper and lower surface, and also assumes that the vorticity outside the layer is zero. Assuming inviscid, 2-D flow, the vorticity in the shear layer remains constant in time. Suppose that upon this base state flow perturbations are superimposed that are proportional to $e^{i\kappa x}$ so that everything is periodic in an x-distance of $\lambda = 2\pi\kappa^{-1}$. Here λ is the wavelength and κ is the wavenumber.

In this flow there is a velocity potential such that a point vortex will induce a tangential velocity a at a point (x, y), whose distance from the point vortex at (x', y') is $r = \sqrt{(x - x')^2 + (y - y')^2}$ (Fig. A.2.1). The magnitude of the induced velocity is

$$u_\theta = -\frac{\Gamma}{2\pi r} = -\frac{\zeta dA}{2\pi r} \qquad \text{(R15)}$$

as derived in Appendix A.1. For consistency with the original derivation, the equation numbers in this Appendix A.2 will correspond to the equation numbers for the equivalent expressions as originally obtained by Rayleigh (1880) and will be denoted with prefix "R" to designate the equation number's origin.

In this problem, we will consider the flow to be composed of a base state upon which infinitesimal perturbations are superimposed. Let the equation for the position of the perturbed sheet be

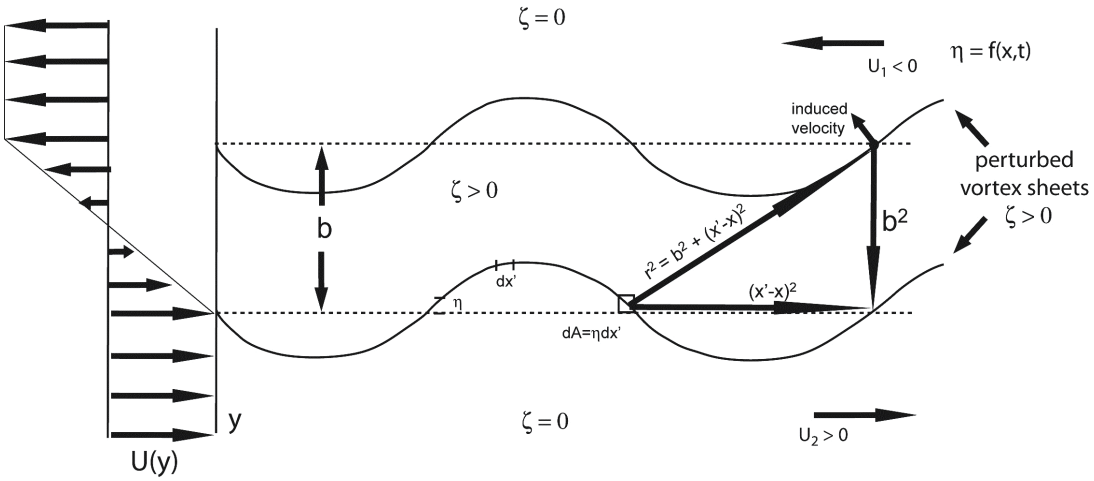

Figure A.2.1. Conceptual model of shear layer employed by Rayleigh (1880) to perform the Rayleigh stability analysis of plane shear flow.

$$\eta = He^{i\kappa x'}. \tag{R16}$$

Then, $dA = \eta dx'$ since η is assumed to be infinitesimal. Now if $\Delta\zeta$ is the difference in vorticity between values in the shear layer and outside the shear layer (where ζ=0), then by (R15),

$$u_\theta = -\frac{\Delta\zeta\eta dx\prime}{2\pi r}, \tag{R17}$$

$$\text{where } r = \sqrt{(x-x')^2 + (y-y')^2} = \sqrt{(x-x')^2 + b^2}. \tag{R18}$$

Here we refer to the induced velocity on one surface by a point on the other surface. Therefore since η is infinitesimal compared to the distance between the sheets, or thickness of the layer b, it follows that $(y-y') \approx b$. The induced velocity $u_\theta \perp r$. Next we resolve the u- and v-components of the velocity by multiplying (R17) by $\frac{b}{r}$ and $\frac{x'-x}{r}$ respectively so that

$$u = -\frac{b\Delta\zeta}{2\pi}\int_{-\infty}^{\infty}\frac{\eta dx'}{r^2}, \quad v = -\frac{\Delta\zeta}{2\pi}\int_{-\infty}^{\infty}\frac{\eta(x'-x)dx'}{r^2}$$

by (R16),

$$u = -\frac{bH\Delta\zeta}{2\pi}\int_{-\infty}^{\infty}\frac{e^{i\kappa x'}dx'}{b^2+(x'-x)^2}, \tag{R19}$$

$$v = -\frac{H\Delta\zeta}{2\pi}\int_{-\infty}^{\infty}\frac{e^{i\kappa x'}(x'-x)dx'}{b^2+(x'-x)^2}\,, \tag{R20}$$

Now make a change of variables such that $X = x' - x$, or $x' = X + x$. From (R19),

$$u = -\frac{bH\Delta\zeta}{2\pi}\int_{-\infty}^{\infty}\frac{e^{i\kappa(X+x)}d(X+x)}{b^2+X^2} \tag{R19a}$$

$$= -\frac{bH\Delta\zeta}{2\pi}\int_{-\infty}^{\infty}\frac{e^{i\kappa X}e^{i\kappa x}(dX+dx)}{b^2+X^2} \tag{R19b}$$

Now the induced velocity at some point (x, y) on a given sheet will be the sum of the induced velocities from *every* point on the other sheet, thus integrating along the entire x-axis. From this viewpoint, $x = const$ and $dx = 0$. Therefore, (R19b) becomes

$$u = -\frac{bH\Delta\zeta e^{i\kappa x}}{2\pi}\int_{-\infty}^{\infty}\frac{e^{i\kappa X}dX}{b^2+X^2}, \tag{R19c}$$

$$u = -\frac{bH\Delta\zeta e^{i\kappa x}}{2\pi}\int_{-\infty}^{\infty}\frac{[\cos(\kappa X)+i\,\sin(\kappa X)]dX}{b^2+X^2}. \tag{R19d}$$

Taking $Re(R19c)$,

$$u = -\frac{bH\Delta\zeta e^{i\kappa x}}{2\pi}\int_{-\infty}^{\infty}\frac{\cos(\kappa X)dX}{b^2+X^2}. \tag{R19e}$$

Using the following identity,

$$\int_{-\infty}^{\infty}\frac{\cos(mx)dx}{a^2+x^2} = \frac{\pi}{a}e^{-ma} \tag{R19f}$$

where $a = b, m = \kappa, x = X$, (R19e) reduces to

$$u = -\frac{1}{2}H\Delta\zeta e^{i\kappa x}e^{-\kappa b}. \tag{R19g}$$

Using the same change of variables, from (R20),

$$v = -\frac{H\Delta\zeta}{2\pi}\int_{-\infty}^{\infty}\frac{e^{i\kappa(X+x)}Xd(X+x)}{b^2+X^2} \tag{R20a}$$

$$= -\frac{H\Delta\zeta}{2\pi}\int_{-\infty}^{\infty}\frac{e^{i\kappa X}e^{i\kappa x}X(dX+dx)}{b^2+X^2} \tag{R20b}$$

$$= -\frac{H\Delta\zeta e^{i\kappa x}}{2\pi}\int_{-\infty}^{\infty}\frac{e^{i\kappa X}XdX}{b^2+X^2} \tag{R20c}$$

$$= -\frac{H\Delta\zeta e^{i\kappa x}}{2\pi}\int_{-\infty}^{\infty}\frac{[\cos(\kappa X)+i\,\sin(\kappa X)]XdX}{b^2+X^2}. \tag{R20d}$$

Now multiplying by *i* and taking $Re(R20d)$,

$$iv = \frac{H\Delta\zeta e^{i\kappa x}}{2\pi}\int_{-\infty}^{\infty}\frac{\mathrm{X}\sin(\kappa X)dX}{b^2+X^2}\,. \tag{R20e}$$

Using the following identity,

$$\int_{-\infty}^{\infty}\frac{x\,\sin(mx)dx}{a^2+x^2} = \pi e^{-ma} \tag{R20f}$$

where $a = b, m = \kappa, x = X$, multiplying again by i , (R20e) reduces to

$$v = -\frac{1}{2} iH\Delta\zeta e^{i\kappa x} e^{-\kappa b}. \tag{R20g}$$

Equations (R19g) and (R20g) correspond to equation (21) in Rayleigh (1880), i.e.,:

$$u = -\frac{1}{2} H\Delta\zeta e^{i\kappa x} e^{-\kappa b},$$
$$v = -\frac{i}{2} H\Delta\zeta e^{i\kappa x} e^{-\kappa b}. \tag{R21}$$

Now to determine the motion of a given sheet, we shall assume that the total motion is the sum of the induced velocities from the other sheet plus the induced velocities of the sheet itself. For the upper sheet, the total motion will be due to the induced velocity from the lower sheet, plus the self-induced velocity of the upper sheet and likewise for the lower sheet. Looking at the v-component, the self-induced velocity can be found by collapsing the shear layer down to a zero width. Therefore $b = 0$, and

$$v = -\frac{i}{2} H\Delta\zeta e^{i\kappa x}. \tag{R22}$$

Now suppose that on the upper part of the sheet, the base state flow is $u = U$ and on the lower side $u = -U$ so that

$$\zeta = \frac{\partial u}{\partial y} = \frac{2U}{b} \tag{R23}$$

inside the shear layer and $\zeta = 0$ outside the layer. Let the equations of the upper and lower surfaces perturbation positions be $\propto e^{int}$, so at time t, respectively,

$$\eta = He^{int} e^{i\kappa x},$$
$$\eta' = H' e^{int} e^{i\kappa x}, \tag{R24}$$

which is equivalent to (R16) with a time dependence added. From (R21),

$$v_o = -iH\mathrm{U}b^{-1} e^{int} e^{i\kappa x} e^{-\kappa b} \tag{R21b}$$

and from (R22)

$$v_s = -iH\mathrm{U}b^{-1} e^{int} e^{i\kappa x} \tag{R22b}$$

Here (R21b) represents the induced velocity at a point on the sheet due to the other sheet, whereas (R22b) represents the self-induced velocity of the sheet (i.e. b has

collapsed to zero). So the total motion for the upper sheet is

$$v_t = v_s + v_o = iH\mathrm{U}b^{-1}e^{int}e^{i\kappa x} - iH'\mathrm{U}b^{-1}e^{int}e^{i\kappa x}e^{-\kappa b},$$
$$v_{upper} = i\mathrm{U}b^{-1}e^{int}e^{i\kappa x}(H - H'e^{-\kappa b}) \qquad \text{(R24)}$$

For the lower sheet,

$$v_t = v_s + v_o = -iH'\mathrm{U}b^{-1}e^{int}e^{i\kappa x} + iH\mathrm{U}b^{-1}e^{int}e^{i\kappa x}e^{-\kappa b},$$
$$v_{lower} = i\mathrm{U}b^{-1}e^{int}e^{i\kappa x}(He^{-\kappa b} - H') \qquad \text{(R25)}$$

From these values of v, the position of the surfaces at time $t + dt$ can be computed. At time t the position of the surface is (x, η), whereas at $t + dt$ the new position is at $(x + udt, \eta + vdt)$. Thus, at time $t + dt$ at position x, the y-component of the sheet is

$$\eta + vdt - u\frac{d}{dx}(\eta + vdt)dt,$$
$$\eta + vdt - u\frac{d\eta}{dx}dt - u\frac{dv}{dx}dt^2 - uv\frac{1}{2}\frac{d}{dx}(dt^2)$$

Neglecting squares of small quantities,

$$\eta(t + dt) = \eta(t) + (v - U\tfrac{d\eta}{dx})dt.$$

From (R24),

$$\tfrac{d\eta}{dt} = in\eta.$$

So that for the upper surface,

$$\tfrac{\eta(t+dt)-\eta(t)}{dt} = v - U\tfrac{d\eta}{dx},$$
$$inHe^{int}e^{i\kappa x} = i\mathrm{U}b^{-1}e^{int}e^{i\kappa x}(H - H'e^{-\kappa b}) - Ui\kappa He^{int}e^{i\kappa x},$$
$$nH = Ub^{-1}(H - H'e^{-\kappa b}) - U\kappa H,$$
$$\left(\tfrac{nb}{U} - 1 + \kappa b\right)H + H'e^{-\kappa b} = 0. \qquad \text{(R26)}$$

For the lower surface,

$$inHe^{int}e^{i\kappa x} = i\mathrm{U}b^{-1}e^{int}e^{i\kappa x}(He^{-\kappa b} - H') - Ui\kappa He^{int}e^{i\kappa x},$$
$$nH = Ub^{-1}(He^{-\kappa b} - H') - U\kappa H,$$
$$\left(-\tfrac{nb}{U} - 1 + \kappa b\right)H' + He^{-\kappa b} = 0. \qquad \text{(R27)}$$

Eliminating the variables H and H' from (R26) and (R27),

$$H = -\left(-\frac{nb}{U} - 1 + \kappa b\right) H' e^{\kappa b},$$
$$\left(\frac{nb}{U} - 1 + \kappa b\right)\left(\frac{nb}{U} + 1 - \kappa b\right) H' e^{\kappa b} + H' e^{-\kappa b} = 0,$$
$$\left(\frac{nb}{U} - 1 + \kappa b\right)\left(\frac{nb}{U} + 1 - \kappa b\right) + e^{-2\kappa b} = 0.$$

Expanding the 1st term,

$$\frac{n^2 b^2}{U^2} + \frac{nb}{U} - \frac{n\kappa b^2}{U} - \frac{nb}{U} - 1 + \kappa b + \frac{n\kappa b^2}{U} + \kappa b - \kappa^2 b^2$$
$$= \frac{n^2 b^2}{U^2} - 1 + 2\kappa b - \kappa^2 b^2$$

So,

$$\frac{n^2 b^2}{U^2} - 1 + 2\kappa b - \kappa^2 b^2 + e^{-2\kappa b} = 0,$$
$$-\frac{n^2 b^2}{U^2} + (\kappa b - 1)^2 - e^{-2\kappa b} = 0,$$
$$n^2 = \frac{U^2}{b^2}[(\kappa b - 1)^2 - e^{-2\kappa b}]. \qquad \text{(R28)}$$

When κb is small (therefore the wavelength is large compared to b), the case approximates that of a sudden transition. Expanding in a Taylor series,

$$n^2 = \frac{U^2}{b^2}[1 - 2\kappa b + \kappa^2 b^2 - (1 - 2\kappa b + 2\kappa^2 b^2 + \cdots)] \approx -\kappa^2 U^2. \qquad \text{(R29)}$$

Since $n^2 < 0$, the motion is unstable. In the other case, when κb is large,

$$n^2 = \kappa^2 U^2. \qquad \text{(R30)}$$

In this case, the motion is stable.

A.3. Growth rate of Rayleigh shearing instability

The growth rate equation (R28) states that

$$n^2 = \frac{U^2}{b^2}[(\kappa b - 1)^2 - e^{-2\kappa b}].$$

A plot of equation (R28) is shown in Fig. A3.1. To determine the most-unstable wavenumber (i.e., the peak in the curve in Fig. A.3.1) differentiate the growth rate with respect to wavenumber and set the result to zero.

$$\frac{\partial n}{\partial \kappa} = \frac{U}{2b}\left[(\kappa b - 1)^2 - e^{-2\kappa b}\right]^{\frac{1}{2}}\left[2(\kappa b - 1) + 2e^{-2\kappa b}\right] = 0$$
$$\left[2b(\kappa b - 1) + 2be^{-2\kappa b}\right] = 0$$

$$e^{-2\kappa b} + \kappa b - 1 = 0\,,$$

which has a solution (and thus the most-unstable wavenumber is when) $\kappa b \approx 0.8$ or $\lambda \approx 7.9b$.

Note that that the neutral mode occurs when the growth rate is zero (i.e., n = 0), which corresponds to $kb \approx 1.279$. Again since

$$n^2 = \frac{U^2}{b^2}[(\kappa b - 1)^2 - e^{-2\kappa b}],$$

it follows that

$$0 = \frac{U^2}{b^2}[(\kappa b - 1)^2 - e^{-2\kappa b}],$$

$$0 = [(\kappa b - 1)^2 - e^{-2\kappa b}],$$

$$0 \approx (1.279 - 1)^2 - e^{-2.558},$$

$$0 \approx (0.279)^2 - 0.07745,$$

and finally

$$0 \approx 0.07784 - 0.07745 \approx 0.00039.$$

Thus to a few parts in 10,000, $kb \approx 1.279$ closely approximates where the neutral mode occurs (also see Fig. A.3.1).

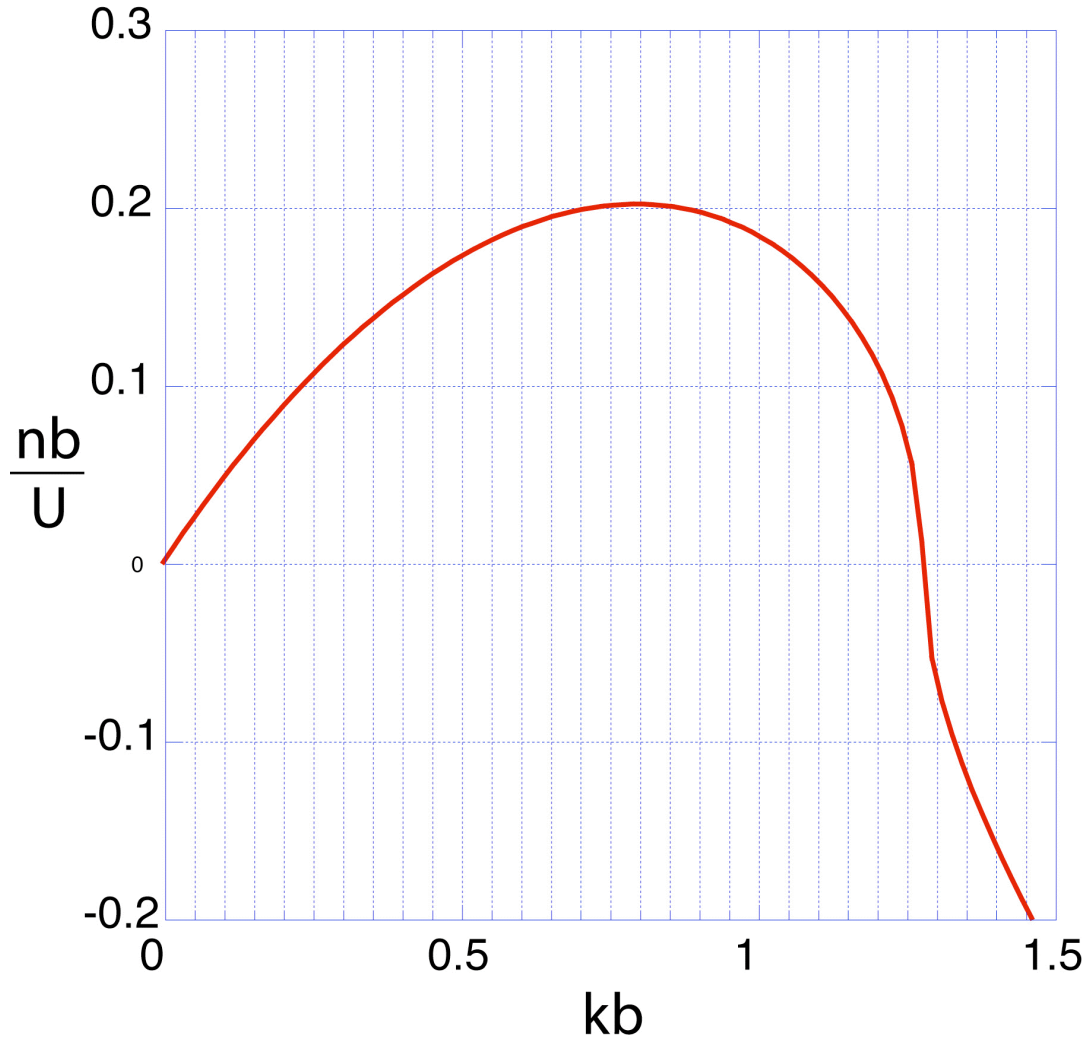

Figure A.3.1. Instability curve as a function of wavenumber. Positive values denote instability. Note that this is an expanded version of Fig. 2.1.

Appendix B: Simulated surface fluxes

Having realistic parameterized surface fluxes is important owing to their influence on simulated BL structure. For example, inclusion of surface heating and specification of unstable stratification at the lateral boundaries from the Lagrangian analyses forces the development of dry-convective plume-like structures in the simulated BL (Fig. 4.8d-f).

Observed surface fluxes obtained from the NCAR Integrated Surface Flux Facility (ISFF) located at Elmwood, OK during IHOP (e.g., Conzemius and Fedorovich 2008) are compared to fluxes calculated at the closest grid point to the ISFF site (Table B1, Fig. B1). The observed and simulated sensible and latent heat fluxes are similar in both magnitude and evolution throughout the 90-minute period. The RMS error between the observed and simulated sensible heat fluxes (30.52 W m^{-2}) is small relative to the flux values (~125 W m^{-2}). The RMS error for the latent heat flux (17.31 W m^{-2}) is smaller as are the actual values (~50 W m^{-2}); hence the normalized RMS error is larger in comparison. However, the RMSE of latent heat flux seems reasonable given the larger range of possible values.

The RMSEs are similarly small for the observed and modeled skin temperatures (0.96 K) compared to the magnitude of temperatures and their ranges. Likewise, the observed and modeled surface temperatures also match closely with a RMSE of 0.76 K. However, there is more variance in the observations than in the simulations. The larger observed variance could be a consequence of the sensors measuring transient features unresolved by the model, the passage of observed (but not modeled) cumuli over the ISFF sensors, or the passage of modeled (but not observed) cumuli over the site location in the model domain. In addition, the formulation of the surface flux parameterization is such that the surface fluxes are rather smooth in the model.

Parameter	RMSE	Bias
Sensible heat flux (W m^{-2})	30.52	-11.72
Latent heat flux (W m^{-2})	17.31	-1.47
Skin temperature (K)	0.96	-0.13
Surface temperature (K)	0.76	0.02

Table B1. Root mean square error (RMSE) and bias between the simulated and observed sensible heat flux, latent heat flux, skin temperature, and surface temperature. Observed values are from the Elmwood, OK flux station and simulated values are from the grid point nearest to this station in the model.

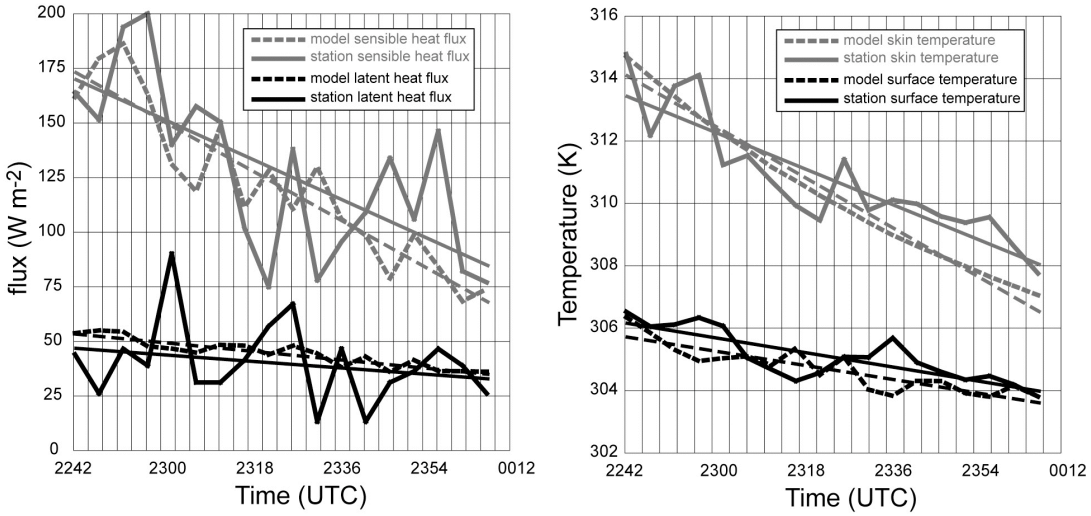

Figure B.1. Time-series of simulated and observed sensible and latent heat fluxes (right) and surface and skin temperatures (left). Also shown are the (solid) linear trend lines.

Appendix C: Idealized simulations sensitivity tests

A barotropic and a baroclinic simulation have been rerun to test sensitivities to the initial perturbation method and grid size. The first barotropic test consists of rerunning the bt8m20s simulation with the same grid spacing with one additional grid point added in the *x*-direction (i.e., NX increased from 150 to 151). Since the model employs the Arakawa C-grid (wherein the v-component point is aligned with the scalar point in the y-direction), adding an additional grid point effectively tests the solution's sensitivity to whether the shear zone is centered on a scalar point or a momentum point. After an initial period of transient growth, a single spectral peak emerges at nearly the same wavenumber (i.e., close to that predicted by linear theory) in both the original and test simulations (Fig. C.1). The perturbations in the test simulation initially grow slightly slower than in the original simulation, then accelerate at later times to achieve nearly the same amplitude as the original simulation by 1980 s. In both the original and test simulations, transient growth in side-bands slows as the main peak emerges.

The second barotropic test simulation uses a different initial perturbation than the original random 0.01 m s^{-1} v-component velocity perturbation, and is designed to address sensitivities at the later stages of the simulation (i.e., 3-D structure) to the nature of the initial perturbation. The v-component wind in the second test simulation is initialized with sine waves in the y-direction, where each wave is prescribed with a random amplitude and random phase angle. The random amplitude ranges from 0 to 0.01 m s^{-1}, while the random phase angle has the range of $-\pi$ to π. Although the chosen value of constant sine wavenumber is equal to the

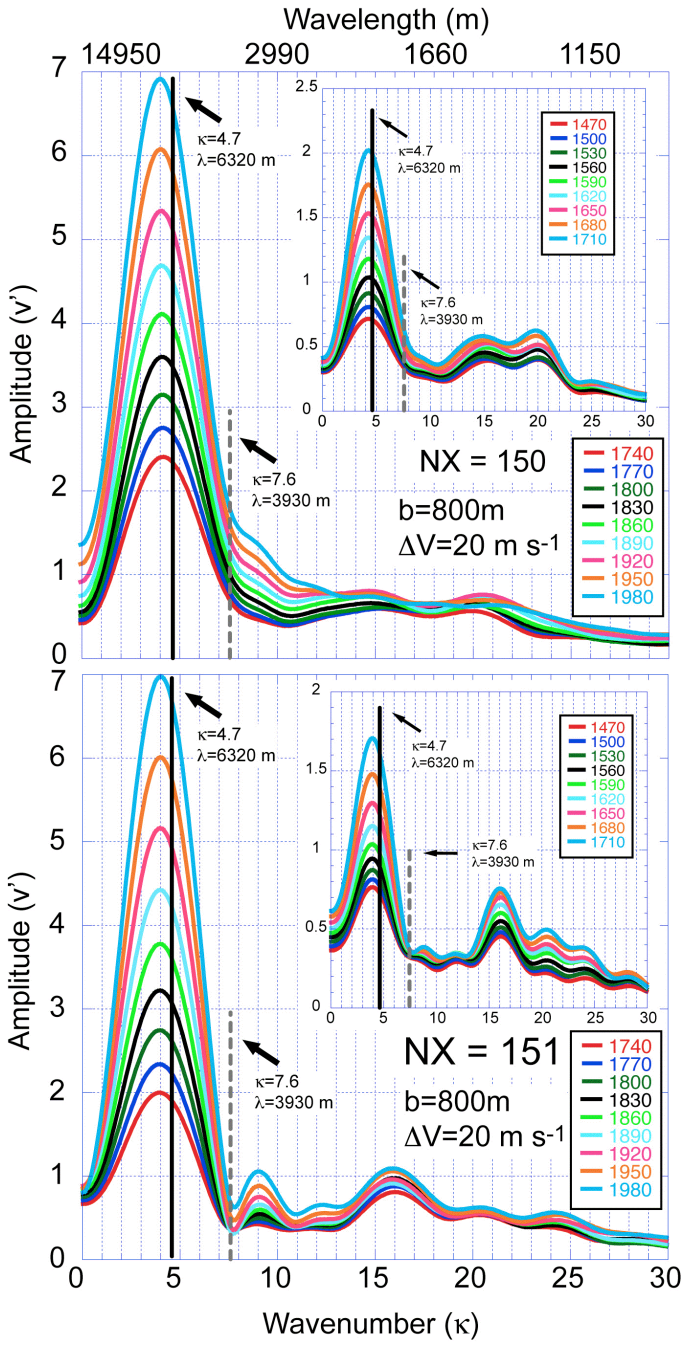

Figure C.1. Spectral density estimates of the v-component perturbation wind amplitude (m s^{-1}) as a function of wavenumber at from the period of 1740-1980 and 1470-1710s (inset) seconds after the start of simulation bt8m20s, for the original simulation (top) and extended grid test (bottom). The vertical black line denotes the most-unstable wavenumber (4.7) and the gray dashed line denotes the neutral wavenumber predicted by linear theory (7.6).

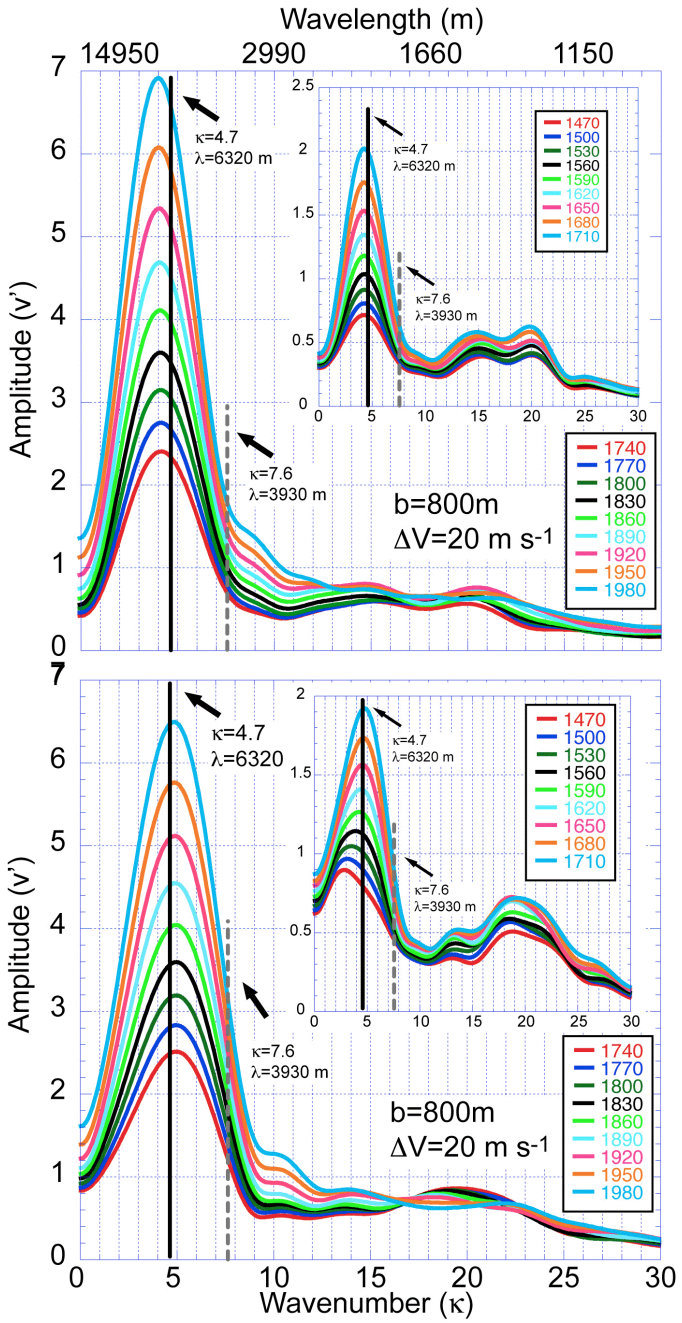

Figure C.2. Spectral density estimates of the v-component perturbation wind amplitude (m s^{-1}) as a function of wavenumber at from the period of 1740-1980 and 1470-1710s (inset) seconds after the start of simulation bt8m20s, for the original simulation (top) and sine wave test (bottom). The vertical black line denotes the most-unstable wavenumber (4.7) and the gray dashed line denotes the neutral wavenumber predicted by linear theory (7.6).

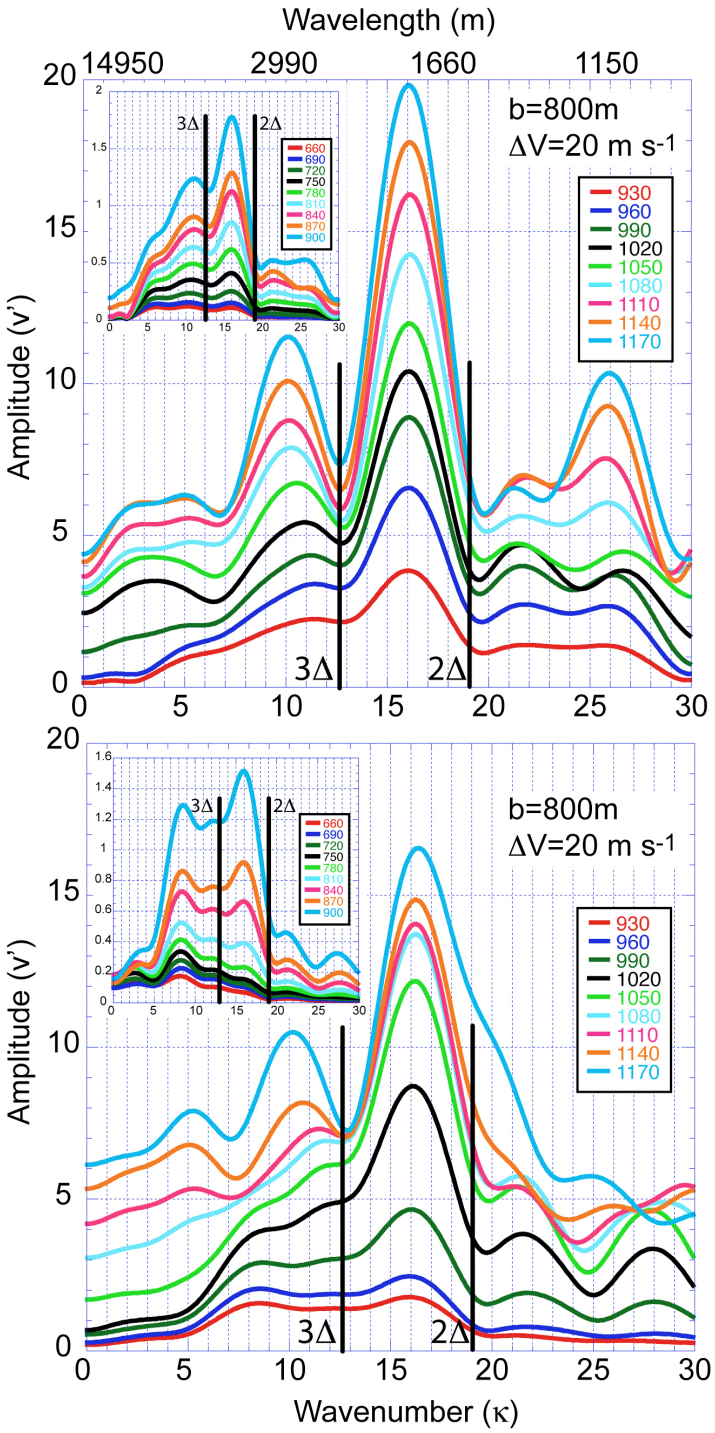

Figure C.3. Spectral density estimates of the v-component perturbation wind amplitude (m s^{-1}) as a function of wavenumber at from the period of 930-1170 and 660-900s (inset) seconds after the start of simulation bt8m20s, for the original simulation (top) and temperature perturbation (bottom). The vertical black lines denote the most-unstable wavenumbers predicted by linear theory for a shear zone width of 2Δ and 3Δ.

theoretical most-unstable wavenumber (k = 4.7), the randomized amplitude and phase angle values effectively produce an initial 2-D (horizontal) white noise spectral density field. Similar to the first test, a single dominant spectral peak in the spectrum emerges in both the original and test simulations after an initial transient period of growth. However, the peak in the original was at a slightly lower wavenumber and the peak in the test was at a slightly higher wavenumber than the theoretical maximum (Fig. C.2).

The last sensitivity test has been conducted for baroclinic simulation bc8m20s. Instead of directly perturbing the v-component wind, a random potential temperature perturbation of 0.007 K was used to initialize the model. Since the baroclinic simulation features a collapsing shear zone and thus variable growth rates, this perturbation value has been chosen so that the resulting overall amplitudes between the test and original simulations are similar at the same times. Both the original and test simulations feature an emerging peak somewhere between the theoretical most-unstable modes of a shear zone width in the range of $2\Delta - 3\Delta$ (Fig. C.3). Additional growth is also observed at wavenumbers in the side-bands adjacent to the peak. The amplitudes of the peaks are similar between the original and test simulations, however the peak amplitude is higher at higher wavenumbers in the test simulation.

These test simulations collectively demonstrate that widely differing initial conditions lead to rather small differences in the growth of the initial perturbations. Most importantly, the results remain consistent with the conclusions of this study that the early growth of small initial perturbations is adequately described by the

linear theory governing horizontal shearing instability (HSI). These sensitivity tests also affirm the corollary conclusion that linear theory may be extended into the nonlinear regime as larger structures emerge from the shear zone.